

Measurement of the inclusive $t\bar{t}$ cross section and search for additional scalars in $t\bar{t}$ final states at the CMS experiment

Dissertation

zur Erlangung des Doktorgrades
an der Fakultät für Mathematik, Informatik und Naturwissenschaften
Fachbereich Physik
der Universität Hamburg

vorgelegt von
Laurids Jeppe

Hamburg
2025

Gutachter der Dissertation:	Prof. Dr. Christian Schwanenberger Dr. Alexander Grohsjean
Zusammensetzung der Prüfungskomission:	Prof. Dr. Christian Schwanenberger Dr. Alexander Grohsjean TBD TBD TBD
Vorsitzender der Prüfungskomission:	TBD
Datum der Disputation:	TBD
Vorsitzender des Fach-Promotionsausschusses PHYSIK:	Prof. Dr. Wolfgang J. Parak
Leiter des Fachbereichs PHYSIK:	Prof. Dr. Markus Drescher
Dekan der Fakultät MIN:	Prof. Dr.-Ing. Norbert Ritter

Abstract

Two measurements and two phenomenological studies of top quark pair ($t\bar{t}$) production at the CMS experiment are presented. The inclusive $t\bar{t}$ production cross section $\sigma_{t\bar{t}}$ is measured for the first time at $\sqrt{s} = 13.6$ TeV, using 1.21 fb^{-1} of early LHC Run 3 data. By combining the dilepton and lepton+jets ($\ell+\text{jets}$) decay channels of $t\bar{t}$ and constraining the lepton and b tagging efficiencies *in situ*, a precision of 3.4% comparable to previous $\sigma_{t\bar{t}}$ measurements is achieved.

Following this, a study of off-shell $t\bar{t}$ production and $t\bar{t}/tW$ interference is performed using the Monte Carlo (MC) generator **bb41**, which is validated for the first time in CMS simulation and compared to other MC generators, finding a significantly improved description of the data.

Finally, a search for spin-0 states decaying to $t\bar{t}$ in the dilepton channels is presented, using 138 fb^{-1} of LHC Run 2 data at $\sqrt{s} = 13$ TeV. The invariant $t\bar{t}$ mass ($m_{t\bar{t}}$) is combined with spin correlation observables to gain sensitivity to the spin and \mathcal{CP} structure of possible new intermediate states. A statistically significant excess of events over the $t\bar{t}$ continuum background is observed at low values of $m_{t\bar{t}}$ and for spin correlations consistent with a pseudoscalar state. It is interpreted in terms of a pseudoscalar $t\bar{t}$ bound state η_t , and its cross section is measured to be $\sigma(\eta_t) = 8.7 \pm 1.1\text{ pb}$ using a simplified model inspired by non-relativistic quantum chromodynamics.

The same data is further interpreted in terms of generic pseudoscalar or scalar bosons, and exclusion regions on their coupling to the top quark are derived both for the dilepton channels alone as well as in a combination with a separate analysis of the $\ell+\text{jets}$ channels. As a third interpretation of the data, Axion-Like Particles (ALPs) decaying to $t\bar{t}$ are considered in the case of vanishing tree-level ALP-gluon couplings, while the more generic case is studied phenomenologically in simulation.

Zusammenfassung

Es werden zwei Messungen und zwei phänomenologische Studien zur Produktion von Top-Quark-Paaren ($t\bar{t}$) am CMS-Experiment vorgestellt. Der inklusive $t\bar{t}$ -Produktionsquerschnitt $\sigma_{t\bar{t}}$ wird zum ersten Mal bei $\sqrt{s} = 13.6 \text{ TeV}$ gemessen, unter Verwendung von frühen LHC Run 3-Daten mit integrierter Luminosität von 1.21 fb^{-1} . Durch Kombination der Dilepton- und Lepton+Jets ($\ell+\text{jets}$)-Zerfallskanäle von $t\bar{t}$ und simultane Bestimmung der Lepton- und b-tagging-Effizienzen *in situ* wird eine mit früheren $\sigma_{t\bar{t}}$ -Messungen vergleichbare Präzision von 3.4% erreicht.

Anschließend wird Produktion von off-shell $t\bar{t}$ und $t\bar{t}/tW$ -Interferenz mit dem Monte Carlo (MC)-Generator **bb41** untersucht, der zum ersten Mal in der CMS-Simulation validiert und mit anderen MC-Generatoren verglichen wird und dabei zu einer deutlich verbesserten Beschreibung der Daten führt.

Schließlich wird eine Suche für nach $t\bar{t}$ zerfallende Spin-0-Zustände in den Dilepton-Kanälen mit Daten von LHC Run 2, einer integrierten Luminosität von 138 fb^{-1} und $\sqrt{s} = 13 \text{ TeV}$ vorgestellt. Die invariante Masse von $t\bar{t}$ ($m_{t\bar{t}}$) wird mit Spinkorrelations-Observablen kombiniert, um die Sensitivität gegenüber dem Spin und der \mathcal{CP} -Struktur möglicher neuer intermediärer Zustände zu erhöhen. Ein statistisch signifikanter Überschuss von Ereignissen im Vergleich zum $t\bar{t}$ -Kontinuums-Hintergrund wird bei geringen Werten von $m_{t\bar{t}}$ und für Spinkorrelationen konsistent mit einem pseudoskalaren Zustand beobachtet. Der Überschuss wird als pseudoskalarer gebundener $t\bar{t}$ -Zustand η_t interpretiert, und dessen Produktionsquerschnitt wird mithilfe eines vereinfachten, von nichtrelativistischer Quantenchromodynamik inspirierten Modells zu $\sigma(\eta_t) = 8.7 \pm 1.1 \text{ pb}$ gemessen.

Die selben Daten werden weiterhin als generische pseudoskalare oder skalare Bosonen interpretiert, und Ausschlussregionen hinsichtlich ihrer Kopplungen zum Top-Quark werden sowohl für die Dilepton-Kanäle allein als auch für eine Kombination mit einer separaten Analyse der $\ell+\text{jets}$ -Kanäle berechnet. Als eine dritte Interpretation der Daten werden zu $t\bar{t}$ zerfallende Axion-Like Particles (ALPs) im Fall verschwindender ALP-Gluon-Kopplungen betrachtet, während der allgemeinere Fall auf phänomenologische Weise in Simulationsdaten untersucht wird.

Eidesstattliche Versicherung

Hiermit versichere ich an Eides statt, die vorliegende Dissertationsschrift selbst verfasst und keine anderen als die angegebenen Hilfsmittel und Quellen benutzt zu haben.

Sofern im Zuge der Erstellung der vorliegenden Dissertationsschrift auf generativer Künstlicher Intelligenz (gKI) basierende elektronische Hilfsmittel verwendet wurden, versichere ich, dass meine eigene Leistung im Vordergrund stand und dass eine vollständige Dokumentation aller verwendeten Hilfsmittel gemäß der guten wissenschaftlichen Praxis vorliegt. Ich trage die Verantwortung für eventuell durch die gKI generierte fehlerhafte oder verzerrte Inhalte, fehlerhafte Referenzen, Verstöße gegen das Datenschutz- und Urheberrecht oder Plagiate.

Datum

Unterschrift des Doktoranden

Contents

1	Introduction	11
2	Theoretical framework	13
2.1	Standard Model	13
2.1.1	Top quark	14
2.1.2	Higgs mechanism	15
2.2	The $p p \rightarrow t\bar{t}$ process	16
2.2.1	Spin state of the $t\bar{t}$ system	18
2.2.2	Spin density matrix	21
2.2.3	Bound state effects in $t\bar{t}$	23
2.3	Beyond the Standard Model	27
2.3.1	Heavy scalars in $t\bar{t}$ production	27
2.3.2	Two-Higgs Doublet Model	30
2.3.3	Axion-Like Particles	30
3	Monte Carlo event generation	33
3.1	Matrix Element generators	33
3.2	Parton showers and matching	35
3.3	Multi-parton interactions	37
3.4	Hadronization	38
3.5	Pileup	39
3.6	Detector and trigger simulation	39
4	Experimental methods	40
4.1	The Large Hadron Collider	40
4.2	The CMS experiment	41
4.3	Object reconstruction	43
4.4	Statistical interpretation	45
5	Measurement of the inclusive $t\bar{t}$ cross section at $\sqrt{s} = 13.6$ TeV	50
5.1	Introduction	50
5.2	Data sets and event selection	51
5.2.1	Data sets	51
5.2.2	Object definition	52
5.2.3	Channel definition	53

5.3	Corrections	54
5.3.1	Experimental corrections	55
5.3.2	Data-driven background estimation	59
5.4	Control distributions	65
5.5	Systematic uncertainties	69
5.6	Fit results	75
5.6.1	Statistical checks	75
5.6.2	Top quark mass dependence	78
5.7	Summary and Outlook	79
6	Simulation of on- and off-shell $t\bar{t}$ production with bb4l	81
6.1	Introduction	81
6.2	The Monte Carlo generator bb4l	81
6.3	Other $t\bar{t}$ Monte Carlo generators	82
6.3.1	hvq	83
6.3.2	ST_wtch	83
6.3.3	ttb_NLO_dec	83
6.4	Technical setup	84
6.4.1	Parton shower matching	84
6.4.2	Same-flavor leptons	85
6.5	Results	85
6.5.1	Comparison between generators	85
6.5.2	Comparison of FSR matching settings	91
6.5.3	Recoil in top decay	93
6.6	Summary and Outlook	94
7	Search for heavy scalar or pseudoscalar bosons in $t\bar{t}$ final states	96
7.1	Introduction	96
7.2	Analysis setup	97
7.2.1	Data sets	97
7.2.2	Object definition	100
7.2.3	Event selection	101
7.2.4	Experimental corrections	101
7.2.5	Reconstruction of the $t\bar{t}$ system	104
7.2.6	Sensitive observables	108
7.3	Higher-order corrections in $t\bar{t}$	108
7.3.1	NNLO QCD corrections	109
7.3.2	NLO EW corrections	109
7.4	Matrix element reweighting for A/H signals	112
7.4.1	Principle of the method	112
7.4.2	Combination of multiple origin samples	113
7.4.3	Validation	114

7.5	Systematic uncertainties	114
7.5.1	Theory uncertainties	116
7.5.2	Experimental uncertainties	117
7.5.3	Uncertainty smoothing	119
7.5.4	Differences between MC generators	121
7.6	Pre-fit distributions	123
7.7	Interpretation of the excess	129
7.7.1	Extraction of $t\bar{t}$ bound state effects	129
7.7.2	Parity of the excess	129
7.7.3	Checks of the result	131
7.7.4	Interpretation in terms of A and H	137
7.7.5	Comparison of η_t and A interpretations	138
7.8	Limits on A/H bosons	140
7.9	Combination with the ℓ +jets channels	146
7.9.1	Analysis strategy in the ℓ +jets channel	146
7.9.2	A/H limits	147
7.9.3	Simultaneous A+H exclusion contours	149
7.10	Comparison to other results	154
7.10.1	ATLAS $t\bar{t}$ threshold measurement	154
7.10.2	ATLAS A/H $\rightarrow t\bar{t}$ search	157
7.10.3	Other $t\bar{t}$ measurements	158
7.11	Summary and Outlook	159
8	Investigation of Axion-Like Particles decaying to $t\bar{t}$	162
8.1	Introduction	162
8.2	Translation of experimental limits	162
8.3	Phenomenological setup	164
8.4	Comparison of ALP and A	166
8.5	Projected limits for ALPs	168
8.6	Summary and Outlook	170
9	Summary and Conclusions	172
A	Bibliography	174
B	Acknowledgements	196
C	Appendices	197
C.1	Sample normalizations in the matrix element reweighting	197

¹ 1 Introduction

² It has always been the goal of high-energy physics to decipher the fundamental rules
³ of nature. The most recent triumph in this journey was undoubtedly the discovery of
⁴ the Higgs boson at the ATLAS and CMS experiments of the Large Hadron Collider
⁵ (LHC) in 2012 [1–3], thus completing the Standard Model of particle physics (SM).
⁶ Since then, the SM has been measured with ever-growing precision in the hope of
⁷ finding and characterizing possible deviations from its predictions, and searches for
⁸ new physics beyond the Standard Model (BSM) have been performed in various
⁹ final states with complementary signatures. So far, no significant discrepancy has
¹⁰ been found.

¹¹ One promising avenue to search for new physics is the top quark, which is the
¹² most massive fundamental particle in the SM. It is thus particularly relevant in the
¹³ search for new particles with Yukawa-like couplings, i.e. couplings proportional to
¹⁴ the particle mass, such as extended Higgs sectors. It is also of interest in the context
¹⁵ of the SM: as the only colored particle that decays before hadronizing, it allows for
¹⁶ measurements of spin properties that are unaccessible for all other quarks.

¹⁷ In this thesis, different aspects of top quark pair ($t\bar{t}$) production in proton-proton
¹⁸ collisions at the LHC are studied at the Compact Muon Solenoid (CMS) experi-
¹⁹ ment [4], which is one of the two large general-purpose LHC experiments. The first
²⁰ topic is a measurement of the inclusive $t\bar{t}$ production cross section, performed at a
²¹ center-of-mass energy of $\sqrt{s} = 13.6 \text{ TeV}$ [5]. This world-record energy was reached
²² by the LHC for the first time in 2022 at the start of Run 3, after three years of shut-
²³ down and technical upgrades. The measurement performed here uses only 1.21 fb^{-1}
²⁴ of data, taken in July and August 2022. To achieve a precision on the $t\bar{t}$ cross sec-
²⁵ tion comparable with previous LHC measurements, experimental corrections such
²⁶ as lepton and b quark jet identification efficiencies have been estimated *in situ*, i.e.
²⁷ as part of the cross section measurement. The result was the first public result of
²⁸ LHC Run 3. It showed the high quality of the then-fresh collision data and provided
²⁹ a first confirmation of the SM at the new energy frontier.

³⁰ Second, the modeling of $t\bar{t}$ production in off-shell regions of phase space as well
³¹ as the interference between $t\bar{t}$ and tW production at CMS is studied [6]. This is
³² done using the Monte Carlo (MC) event generator **bb41** [7], which computes the full
³³ $pp \rightarrow b\bar{b}\ell^+\ell^-\nu_\ell\bar{\nu}_\ell$ matrix element for the dilepton decay channel of $t\bar{t}$, thus naturally
³⁴ including off-shell and interference effects. **bb41** is validated for the first time in
³⁵ the CMS simulation setup, and compared to other MC generators for $t\bar{t}$ production,
³⁶ preparing its use in future precision measurements at CMS.

Finally, a search for new spin-0 resonances decaying to $t\bar{t}$ is presented, utilizing the complete CMS Run 2 data set corresponding to an integrated luminosity of 138 fb^{-1} [8, 9]. The analysis focuses on the dileptonic decay channel. In addition to the invariant mass of the $t\bar{t}$ pair $m_{t\bar{t}}$, spin correlation observables derived from the kinematics of the leptons and top quarks are employed to probe the spin and \mathcal{CP} nature of potential new intermediate resonances. Notably, a statistically significant excess over SM predictions is observed at low $m_{t\bar{t}}$, with features consistent with a pseudoscalar hypothesis. The excess is found to be consistent with a pseudoscalar $t\bar{t}$ (quasi-)bound state, which is expected to exist in the SM according to non-relativistic QCD calculations, though its modeling remains a challenge. This constitutes the first time such a $t\bar{t}$ bound state is experimentally observed.

Alternatively, the results are interpreted in terms of generic pseudoscalar or scalar bosons, as expected e.g. in a Two-Higgs-Doublet Model. The interference of these new bosons decaying to $t\bar{t}$ and SM $t\bar{t}$ production is taken into account, leading to complex signatures in the $m_{t\bar{t}}$ spectrum. In addition to an interpretation of the same low- $m_{t\bar{t}}$ excess, exclusion regions are derived for the presence of either one or two such new bosons in terms of their couplings to the top quark. For this purpose, the analysis of the dilepton decay channel of $t\bar{t}$ is further combined with a separate analysis of the lepton+jets decay channel.

As a third interpretation, heavy Axion-Like Particles (ALPs) decaying to $t\bar{t}$ are considered for the first time [10]. After explicitly translating the experimental results for generic pseudoscalars to ALPs in the case of no explicit gluon couplings, the general case is studied in simulated events. Sensitivity estimates for heavy ALPs coupling to top quarks, and for the prospects to distinguish them from other pseudoscalars, are derived for the currently available luminosity as well as future projections.

The thesis is organized as follows. In Chapters 2 to 4, the framework used for the analyses is outlined. In particular, Chapter 2 describes aspects of the SM and BSM theories relevant for this work, Chapter 3 briefly discusses the machinery of Monte Carlo generators, and Chapter 4 describes the LHC and the CMS detector as well as object reconstruction and statistical inference techniques. Following that, Chapters 5 to 8 each discuss one of the experimental or phenomenological results that comprise this work: the inclusive $t\bar{t}$ cross section measurement in Chapter 5, the study of off-shell $t\bar{t}$ production and $t\bar{t}/tW$ interference in Chapter 6, the search for spin-0 states in $t\bar{t}$, including its interpretation as a $t\bar{t}$ bound state, in Chapter 7, and the investigation of ALPs decaying to $t\bar{t}$ in Chapter 8. Chapters 5 and 6 fully consist of work done as part of this thesis, while in Chapters 7 and 8 the major contributions from this thesis are summarized at the beginning of the chapters. Finally, a short summary and outlook is given in Chapter 9.

⁷⁶ 2 Theoretical framework

⁷⁷ This chapter gives an outline of the theoretical concepts and models used in this
⁷⁸ thesis. It is split into two parts: First, the Standard Model of elementary par-
⁷⁹ ticle physics is discussed, with an emphasis on the top quark. Secondly, several
⁸⁰ hypothesized extensions of the Standard Model, relevant for the searches presented
⁸¹ in Chapters 7 and 8, are briefly introduced and compared.

⁸² 2.1 Standard Model

⁸³ The Standard Model of elementary particle physics, often simply called the Standard
⁸⁴ Model or SM, is, at the time of writing, the most successful theory describing the
⁸⁵ fundamental particles making up our universe [11, 12]. It is the result of a steady
⁸⁶ progression of increasingly complex models, starting with the introduction of quan-
⁸⁷ tum mechanics in the early 20th century and ending - for now - with the discovery
⁸⁸ of the Higgs boson at the LHC in 2012. The model has been extensively tested
⁸⁹ at many different experiments, most importantly the large collider experiments like
⁹⁰ PETRA, LEP, HERA, the Tevatron, and the LHC. So far, it has survived most of
⁹¹ these tests with excellence, the biggest exception being the observation of neutrino
⁹² masses (cf. Sec. 2.3).

⁹³ The SM is formulated as a relativistic quantum field theory (QFT). That is, its
⁹⁴ most fundamental objects are fields acting on four-dimensional spacetime which,
⁹⁵ after a quantization procedure, yield physically observable particles as fundamental
⁹⁶ excitations. By the usual counting scheme, there exist seventeen different such fields,
⁹⁷ which can be classified into different groups, as schematically shown in Fig. 2.1.

⁹⁸ The first group consists of the twelve fermions, which have spin $\frac{1}{2}$ and make up
⁹⁹ all visible matter. They are further split into the leptons, consisting of three elec-
¹⁰⁰ trically charged leptons - electron, muon, and tau lepton - and three corresponding
¹⁰¹ electrically neutral neutrinos, as well as the quarks, of which there are six differ-
¹⁰² ent flavors, called up, down, strange, charm, bottom, and top. The quarks have
¹⁰³ fractional electric charge, and in addition carry color charge as their defining prop-
¹⁰⁴ erty. Of note is that the fermions are also split into three generations, with each
¹⁰⁵ generation consisting of a charged lepton, a neutrino, and two quarks. The only fun-
¹⁰⁶ damental differences between the particles of different generations are their masses,
¹⁰⁷ though the resulting physically observable properties, such as the lifetime, might be
¹⁰⁸ dramatically different.

¹⁰⁹ The second group of particles are the bosons, which have integer spin. Here,

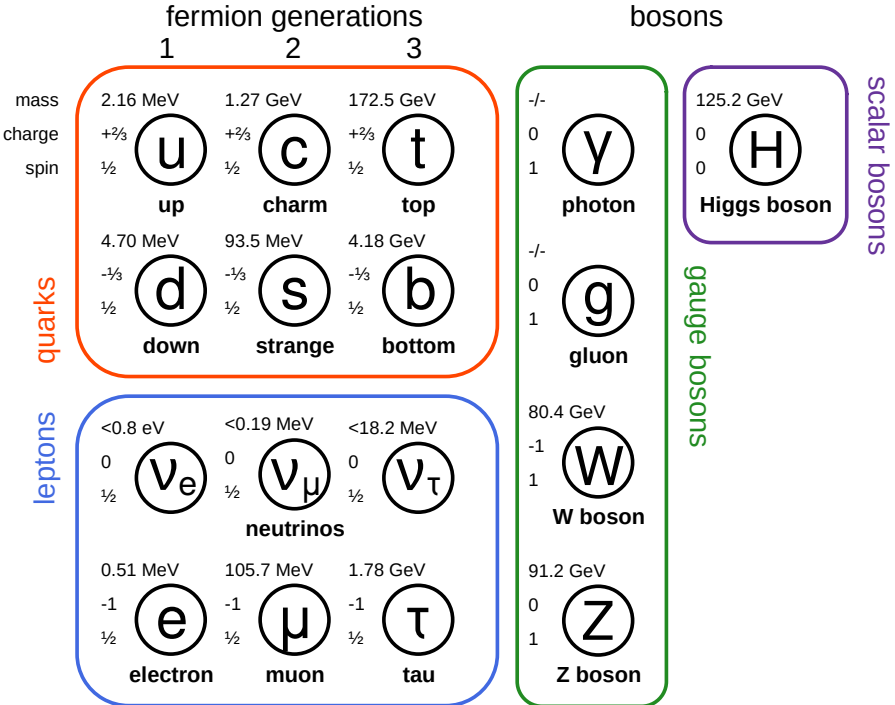


Figure 2.1: **The Standard Model.** A schematic depiction of the particle content of the SM, showing the seventeen fundamental particles, split into six quarks, six leptons, four gauge bosons, and the Higgs boson. The mass, electromagnetic charge, and spin of the particles is given next to the labels. Mass information is taken from Ref. [13].

the four gauge bosons with spin 1 act as the force carriers of the four fundamental interactions described by the SM: the photon, for the electromagnetic interaction with coupling strength α_{elm} ; the W and Z bosons, for the weak interaction with coupling strength α_W ; and the gluon, for the strong interaction with coupling strength α_S . At high enough energies, the electromagnetic and weak interaction unify into the electroweak interaction (coupling strength α_{EW}). The last and final particle is the Higgs boson, which has spin 0. Its most important role in the SM is to give mass to the fermions, as well as the W and Z bosons, through the so-called Higgs mechanism [14, 15], which is briefly outlined in Sec. 2.1.2.

2.1.1 Top quark

This thesis focuses on one particular fundamental particle: the top quark. As such, it will be described in further detail in this section.

The top quark was first discovered in 1995 at the Tevatron by the CDF and D0 experiments [16, 17]. With a rest mass of $m_t \approx 172.5 \text{ GeV}$ [18], the top quark is the

124 most massive known fundamental particle, and as a result it has unique properties
 125 compared to the other quarks: Its extremely short lifetime of $\sim 5 \times 10^{-25}$ s is lower
 126 than the typical time needed for a quark to hadronize under the strong interaction,
 127 making it the only bare quark - that is, the only quark which, via its decay products,
 128 is observable outside of hadrons. Among others, a consequence of this is that it fully
 129 preserves spin information during its decay, while such information is typically lost
 130 for other quarks during hadronization. More details on this are found in Sec. 2.2.2.

131 A second important property of the top quark that follows from its high mass is
 132 its large Yukawa coupling to the SM Higgs boson, which is of order one. As a result,
 133 the Higgs boson couples preferentially to the top quark of all SM fermions, and the
 134 study of both the SM Higgs boson and hypothetical additional Higgs bosons (see
 135 Sec. 2.3) is tightly connected to the top quark.

136 In the SM, the top quark decays to a bottom quark and a W boson with a branch-
 137 ing ratio (BR) of almost 100% (to the degree that all other decays are commonly
 138 neglected). The W boson, in turn, can decay either to a charged lepton (e , μ or τ)
 139 and the corresponding neutrino with a BR of $\sim 32.6\%$, or to a pair of quarks (one
 140 up- and one down-type) with a BR of $\sim 67.4\%$. This results in different final states
 141 for top production processes, which are discussed more in Sec. 2.2.

142 2.1.2 Higgs mechanism

143 The Higgs boson is the most recently discovered particle of the SM. Its existence
 144 was confirmed in 2012 at the LHC by the ATLAS and CMS collaborations [1–3],
 145 establishing the SM in its current form as the accepted description of elementary
 146 particle physics. In the SM, the Higgs boson is described by the so-called Higgs
 147 mechanism. It is briefly discussed in this section due to its relevance for many SM
 148 extensions involving additional Higgs bosons, as searched for in Chapters 7 and 8.

149 In the SM Lagrangian, the Higgs boson appears as a complex doublet ϕ in the
 150 form

$$\mathcal{L}_{\text{SM}} \subset (D_\mu \phi)^\dagger D^\mu \phi + V(\phi) \quad (2.1)$$

151 where D_μ is the covariant derivative, containing the minimal coupling to the gauge
 152 fields, and the Higgs potential $V(\phi)$ is

$$V(\phi) = \mu^2 \phi^\dagger \phi - \lambda (\phi^\dagger \phi)^2. \quad (2.2)$$

153 Here, μ^2 and λ are free parameters of the model. If both parameters are positive,
 154 this potential (known as the “Mexican hat potential”) has a minimum at a non-zero
 155 value of

$$|\phi| = \frac{\mu}{\sqrt{2\lambda}} \equiv \frac{v}{\sqrt{2}} \quad (2.3)$$

156 with the vacuum expectation value $v = \mu/\sqrt{\lambda}$. On the other hand, the minimum -
 157 corresponding to the vacuum state - is degenerate with respect to the three phases
 158 (i.e. the $SU(2)$ symmetry) of the complex doublet.

159 In the Higgs mechanism, this symmetry is now spontaneously broken in the trans-
 160 sition from the high-energy state of the early universe (where the minimum is at
 161 $|\phi| = 0$) to the low-energy state observed today. The physical particles after sym-
 162 metry breaking are then described by fluctuations around the new vacuum state.
 163 If the Higgs field were to be considered on its own, this would lead to one massive
 164 (corresponding to fluctuations in the $|\phi|$ direction) and three massless degrees of
 165 freedom (corresponding to the phases).

166 However, the interaction with the electroweak gauge fields encoded within D_μ
 167 leads to the massless degrees of freedom being absorbed into the gauge fields. This
 168 turns three of the four massless spin-1 gauge fields of the electroweak Lagrangian
 169 (with two degrees of freedom each) into massive fields instead (which have an ad-
 170 ditional longitudinal polarization, and thus three degrees of freedom). These three
 171 massive gauge fields are identified with the W and Z bosons, while the remaining
 172 massless field is identified with the photon. Finally, the leftover massive degree of
 173 freedom from the Higgs doublet ϕ is identified with the spin-0 boson observed at
 174 the LHC.

175 The resulting masses of the Z, W and Higgs bosons can be calculated as a function
 176 of μ^2 , λ and the electroweak couplings and thus used to test the Higgs mechanism.
 177 In addition to the electroweak bosons, the Higgs mechanism can also give masses
 178 to fermions (charged leptons and quarks) by including a Yukawa interaction term
 179 in the Lagrangian. This results in couplings between the SM Higgs boson and the
 180 different fermions that are proportional to the respective fermion mass.

181 In many possible extensions of the SM, the simple Higgs mechanism as presented
 182 here is extended or replaced by more complex theories. This can lead to modifica-
 183 tions to the Yukawa couplings, making Yukawa coupling measurements attractive
 184 as tests of the SM. Two examples of such extensions are discussed in Secs. 2.3.2
 185 and 2.3.3.

186 2.2 The $p p \rightarrow t \bar{t}$ process

187 In proton-proton collisions at the LHC, the dominant production mode of top quarks
 188 is the production of a top-antitop quark pair ($t\bar{t}$). The different parts of this thesis all
 189 focus on this process in different ways, and so this chapter gives a detailed overview
 190 of relevant effects.

191 At LO in QCD, there are three diagrams (up to permutations of initial and final
 192 states) contributing to $t\bar{t}$ production, which can be seen in Fig. 2.2. They differ in
 193 their initial states: the first two diagrams are induced by gluon fusion, while the
 194 last one is induced by quark fusion (mostly from $u\bar{u}$ and $d\bar{d}$). The fraction of these

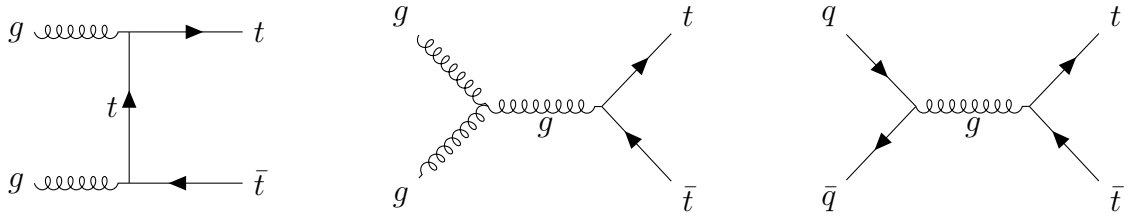


Figure 2.2: **Feynman diagrams for $pp \rightarrow t\bar{t}$.** The three diagrams (up to permutations) that contribute to the $pp \rightarrow t\bar{t}$ process at LO in QCD.

is determined by the corresponding parton densities; at a center-of-mass energy of $\sqrt{s} \geq 13$ TeV, gluon fusion dominates with a fraction of roughly 90%.

At NLO in QCD, many more diagrams become relevant, including those induced by the fusion of one quark and one gluon, while radiating a real quark. Similarly, real emissions of gluons can take place in gg or $q\bar{q}$ fusion diagrams. These effects change the kinematic properties of the produced top quarks, leading to NLO corrections for predicted distributions.

After production, both the top and antitop quark in the $t\bar{t}$ pair dominantly decay into a W boson and a b (anti)quark each. This leads to three different decay channels of the $t\bar{t}$ pair depending on the decays of the two W bosons, which are classified according to their number of leptons: The dilepton channel, with final state $b\bar{b}\ell^+\ell^-\nu\bar{\nu}$; the lepton+jets channel, with final state $b\bar{b}\ell\nu q\bar{q}$; and the all-hadronic channel, with final state $b\bar{b}qq\bar{q}\bar{q}$. Here, q stands in for any light quark (u, d, s or c).

The three channels differ greatly in their experimental challenges: The dilepton channel has the lowest branching ratio of $\sim 10.6\%$, which is further reduced to $\sim 6.4\%$ when excluding τ leptons decaying to hadrons due to them being experimentally hard to reconstruct. It also suffers from the fact that the two produced neutrinos escape the detector unobserved and are only measured as missing transverse momentum, losing both information in the forward direction as well as the ability to disentangle the two neutrinos. On the other hand, the final state of two opposite-sign charged leptons, two b jets, and missing transverse momentum does not have many other contributing processes in the SM, leading to very pure selections (particularly when the two leptons are an electron and a muon). All results in this thesis make use of this channel prominently.

By contrast, the lepton+jets channel has a large BR of $\sim 43.9\%$ ($\sim 30.4\%$ when excluding τ leptons decaying to hadrons), leading to high data statistics, and allows for easier interpretation of the missing transverse momentum due to only one neutrino. However, it can suffer from contamination by W+jets and multijet QCD background (the latter with non-prompt or fake leptons), from issues with combinatorics (i.e. the assignment of experimentally measured jets to the decay products) and from hadronic jet uncertainties, which can be large. This decay channel is employed for the result in Chapter 5 as well as in the combination in Chapter 7.

Term symbol	Spin multiplicity	\mathcal{P}	\mathcal{C}
1S_0	singlet	-1	+1
3P_0	triplet	+1	+1
3S_1	triplet	-1	-1
1P_1	singlet	+1	-1
3P_1	triplet	+1	+1
3D_1	triplet	-1	-1

Table 2.1: **Spin states of $t\bar{t}$.** Overview of the possible angular momentum states of the $t\bar{t}$ system with $J \leq 1$, including the spin multiplicity, the parity \mathcal{P} and the charge-parity \mathcal{C} .

Finally, the all-hadronic channel, with a similar BR of $\sim 45.4\%$, is typically difficult to isolate from the background of QCD multijet production, and in addition suffers even more strongly from combinatorics and jet uncertainties than the lepton+jets channel. As a result, it is in many cases the least precise of the three channels, and is not studied further in this work.

2.2.1 Spin state of the $t\bar{t}$ system

As fermions with spin $\frac{1}{2}$, top quarks have two possible spin states. As a result, the relative spins of the $t\bar{t}$ system can be either aligned, leading to a total vector state with spin $S = 1$, or anti-aligned, leading to a scalar state with spin $S = 0$. Furthermore, the $t\bar{t}$ system as a whole can have orbital angular momentum L , where L is a non-negative integer. In analogy to atomic orbitals, the total angular momentum is then $\vec{J} = \vec{L} + \vec{S}$, and for any chosen basis the set of quantum numbers $\{S, L, J, J_z\}$ consists of conserved quantities. The angular momentum state is commonly written using a term symbol $^{2S+1}L_J$, where $2S+1$ denotes the multiplicity of the spin state, and the orbital angular momentum L is written using spectroscopic notation (S for $L = 0$, P for $L = 1$, D for $L = 2$ etc). An overview of the lowest possible states ($J \leq 1$) is given in Tab. 2.1, including also the parities and charge-parities \mathcal{P} and \mathcal{C} , which can be inferred from the intrinsic parities of top and antitop as well as the orbital angular momentum. In proton-proton collisions, a mixture of all these states is produced, with the ratio depending on the production mode (gg , $q\bar{q}$ or gq) as well as the energy.

In practice, the spins of the top (anti)quarks cannot be observed directly, and instead must be inferred from their decay products. The way in which the spin information is passed to the decay products is determined by the maximally parity-violating nature of the weak interaction together with conservation of angular momentum. This is illustrated in Fig. 2.3 for the leptonic decay of the top (anti)quark: Since the b quark is almost massless compared to the top quark, so that $m_b = 0$ can

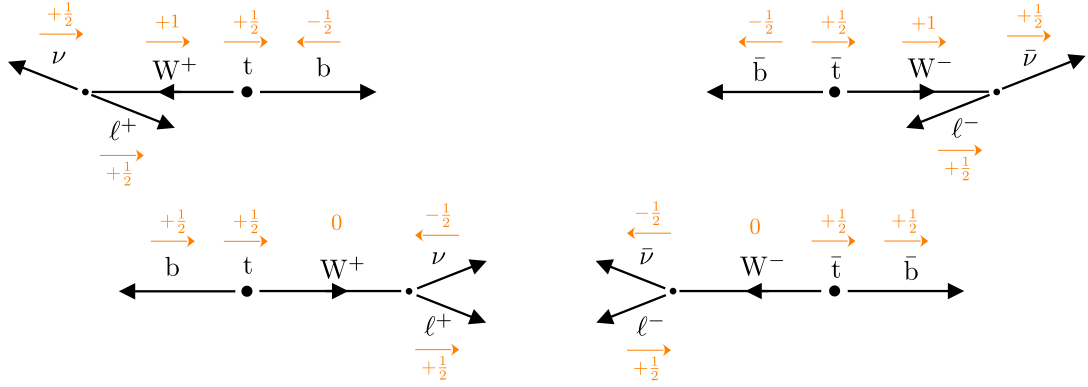


Figure 2.3: **Helicity in top decays.** Sketch of the allowed helicity configurations in a top (left) and antitop quark decay (right) in the rest frame of the quark, involving either a transversely (top, $S_z = 1$) or longitudinally polarized W boson (bottom, $S_z = 0$). The z axis corresponds to the spin of the top (anti)quark, and the orange arrows and numbers illustrate the spin in the z direction of the respective particles. It can be seen that, due to conservation of angular momentum and the parity-violating nature of the weak interaction, the ℓ^+ is preferred to be emitted in the direction of the t spin, while the ℓ^- is preferred to be emitted opposite to the direction of the \bar{t} spin.

be assumed in the following, it will be ultra-relativistic. Like for all fermions, its helicity is thus determined by its chirality. As a result, for the decay $t \rightarrow W^+ b$ the b quark - left-handed due to the weak interaction - has negative helicity (spin opposite to its direction of flight), leading to two possibilities for the W boson through conservation of angular momentum: transversely polarized (spin 1, top left in Fig. 2.3) or longitudinally polarized (spin 0, bottom left in Fig. 2.3).

Since the decay of the W^+ into $\ell^+\nu$ is again mediated by the weak interaction, and both decay products are nearly massless, the helicities of ℓ^+ and ν must be positive and negative, respectively. Applying again conservation of angular momentum, one then finds from the sketch that in both cases, the charged lepton is emitted preferably in the direction of the top quark spin.

Repeating the same line of arguments for the decay of the antitop (Fig. 2.3 on the right), one finds that the opposite holds there: the charged lepton is emitted preferably opposite to the antitop spin. As a result, the direction of flight of the charged lepton in the center-of-mass system of its parent (anti)top can be used as a proxy for the (anti)top spin (or, equivalently, its polarization). It should be noted that this property of the top quark is unique among the quarks of the SM, since all other quarks hadronize via the helicity-ignorant strong interaction and thus lose the

²⁷² largest part of their spin information¹.

²⁷³ Returning to the full $t\bar{t}$ system, and applying the above observation to both
²⁷⁴ top and antitop, one can now define observables to probe the $t\bar{t}$ spin state, or
²⁷⁵ equivalently, the spin correlation between t and \bar{t} . A simple such variable is the
²⁷⁶ azimuthal difference $\Delta\phi_{\ell\ell}$ between the two leptons in a dileptonic decay. Assuming
²⁷⁷ that the top and antitop are emitted back-to-back, a state with the top and antitop
²⁷⁸ spins aligned (i.e. $S = 1$) will cause the two leptons to be emitted preferably in
²⁷⁹ opposite directions, leading to large $\Delta\phi_{\ell\ell}$, while anti-aligned spins ($S = 0$) will
²⁸⁰ lead preferably to parallel leptons and thus small $\Delta\phi_{\ell\ell}$. While this variable has
²⁸¹ the advantage of being easy to define and experimentally clean to measure, it is
²⁸² suboptimal in that it is also strongly affected by the kinematics of the $t\bar{t}$ production,
²⁸³ including higher-order corrections in QCD, and is heavily sculpted when selecting
²⁸⁴ certain areas of $t\bar{t}$ phase space. Thus, it is afflicted with large modeling uncertainties.

²⁸⁵ A more powerful variable can be defined by employing suitable reference systems
²⁸⁶ as follows: the lepton and antilepton are first Lorentz boosted into the center-of-
²⁸⁷ mass frame of the $t\bar{t}$ system, and then further boosted into the center-of-mass frame
²⁸⁸ of their parent (anti)tops. Then, a correlation variable c_{hel} is defined as the scalar
²⁸⁹ product of their direction unit vectors in these reference frames²:

$$c_{\text{hel}} = \hat{\ell}_t^+ \cdot \hat{\ell}_{\bar{t}}^- \quad (2.4)$$

²⁹⁰ It can be shown that, irrespective of the mode of production of the $t\bar{t}$ system and
²⁹¹ inclusive in the rest of the phase space, the distribution of this observable always
²⁹² follows a straight line [21], i.e.

$$\frac{1}{\sigma} \frac{d\sigma}{dc_{\text{hel}}} = \frac{1}{2} (1 - D c_{\text{hel}}) \quad (2.5)$$

²⁹³ The slope D depends on the spin and angular momentum of the produced $t\bar{t}$
²⁹⁴ state. At LO in QCD, it can be shown that $D = -1$ for pure singlet states (anti-
²⁹⁵ aligned spins, e.g. 1S_0 , 1P_1) and $D = +\frac{1}{3}$ for pure triplet states (aligned spins, e.g.
²⁹⁶ 3S_1 , 3P_0) [22, 23]. Higher-order corrections in QCD can slightly reduce these slopes
²⁹⁷ through emissions of real gluons in the decay, which weaken the correlations, but
²⁹⁸ these effects are on the order of 0.2% at NLO for leptons [24, 25].

²⁹⁹ In practice, any observed ensemble of $t\bar{t}$ pairs will be a mixture of the different spin
³⁰⁰ states depending on the production mechanism and underlying theory, which can
³⁰¹ be probed by measuring the slope D . As will be discussed in Sec. 2.3, extensions of
³⁰² the SM can change the predicted slope, making measurements of D attractive tests
³⁰³ for new physics. The value of D has been measured e.g. in Refs. [26–28], as well

¹See e.g. Ref. [19] for the greatly reduced possibilities of measuring spin correlations in $b\bar{b}$ or $c\bar{c}$ systems at the LHC.

²In this work, the naming convention from Ref. [20] is followed for c_{hel} . In e.g. Ref. [21], this variable is instead called $\cos\varphi$.

304 as more recently as a proxy variable in the context of measurements of quantum
305 entanglement in $\text{t}\bar{\text{t}}$ production [29, 30].

306 2.2.2 Spin density matrix

307 A more detailed way to quantify the spin properties of the $\text{t}\bar{\text{t}}$ system, respective
308 to an arbitrary spin basis, is the production spin density matrix \mathbf{R} , which (when
309 averaged over initial spins and colors, and summed over final colors) can be written
310 as [22, 23, 31]

$$\mathbf{R} = A \mathbb{1} \otimes \mathbb{1} + B_i^1 \sigma_i \otimes \mathbb{1} + B_i^2 \mathbb{1} \otimes \sigma_i + C_{ij} \sigma_i \otimes \sigma_j. \quad (2.6)$$

311 Here, $\mathbb{1}$ is the two-dimensional identity matrix, σ_i with $i = 1, 2, 3$ are the Pauli
312 matrices, and the first and second components of the tensor product refer to the
313 spin of the top and antitop quark, respectively. The scalar coefficient A describes
314 the overall amplitude (i.e. the differential cross section as a function of the top and
315 antitop kinematics) of $\text{t}\bar{\text{t}}$ production, the vectors \vec{B}^1 and \vec{B}^2 describe the polarization
316 of the top and antitop quark, and the matrix \mathbf{C} describes the correlation between
317 their spins. All of them are, in general, functions of the partonic center-of-mass
318 energy and the scattering angle of the top quark relative to the incoming partons.

319 As explained in Sec. 2.2.1, in a dileptonic decay the spin information is transferred
320 almost completely to the charged leptons. Defining the lepton directions of flight in
321 their parent frames $\hat{\ell}_t^+$ and $\hat{\ell}_{\bar{t}}^-$ as in Eq. (2.4), the resulting differential cross section
322 in terms of the lepton angles, collectively denoted as Ω , is [31]

$$\frac{1}{\sigma} \frac{d\sigma}{d\Omega} = 1 + \vec{B}^1 \cdot \hat{\ell}_t^+ + \vec{B}^2 \cdot \hat{\ell}_{\bar{t}}^- + (\hat{\ell}_t^+)^T \mathbf{C} \hat{\ell}_{\bar{t}}^-. \quad (2.7)$$

323 By integrating out the remaining angles, it can be shown from this that irrespec-
324 tive of the chosen basis the slope D as defined in Eq. (2.5) can be recovered from
325 the matrix \mathbf{C} as [21, 32]

$$D = \frac{1}{3} \text{Tr} [\mathbf{C}]. \quad (2.8)$$

326 As discussed in Sec. 2.2.1, D is maximally negative for pure singlet states (corre-
327 sponding to a positive slope in c_{hel}), and thus is ideal for separating those in a mixed
328 ensemble. One can define similar separating observables for other states using the
329 spin density matrix by choosing a suitable spin basis. In this work, the so-called
330 helicity basis proposed in Ref. [33] is used. The three axes of this basis, denoted \hat{k} ,
331 \hat{r} and \hat{n} , are defined as follows: \hat{k} is simply the direction of flight of the top quark in
332 the center-of-mass frame of the $\text{t}\bar{\text{t}}$ system, such that the top quark spin with respect
333 to \hat{k} is equal to the helicity. The second axis, \hat{r} , is orthogonal to \hat{k} in the scattering
334 plane of the $\text{pp} \rightarrow \text{t}\bar{\text{t}}$ process. Finally, the third axis \hat{n} is orthogonal on both \hat{k} and

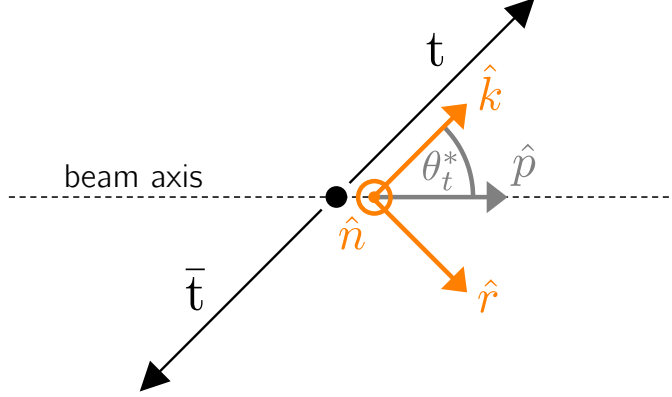


Figure 2.4: **Helicity basis.** Sketch of the helicity basis used to define the top and antitop quark spins. The unit vectors \hat{k} , \hat{r} and \hat{n} define the right-handed basis, while the beam axis is given by \hat{p} and the top quark scattering angle by θ_t^* .

³³⁵ \hat{r} , oriented such that the $\{\hat{k}, \hat{r}, \hat{n}\}$ system is left-handed. If \hat{p} denotes the beam axis
³³⁶ and θ_t^* the top scattering angle, the latter two axes are given by

$$\hat{r} = \frac{\hat{p} - \cos \theta_t^* \hat{k}}{|\hat{p} - \cos \theta_t^* \hat{k}|} \quad \text{and} \quad \hat{n} = \hat{r} \times \hat{k} = \frac{\hat{p} \times \hat{k}}{|\hat{p} \times \hat{k}|}. \quad (2.9)$$

³³⁷ This coordinate system is visualized in Fig. 2.4. It is used, among others, in
³³⁸ Refs. [27, 28] to measure both the polarizations \vec{B}^1 and \vec{B}^2 and spin correlation
³³⁹ coefficients C_{ij} ($i, j = k, r, n$). In this work, only the spin correlation is considered.
³⁴⁰ Particularly, in addition to c_{hel} , the following observable is defined:

$$c_{\text{han}} = -(\hat{\ell}_t^+)_k (\hat{\ell}_{\bar{t}}^-)_k + (\hat{\ell}_t^+)_r (\hat{\ell}_{\bar{t}}^-)_r + (\hat{\ell}_t^+)_n (\hat{\ell}_{\bar{t}}^-)_n \quad (2.10)$$

³⁴¹ where $(\hat{\ell})_i$, $i = k, r, n$ refers to the i -th component of the respective vector in the
³⁴² $\{k, r, n\}$ basis. This observable, like c_{hel} , has the advantage of always being linear
³⁴³ in the absence of phase space cuts, i.e.

$$\frac{1}{\sigma} \frac{d\sigma}{dc_{\text{han}}} = \frac{1}{2} (1 + D^{(k)} c_{\text{han}}) \quad (2.11)$$

³⁴⁴ where [22]

$$D^{(k)} = \frac{1}{3} (C_{kk} - C_{rr} - C_{nn}). \quad (2.12)$$

³⁴⁵ From Eq. (2.12), it can be seen that the slope is maximally negative, $D^{(k)} = -1$,
³⁴⁶ when the top and antitop spins are anti-correlated along the top direction of flight

347 ($C_{kk} = -1$) and correlated along the orthogonal directions ($C_{rr} = C_{nn} = +1$). The
348 (unpolarized) state described by these correlations is a pure triplet state ($S = 1$) [22].

349 Particularly, the 3P_0 state of $t\bar{t}$ always corresponds to this spin state: It has no
350 total angular momentum, so that its total spin and orbital angular momentum must
351 be anti-aligned. Since the orbital angular momentum is always exactly zero in the
352 direction of flight of the top quarks, the $t\bar{t}$ system must be in an orbital angular
353 momentum eigenstate with $L_k = 0$, and thus also in a total spin eigenstate with
354 $S_k = 0$. In other words, the spins in the \hat{k} direction are anti-aligned, corresponding
355 to $C_{kk} = -1$. In order to arrive at $S = 1$, i.e. a pure triplet state, it is required that
356 the other entries fulfill $C_{rr} = C_{nn} = 1$.

357 2.2.3 Bound state effects in $t\bar{t}$

358 When predicting distributions of observables for hard scattering processes such as
359 $t\bar{t}$ production, one usually employs perturbative calculations at a fixed order in the
360 strong coupling constant α_S , possibly matched to a parton shower (see Chapter 3).
361 However, at low energy scales (or equivalently, long distances) the strong interaction
362 becomes non-perturbative, leading to effects that cannot be captured in the usual
363 perturbative expansion irrespective of the order in α_S (though they might or might
364 not be captured in expansions or resummations with other parameter choices).

365 In the $pp \rightarrow t\bar{t}$ process, such effects might play a role in the vicinity of the
366 $t\bar{t}$ production threshold, i.e. for $m_{t\bar{t}} \sim 2m_t$, where the relative velocities of the
367 produced top quarks become small. In particular, one possible class of effects not
368 included in simple expansions in α_S are $t\bar{t}$ bound states (“toponium”). Such states
369 (also called quarkonia) are well-known in $c\bar{c}$ and $b\bar{b}$ production, where they lead to
370 composite particles such as J/ψ , η_c or Υ . When translating this knowledge to $t\bar{t}$,
371 however, there is a significant difference: due to the large top quark mass, the lifetime
372 of the top quark is expected to be shorter than the (formal) lifetime of any possible
373 $t\bar{t}$ bound state. As a result, the state would in the majority of cases not decay e.g.
374 to photons, gluons or hadrons like the lighter quarkonia, but instead disassociate
375 by one of the constituent top quarks decaying normally to Wb . This phenomenon,
376 sometimes called a “quasi-bound state” or a “virtual bound state”, would lead to a
377 possible peak in the $m_{WWb\bar{b}}$ spectrum slightly below the $t\bar{t}$ threshold.

378 Calculations of the $m_{WWb\bar{b}}$ spectrum at the $t\bar{t}$ threshold including the effects
379 from a possible bound state have been performed independently in Refs. [34–38].
380 All of these calculations work in the framework of non-relativistic QCD (NRQCD),
381 which treats the slowly moving ($v \ll c$) top (anti)quarks as non-relativistic particles.
382 This approach can be seen as a low-energy effective field theory (EFT) of the SM
383 where high-energy modes have been integrated out, or alternatively, as an alternate
384 perturbative expansion in the ratio α_S/β , where β is the top quark velocity. The
385 result is a non-relativistic Schrödinger equation for the wavefunction of the $t\bar{t}$ system,
386 with the interaction between the top quarks described by the low-energy limit of

2 Theoretical framework

³⁸⁷ the QCD Coulomb potential, representing the exchange of soft gluons. At LO, it is
³⁸⁸ given by [35]

$$V_{\text{QCD}}^{[1,8]}(q) = -\frac{4\pi\alpha_S C^{[1,8]}}{q^2}, \quad (2.13)$$

³⁸⁹ where the color factor is $C^{[1]} = 4/3$ for color-singlet and $C^{[8]} = -1/6$ for color-octet
³⁹⁰ states. As a result, only $t\bar{t}$ systems in a color-singlet state feel an attractive force
³⁹¹ and can possibly form a bound state, while color-octet states are instead repulsed.
³⁹² At the LHC, $t\bar{t}$ bound states can thus at LO be produced only from gg initial states,
³⁹³ since $q\bar{q}$ systems are always color-octets. From this, the spin state of the produced
³⁹⁴ bound state can be inferred: Since both of the top quarks have low velocity, states
³⁹⁵ with orbital angular momentum $L \neq 0$ will be strongly suppressed (beyond NLO
³⁹⁶ in NRQCD [35]). Furthermore, the gg initial state in $t\bar{t}$ production close to the
³⁹⁷ $t\bar{t}$ threshold always has spin $S = 0$ (and thus total angular momentum $J = 0$),
³⁹⁸ with $S = 2$ contributions suppressed by powers of the top velocity [23], so that the
³⁹⁹ resulting $t\bar{t}$ system must be in the ${}^1S_0^{[1]}$ state. At NLO in QCD, also ${}^3S_1^{[1]}$ states can
⁴⁰⁰ be produced; however, the contribution is very small (less than 0.1% of the total
⁴⁰¹ cross section [35]).

⁴⁰² Refs. [35–38] agree that the binding energy of the $t\bar{t}$ bound state, defined as the
⁴⁰³ difference of the peak position in the $m_{WWb\bar{b}}$ spectrum to $2m_t$, is around -2 GeV,
⁴⁰⁴ resulting in a “mass” of 343 GeV for the $t\bar{t}$ bound state for a top mass of 172.5 GeV.
⁴⁰⁵ The exact line shape of the peak is less well known. However, the experimental
⁴⁰⁶ resolution of $m_{WWb\bar{b}}$ is expected to be much larger than the bound state width of
⁴⁰⁷ order $\sim 2\Gamma_t$ (see Sec. 7.2.5), making the details of the spectrum irrelevant to an
⁴⁰⁸ experimental search.

⁴⁰⁹ The existing NRQCD calculations predict only certain differential distributions
⁴¹⁰ and cannot be directly compared to experimental data on a per-event level. Because
⁴¹¹ of this, a simplified model for the $t\bar{t}$ bound state is introduced following Refs. [22,
⁴¹² 39–41]. Instead of a first-principles calculation, the bound state effects are modeled
⁴¹³ as an additional state spin-0 state η_t , which is added to the conventional perturbative
⁴¹⁴ QCD (pQCD) calculation of $t\bar{t}$. η_t is defined to couple directly to gluons and top
⁴¹⁵ quarks via the Lagrangian

$$\mathcal{L}_{\eta_t} = -\frac{1}{4}g_{gg\eta_t}\eta_t G_{\mu\nu}^a \tilde{G}^{a\mu\nu} - ig_{t\bar{t}\eta_t}\eta_t \bar{t}\gamma_5 t \quad (2.14)$$

⁴¹⁶ where $G_{\mu\nu}^a$ is the gluon field strength tensor, $\tilde{G}_{\mu\nu}^a$ its dual, and $g_{gg\eta_t}$ as well as $g_{t\bar{t}\eta_t}$
⁴¹⁷ are arbitrary coupling strengths. The resulting model has three free parameters: the
⁴¹⁸ binding energy $E_b = m(\eta_t) - 2m_t$, the total width $\Gamma(\eta_t)$ and the production cross
⁴¹⁹ section $\sigma(\eta_t)$ (the latter determining the couplings $g_{gg\eta_t}$ and $g_{t\bar{t}\eta_t}$). In Ref. [40], they
⁴²⁰ are determined by fitting them to the NRQCD calculation from Ref. [36], yielding

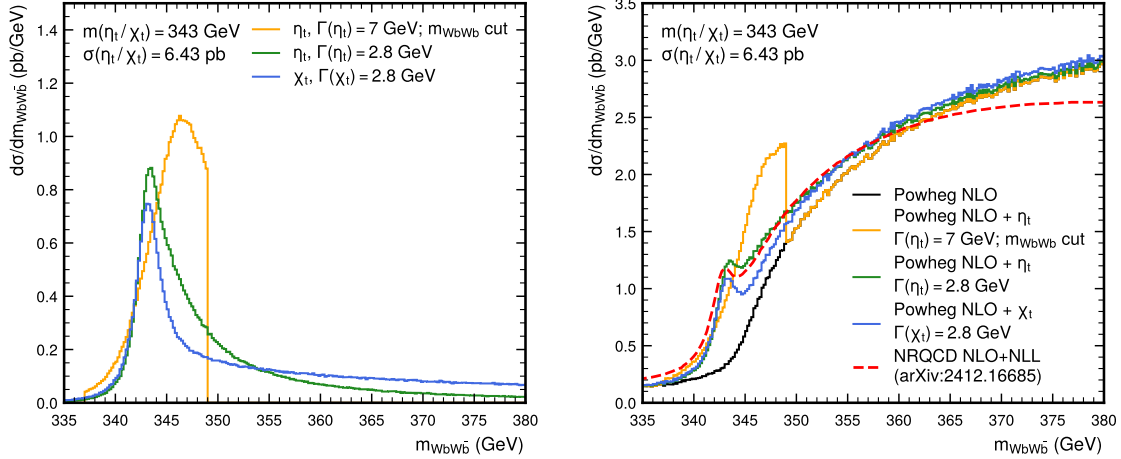


Figure 2.5: **Line shape of η_t and χ_t .** The $m_{WWb\bar{b}}$ distribution close to the $t\bar{t}$ threshold, as predicted by the η_t and χ_t models on their own (left) and stacked on top of a pQCD $t\bar{t}$ prediction from Powheg `hvq` (right, see Sec. 3.1). For the orange line, the η_t width is chosen to be 7 GeV, and a cut on $|m_{WWb\bar{b}} - m(\eta_t)|$ is applied (Eq. (2.15)), while for the green line, the η_t width is chosen as 2.8 GeV, and no further cuts are made (Eq. (2.16)). The blue line shows χ_t for a width of 2.8 GeV. In the right plot, all models are compared to an NRQCD prediction from Ref. [38].

$$E_b = -2 \text{ GeV} \implies m(\eta_t) = 343 \text{ GeV}, \quad \Gamma(\eta_t) = 7 \text{ GeV}, \quad \sigma(\eta_t) = 6.4 \text{ pb} \quad (2.15)$$

In the generation of events, the top quarks are allowed to be fully off-shell by calculating the full amplitude $pp \rightarrow \eta_t \rightarrow W^+W^-b\bar{b}$, thus making sure that the phase-space region $m_{WWb\bar{b}} < 2m_t$ is populated. Furthermore, Ref. [40] recommends that the contribution of η_t should be restricted to the region $|m_{WWb\bar{b}} - m(\eta_t)| \leq 6 \text{ GeV}$ so that the bulk of the $t\bar{t}$ phase space, in which the pQCD calculation is expected to be accurate while the NRQCD calculation misses relativistic corrections, is not affected.

However, Refs. [39, 41] recommend instead

$$E_b = -2 \text{ GeV} \implies m(\eta_t) = 343 \text{ GeV}, \quad \Gamma(\eta_t) = 2\Gamma_t = 2.8 \text{ GeV} \quad (2.16)$$

and no cut on $|m_{WWb\bar{b}} - m(\eta_t)|$.

The resulting $m_{WWb\bar{b}}$ distribution for the combination of pQCD $t\bar{t}$ and η_t is shown in Fig. 2.5 at the level of hard scattering for both parameterizations, on its own as well as stacked on top of a pQCD prediction of the $t\bar{t}$ continuum at NLO in QCD. The stacked distributions are compared to an NRQCD prediction from Ref. [38].

2 Theoretical framework

At the level of hard scattering, the lower width of $\Gamma(\eta_t) = 2\Gamma_t$ agrees much better with the predicted NRQCD spectrum and avoids an unphysical discontinuity due to the $m_{WWb\bar{b}}$ cutoff. Thus, this parameterization will be used in this work wherever possible, i.e. in Secs. 7.7 and 7.8, though the parameterization of Eq. (2.15) is retained for the sake of consistency with other results in Sec. 7.9. For more details, see these sections.

In the final stages of this work, a more involved model for $t\bar{t}$ bound states was published in Ref. [42]. There, instead of simulating an additional pseudoscalar state η_t , the bound state effects are included in leading-order color-singlet $t\bar{t}$ production by directly reweighting produced events with the ratio of Green's functions. This model is in principle fully predictive, i.e. it does not require fitting parameters to external calculations. However, it could not be validated in time for inclusion in the results of Chapter 7, it does not explicitly distinguish between $t\bar{t}$ spin states, and it is also unclear on how to match it to the $t\bar{t}$ continuum. Because of this, it is not further considered here and its investigation left for future work.

While NRQCD predicts any possible $t\bar{t}$ bound state contribution in pp collisions to be dominated by the ${}^1S_0^{[1]}$ state, with contributions from excited states strongly suppressed, experimentally it will still be useful to compare this spin state to other possibilities. To this end, a second toy model, denoted χ_t , is defined in analogy to η_t by the interaction Lagrangian

$$\mathcal{L}_{\chi_t} = -\frac{1}{4}g_{gg\chi_t}\chi_t G_{\mu\nu}^a \tilde{G}^{a\mu\nu} - g_{t\bar{t}\chi_t}\chi_t \bar{t}t \quad (2.17)$$

where $g_{gg\chi_t}$ and $g_{t\bar{t}\chi_t}$ are again arbitrary couplings. This Lagrangian contains a \mathcal{CP} -even coupling to the top quark, compared to the \mathcal{CP} -odd coupling in Eq. (2.14). It thus produces $t\bar{t}$ systems in the ${}^3P_0^{[1]}$ state, which is the only other possible state with $J=0$ (cf. Tab. 2.1). The free parameters of this model are again cross section, mass, and width; they are set here to the same values as for η_t in all cases³. The resulting $m_{WWb\bar{b}}$ line shape is also seen in Fig. 2.5. It shows a small peak similar to η_t at ~ 343 GeV, though it exhibits a more pronounced tail at high $m_{WWb\bar{b}}$ since the 3P_0 state carries one unit of orbital angular momentum and thus favors higher top quark velocities. In Sec. 7.7.2, the χ_t model will be used in conjunction with η_t to probe the spin state of the observed excess. Other possible states, such as the vector state ${}^3S_1^{[1]}$, are not considered here and instead left for future work.

³Based on analogies to $c\bar{c}$ and $b\bar{b}$ quarkonia [43], it is likely that a true 3P_0 bound state would have a slightly higher mass, though it is unknown whether this would be noticeable even in the hard-scattering level spectrum due to the large smearing from the top width. It is anyway expected to be irrelevant within the experimental resolution.

465 2.3 Beyond the Standard Model

466 The Standard Model, greatly successful as it is at describing the results of collider
 467 experiments so far, is nonetheless known to be incomplete. In fact, there exist
 468 several experimental results which cannot be explained by SM predictions, such
 469 as the observation of dark matter in many astrophysical contexts [44–46] or the
 470 observed masses of the neutrinos [47, 48].

471 In addition, the SM is plagued by several theoretical challenges that will likely not
 472 be overcome without major modifications to the theory. Chief among these is the
 473 unification of the forces of the SM - the electroweak and strong interactions - with
 474 gravity as described by General Relativity, which is not included in the SM at all.
 475 Doing so has proven extremely challenging, and no fully consistent unified theory
 476 of all forces is known yet. Further open questions are, for example, the hierarchy or
 477 naturalness problem [49–51] or the strong \mathcal{CP} problem [52, 53].

478 In order to solve these problems in a satisfactory manner, a more general theory
 479 will have to be found, which should include the SM as its low-energy limit. In
 480 many cases, this will result in additional as of yet undiscovered particles. There is
 481 a multitude of such Beyond the Standard Model (BSM) extensions, each attacking
 482 different parts of the problems, and one of the major tasks of particle physics is to
 483 explore which parts of the parameter space of these models can be probed with the
 484 current experiments.

485 This work, in particular, aims to probe models predicting new, heavy spin-0 states
 486 coupling strongly to the top quark. Such states can be searched for in the $pp \rightarrow t\bar{t}$
 487 process, as outlined in a generic fashion in Sec. 2.3.1. Following that, two explicit
 488 realizations of such models are discussed, namely the Two-Higgs Doublet Model
 489 (2HDM) (Sec. 2.3.2) and Axion-Like Particle (ALP) models (Sec. 2.3.3).

490 2.3.1 Heavy scalars in $t\bar{t}$ production

491 Consider an unspecified BSM extension predicting (possibly among others) a massive
 492 spin-0 state Φ coupling to top quarks via a Yukawa interaction. In the absence of
 493 couplings to other particles, the Lagrangian of such a state can be written as [22]

$$\mathcal{L}_\Phi = \frac{1}{2}(\partial_\mu \Phi)(\partial^\mu \Phi) + \frac{m_\Phi^2}{2}\Phi^2 + g_{\Phi t\bar{t}} \frac{m_t}{v} \bar{t}\Phi (\cos \alpha + i\gamma_5 \sin \alpha) t. \quad (2.18)$$

494 where m_Φ is the mass of the new state and $g_{\Phi t\bar{t}}$ is a coupling modifier, scaled to
 495 the SM Higgs-top Yukawa coupling with the SM Higgs vacuum expectation value v .
 496 The phase α is a free parameter determining the \mathcal{CP} structure of the $\Phi t\bar{t}$ coupling:
 497 For $\alpha = 0$, the coupling is purely \mathcal{CP} -even or scalar, while for $\alpha = \pi/2$, the coupling
 498 is purely \mathcal{CP} -odd or pseudoscalar. Intermediate values for α will cause \mathcal{CP} -mixed
 499 couplings, which in general will result in \mathcal{CP} violation in processes involving top
 500 quarks. Possible experimental indicators of such \mathcal{CP} violation in $pp \rightarrow t\bar{t}$ are e.g.

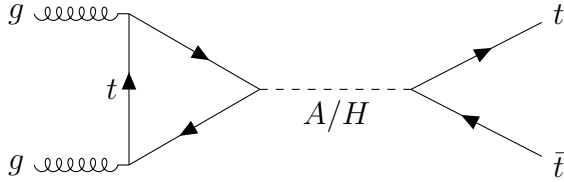


Figure 2.6: **Feynman diagram for $gg \rightarrow A/H \rightarrow t\bar{t}$.** Only the leading-order gluon fusion diagram is shown, with a top quark running in the loop.

discussed in Ref. [32].

In the scope of this work, only the \mathcal{CP} -conserving cases of Φ are considered. For convenience, the pure pseudoscalar case will in the following be called A, while the pure scalar case will be called H.

Similar to the SM Higgs boson, the most important production channel of either state at the LHC will be through loop-induced gluon fusion, followed by associated production with either $t\bar{t}$ or a single top quark. Only the former is considered here; experimental searches for the latter case can be found e.g. in Ref. [54]. Furthermore, the decay of the new state will depend on its mass: For low masses, the particle will decay either through loop-induced couplings to e.g. gg or $\gamma\gamma$ or, if present, through couplings to other SM or BSM particles than the top quark. For masses of $m_{A/H} > 2m_t$, however, the decay to $t\bar{t}$ is kinematically allowed and will in many cases be dominant due to the large Yukawa coupling. In this case, the process $gg \rightarrow A/H \rightarrow t\bar{t}$ will lead to the same final state as SM $t\bar{t}$ production, as illustrated in Fig. 2.6. This process will be considered in more detail in the rest of this chapter, and one of the main results of this thesis is an experimental search for such a signature (Chapter 7).

Fig. 2.7 shows the predicted differential cross sections of this model in terms of $m_{t\bar{t}}$, the invariant mass of the $t\bar{t}$ pair, for different A/H masses. The cross section is shown as the difference to the SM prediction at the level of the hard scattering and at LO in QCD. It can be seen that the total effect of A and H is a very distinct peak-dip structure around the A/H mass. This is because the $gg \rightarrow A/H \rightarrow t\bar{t}$ production channel interferes with SM $gg \rightarrow t\bar{t}$ production, which leads to deficits in certain regions of phase space due to destructive interference. For high A/H masses, there is an additional broad peak at low masses of $m_{t\bar{t}}$. This originates from the gluon PDF, which is steeply increasing for small parton momentum fractions, corresponding to low $m_{t\bar{t}}$, and thus compensates the suppression by the off-shell A/H at low $m_{t\bar{t}}$ for the A/H-SM interference.

A further consequence of the interference is that the differential cross section scales non-linearly with the coupling modifiers $g_{At\bar{t}}$ and $g_{Ht\bar{t}}$. The dependence (for arbitrary observables) can be parameterized as

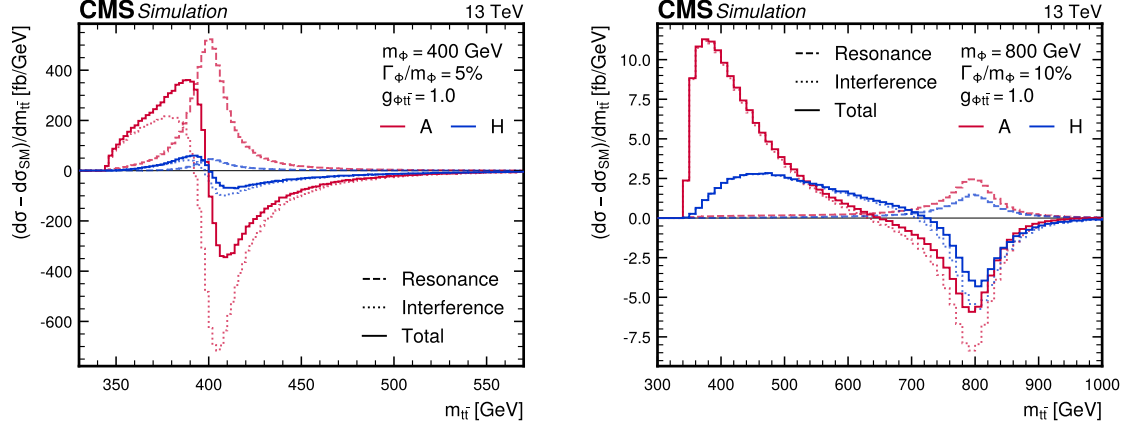


Figure 2.7: **Differential cross sections for $A/H \rightarrow t\bar{t}$.** The hadronic differential cross section as a function of the invariant $t\bar{t}$ mass, with the SM prediction subtracted, for $m_{A/H} = 400 \text{ GeV}$, $\Gamma_{A/H}/m_{A/H} = 5\%$ (left) and $m_{A/H} = 800 \text{ GeV}$, $\Gamma_{A/H}/m_{A/H} = 10\%$ (right) as well as for A (red) and H (blue), at a coupling modifier of $g_{A/Ht\bar{t}} = 1$. The resonance and interference components as well as their sum are shown as dashed, dotted and solid lines, respectively. They are calculated from same the Monte Carlo simulation samples described in Sec. 7.2.1.

$$d\sigma = d\sigma^{\text{SM}} + g_{A/Ht\bar{t}}^2 d\sigma^{\text{int}} + g_{A/Ht\bar{t}}^4 d\sigma^{\text{res}} \quad (2.19)$$

where the superscripts ‘‘SM’’, ‘‘int’’ and ‘‘res’’ refer to the SM, SM- A/H interference, and resonant A/H contributions, respectively.

In addition to the $m_{t\bar{t}}$ spectrum, an A/H contribution is also expected to modify the spin state of the $t\bar{t}$ system. As a single spin-0 particle, an intermediate A/H resonance has neither spin nor orbital angular momentum. Due to conservation of angular momentum, this implies that the $t\bar{t}$ system will be produced in a state with $J = 0$, which leaves only the 1S_0 and 3P_0 states (compare Tab. 2.1).

Furthermore, the spin-0 intermediate state has positive intrinsic parity and is charge-neutral. This implies that for H , whose interaction with the top quark is separately \mathcal{C} - and \mathcal{P} -conserving, the $t\bar{t}$ system will have quantum numbers of $\mathcal{C} = +1$ and $\mathcal{P} = +1$, which is true for the 3P_0 state. For A , on the other hand, the interaction is maximally \mathcal{P} -violating, leading to quantum numbers of $\mathcal{C} = +1$ and $\mathcal{P} = -1$, which matches the 1S_0 state. As a result, the process $gg \rightarrow A \rightarrow t\bar{t}$ will always produce the 1S_0 spin singlet state, while $gg \rightarrow H \rightarrow t\bar{t}$ will produce the 3P_0 spin triplet state.

As explained in Secs. 2.2.1 and 2.2.2, the observable c_{hel} has maximal slope D for spin-singlet states, making it a good discriminator between A and the SM. For H , it can be shown that the produced triplet state instead maximizes the slope $D^{(k)}$ of

549 the observable c_{han} , as defined in Eq. (2.10) [22]. Consequently, both c_{hel} and c_{han}
 550 will be used in the experimental search for such states presented in Chapter 7.

551 2.3.2 Two-Higgs Doublet Model

552 A common class of models predicting additional scalars as discussed in Sec. 2.3.1
 553 are Two-Higgs-Doublet Models (2HDMs) [55, 56]. In these models, there are two
 554 complex $SU(2)$ Higgs doublets with eight degrees of freedom in total (as opposed
 555 to a single doublet in the SM), which after electroweak symmetry breaking results
 556 in five physical states (compare Sec. 2.1.2). Such a structure for the Higgs sector
 557 arises, for example, in many supersymmetric models [57] or axion models [58].

558 In general, 2HDMs can include \mathcal{CP} -violating interactions (similar to Sec. 2.3.1)
 559 as well as flavor-changing neutral currents (FCNCs). Both of these phenomena are
 560 experimentally well constrained, and so it makes sense to restrict oneself to \mathcal{CP} -
 561 and flavor-conserving limits. Doing so leads to definite quantum numbers of the
 562 five physical scalar states of the 2HDM: two neutral scalar (\mathcal{CP} -even) states h and
 563 H , a neutral pseudoscalar (\mathcal{CP} -odd) state A , and two charged states H^+ and H^- .
 564 Usually, the state h is identified with the SM Higgs boson at a mass of 125 GeV.
 565 Then, the two other neutral states H and A - if massive enough - could play the role
 566 of additional Higgs bosons decaying to $t\bar{t}$ as discussed in Sec. 2.3.1.

567 Depending on the nature of the discrete symmetry that is used to impose flavor
 568 conservation, there can be different types of 2HDMs, which differ in the structure of
 569 the couplings to the SM. No particular 2HDM type is assumed in this work, and the
 570 results of Chapter 7 are instead presented in terms of the generic model of Sec. 2.3.1.

571 2.3.3 Axion-Like Particles

572 Another very generic class of BSM scalars relevant to the $pp \rightarrow t\bar{t}$ process are ax-
 573 ions and Axion-Like Particles (ALPs), denoted here as a . Axions were originally
 574 conceived as solutions to the strong \mathcal{CP} problem [52, 53, 59, 60], which is a re-
 575 sult of the non-trivial vacuum structure of QCD. When deriving the effective QCD
 576 Lagrangian, the presence of certain classes of topological solutions to the classical
 577 Yang-Mills equations leads to an additional \mathcal{CP} -violating term [61]

$$\mathcal{L}^{QCD} \supset \theta \frac{\alpha_S}{8\pi} G_{\mu\nu}^a \tilde{G}^{a\mu\nu}, \quad (2.20)$$

578 where $G_{\mu\nu}^a$ is again the gluon field strength and $\tilde{G}_{\mu\nu}^a$ its dual. The coefficient θ of this
 579 term is a free parameter in the range $[0, 2\pi]$, with no particular value preferred from
 580 first principles. However, experimentally, no \mathcal{CP} violation in pure QCD has been
 581 observed, and θ is strongly bounded at $|\theta| \leq 10^{-10}$ (the strongest bounds coming
 582 from measurements of the electromagnetic dipole moment of the neutron [61–63]).

583 The strong \mathcal{CP} problem thus consists of explaining why the \mathcal{CP} -violating $G_{\mu\nu}^a \tilde{G}^{a\mu\nu}$
 584 term vanishes.

585 The most prominent way to solve the strong \mathcal{CP} problem is by introducing a new
 586 real scalar field a , the axion field, with a Lagrangian [61]

$$\mathcal{L}^{\text{ax}} = \frac{1}{2} \partial_\mu a \partial^\mu a + \frac{\alpha_S}{8\pi} \frac{a}{f_a} G_{\mu\nu}^a \tilde{G}^{a\mu\nu} + \text{interaction terms} \quad (2.21)$$

587 where f_a is called the axion scale, and all other interaction terms with SM fields are
 588 required to be invariant under a shift $a \rightarrow a + \kappa f_a$ with arbitrary κ . It can be shown
 589 that this Lagrangian, when added to the SM QCD Lagrangian including the term
 590 in Eq. (2.20), leads to a global minimum at $a/f_a + \theta = 0$, so that after a field shift
 591 the \mathcal{CP} -violating term is absorbed in the axion-gluon coupling and no \mathcal{CP} violation
 592 is expected in QCD alone. This is known as the Peccei-Quinn mechanism.

593 In Eq. (2.21), the axion-gluon interaction term has dimension 5 and is thus non-
 594 renormalizable, with the cutoff scale given by f_a . The axion must thus be necessarily
 595 be seen as a low-energy EFT description of different physics at the higher scale f_a .
 596 Many different UV-complete models including axions exist [61, 64–67], which lead
 597 to different interaction terms with other SM particles such as photons, electroweak
 598 bosons or massive fermions.

599 In this work, a focus is placed upon models which predict couplings to SM
 600 fermions, particularly the top quark. The EFT Lagrangian is parameterized in
 601 a model-independent approach as [68]

$$\begin{aligned} \mathcal{L}^{\text{ALP}} = & \frac{1}{2} \partial_\mu a \partial^\mu a + \frac{m_a^2}{2} a^2 - c_G \frac{a}{f_a} G_{\mu\nu}^a \tilde{G}^{a\mu\nu} - c_B \frac{a}{f_a} B_{\mu\nu} \tilde{B}^{\mu\nu} \\ & - c_W \frac{a}{f_a} W_{\mu\nu}^a \tilde{W}^{a\mu\nu} - \sum_f c_f \frac{\partial^\mu a}{f_a} \bar{\Psi}_f \gamma_\mu \Psi_f, \end{aligned} \quad (2.22)$$

602 where the index f runs over the SM fermions, Ψ_f are the fermion fields, $B_{\mu\nu}$ and
 603 $W_{\mu\nu}^a$ are the EW boson fields before symmetry breaking, and the free parameters
 604 are the scale f_a , the mass m_a , and the couplings to gluons c_G , to EW bosons c_B
 605 and c_W and to fermions c_f (where no flavor mixing was assumed). This Lagrangian,
 606 depending on the choice of the free parameters, might or might not correspond to
 607 a UV-complete model and solve the strong \mathcal{CP} problem. Because of this, the field a
 608 is here called an Axion-Like Particle. Even when it does not correspond to a true
 609 axion, it might be a physically well-motivated extension of the SM, e.g. as a dark
 610 matter candidate or mediator.

611 In the ALP-fermion interaction term in Eq. (2.22), the shift symmetry of a is
 612 directly manifest since it only depends on the derivative of a . However, by employing
 613 the equations of motion for a as well as the Higgs mechanism, one can rewrite
 614 Eq. (2.22) with a Yukawa-like interaction instead. Dropping the EW bosons and

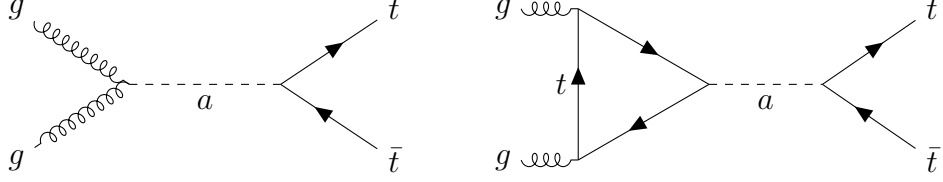


Figure 2.8: **Feynman diagrams for $gg \rightarrow a \rightarrow t\bar{t}$.** The left diagram corresponds to the gluon-ALP contact interaction and scales with $c_{\tilde{G}}c_t$, while the right diagram shows the top quark loop and scales with c_t^2 .

615 fermions other than the top quark leads to

$$\mathcal{L}^{\text{ALP}} = \frac{1}{2}\partial_\mu a\partial^\mu a + \frac{m_a}{2}a^2 - c_{\tilde{G}}\frac{a}{f_a}G_{\mu\nu}^a\tilde{G}^{a\mu\nu} + i c_t m_t \frac{a}{f_a} \bar{t} \gamma^5 t. \quad (2.23)$$

616 Performing this basis change induces an additional ALP-gluon coupling term (in
 617 general dependent on the other SM couplings), which was absorbed by redefining
 618 the Wilson coefficient from c_G to $c_{\tilde{G}}$. This basis will be used in the remainder of
 619 this work.

620 It can be seen by comparing Eq. (2.23) to Eq. (2.18) that the ALP-top coupling
 621 has the exact same structure as the generic \mathcal{CP} -odd boson introduced in Sec. 2.3.1.
 622 Thus, if the ALP is heavy enough to be produced at the LHC and decay to $t\bar{t}$, it
 623 can be searched for in $t\bar{t}$ final states similarly to the generic pseudoscalar A. Such
 624 heavy ALP masses can be reached naturally and serve as solutions to the strong \mathcal{CP}
 625 problem e.g. in UV models containing extra non-abelian gauge groups, resulting in
 626 containing forces with large containment scales [69–72].

627 If, in addition, the ALP couplings also satisfy $c_{\tilde{G}} = 0$, the two Lagrangians in
 628 Eqs. (2.18) and (2.23) are identical, and all conclusions drawn on A can be directly
 629 transferred to the ALP. On the other hand, if $c_{\tilde{G}} \neq 0$, an additional production
 630 diagram involving a gluon contact interaction becomes available, as depicted in
 631 Fig. 2.8. A phenomenological study characterizing both cases in detail forms the
 632 core of Chapter 8 of this work.

633 3 Monte Carlo event generation

634 In order to test the Standard Model or extract any of its parameters at the LHC,
635 one requires a prediction which can be compared to the experimental data recorded
636 by the detectors in the form of collision events. This is, in general, a very complex
637 task consisting of many different subprocesses and physical scales. The generation
638 starts with the hard parton scattering, then continues with the emission of addi-
639 tional radiation, effects of interactions with other partons in the colliding protons,
640 hadronization, interactions between other protons in the same bunch, and ends with
641 the simulation of the different subdetectors and triggers. Many of these processes
642 are not only probabilistic, but intractable through direct analytical or numeric inte-
643 gration due to the large phase space and the complexity of the problems involved.

644 Instead, the Monte Carlo (MC) method is used for this purpose. Here, it amounts
645 to randomly sampling an event from the phase space of the starting distribution - in
646 this case, the hard scattering - and then passing it through a chain of simulation tools
647 for the remaining steps until one arrives at an event that is directly comparable to
648 events recorded experimentally. This method is advantageous in that the numerical
649 error in an arbitrary region of phase space always scales with $1/\sqrt{N}$, where N is
650 the total number of events produced, independently of the dimensionality of the
651 problem. Thus, getting a numerically accurate prediction is mostly a matter of
652 producing a sufficient number of MC events.

653 In this chapter, the different tools used in the CMS simulation chain are discussed.
654 A focus is laid on the hard scattering or matrix element generators (Sec. 3.1) as well
655 as the parton showering (Sec. 3.2) since these are the focus of the studies presented
656 in Chapter 6, while interactions with other partons in the colliding protons (“multi-
657 parton interactions”, Sec. 3.3), hadronization (Sec. 3.4), interactions between other
658 protons in the same bunch (“pileup”, Sec. 3.5), as well as the detector and trigger
659 simulation (Sec. 3.6) are only briefly touched upon.

660 3.1 Matrix Element generators

661 At the LHC, protons are collided with large center-of-mass energies of multiple
662 TeV. Because protons are not fundamental particles, but bound states of QCD
663 which cannot be perturbatively described from first principles, providing accurate
664 predictions for proton-proton collisions is generally a very challenging task. For the
665 specific case of hard scattering processes, i.e. processes in which the particles in
666 the final state X have large transverse momenta, one can employ the factorization

⁶⁶⁷ theorem of QCD [73]:

$$\sigma(pp \rightarrow X) = \int_0^1 dx_1 \int_0^1 dx_2 \sum_{a,b} f_a(x_1, \mu_F) f_b(x_2, \mu_F) \hat{\sigma}(a(x_1 P) + b(x_2 P) \rightarrow X) \quad (3.1)$$

⁶⁶⁸ where P is the incoming momentum of the protons, assumed to be purely longitudinal and thus $P = \sqrt{s}/2$, and the sum runs over all possible combinations a, b of ⁶⁶⁹ initial state partons (quarks and gluons). This formula factorizes the total hadronic ⁶⁷⁰ cross section into two parts: The partonic cross section $\hat{\sigma}(a + b \rightarrow X)$ describes the ⁶⁷¹ scattering of two partons at high energies, and can be computed perturbatively in ⁶⁷² α_S due to asymptotic freedom of QCD. The functions $f_a(x, \mu_F)$ on the other hand ⁶⁷³ are the parton distribution functions (PDFs) and describe the probability of finding ⁶⁷⁴ a parton of type a with momentum fraction $p_a/P = x$ in the proton structure. ⁶⁷⁵ Since they probe low momentum scales where α_S is large, they cannot be computed ⁶⁷⁶ perturbatively and instead need to be measured experimentally. In addition to x , ⁶⁷⁷ they also depend on the factorization scale μ_F , which is the energy scale defining the ⁶⁷⁸ separation between hard (perturbative) and soft (non-perturbative) QCD. It is typically ⁶⁷⁹ set to be equal to the characteristic energy of the incoming partons, e.g. half ⁶⁸⁰ the partonic invariant mass. In contrast to the dependence on x , the dependence on ⁶⁸¹ μ_F is a prediction of QCD and follows from the DGLAP equations [74, 75]. ⁶⁸²

⁶⁸³ The partonic cross section can further be written differentially as [73]

$$d\hat{\sigma}(ab \rightarrow X) = \frac{1}{2\hat{s}} \left(\prod_f \frac{d^3 p_f}{(2\pi)^3} \frac{1}{2E_f} \right) |\mathcal{M}(ab \rightarrow X)|^2 (2\pi)^4 \delta^{(4)} \left(\sum_f p_f \right) \quad (3.2)$$

⁶⁸⁴ where $\hat{s} = x_1 x_2 s$ is the partonic center-of-mass energy squared, the term in the ⁶⁸⁵ brackets refers to the integral over the final state phase space and depends only ⁶⁸⁶ on the number and masses of the final state particles f , the δ function encodes ⁶⁸⁷ momentum conservation, and only the scattering matrix element \mathcal{M} depends on the ⁶⁸⁸ details of the process considered.

⁶⁸⁹ Events are now generated by drawing randomly from the full kinematically allowed ⁶⁹⁰ final state phase space, as well as from the PDFs characterizing the initial state, and ⁶⁹¹ keeping them with a probability proportional to the corresponding hadronic cross ⁶⁹² section according to Eq. (3.1). The partonic cross section here might be known analytically ⁶⁹³ for simple processes, or might need to be integrated numerically for complex ⁶⁹⁴ processes (especially at NLO or higher). The PDFs, based on fits to experimental ⁶⁹⁵ data, are usually tabulated and interpolated; in this work, the NNPDF 3.1 PDF set ⁶⁹⁶ is most commonly used for this purpose [76]. In practice, codes usually employ an ⁶⁹⁷ adaptive sampling algorithm to enhance the fraction of events that pass and thus ⁶⁹⁸ speed up the calculation, see e.g. Ref. [77].

699 ME generators exist at LO, NLO, and (approximate) NNLO in QCD, all of which
 700 are used at different points in this work. For NLO and NNLO processes, care must
 701 be taken to cancel ultraviolet (UV) as well as infrared (IR) divergences that often
 702 appear in the integration of the matrix element. The former is done in the framework
 703 of renormalization, which usually introduces a dependence on an additional scale,
 704 the renormalization scale μ_R . Similar to μ_F , it is typically set to the energy scale
 705 of the process, and, since the dependence is expected to vanish at infinite order in
 706 QCD, variations of μ_R and μ_F are often used to asses the size of uncertainties due
 707 to missing higher orders [12]¹.

708 IR divergences, on the other hand, arise when the momenta of massless particles
 709 in loop diagrams, such as gluons or light quarks, approach zero. They need to
 710 be canceled with corresponding divergent diagrams containing the emission of a
 711 real particle, which occur when the emission is soft or collinear with respect to the
 712 emitter. As a result, NLO calculations for the final state X will always need to also
 713 take into account the final state $X + j$, where j can be a gluon or light quark [79].

714 In this work, two different ME generators are used. The first is MG5_AMC@NLO,
 715 a general-purpose ME generator that can work both at LO and NLO [80]. It features
 716 fully automated computation of arbitrary processes in the SM or BSM, where the
 717 model is specified in the Universal FeynRules Output (UFO) format [81]. It is used
 718 in this work for both SM and BSM processes.

719 The second ME generator used is POWHEG Box (short for Positive Weighted Hard-
 720 est Emission Generator), which is a generic framework for NLO and approximate
 721 NNLO generators [82–84]. In contrast to MG5_AMC@NLO, it is not automated,
 722 and requires the manual implementation of each process. Many processes are pub-
 723 licly available as part of the POWHEG Box collection, and several are used in this
 724 work. Importantly, $pp \rightarrow t\bar{t}$ is generated at NLO with the POWHEG Box process
 725 hvq [85] in Chapters 5, 7 and 8. The two generators also differ in the scheme used
 726 to match to the parton shower, which is explained in the next section.

727 3.2 Parton showers and matching

728 The output of ME generators are events whose final states typically involve quarks
 729 and gluons with high momenta. Formally, such computations are accurate to some
 730 fixed order in α_S at which the calculation was performed, and all further emissions
 731 of gluons, as well as splittings of gluons into quark-antiquark-pairs, is suppressed

¹Using μ_R and μ_F variations as estimates of missing higher order uncertainties, while common, can only give a rough estimate of the magnitude of missing higher order contributions and does not truly give information about shape deficiencies in differential distributions. A recent, more thorough approach are *theory nuisance parameters* quantifying the uncertainty in specific parts of the theory calculation [78]. This method has however not yet been extended to $t\bar{t}$ production and is thus not considered here.

732 by additional powers of α_S . However, the matrix elements for such splittings be-
 733 come singular in the limit that the emitted partons are *soft* and/or *collinear* to the
 734 emitting particle, leading to IR divergences. The divergences can be regulated by
 735 absorbing them in renormalized PDFs, from which the DGLAP equations can be de-
 736 rived [12, 75]. They still lead to large corrections for each additional soft or collinear
 737 splitting considered, proportional to $\alpha_S \log(\hat{s}/\Lambda_{\text{QCD}}^2)$, where $\Lambda_{\text{QCD}} \approx 250 \text{ MeV}$ is the
 738 scale at which QCD becomes nonperturbative. This term is of order 1 and thus
 739 spoils the convergence of the perturbative series if it is cut off at a fixed order in
 740 α_S [73, 75].

741 A way to approximately incorporate these corrections is by using parton show-
 742 ers. For a parton associated with some scale Q_0 , the probability for no splitting to
 743 occur above some scale Q (with $Q < Q_0$) is called the *Sudakov factor* $\Delta(Q_0, Q)$.
 744 Because the structure of the IR singularities in QCD is universal, i.e. depending
 745 only on the types of particles in the splitting but not the rest of the process, its
 746 leading-logarithmic behavior can be computed from the matrix elements of $q \rightarrow qg$
 747 and $g \rightarrow q\bar{q}$ splittings (the *splitting kernels*). The parton shower algorithm now
 748 iteratively draws random numbers from this distribution, thus generating real emis-
 749 sions and splittings with successively lower scales Q down to Λ_{QCD} . In practice, the
 750 Sudakov factor usually contains additional terms beyond the leading-logarithmic
 751 behavior depending on the details of the algorithm [75].

752 The scale Q which determines in which order the splittings are performed is also
 753 called the *ordering variable*, and its form can be freely chosen as long as it correctly
 754 captures the soft and collinear singularities. Two common choices are the transverse
 755 momentum of the emission (p_T -ordered shower) or the emission angle respective to
 756 the emitting particle (angular-ordered shower). The result of either choice is an
 757 effective resummation of the logarithms associated to each emission, which is why
 758 parton showers are said to be leading-log (LL) accurate for certain observables.

759 The main parton shower used in this work is a p_T -ordered dipole shower, included
 760 as part of the PYTHIA multi-purpose event generator [86, 87]. It works by collecting
 761 quark-antiquark pairs into color dipoles, which radiate gluons together so that the
 762 recoil is distributed between the quarks. Here, it is mostly used by matching it to
 763 the ME generators described in Sec. 3.1. This is usually trivial at LO: the parton
 764 shower simply starts from the final state as given by the ME generator.

765 At NLO or higher, however, care must be taken that there is no double-counting
 766 between the additional real emissions in the final state of the ME generator and the
 767 emissions of the shower, as well as between the virtual corrections that are exact in
 768 the ME generator and approximated in the shower [75]. Several matching schemes
 769 exist to solve this issue. In this work, the MC@NLO and POWHEG schemes are
 770 used and briefly explained in the following.

771 In the MC@NLO scheme [88], as implemented in MG5_AMC@NLO, the double-
 772 counting is corrected for using a subtraction scheme: During the generation of the
 773 real and virtual correction terms in the matrix elements, the approximate corrections

774 that would be used in the parton shower are subtracted from the squared amplitude.
775 When the events generated in this way are then showered, the approximate correc-
776 tion terms are effectively added back, so that formally the exact result is recovered
777 at NLO accuracy. This strategy is conceptually simple and easy to generalize (and
778 thus automatize, as done in MG5_AMC@NLO). However, at phase-space points
779 where the approximate terms are larger than the exact ones, it inherently results in
780 events with negative weights, which can greatly increase the MC statistics required.

781 In the POWHEG scheme [82, 83], as used in the POWHEG Box, the fraction
782 of negative weights is greatly reduced by always generating the first real emission
783 in the ME generator, so that the real emission term is already exact, and then
784 only subtracting the approximate virtual correction term. The parton shower then
785 needs to only generate the second-hardest and higher emissions, which is typically
786 achieved by starting the shower evolution at the scale of the first, ME-level emission
787 (sometimes called “wimpy shower”).

788 This approach assumes that the scale definitions in the ME generator and the
789 parton shower are identical, which in general will not always be the case. In par-
790 ticular, for the important case of POWHEG matched to PYTHIA, used in this work
791 for the simulation of $pp \rightarrow t\bar{t}$, there is a mismatch in the scales which might lead to
792 double-counting. A more refined approach here is to use a vetoed shower: the shower
793 is started at the kinematically allowed limits and evolved downwards as usual, or-
794 dered by the scale as defined by PYTHIA. For the first emission the scale is then
795 recomputed according to the POWHEG definition, and it is vetoed and re-showered
796 if this scale is higher than the one in the ME.

797 A further improvement in the accuracy of the MC prediction can be achieved by
798 generating any number of additional jets in the matrix element at either LO or NLO,
799 so that these jets are described exactly by the ME generator instead of approximately
800 by the shower. This, however, requires complex matching procedures, such as MLM
801 matching [89] for LO and FxFx matching [90] for NLO matrix elements. In this
802 work, both schemes are only used tangentially for either background processes in
803 Chapter 5 or an alternative $t\bar{t}$ prediction in Chapter 7.

804 More complicated procedures have to be invoked in the case that the ME contains
805 more than one real emission. This case is studied in detail for the ME generator bb41
806 in Chapter 6. Furthermore, besides PYTHIA, multi-purpose generator HERWIG [91,
807 92] is considered in parts of Chapter 7, and briefly described there.

808 3.3 Multi-parton interactions

809 In addition to the hard scattering, additional soft QCD interactions might occur
810 between the other partons in the two colliding protons. This is referred to as multi-
811 parton interactions (MPI) or underlying event (UE). It is handled by PYTHIA based
812 on heuristic models, interleaved with the parton shower. In general, MPI parameters

813 need to be tuned to experimental data. This was done by the PYTHIA authors, such
 814 as the different versions of the Monash tune [93], and building on top of this by
 815 the CMS collaboration in the form of the CP tune family, most recently the CP5
 816 tune [94]. Both tunes are based on a large data set of e^+e^- , ep , $p\bar{p}$, and pp collision
 817 data from many different experiments. The CP5 tune will be used in all parts of
 818 this work.

819 3.4 Hadronization

820 The result of the MPI-interleaved parton shower consists of a collection of bare
 821 quarks and gluons at energies of $\mathcal{O}(\Lambda_{\text{QCD}})$, at which QCD becomes non-perturbative.
 822 The hadronization of these quarks and gluons into hadrons as well as their subse-
 823 quent decays thus need to be described heuristically.

824 For most of this work, this is done using the Lund string fragmentation model [95,
 825 96], again implemented in PYTHIA. In this model, the strong force between a quark
 826 and an antiquark of opposite color is modeled as a string in space-time, standing in
 827 for e.g. a three-dimensional flux tube. The energy stored in the string is proportional
 828 to its length, consistent with the long-distance behavior of QCD observed e.g. in
 829 lattice QCD. Hard gluons can be accommodated in this model as kinks in the string,
 830 i.e. for a $q\bar{q}g$ state, the q and \bar{q} are connected through the gluon instead of directly.

831 As the quarks move apart, the energy stored in the string increases, until it is
 832 large enough that the string fragments by creating an additional $q\bar{q}$ pair from the
 833 vacuum. If the energy in the resulting strings is still large enough, the procedure
 834 repeats. Otherwise, the low-mass $q\bar{q}$ pair is considered a meson, based on the flavors
 835 of its constituents. In its purest form, this model has only two free parameters
 836 which parameterize the distribution of the momentum fraction of the $q\bar{q}$ pair in each
 837 fragmentation. However, in order to correctly describe e.g. flavor composition and
 838 p_T spectra of jets, many more parameters are usually needed. For more details on
 839 string fragmentation in PYTHIA, see e.g. Ref. [87]. Similar to MPI, hadronization
 840 parameters need to be tuned to data, and are also included in the Monash and CP5
 841 tunes.

842 One shortcoming of the default MPI and hadronization models is that both work
 843 in the leading color (LC) approximation, i.e. in the limit of a large number of
 844 QCD colors ($N_c \rightarrow \infty$). This simplifies the models greatly because the chance
 845 of two unrelated color lines sharing the same color becomes infinitesimally small.
 846 Corrections to this approximation are typically of order $1/N_c^2 = 1/9$, and can be done
 847 via color reconnection (CR), for which different models exist, see e.g. Refs. [97, 98].
 848 The difference between different models is often considered a source of uncertainty
 849 in measurements, such as in Secs. 5.5 and 7.5, and can be a limiting factor for some
 850 analyses (e.g. top quark mass measurements).

851 Finally, decays of produced unstable hadrons, including possible decay chains,

852 are also handled by PYTHIA. Branching ratios are taken from experimental mea-
853 surements where available, and predicted from heuristic models where not, see e.g.
854 Ref. [87].

855 3.5 Pileup

856 At the currently achieved instantaneous luminosities, the proton bunches colliding at
857 the LHC contain more than 10^{11} protons on average. Because of this large number, it
858 is expected that a single collision event contains interactions between more than one
859 pair of protons from the two colliding bunches. This is known as pileup. It differs
860 from MPI, in which the different interactions are between multiple partons in the
861 same proton and are thus correlated from a QFT perspective, while different pileup
862 interactions are in principle independent from each other. In Run 2, the average
863 number of pileup interactions per bunch crossing ranged from 23-32 depending on
864 the era of data taking [99], while it is 40 or higher in Run 3.

865 In simulation, pileup interactions are considered by mixing the generated hard
866 interaction process with a dedicated sample of purely soft-QCD interactions, also
867 generated in PYTHIA. The probability distribution of the number of pileup interac-
868 tions is an input to this procedure, and is typically corrected after the generation
869 is finished by reweighting in a suitable variable. In Sec. 5.3.1, an experimental ap-
870 proach to this problem is taken by correcting experimentally accessible pileup-related
871 parameters directly to data. In Sec. 7.2.4, on the other hand, the distribution of the
872 true number of interactions is instead reweighted based on a theory prediction, using
873 the measured total inelastic cross section and integrated luminosity as inputs [100].

874 3.6 Detector and trigger simulation

875 After the simulation of the interaction processes, the resulting collection of particles
876 produced in an event is propagated to a full detector simulation using the program
877 GEANT4 [101]. The result is a set of detector information from all subdetectors as
878 well as the outputs of different triggers, similar to true experimental data, and so it
879 can be passed to the different object reconstruction algorithms (cf. Sec. 4.3) in the
880 same way as the data. Events are then analyzed by comparing the reconstructed ob-
881 jects and quantities between data and simulation, ensuring a one-to-one comparison.
882 Possible residual differences between data and simulation are often corrected for by
883 applying calibration factors measured using well-known processes. The details of
884 such calibrations will be explained in Chapters 5 and 7 where relevant.

885 4 Experimental methods

886 4.1 The Large Hadron Collider

887 At the time of writing, the Large Hadron Collider [102] is the largest and most
888 powerful particle accelerator in the world. Located underground at the border of
889 France and Switzerland close to Geneva, it consists of two circular beamlines of
890 roughly 27 km circumference, in which proton bunches are accelerated and collided.
891 Superconducting magnets, cooled with liquid helium at around 4 K temperatures,
892 generate magnetic fields of over 8 T to keep the protons on their circular orbit,
893 and similarly superconducting electromagnetic radio-frequency cavities accelerate
894 the protons to beam energies up to 7 TeV. When operating as designed, around
895 2800 proton bunches per beam containing 3×10^{14} protons total are present in the
896 beamline simultaneously, revolving with a frequency of about 11.245 kHz. From
897 this, peak instantaneous luminosities of about $20 \text{ kHz} \mu\text{b}^{-1}$ can be reliably reached.
898 Alternatively, the LHC can also collide heavy ions, such as lead or oxygen, instead
899 of protons.

900 There are four large experiments making use of the colliding beams at the LHC,
901 located at the four interaction points. The two larger of these are ATLAS [103]
902 and CMS [4], both of which are general-purpose experiments intended to study
903 all aspects of the Standard Model in proton-proton collisions. The work of thesis
904 was performed as part of the CMS collaboration, and so the CMS experiment is
905 described in Sec. 4.2 in more detail. The two smaller experiments, on the other
906 hand, are specialized for certain tasks, namely the study of B physics and exotic
907 hadrons for LHCb [104] and the study of heavy-ion collisions for ALICE [105].

908 The data taken at the LHC so far can be divided into three Runs. Run 1 lasted
909 from 2010–2012, during which the LHC operated at center-of-mass energies of 7 and
910 8 TeV, significantly below the original target values, and yielded a total integrated
911 luminosity of about 29 fb^{-1} . It is this data that led to the original discovery of the
912 Higgs boson. Following this, after two years of pause, Run 2 resumed in 2015 with
913 a center-of-mass energy of 13 TeV and lasting to 2018. Around 140 fb^{-1} of data was
914 collected during this time. This complete data set, save for the small contribution
915 from 2015, is analyzed in Chapter 7 of this thesis.

916 Finally, Run 3 of the LHC started in 2022 after another three years of pause, and
917 is planned to last until 2026 at the time of writing. The center-of-mass energy was
918 again increased slightly to 13.6 TeV, and in the years 2022–2024 around 196 fb^{-1}
919 have been recorded, already surpassing Run 2. In Chapter 5 of this thesis, the very

920 first data of Run 3, corresponding to 1.21 fb^{-1} taken in July and August 2022 at
921 CMS, are analyzed in the context of a $t\bar{t}$ cross section measurement.

922 In the future, it is planned to upgrade the LHC to be able to run at higher
923 instantaneous luminosities as well as a further increased energy of 14 TeV [106].
924 The CMS detector will similarly be upgraded to replace aging components and deal
925 with the increased pileup conditions [107, 108], and a total integrated luminosity of
926 around 3 ab^{-1} is expected to be collected. In Chapter 8, among others, sensitivity
927 projections for this luminosity are made for Axion-Like Particles decaying to $t\bar{t}$.

928 4.2 The CMS experiment

929 The Compact Muon Solenoid experiment [4, 108], located at Interaction Point 5 of
930 the LHC close to Cessy, France, is a general-purpose particle detector targeting a
931 broad range of SM and BSM phenomena. Its main feature is a superconducting
932 solenoid magnet creating a strong magnetic field of 3.8 T. CMS is a hermetic detec-
933 tor, covering almost the full solid angle in space, and is split into a *barrel*, covering
934 pseudorapidities of $|\eta| \lesssim 1.5$, and two forward *endcaps*, covering high $|\eta|$ values. It
935 consists of several subdetectors, which are geared towards different particle types
936 and properties.

937 **Subdetectors** The innermost part of CMS is the *tracker*, which is a silicon de-
938 tector comprised of several layers of silicon pixel and strip sensors [110, 111]. These
939 record interactions with particles (“tracker hits”) shooting outwards from the inter-
940 action point in the center in three-dimensional space. Through reconstruction of the
941 particle tracks and fits of the curvature due to the magnetic field, the tracker thus
942 allows for the measurement of particle momenta. Furthermore, extrapolating the
943 tracks back to their origin allows for the determination of the point of interaction,
944 and thus for discrimination between particles arising from different proton-proton
945 interactions. Due to the presence of the beam pipe, the tracker covers only pseu-
946 dorapidities of $|\eta| < 2.5$, enabling high precision momentum determination in this
947 range only.

948 The second-to-innermost subdetector is the *electromagnetic calorimeter* (ECAL),
949 which is intended to measure the energy of electrons and photons [112, 113]. It
950 consists of transparent lead tungstate cells, in which incoming electrons or photons
951 create electromagnetic showers leading to avalanches of electron-positron pairs and
952 photon radiation. These are then recorded by photo diodes, and the energy of
953 the incoming particle can be reconstructed from the amount of measured photons.
954 Pseudorapidities of $|\eta| < 1.48$ and $1.65 > |\eta| < 3$ are covered for the barrel and the
955 endcaps, respectively. The majority electrons and photons are fully stopped in the
956 ECAL and do not interact with the further subdetectors.

4 Experimental methods

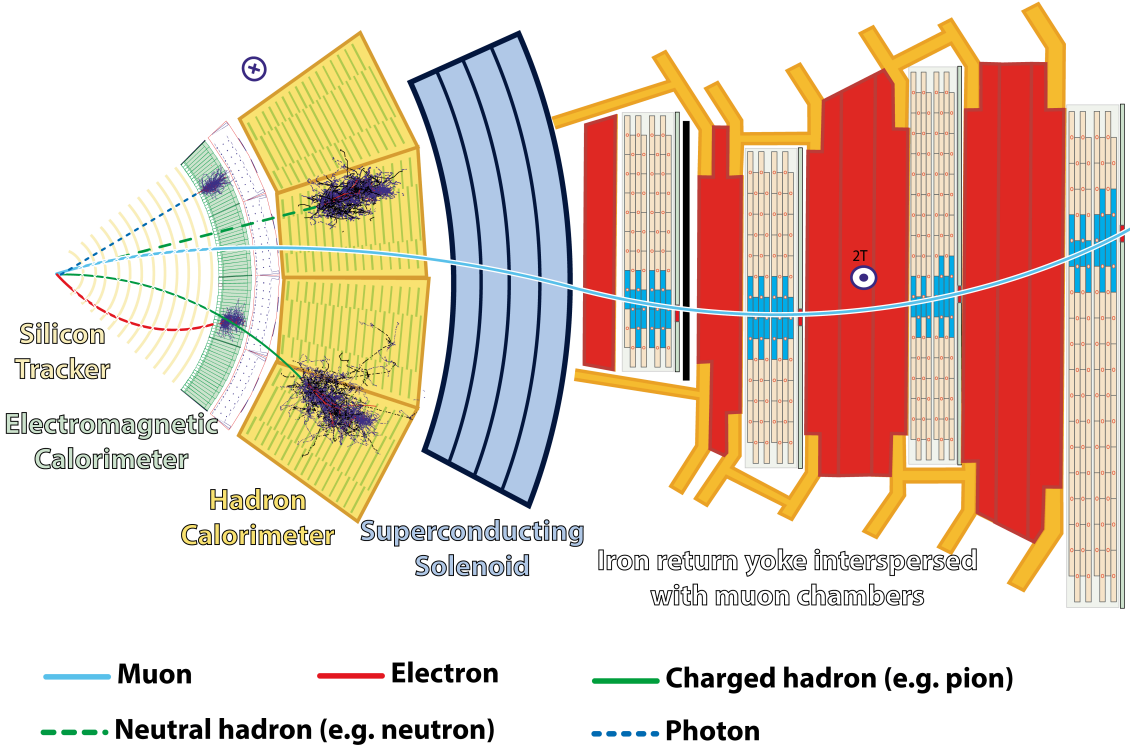


Figure 4.1: **The CMS detector.** A cross section view of the different CMS subdetectors, with the trajectories of example particles and their interactions. *Figure taken from Ref. [109].*

Following the ECAL, and similar in functionality, the *hadronic calorimeter* (HCAL) measures the energy of charged or neutral hadrons [114, 115]. It consists of interleaved absorber plates, which initiate hadronic showers through the strong interaction with the nuclei of the material, and scintillators, which transmute the hadronic showers into photons to be detected by photodetectors. The HCAL covers $|\eta| < 1.4$ and $1.4 < |\eta| < 3$ for the barrel and endcaps, respectively, and additionally features a forward section ranging up to $|\eta| < 5$, though the latter is not used anywhere in this work.

Surrounding the HCAL lies the superconducting solenoid, followed by the final subdetector: the *muon chambers* [116, 117]. They are interspersed with four layers of the iron return yoke of the magnet, which confines the magnetic field. Since muons interact only sparsely with matter, they escape the calorimeters and the solenoid unhindered, and are detected in four muon subsystems working in accord at different pseudorapidities: the drift tubes ($|\eta| < 1.2$), cathode strip chambers ($0.9 < |\eta| < 2.4$), resistive plate chambers ($|\eta| < 1.9$) and gas electron multipliers ($1.6 < |\eta| < 2.4$). All of them are gas detectors, which are sensitive to the ionization of a gas when a muon passes through it, and record hits of the muon trajectory,

thus allowing for a momentum measurement similar to the tracker.

Trigger system Besides the different subdetectors, a crucial part of the CMS experiment is the *trigger system* [118]. It is necessary due to the large number of bunch crossings at the LHC, which, if they were all recorded, would produce data rates far in excess of the computational bandwidth and storage capacities available. To combat this, only events which are of physical interest should be recorded. It is the task of the trigger system to determine what these events should be.

The trigger system is split into two parts. The first is the low-level or level-one trigger (L1T) [119], which is a hardware trigger consisting of custom electronics and whose inputs are directly the output signals of several of the subdetectors. It is designed to trigger on signatures consistent with specific objects, such as electrons, muons or hadronic jets, with significant energy. Since it needs to take a decision for every collision event, it only has a time interval of around $4\mu\text{s}$ to do so, requiring purpose-build low-latency electronics. Its target is a output event rate of 100 kHz, which can be adjusted by prescaling certain trigger paths so that only a fraction of passing events is recorded.

The second part of the trigger system is the high-level trigger (HLT) [120, 121]. It is a software trigger, running on a GPU-accelerated server farm directly in the CMS service cavern, on which a dedicated, speed-optimized version of the standard CMS object reconstruction algorithm is executed for each event passing the L1T. Specific triggers are then implemented as decisions based on these reconstructed trigger objects, allowing large freedom in selecting events based on the desired physics program. Typical triggers require, for example, the presence of different numbers or combinations of electrons, muons, photons, hadronic jets or missing transverse momentum. The transverse momentum thresholds and further requirements on these objects need to be adjusted so that the total trigger rate is reduced to an average of around 400 Hz. Only these events are then saved to hard drives, and kept for further analysis.

4.3 Object reconstruction

In order to interpret the physics behind a collision event, the outputs of the subdetectors have to be translated into physics objects which can be mapped to the underlying physical particles. At CMS, this is done with a single unifying method, the Particle Flow (PF) algorithm [122], which is designed to combine the information from the several subdetectors to build physics objects (called PF candidates) as appropriate. The physics objects relevant to this work are listed in the following.

Charged particle tracks are obtained from the tracker by fitting recorded tracker hits using a χ^2 minimization, and their momentum and charge are estimated from

4 Experimental methods

their curvature as described above [110]. By extrapolating the tracks back to their origin, the position of vertices in space can also be determined.

From the tracks, the *primary vertices* (PVs) can be determined, which are the locations of the proton-proton interactions that caused the tracks in the first place. By contrast, secondary vertices arise from the decays of particles with long enough lifetime that they move a significant distance from the PV. PVs are determined by a likelihood fit to all tracks of sufficient quality [110]. In each event, the PV whose tracks show the largest p_T sum is designated the hard-scattering PV, assumed to correspond to the physical process of interest, while further PVs are due to soft-QCD pileup interactions. The number of PVs per event is thus a good measure of the amount of pileup.

The other main ingredient besides tracks and vertices are *calorimeter clusters* from either the ECAL or the HCAL. A clustering algorithm is required here because particles typically deposit their energy in more than one calorimeter crystal.

By matching the positions of calorimeter clusters and charged particle tracks, *electrons* (for the ECAL) and *charged hadrons* (for the HCAL) can be constructed. The combined measurements of the momentum (from the curvature) and the deposited energy (from the calorimeter) allows for the reconstruction of the mass, and thus the identification of the particle. For electrons, the effect of bremsstrahlung originating in the tracker volume has to be considered, usually resulting in multiple calorimeter clusters per electron (called a supercluster) which need to be combined together. Isolation criteria on the clusters are also required to veto electrons that are part of a hadronic jet. By contrast, calorimeter clusters which do not have charged tracks are assigned to *photons* (for the ECAL) or *neutral hadrons* (for the HCAL). CMS furthermore employs algorithms to remove hadrons that are believed to originate from pileup instead of the hard-scattering vertex. In Run 2, the Charged Hadron Subtraction (CHS) method [122] was used for this purpose, while in Run 3, the better performing PUPPI method [99, 123] was used instead.

Muons interact only very rarely with the calorimeter, and are instead built by directly combining charged tracks with hits in the muon chambers. In this work, muons are only considered if they match to hits in both subdetectors.

From these definitions, further high-level objects can be build. The first are *hadronic jets*, which are clustered from all other PF candidates using the anti- k_T algorithm with a distance parameter of $\Delta R = 0.4$ [124] (referred to as AK4 jets). This algorithm is infrared- and collinear-safe, i.e. it is not strongly sensitive to soft nonperturbative QCD effects [75], and has the advantage that the resulting jets are approximately circular in the $\varphi-\eta$ plane. Since leptons or photons can be created from electroweak decays of hadrons, these also need to be included in the jet clustering; to ensure that they are not double-counted, leptons and photons that are included in jets are removed from further consideration through isolation criteria.

Hadronic jets can further be *b tagged*, that is, identified as originating from a B hadron. Since the strong interaction is flavor-conserving, the decay of B hadrons

1053 to hadrons of other flavors has to be mediated by the flavor-mixing in the weak
 1054 interaction, leading to comparatively long lifetimes. B hadrons can thus be identified
 1055 through secondary vertices corresponding to the B hadron decay, which can be
 1056 displaced from the PV by several millimeters. In practice, machine learning-based
 1057 classifiers like the DEEPJET algorithm [125] are used, which take more properties
 1058 of the jet into account besides the displacement of the secondary vertex.

1059 Finally, the *missing transverse momentum* \vec{p}_T^{miss} can be calculated as the negative
 1060 of the vectorial sum of all transverse momenta in the event [126]. Since the initial
 1061 state of a collision at the LHC has negligible transverse momentum, \vec{p}_T^{miss} represents
 1062 the total transverse momentum of the particles that left the detector unobserved.
 1063 In the SM, this is the case for neutrinos, but it could also be BSM particles such as
 1064 e.g. dark matter candidates.

1065 4.4 Statistical interpretation

1066 In experimental particle physics, results are typically extracted by comparing detector-
 1067 level predictions, for example obtained using MC simulation, to the observed data
 1068 for suitably chosen observables. The measured data here are necessarily afflicted by
 1069 statistical uncertainties, both due to the inherent randomness of quantum mechanics
 1070 and the probabilistic behavior of the detector. They should thus be seen as a sample
 1071 drawn from a random distribution, and in order to extract underlying parameters
 1072 of any model, statistical methods are required.

1073 In this work, all statistical interpretation is performed in the framework of *binned*
 1074 *profile maximum likelihood fits*. This method follows the Frequentist approach of
 1075 considering physical properties that should be extracted to be fixed, if unknown,
 1076 quantities, which enter the random distribution of the observed data as parameters.
 1077 In order to estimate the desired properties, the observed data points are sorted
 1078 into orthogonal bins according to one or more sensitive observables, and each bin
 1079 is treated as an independent counting experiment where the observed number of
 1080 events is given by a Poisson distribution.

1081 **Likelihood definition** Denoting the set of physical properties to be estimated
 1082 (the parameters of interest or POIs) collectively as $\vec{\mu}$, the likelihood of $\vec{\mu}$ for bin i ,
 1083 given that N_i events were observed, is [127]

$$L_i(\vec{\mu}, \vec{\theta}) = \text{Pois}\left(N_i | n_i(\vec{\mu}, \vec{\theta})\right). \quad (4.1)$$

1084 Here, Pois refers to the Poisson distribution, and $n_i(\vec{\mu}, \vec{\theta})$ is the mean expected
 1085 number of events in bin i as predicted by the physics model under consideration.
 1086 The set of parameters $\vec{\theta}$ are *nuisance parameters* (NPs), which encode the effects

4 Experimental methods

1087 of different sources of systematic uncertainty affecting the measurement. The full
1088 likelihood of the measurement is now given as the product of all bins:

$$L(\vec{\mu}, \vec{\theta}) = \prod_i L_i(\vec{\mu}, \vec{\theta}) \cdot G(\vec{\theta}). \quad (4.2)$$

1089 The function $G(\vec{\theta})$ represents the *constraint terms* of the NPs, encoding any possi-
1090 ble prefit uncertainties on them. For example, an experimental source of uncertainty
1091 (e.g. a scale factor) f might be measured with a mean value of \hat{f} and standard de-
1092 viation σ_f . Then, the corresponding NP would be normalized as $\theta_f = (f - \hat{f})/\sigma_f$,
1093 and the constraint terms $G(\vec{\theta})$ would include a factor $\mathcal{N}(\theta_f | 0, 1)$, i.e. the standard
1094 normal distribution for θ_f . This way, the range $\theta_f = \pm 1$ corresponds to one standard
1095 deviation of the corresponding systematic uncertainty source.

1096 In practice, the functional form of the expectation n_i must be given by the physics
1097 model studied in the experiment. In this work, the events are modeled as a sum of
1098 signal and background processes. An important case is a linear signal, where the
1099 only POI is the *signal strength* μ and the expectation for bin i is

$$n_i(\mu, \vec{\theta}) = \mu s_i(\vec{\theta}) + b_i(\vec{\theta}). \quad (4.3)$$

1100 The functions s_i and b_i are the signal and background expectations, respectively,
1101 which both can be influenced by NPs.

1102 To extract a best-fit value of the POI (or multiple POIs), one now maximizes
1103 the full likelihood simultaneously over both the POIs $\vec{\mu}$ and the NPs $\vec{\theta}$, giving the
1104 *maximum likelihood estimator* for $\vec{\mu}$. In practice, usually the function $-2 \ln L$ is
1105 minimized instead to have numerically tractable quantities.

1106 **Confidence intervals** In the Frequentist approach to statistics, an uncertainty
1107 can be assigned to the estimate in the form of *confidence intervals*. To do so, a *test*
1108 *statistic* has to be defined, which usually takes the form of a *profile likelihood ratio*,
1109 e.g. [127]

$$\lambda(\vec{\mu}) = -2 \ln \frac{\hat{L}(\vec{\mu})}{\max_{\vec{\mu}'} \hat{L}(\vec{\mu}') \quad \text{with} \quad \hat{L}(\vec{\mu}) = \max_{\vec{\theta}} L(\vec{\mu}, \vec{\theta}). \quad (4.4)}$$

1110 $\hat{L}(\vec{\mu})$ is the profile likelihood, i.e. the likelihood maximized over the NPs, and the
1111 ratio is taken between the probed POI values $\vec{\mu}$ and the best-fit values $\vec{\mu}'$. Small
1112 values of $\lambda(\vec{\mu})$ now signalize good agreement with the data for the POI values $\vec{\mu}$.
1113 The value of the test statistic λ depends on the observed data N_i , and can thus be
1114 seen as a random variable with a probability density $f(\lambda|\vec{\mu})$, which again depends
1115 on the POIs as parameters. Then, given an observed value of the test statistic λ^{obs} ,
1116 a set of POIs $\vec{\mu}$ is excluded at confidence level (CL) α if

$$P(\lambda(\vec{\mu}) < \lambda^{\text{obs}}) = \int_0^{\lambda^{\text{obs}}} f(\lambda|\vec{\mu}) d\lambda > \alpha. \quad (4.5)$$

1117 The probability density $f(\lambda|\vec{\mu})$ can be evaluated numerically using toy data sets.
 1118 Alternatively, for simple signal models like the linear signal given in Eq. (4.3), it
 1119 can be analytically shown that λ is approximately χ^2 -distributed, with the degrees
 1120 of freedom equaling the number of POIs [128, 129].

1121 In particular, for the case of one POI μ with best-fit value $\hat{\mu}$, a two-sided confi-
 1122 dence interval at $\sim 68\%$ CL (corresponding to one standard deviation of the normal
 1123 distribution) is then simply given as [127]

$$\lambda(\hat{\mu} \pm \Delta\mu) = -2(\ln \hat{L}(\hat{\mu} \pm \Delta\mu) - \ln \hat{L}(\hat{\mu})) = 1. \quad (4.6)$$

1124 That is, the uncertainty corresponds to a change in negative profile log-likelihood
 1125 $-2 \ln \hat{L}$ by 1 with respect to the best-fit point.

1126 **Significance** The framework of confidence intervals can also be used to define the
 1127 *significance* of an observed signal. To do so, a hypothesis test is performed, with the
 1128 background-only case as the null hypothesis to be rejected. For an observed value
 1129 of the test statistic λ^{obs} (defined again by Eq. (4.4)), the probability to make this
 1130 observation under the background-only hypothesis (the *p-value*) is

$$p_0 = \int_0^{\lambda^{\text{obs}}} f(\lambda|\vec{\mu} = 0) d\lambda. \quad (4.7)$$

1131 To translate this into a significance, the *p*-value is compared to the area under
 1132 the curve of a standard normal distribution: a significance of 2 standard deviations,
 1133 giving $\approx 95\%$ probability under the normal distribution, corresponds to a *p*-value
 1134 of 0.05. Similar to the case described above, the *p*-value can be obtained from
 1135 analytical approximate distributions in the case of a simple linear signal.

1136 **Exclusion limits** A different application of confidence intervals are *exclusion limits*,
 1137 used in experiments where no or little signal was observed. Here, for a POI that
 1138 is bounded from below (usually by zero, e.g. a signal strength), an upper limit μ^{up}
 1139 is sought such that all values $\mu > \mu^{\text{up}}$ are excluded at a certain CL. At the LHC,
 1140 the CL_s method [130, 131] is commonly used for this purpose. The test statistic is
 1141 modified from Eq. (4.4) to be

$$q(\mu) = \begin{cases} \lambda(\mu), & \hat{\mu} \leq \mu \\ 0, & \hat{\mu} > \mu \end{cases} \quad (4.8)$$

1142 where $\hat{\mu}$ again refers to the best-fit value of μ . The point of this modification is that
 1143 a certain value of μ should not be seen as excluded if the data is more compatible

4 Experimental methods

1144 with a higher μ value; thus, the test statistic is set to zero in this case.

1145 Following that, for an observed test statistic q^{obs} , the CL_s value is defined as

$$\text{CL}_s(\mu) = \frac{p_{s+b}(\mu)}{1 - p_b} \quad (4.9)$$

1146 with

$$p_{s+b}(\mu) = \int_0^{q^{\text{obs}}} f(q|\mu) dq \quad \text{and} \quad p_b = \int_0^{q^{\text{obs}}} f(q|\mu = 0) dq. \quad (4.10)$$

1147 p_{s+b} and p_b are the probabilities to observe a test statistic of q^{obs} under the
1148 signal+background and background-only hypotheses, respectively, defined similarly
1149 as in Eq. (4.7). The ratio of the two probabilities is used instead of p_{s+b} directly to
1150 prevent exclusion of small signals in the case that the data is not well compatible
1151 with neither the background-only or the signal+background hypothesis (particularly
1152 if the experiment is not very sensitive to a certain kind of signal and p_{s+b} and p_b are
1153 thus similar). The exclusion limit at CL α is then simply given by $\text{CL}_s(\mu^{\text{up}}) = 1 - \alpha$.
1154 A common choice, used in this work, is $\alpha = 95\%$ (corresponding to a p -value of 0.05).

1155 **Nuisance parameter diagnostics** Real maximum likelihood fits used in anal-
1156 yses at the LHC are often very complex, with more NPs than there are bins. In
1157 such under-constrained fits, the behavior of the different NPs - encoding the dif-
1158 ferent sources of uncertainty - is often not intuitively clear a priori, and it is thus
1159 important to investigate their postfit behavior to check whether the fit is healthy
1160 and numerically stable.

1161 To do so, first, the *pulls and constraints* of the NPs are defined as their best-
1162 fit values and profiled postfit uncertainties, similar as for the POIs above, relative
1163 to their prefit uncertainties. To have a NP pulled means that its best-fit value is
1164 different from the prefit expectation. Similarly, to have it constrained means that its
1165 estimated postfit uncertainty is smaller than the assumed prefit value. Both of these
1166 effects are not necessarily a sign of an unhealthy fit: If the observables considered in
1167 the fit are sensitive to a particular physical or experimental parameter as encoded
1168 by the NP in question, a constraint, and possibly a pull, are expected, and simply
1169 show the power of the fit to measure that particular parameter.

1170 If, on the other hand, a strong constraint or pull (beyond what is expected from
1171 statistical fluctuations) is seen in a NP to which no sensitivity is expected, it might
1172 be a sign of problems with the fit, such as spurious constraints from noisy inputs,
1173 missing degrees of freedom to describe the data, or too small prefit uncertainties.
1174 Whether this casts doubt on the result or not needs to be gauged on a case-by-case
1175 basis, and depends on the relevance of the NP in question.

1176 The relevance of individual NPs to the result can be quantified using *impacts*.
1177 The impact of a NP θ with best-fit value $\hat{\theta}$ and postfit uncertainty $\Delta\theta$ is defined by

repeating the maximum likelihood fit at values of $\hat{\theta} \pm \Delta\theta$, with θ then held fixed in the maximization of Eq. (4.4). The shift in the resulting POI values with respect to the best-fit POI is the impact on that particular POI. In a fit with a single POI, the impacts can be used to rank the NPs and the systematic uncertainties they encode in order of importance to the fit result. In particular, NPs with very small impact can be considered irrelevant for the fit result. However, it should be kept in mind that this procedure does not fully account for possible correlations between the NPs.

Uncertainty breakdown Related but not identical to the concept of impacts is an *uncertainty breakdown*, which can be used to quantify the contribution from different sources of uncertainty to the total postfit uncertainty on the POI. To do so, either a single NP or a group of NPs originating from the same source (e.g. all NPs corresponding to a certain correction) are frozen at their postfit values, and the fit is repeated with the POI and remaining parameters left untouched. The result will yield the same best-fit value for the POI, but with a possibly reduced uncertainty (as estimated from the likelihood). The uncertainty due to the frozen NP or NP group is then defined as the quadratic difference to the nominal uncertainty. This method does not account for correlations between different uncertainty sources (though it does consider correlations between the NPs in a certain group). As a result, the uncertainties obtained in this way will in general not sum up in quadrature to the original uncertainty.

A further use of this method is to define the statistical component of the uncertainty on a POI: it is simply the remaining uncertainty when all considered NPs are frozen to their postfit values simultaneously. Conversely, the quadratic difference between the total and the statistical uncertainty can be considered the systematic uncertainty.

Technical implementation In this work, two different tools are used to implement the methods described above. In Chapters 5 and 7, where experimental data is analyzed, the CMS general-purpose statistics tool `combine` is used [132]. In Chapter 8, on the other hand, the Python-based tool `pyhf` [133] is employed for the purpose of calculating expected significances and limits.

1208 **5 Measurement of the inclusive $t\bar{t}$ cross**
1209 **section at $\sqrt{s} = 13.6$ TeV**

1210 **5.1 Introduction**

1211 In July 2022, the LHC officially resumed collecting data after over three years of
1212 shutdown, thereby starting LHC Run 3. It did so at a new, unprecedented center-
1213 of-mass energy of $\sqrt{s} = 13.6$ TeV, inviting the experiments to measure physical
1214 observables at the new energy frontier.

1215 One important such observable is the inclusive $t\bar{t}$ production cross section. It is, in
1216 essence, the total rate of top quark pair production at the LHC, integrated over the
1217 kinematic distributions of the particles produced. As mentioned in Chapter 2, the
1218 top quark has a special place in the standard model as the heaviest known elementary
1219 particle, as well as the only colored particle that decays before hadronizing. It is
1220 thus important for many potential BSM scenarios, such as models with additional
1221 Higgs bosons, which might couple strongly to the top quark. As such, measurements
1222 of top quark-related observables at the highest possible energies are attractive tests
1223 of the SM. The inclusive $t\bar{t}$ production cross section, as one of the simplest top quark
1224 observables, is well suited for a first measurement at the new center-of-mass energy.

1225 Simultaneously, restarting such a large experiment as CMS after a three-year
1226 shutdown poses many experimental challenges. Due to the change in energy, as
1227 well as physical changes in the accelerator and detector, new calibrations as well as
1228 validations of some previous calibrations are required to ensure that the detector
1229 performance is understood. An early measurement of the inclusive $t\bar{t}$ cross section
1230 is well suited to serve as such a cross-check: Because of the decay chain of the top
1231 quark, a top quark measurement involves many of the different objects reconstructed
1232 at CMS, which allows for a check of a wide landscape of calibrations.

1233 The measurement described in this chapter was designed specifically with these
1234 motivations in mind, and as such exhibits several novel features. Firstly, it com-
1235 bines events from both the dilepton and ℓ +jets decay channels of $t\bar{t}$, categorized
1236 by lepton flavor content, combining the higher statistics of the ℓ +jets channel with
1237 the high purity of the e μ channel and allowing to constrain uncertainties on the
1238 lepton identification efficiency directly from the data. This is done using a sim-
1239 taneous maximum likelihood fit to the event yields in the different categories, with
1240 experimental and theoretical uncertainties treated as nuisance parameters.

1241 Secondly, the events are additionally categorized by their number of b-tagged jets,

which similarly allows for an in-situ measurement of the b-tagging efficiencies. This averts needing to wait for external b-tagging calibrations, allowing for a measurement as early as possible.

The results of this work were first presented as a Physics Analysis Summary in September 2022 [134], only two months after the start of data taking, as the first public physics result of LHC Run 3. It was later published in *JHEP* as Ref. [5], again representing the first published Run 3 result. A similar result by ATLAS was later published in Ref. [135].

This chapter is structured as follows: In Sec. 5.2, the used data sets, object definitions, and event selection criteria are described, followed by the derivation and application of needed corrections in Sec. 5.3, and the resulting data-MC agreement is shown in Sec. 5.4. The considered systematic uncertainties are listed in Sec. 5.5, and the fit results are presented in Sec. 5.6. The chapter is concluded by a short summary and outlook in Sec. 5.7.

5.2 Data sets and event selection

In this section, the choice of data sets for experimental data and for simulation, as well as the choice of triggers, is described. Following that, the object and event selection procedure is outlined and several event categories to be used in the likelihood fit are defined.

5.2.1 Data sets

Experimental data The measurement is performed on data recorded during the period between July 27th and August 02nd 2022, corresponding to an integrated luminosity of 1.21 fb^{-1} . This amount of data is chosen as a balance between sensitivity and speed for the early measurement: It roughly corresponds to the point where the measurement precision is no longer primarily limited by the quantity of the data, while at the same time restricting to a data set where beam and detector conditions were stable and comparable to the data-taking in Run 2.

Both single-lepton and dilepton triggers were used to select events used in this measurement during detector operation, identifying leptons in the range of $|\eta| < 2.5$. The p_T requirements of the triggers are summarized in Tab. 5.1.

Simulation To compare the data with predictions, Monte Carlo (MC) simulation is used to simulate both the $t\bar{t}$ signal as well as most important background processes, specifically single-top quark production in the t -channel, associated tW production, $Z+jets$ production, $W+jets$ production, and diboson (WW , WZ and ZZ) production. The MC generator POWHEG v2 [82–84] is used to generate $t\bar{t}$, t -channel single-top, and tW events at next-to-leading order (NLO) in perturbative QCD, while the

Trigger	Lepton requirement
e+jets	$e(p_T > 32 \text{ GeV})$
$\mu + \text{jets}$	$\mu(p_T > 27 \text{ GeV})$
ee	$e(p_T > 23 \text{ GeV}) \text{ and } e(p_T > 12 \text{ GeV})$
$\mu\mu$	$\mu(p_T > 17 \text{ GeV}) \text{ and } \mu(p_T > 8 \text{ GeV})$
$e\mu$	$e(p_T > 23 \text{ GeV}) \text{ and } \mu(p_T > 8 \text{ GeV}) \text{ or }$ $e(p_T > 12 \text{ GeV}) \text{ and } \mu(p_T > 23 \text{ GeV})$

Table 5.1: **Trigger definitions** as used for the $t\bar{t}$ cross section measurement. The leptons are required to be isolated and in the pseudorapidity range $|\eta| < 2.5$.

generators MADGRAPH5_AMC@NLO [80] and PYTHIA 8 [86] are used to generate Z+jets/W+jets and diboson events, respectively, at leading order (LO). For Z+jets and W+jets, up to four additional jets are included in the matrix element using the MLM matching scheme [89]. For t -channel single-top, MADSPIN is used to simulate the top decay.

All of the generated events are interfaced to PYTHIA 8 for parton showering and hadronization, and further processed in a full simulation of the CMS detector as described in Chapter 3. The proton structure in the matrix element calculation is described by the NNPDF3.1 parton distribution function (PDF) set at NNLO. Note that another background contribution, from QCD-produced multijet events with fake or non-prompt leptons, is not simulated, but estimated from data (see Sec. 5.3.2).

Theoretical predictions, as well as the measured integrated luminosity, are used to normalize the cross sections of the signal and background samples as follows: The $t\bar{t}$ signal, is normalized to a cross section of 921^{+29}_{-37}pb computed at NNLO+NNLL in QCD [136], which is also used as a prediction for comparison with the SM. For the other backgrounds, the following orders in QCD and methods or programs are used: MCFM [137] (NNLO) for single-top, DYTURBO [138] (NNLO) for W+jets and Z+jets, MATRIX [139] (NLO) for diboson, and an NNLO calculation from Ref. [140] for tW.

5.2.2 Object definition

Leptons Electrons or muons are considered for the analysis if they have $p_T > 10$ GeV and $|\eta| < 2.4$. For electrons, the range $1.44 < |\eta_{\text{SC}}| < 1.57$ is removed, where η_{SC} is the pseudorapidity of the ECAL supercluster from which the electron was reconstructed and the interval corresponds to the transition region between barrel and endcaps in the ECAL. Furthermore, additional identification criteria (ID) are applied to remove non-prompt or fake (i.e. wrongly reconstructed) leptons and

enrich the selection with $t\bar{t}$ events.

For electrons, the “tight” working point of the cut-based ID described in Ref. [113] is applied, which includes information from both the details of the electromagnetic shower in the ECAL and the track, as well as the matching between the two. It also includes a requirement for the electron to be isolated from other particles such as hadrons, which is implemented in the form of the relative isolation variable I_{rel} . It is defined as the scalar p_T sum of all particles in a cone around the lepton in question, divided by the lepton p_T . Here, $\Delta R = \sqrt{(\Delta\eta)^2 + (\Delta\varphi)^2} < 0.3$ is used for the radius of the cone. Additional corrections accounting for pileup particles are applied.

For muons, a similar cut-based ID is used as described in Ref. [141], also at the tight working point. Here, criteria on the compatibility of tracks in the inner tracker, the muon detectors and the reconstructed primary vertex are employed. Again, a cut on I_{rel} is used, defined equivalently but with a cone size of $\Delta R < 0.4$.

Jets The anti- k_T algorithm [124] is used to cluster reconstructed particles into jets with a distance parameter of 0.4. In order for a jet to be considered, it is required to have $p_T > 30$ GeV and $|\eta| < 2.4$, and jets overlapping with any considered leptons (i.e. fulfilling the above criteria) are removed.

Tagging of b jets A special role is played by jets originating from the showering and hadronization of b quarks. Naively, two such jets are expected per $t\bar{t}$ event from the two top decays, although in practice one or both jets may fall out of acceptance of the detector or otherwise not be identified. Furthermore, additional b quarks may be produced by radiation at higher orders in QCD. Correctly tagging these jets as such can greatly improve signal purity by cutting away backgrounds such as Z+jets, W+jets and QCD multijet events.

Here, the DEEPJET algorithm [125, 142], which is based on a deep neural network (DNN) classifier, is used to identify (“tag”) b jets. A working point with an identification efficiency of more than 75% is used, with misidentification rates of around 17% for charm jets and around 1% for other jets from light quarks or gluons.

5.2.3 Channel definition

Events are selected with either one or two leptons, corresponding respectively to the ℓ +jets and dilepton decay channels of $t\bar{t}$. They are categorized into separate channels by their lepton flavor content, and additional requirements are applied for the different channels.

Dilepton channels Events with exactly two leptons, required to have opposite electric charge, are sorted into three dilepton channels ($e\mu$, ee , and $\mu\mu$). The presence of at least one jet is required, and in the same-flavor channels (ee and $\mu\mu$), at least

1341 one jet is required to be b tagged in order to reject Z+jets and QCD multijet
1342 background. In the much purer epi channel, on the other hand, events without b
1343 tags are retained to later help constrain the b tagging efficiency in the fit to data.

1344 In order to reject even more Z+jets background, events in the same-flavor channels
1345 with an invariant dilepton mass of $|m_{\ell\ell} - m_Z| < 15$ GeV, where m_Z is the Z boson
1346 mass, are removed.

1347 **ℓ +jets channels** Events with exactly one lepton are sorted into the e+jets or
1348 μ +jets channels based on their flavor. At least three jets are required, of which
1349 at least one needs to be b tagged. Note that regardless of these selections, there
1350 is still non-negligible background from QCD multijet events where the lepton is
1351 non-prompt or fake, which is estimated from data (see Sec. 5.3.2).

1352 **p_T requirement** In all channels, the considered leptons are required to have $p_T >$
1353 35 GeV. This requirement is needed in the ℓ +jets channels in order to stay above the
1354 single-lepton trigger p_T thresholds (compare Tab. 5.1). In this measurement, the
1355 choice is made to apply the same p_T requirement also both leptons in the dilepton
1356 channels to ensure consistency between the lepton definitions. This is done to help
1357 constrain the lepton ID scale factors using the combination of lepton flavor channels,
1358 which otherwise might not be accurate since the scale factors for different lepton
1359 definitions might differ. In particular it opens up the possibility to extract a result
1360 on the cross section without any prior knowledge on the lepton ID efficiencies, which
1361 was done in the first published version of this analysis [134].

1362 **b tag and jet categorization** In practice, the efficiency of the b tagging algo-
1363 rithm used might be different between simulation and data, necessitating a correc-
1364 tion to prevent bias. In this analysis, this efficiency is measured simultaneously with
1365 the cross section directly in the data. To do so, the lepton flavor channels are ad-
1366 ditionally split into categories based on the number (exactly 0, 1, or 2) of b tagged
1367 jets. Since only the ep channel allows events with 0 b tags, this results in 11 cate-
1368 gories total. To gain further sensitivity to the b tagging efficiency and to increase
1369 possible separation between $t\bar{t}$ signal and background, the selected events are finally
1370 coarsely binned into the number of accepted jets for the eventual fit, giving a total
1371 number of 40 bins.

1372 5.3 Corrections

1373 While the simulation used in CMS tries to describe as many physics and detector
1374 effects as possible, in practice it should always be expected that not all observables
1375 agree with the experimental data perfectly. This is especially true for an early
1376 analysis such as this, as the detector conditions might have changed significantly

1377 during the long shutdown between LHC Runs 2 and 3, and the simulation had not
1378 been recalibrated at the time of the measurement.

1379 Because of this, the analysis setup is designed to either directly measure or cross-
1380 check as many required experimental calibration and correction factors as possible.
1381 This includes pileup corrections, efficiency scale factors for triggers, electrons, muons
1382 and b tags, as well as jet energy corrections, all of which are briefly described in this
1383 section.

1384 In addition to these experimental corrections, background processes might also
1385 be imperfectly described by the simulation because of theoretical shortcomings. In
1386 this case, ways have to be found to correct them directly from the experimental
1387 data. Here, two such cases are relevant and will be presented in the latter half of
1388 this section: The Z+jets background in the dilepton channels and in the presence
1389 of b tagged jets, for which the normalization is taken from data; and the QCD
1390 background in the ℓ +jets channels, which uses a fully data-driven estimation and
1391 foregoes simulation entirely.

1392 5.3.1 Experimental corrections

1393 **Pileup reweighting** The simulation samples used in this analysis were generated
1394 before the start of Run 3 data taking using a projected estimate of the average
1395 pileup. As a result, the pileup distribution in the simulation does not match the
1396 one observed in data, which could influence mostly jet-related variables such as the
1397 number of jets and the jet p_T .

1398 Since at the time of the measurement, no theory-based calculation for the cor-
1399 rect pileup distribution were available, an experimental approach was taken. Three
1400 experimental observables that are strongly correlated with pileup were identified:

- 1401 • The number of well-reconstructed primary vertices per event n_{PV} ;
- 1402 • The median p_T density in the calorimeter, calculated from calorimeter-only
1403 jets as $\rho^{\text{calo}} = \text{med}(p_T/A)$, where A is the jet area defined in the φ - η plane
1404 and the median is taken over all jets in the event;
- 1405 • The median p_T density in the tracker ρ^{trk} , defined equivalently as ρ^{calo} , but
1406 for jets calculated only from tracker information.

1407 A binned reweighting from simulation to data is derived for each observable based
1408 on the full data sample, and the average of the three weights is applied to the
1409 simulation, so that approximate agreement is achieved in all three variables. The
1410 distributions before and after reweighting can be seen in Fig. 5.1.

5 Measurement of the inclusive $t\bar{t}$ cross section at $\sqrt{s} = 13.6$ TeV

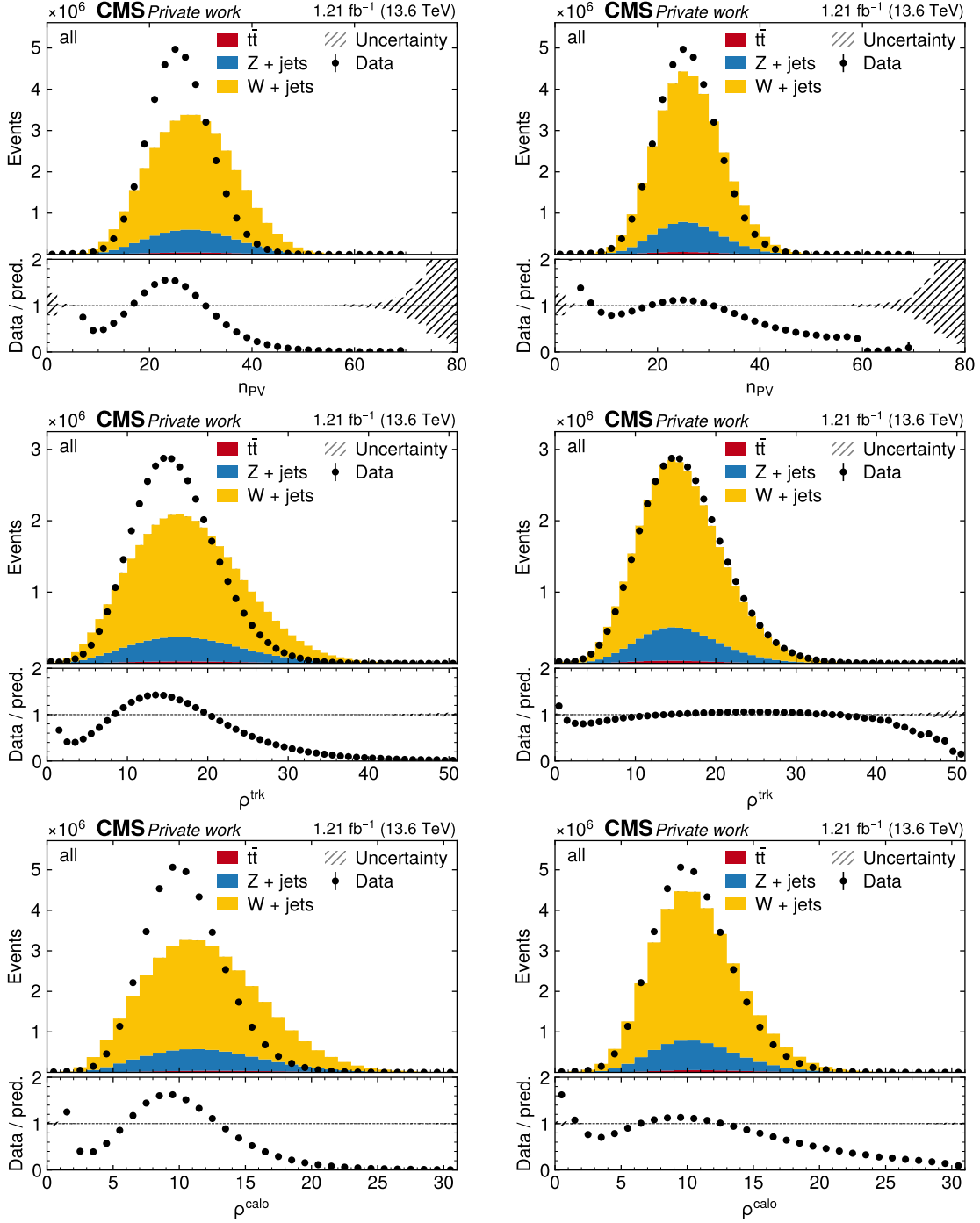


Figure 5.1: Pileup reweighting. Pileup-related distributions in MC and data in before (left) and after reweighting (right). From top to bottom: number of primary vertices as well as the mean energy densities ρ^{trk} (calculated using tracker input) and ρ^{calo} (calculated using calorimeter input).

1411 **Trigger scale factors** The trigger efficiency, i.e. the probability for an event
 1412 falling into the selection phase space to be triggered by the low- and high-level
 1413 triggers, can differ between simulation and data. In principle, both dilepton and
 1414 single-lepton triggers are used for this measurement and should be considered for
 1415 the efficiency calculation. However, due to the high offline p_T requirements for the
 1416 two leptons applied in all channels, the fraction of events that are triggered only
 1417 by the dilepton triggers is negligibly small, and can be neglected for the purpose of
 1418 determining the scale factor. Thus, only the single-lepton triggers are considered in
 1419 this section for simplicity.

1420 The efficiency measurement is performed by the so-called tag-and-probe (T&P)
 1421 method, using $Z \rightarrow e^+e^-$ and $Z \rightarrow \mu^+\mu^-$ events. They are selected using the same
 1422 definitions presented above, including the lepton identification, except for requiring
 1423 their invariant mass to fulfill $|m_{\ell\ell} - m_Z| < 20$ GeV. At least one of the leptons
 1424 is required to pass the relevant single-lepton trigger and is then designated the
 1425 tag, while the other lepton might or might not pass the trigger and is designated
 1426 the probe. Assuming the probability for the two leptons to pass the trigger to be
 1427 independent of each other, the trigger efficiency, given by probability of the probe
 1428 to pass, can be written as

$$\epsilon_{\text{tr}} = \frac{N(\text{Probe passes})}{N(\text{Probe passes}) + \frac{1}{2}N(\text{Probe fails})} \quad (5.1)$$

1429 where N corresponds to the number of events in which the second lepton either
 1430 passes or fails the trigger, and the combinatoric factor $\frac{1}{2}$ comes from the fact that
 1431 either one or the other lepton can fail.

1432 The efficiency is measured in this way in coarse bins of lepton p_T and $|\eta|$, separately
 1433 for muons and electrons, in both simulation and experimental data. It is then applied
 1434 to simulation in the following way: For $\ell+\text{jets}$ events, a simple ratio $\epsilon_{\text{tr,data}}/\epsilon_{\text{tr,sim}}$
 1435 is applied to each simulation event as a scale factor, which is displayed in Fig. 5.2.
 1436 For dilepton events, on the other hand, the fact that only one lepton needs to pass
 1437 the single-lepton trigger needs to be taken into account. This leads to a per-event
 1438 efficiency given by

$$\epsilon_{\text{tr},\ell\ell} = \epsilon_{\text{tr},\ell 1} + \epsilon_{\text{tr},\ell 2} - \epsilon_{\text{tr},\ell 1}\epsilon_{\text{tr},\ell 2} \quad (5.2)$$

1439 where $\epsilon_{\text{tr},\ell 1}$ and $\epsilon_{\text{tr},\ell 2}$ are the efficiencies evaluated at the p_T and $|\eta|$ of the two
 1440 leptons, respectively. Again, the ratio of this event efficiency in data and simulation
 1441 is applied to the simulation.

1442 **Lepton scale factors** Similarly to the triggers, the reconstruction and identifi-
 1443 cation of leptons can exhibit different efficiencies between simulation and data, and
 1444 thus require scale factors. The efficiencies are measured with a similar tag-and-
 1445 probe method as for the triggers, and the simulation is corrected to the data. This

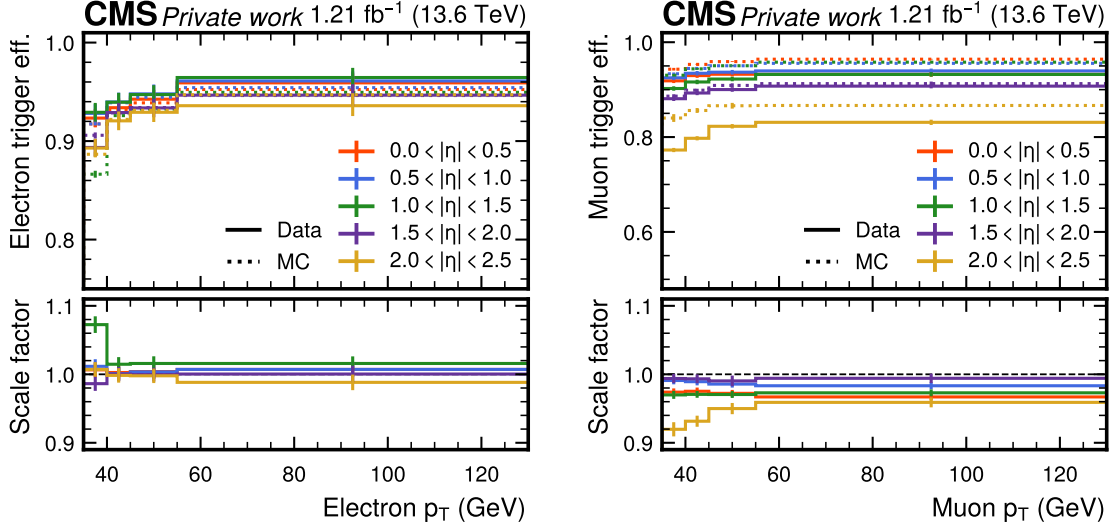


Figure 5.2: **Trigger scale factors.** Single-lepton trigger efficiencies in data and MC (top) and scale factors (bottom) for electrons (left) and muons (right) as a function of lepton p_T and $|\eta|$, calculated using a tag-and-probe-method. The error bars designate both statistical and systematic uncertainties.

is the standard approach commonly taken in CMS, detailed in Refs. [113, 141] for electrons and muons, respectively. The efficiency measurement was not performed as part of this thesis, but is still shown in Figs. 5.3 and 5.4 for reference. The muon scale factors are split into a reconstruction and an identification part, while these are combined for the electron scale factors.

b tagging scale factors The performance of b tagging algorithms, such as the DEEPJET algorithm used in this analysis, is known to differ between simulation and data, necessitating corrections. This is particularly relevant here, as the multivariate classifier behind DEEPJET had not been re-trained on Run 3 data at the time of the measurement; instead, the Run 2 calibration was used.

Since no external calibration of b tagging efficiencies for Run 3 was available within the timeframe of this study, the b tagging efficiency in data is extracted directly from the data itself. This is achieved by performing a simultaneous likelihood fit with the ttbar cross section, as described in Sec. 5.5. As a result, no b tagging scale factors are applied beforehand.

Jet energy corrections Another observable that often differs significantly between observed data and simulation is the measured energy response of the jets. Both its mean value, the jet energy scale (JES), and the jet energy resolution (JER) require corrections, which are together referred as jet energy corrections (JECs).

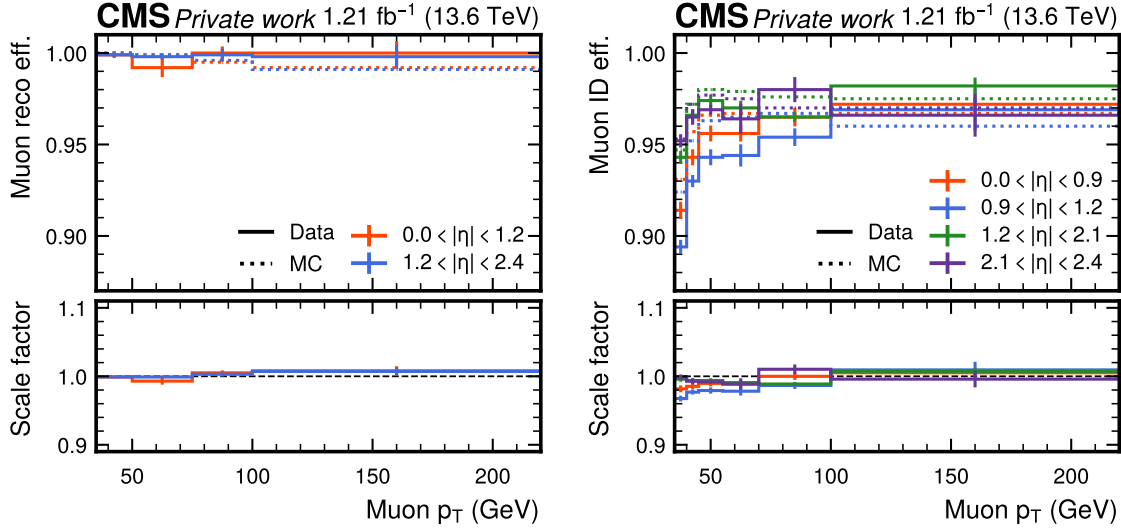


Figure 5.3: **Muon scale factors.** Muon efficiencies in data and MC (top) and scale factors (bottom), split into reconstruction (left) and identification (right) and shown as a function of lepton p_T and $|\eta|$, calculated using a tag-and-probe-method. The error bars designate both statistical and systematic uncertainties.

1465 Both are centrally provided by CMS following the methods of Ref. [143].

1466 The derivation of the JES is performed in multiple steps: first, the expected
1467 fraction of jet energy due to pileup, determined from MC simulation, is removed
1468 from all jets in data and MC. Second, the difference in jet energy between detector-
1469 and particle-level jets in simulation is determined as a function of jet kinematics,
1470 and detector-level jets are corrected accordingly in both data and simulation.
1471 Third, residual disagreements of the simulation with the data are corrected using
1472 experimental jet measurements in dijet, γ +jets, Z+jets, and multijet events, again
1473 parametrized as a function of jet kinematics [143].

1474 Similarly, JER scale factors are determined by correcting the resolution in simu-
1475 lation to the one seen in data, based on dijet, γ +jets and Z+jets events [144]. They
1476 are then applied to jets in simulation by scaling the difference between detector- and
1477 particle-level jet energy for jets where a matched particle-level jet is found, while a
1478 stochastic smearing is used otherwise.

1479 5.3.2 Data-driven background estimation

1480 **QCD background** A significant background contribution in the ℓ +jets channels,
1481 especially in the categories with only one b tag, is given by QCD multijet events
1482 with one reconstructed lepton. The lepton in question might be non-prompt, e.g.

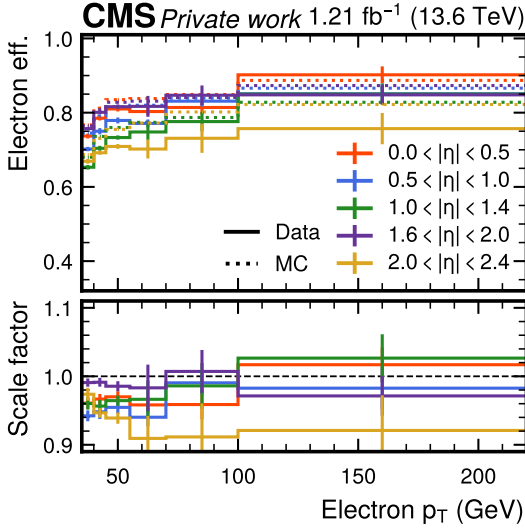


Figure 5.4: **Electron scale factors.** Combined electron efficiencies in data and MC (top) and scale factors (bottom) as a function of lepton p_T and $|\eta|$, calculated using a tag-and-probe-method. The error bars designate both statistical and systematic uncertainties.

from radiated photons splitting into leptons or decays of heavy flavor hadrons, or it might be fake, i.e. a different particle (such as a photon or pion in the case of electrons) misidentified as a lepton.

It is often not practical to estimate this background using MC simulation as is done for the other backgrounds in this analysis. The reason is that, due to the large cross section of QCD multijet events at the LHC but low ratio of events with a fake or non-prompt lepton, very large MC data sets are needed to achieve significant statistics in the selected phase space, requiring excessive computing power. In addition to that, fake leptons are known not to be well-described by the simulation.

Instead, a fully data-driven approach is taken to estimate the QCD background in the $\ell+jets$ channels. For this, multiple control regions (CRs) orthogonal to the signal region (SR) are defined. In the first CR, denoted “QCD CR”, the same cuts as in the SR are applied, except that the requirement for the single lepton to be isolated from other particles (I_{rel} , see Sec. 5.2.2) is inverted. It is expected that QCD events that fall in either the QCD CR or the SR show similar shapes in observable distributions, as long as said observables are uncorrelated with the lepton isolation. Thus, the shape of the QCD background can be extracted from the CR and applied in the SR. Figs. 5.5 and 5.6 show the distributions of several key distributions for the QCD background in the $\mu+jets$ and $e+jets$ channels, respectively, which is estimated by subtracting all simulated (MC) processes from the data.

The normalization of the QCD background is fixed through the so-called *ABCD*

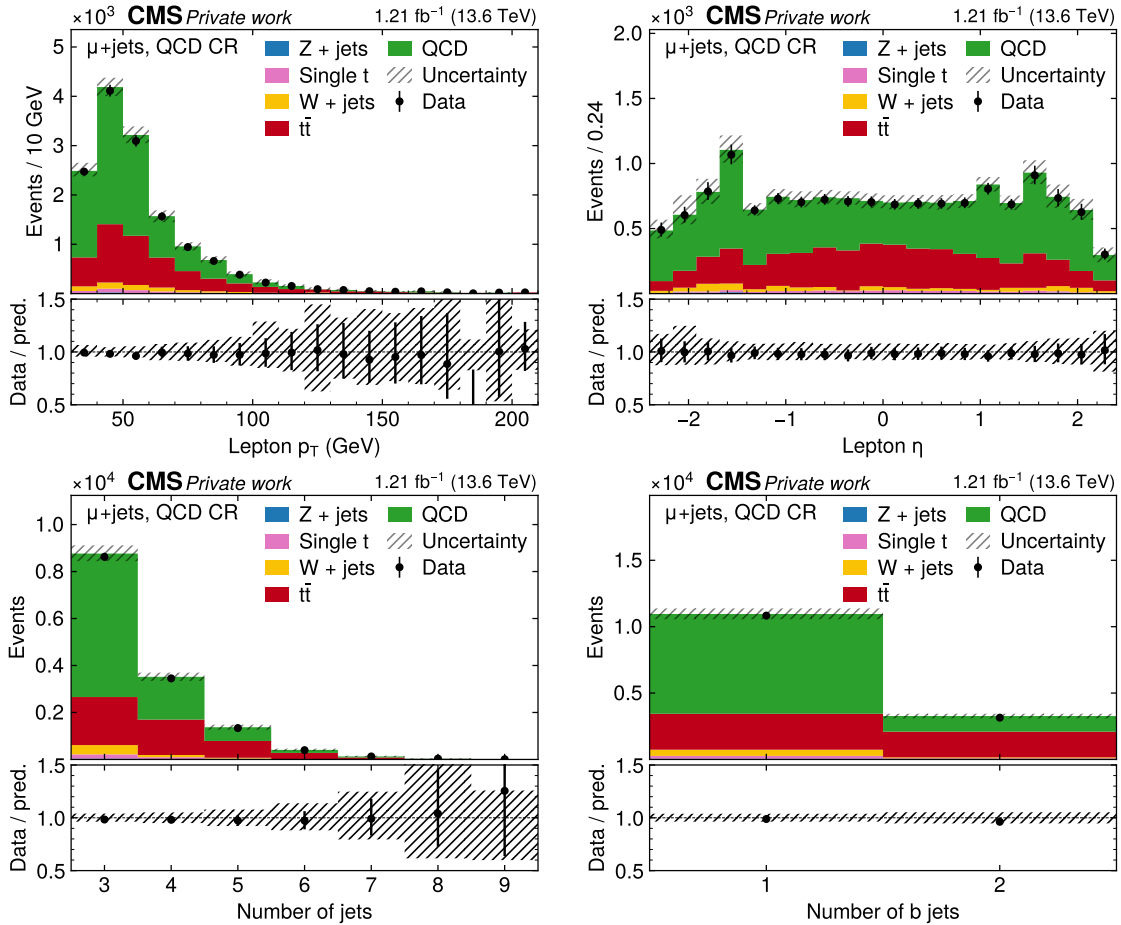


Figure 5.5: **QCD control region for $\mu + \text{jets}$.** Distributions in the QCD CR for the $\mu + \text{jets}$ channel. From top left to bottom right: p_T of the lepton, η of the lepton, the number of jets, and the number of b-tagged jets. The uncertainty bands include MC statistical and systematic uncertainties. The difference between data and MC prediction is considered QCD background and shown in green.

1504 method [145, 146], for which an additional CR (the “1-jet CR”) is defined. It again
 1505 contains events that pass the main selection, except for requiring exactly one jet (as
 1506 opposed to at least three jets in the SR or QCD CR). These events are enriched with
 1507 QCD events and contain negligible amounts of $t\bar{t}$ signal. They are used to measure
 1508 the ratio f_{fake} of QCD events that pass or fail the lepton isolation requirement, given
 1509 by

$$f_{\text{fake}} = \frac{N_{1 \text{ jet, pass}}^{\text{data}} - N_{1 \text{ jet, pass}}^{\text{MC}}}{N_{1 \text{ jet, fail}}^{\text{data}} - N_{1 \text{ jet, fail}}^{\text{MC}}} \quad (5.3)$$

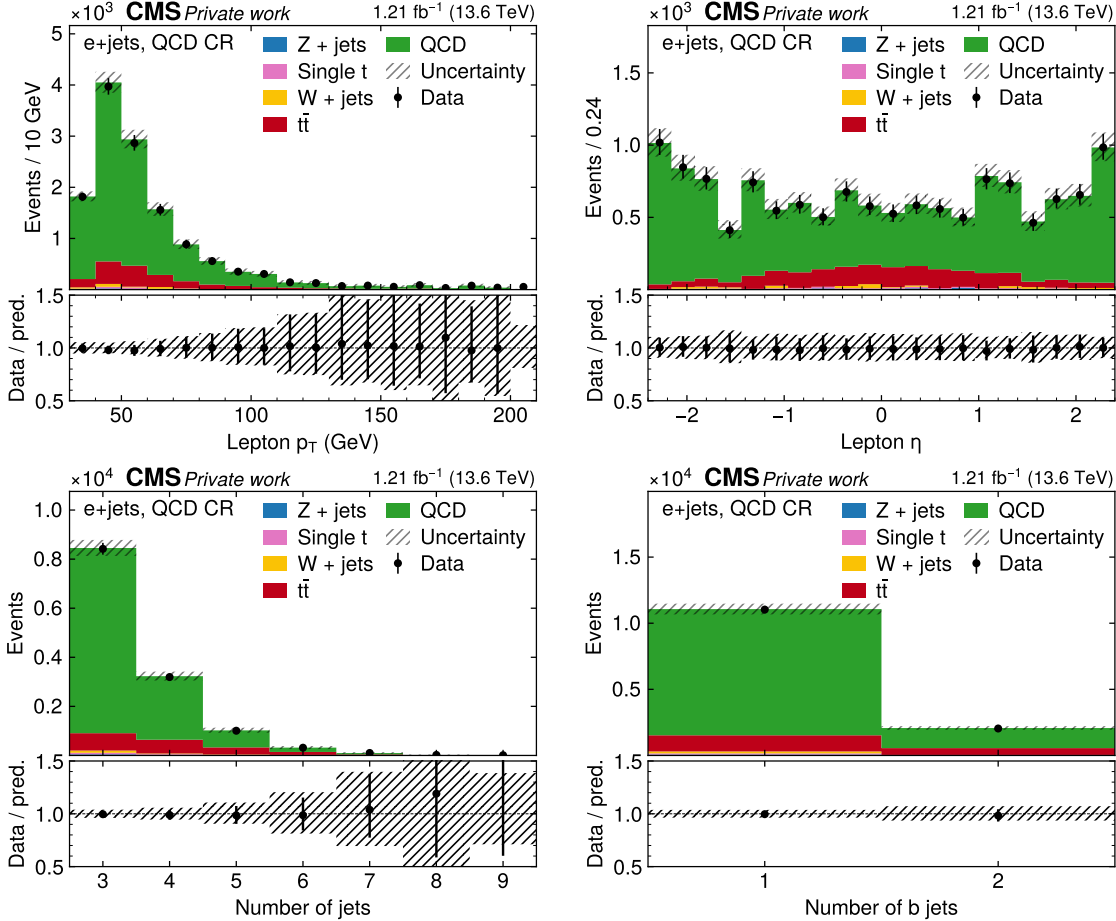


Figure 5.6: **QCD control region for e+jets.** Distributions in the QCD CR for the e+jets channel, same as in Fig. 5.5. The difference between data and MC prediction is considered QCD background and shown in green.

where $N_{1 \text{ jet, pass}}$ and $N_{1 \text{ jet, fail}}$ denote 1-jet-events that pass and fail the lepton isolation requirement, respectively; “data” refers to the experimental data, and “MC” refers to the sum of all non-QCD processes, which are estimated by MC simulation. Here, this ratio is measured in four coarse bins of lepton p_T and $|\eta|$ to accurately model lepton-related distributions; it can be seen in Fig. 5.7.

Naively, the full distribution of the QCD background in the SR for any observable can then be written as

$$N_{\text{SR}}^{\text{QCD}} = (N_{\text{CR}}^{\text{data}} - N_{\text{CR}}^{\text{MC}}) \times f_{\text{fake}} \quad (5.4)$$

where $N_{\text{CR}}^{\text{data}}$ and $N_{\text{CR}}^{\text{MC}}$ refer to the total data and non-QCD MC yields in the QCD CR.

In practice, this is complicated by the fact that a non-negligible amount of $t\bar{t}$

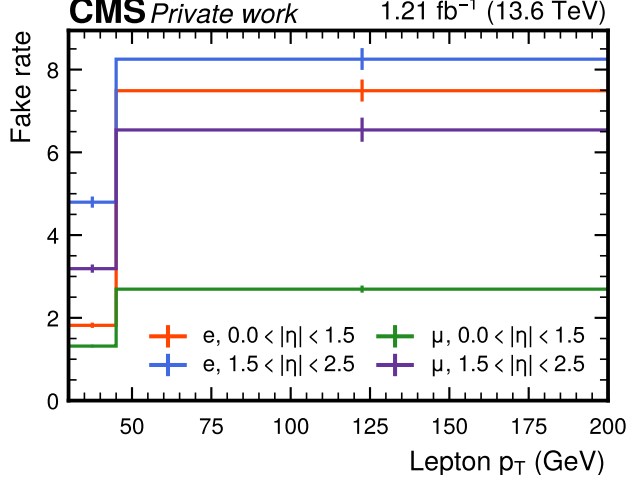


Figure 5.7: **QCD fake rate.** The fake rate for the QCD background estimated in the 1 jet bin, separately for electrons and muons as, a function of lepton p_T and $|\eta|$. The error bars designate statistical uncertainties only.

1520 signal is present in the QCD CR, whose cross section, as the parameter of interest
 1521 in the measurement, is not known *a priori*. To circumvent this problem, a modified
 1522 method is introduced, which is agnostic about the prediction for the $t\bar{t}$ cross section.
 1523 One sets for the SR

$$N_{\text{SR}}^{\text{data}} = N_{\text{SR}}^{t\bar{t}} + N_{\text{SR}}^{\text{MC,BG}} + N_{\text{SR}}^{\text{QCD}} \quad (5.5)$$

1524 and similarly for the QCD CR

$$N_{\text{CR}}^{\text{data}} = N_{\text{CR}}^{t\bar{t}} + N_{\text{CR}}^{\text{MC,BG}} + N_{\text{CR}}^{\text{QCD}}, \quad (5.6)$$

1525 where N^{data} is the total data yield, $N^{t\bar{t}}$ is the $t\bar{t}$ signal contribution, $N^{\text{MC,BG}}$ is the
 1526 contribution of non-QCD backgrounds as predicted by MC, and N^{QCD} is the QCD
 1527 contribution. It is assumed that the ratio f_{sig} of signal events in the SR and QCD
 1528 CR (but not necessarily the normalization) is correctly predicted by MC:

$$f_{\text{sig}} := \frac{N_{\text{CR}}^{t\bar{t}}}{N_{\text{SR}}^{t\bar{t}}} = \frac{N_{\text{CR}}^{t\bar{t},\text{MC}}}{N_{\text{SR}}^{t\bar{t},\text{MC}}} \quad (5.7)$$

1529 Furthermore, one sets similar to Eq. (5.4)

$$N_{\text{SR}}^{\text{QCD}} = N_{\text{CR}}^{\text{QCD}} \times f_{\text{fake}} \quad (5.8)$$

1530 where f_{fake} is still given by Eq. (5.3), which is unaffected since the $t\bar{t}$ signal contam-
 1531 ination in the 1-jet CR is negligible.

1532 Combining all these equations, one can first replace $N_{\text{CR}}^{t\bar{t}}$ in Eq. (5.6) by $f_{\text{sig}} N_{\text{SR}}^{t\bar{t}}$

1533 according to Eq. (5.7), then eliminate $N_{\text{SR}}^{t\bar{t}}$ in favor of $N_{\text{SR}}^{\text{data}}$, i.e. the total data yield
1534 in the SR, and get

$$N_{\text{SR}}^{\text{QCD}} = f_{\text{fake}} \left(N_{\text{CR}}^{\text{data}} - N_{\text{CR}}^{\text{MC,BG}} - f_{\text{sig}} \left(N_{\text{SR}}^{\text{data}} - N_{\text{SR}}^{\text{MC,BG}} - N_{\text{SR}}^{\text{QCD}} \right) \right). \quad (5.9)$$

1535 Solving this equation for $N_{\text{SR}}^{\text{QCD}}$ finally yields the corrected QCD contribution in
1536 the SR:

$$N_{\text{SR}}^{\text{QCD}} = \left(N_{\text{CR}}^{\text{data}} - N_{\text{CR}}^{\text{MC,BG}} - f_{\text{sig}}(N_{\text{SR}}^{\text{data}} - N_{\text{SR}}^{\text{MC,BG}}) \right) \times \frac{f_{\text{fake}}}{1 - f_{\text{sig}}f_{\text{fake}}} \quad (5.10)$$

1537 The resulting QCD distributions from this method are further treated in the same
1538 way as the MC backgrounds, and can be seen together with them in Figs. 5.8 to 5.10.

1539 **Z+jets background** In contrast to the QCD background, the Z+jets background
1540 is generally well-described by MC simulation. However, in the considered phase
1541 space, the requirement of at least one reconstructed b jet can introduce modeling
1542 challenges, as b quarks are treated as massless at the matrix-element level. This
1543 approximation may lead to inaccuracies in the predicted kinematic properties of b
1544 quarks compared to those observed in data.

1545 Here, a data-driven normalization is derived for Z+jets events with one or two b
1546 tags in the dilepton channels, following the method of Ref. [54]. This is important
1547 especially in the same-flavor channels, where Z+jets is a dominant background.

1548 The normalization is derived using a CR in which the cut on $m_{\ell\ell}$ is inverted, i.e.
1549 in events with $|m_{\ell\ell} - m_Z| < 15$ GeV (“inside the Z window”), which are strongly
1550 enriched in Z+jets contributions. It is assumed that the Z+jets contribution in the
1551 e μ channel (which stems mostly from $Z \rightarrow \tau\tau$ events) is negligible compared to the
1552 ee and $\mu\mu$ channels, and that all other backgrounds (including $t\bar{t}$) are approximately
1553 equal in the three dilepton channels up to combinatorics, in the sense that their
1554 differences are small compared to the Z+jets event yield. Then, said Z+jets yield
1555 in the Z window in the same-flavor channels can be estimated directly from data by
1556 subtracting the e μ channel – and with it, the other backgrounds – from the ee and
1557 $\mu\mu$ channels. This results in

$$N_{\text{ee}/\mu\mu}^{\text{Z+jets}} = N_{\text{ee}/\mu\mu, \text{in}}^{\text{data}} - \frac{1}{2} N_{\text{e}\mu, \text{in}}^{\text{data}} k_{\text{ee}/\mu\mu, \text{in}} \quad (5.11)$$

1558 where $N_{\ell\ell, \text{in}}^{\text{data}}$ refers to the number of observed events inside the Z window for the
1559 respective channel, and $k_{\text{ee}} = k_{\mu\mu}^{-1} = \sqrt{N_{\text{ee}, \text{in}}^{\text{data}} / N_{\mu\mu, \text{in}}^{\text{data}}}$ is a efficiency factor to correct
1560 for the different acceptance of electrons and muons.

ee	ep	$\mu\mu$
1.36 ± 0.04	1.32 ± 0.03	1.28 ± 0.03

Table 5.2: **Z+jets scale factors.** Ratio of the Z+jets event yields estimated in data using the method described in Sec. 5.3.2 to the prediction by the MC simulation. Uncertainties are statistical only.

To estimate the Z+jets background in the SR, the ratio $R_{\text{in/out}} = N_{\text{in}}^{\text{Z+jets}}/N_{\text{out}}^{\text{Z+jets}}$, defined as the number of Z+jets events inside and outside the Z mass window, needs to be determined. While this ratio could be taken directly from simulation (as done in Refs. [20, 147]), it may be inaccurately modeled in MC. To reduce potential bias, a more conservative strategy is adopted. A second CR with zero b-tagged jets, which is not used in the main measurement for the same-flavor channels, is introduced to estimate the ratio under looser assumptions:

$$\frac{R_{\text{in/out}}^{\text{data}}(\geq 1 \text{ b tag})}{R_{\text{in/out}}^{\text{MC}}(\geq 1 \text{ b tag})} = \frac{R_{\text{in/out}}^{\text{data}}(0 \text{ b tags})}{R_{\text{in/out}}^{\text{MC}}(0 \text{ b tags})} \quad (5.12)$$

This equation means that the *ratio of ratios* $R_{\text{in/out}}(\geq 1 \text{ b tag})/R_{\text{in/out}}(0 \text{ b tags})$ is assumed to be well described by MC. It can be solved for the Z+jets yield outside of the Z window in the same-flavor channels, yielding

$$\begin{aligned} N_{\text{out}}^{\text{Z+jets}} &= \frac{N_{\text{in}}^{\text{Z+jets}}}{R_{\text{in/out}}^{\text{data}}(\geq 1 \text{ b tag})} \\ &= \frac{R_{\text{in/out}}^{\text{MC}}(0 \text{ b tags})}{R_{\text{in/out}}^{\text{data}}(0 \text{ b tags})} \frac{N_{\text{in}}^{\text{Z+jets}}}{R_{\text{in/out}}^{\text{MC}}(\geq 1 \text{ b tag})} \end{aligned} \quad (5.13)$$

where $N_{\text{in}}^{\text{Z+jets}}$ is given by Eq. (5.11). In practice, this yield is quoted as a scale factor compared to the nominal MC prediction. For the ep channel (in which Z+jets is much less important), the scale factor is simply assumed to be the geometric mean of the ee and $\mu\mu$ scale factors.

The final scale factors can be seen in Tab. 5.2.

5.4 Control distributions

The agreement between simulation and data in several control distributions is presented in Figs. 5.8 to 5.10. All corrections described in the previous section are applied in these figures. In addition, they are scaled by the b tagging efficiency scale factors obtained in the final likelihood fit (Sec. 5.6) to better reflect the estimates for essential calibrations.

5 Measurement of the inclusive $t\bar{t}$ cross section at $\sqrt{s} = 13.6$ TeV

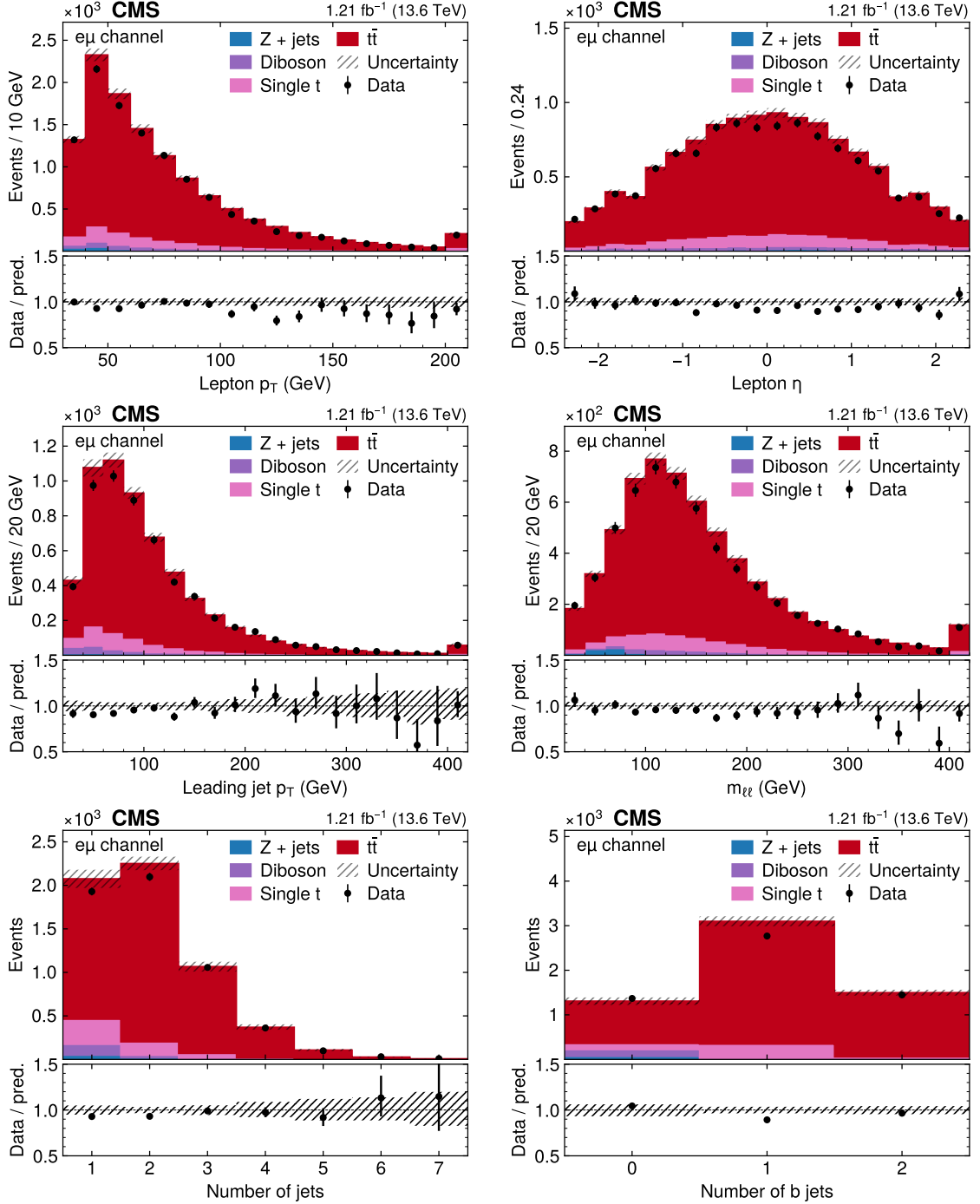


Figure 5.8: Control distributions in the $e\mu$ channel. Shown are (from top left to bottom right) the distributions of p_T of both leptons, $|\eta|$ of both leptons, p_T of the leading jet, the invariant lepton mass $m_{\ell\ell}$, the number of jets and the number of b jets. All figures show both data (black dots) and different simulated background processes (colored bars). For the latter, all corrections described in Sec. 5.3 as well as post-fit b tagging scale factors (Sec. 5.6) are applied, and the shaded area covers both statistical and systematic uncertainties. *Figure taken from Ref. [5].*

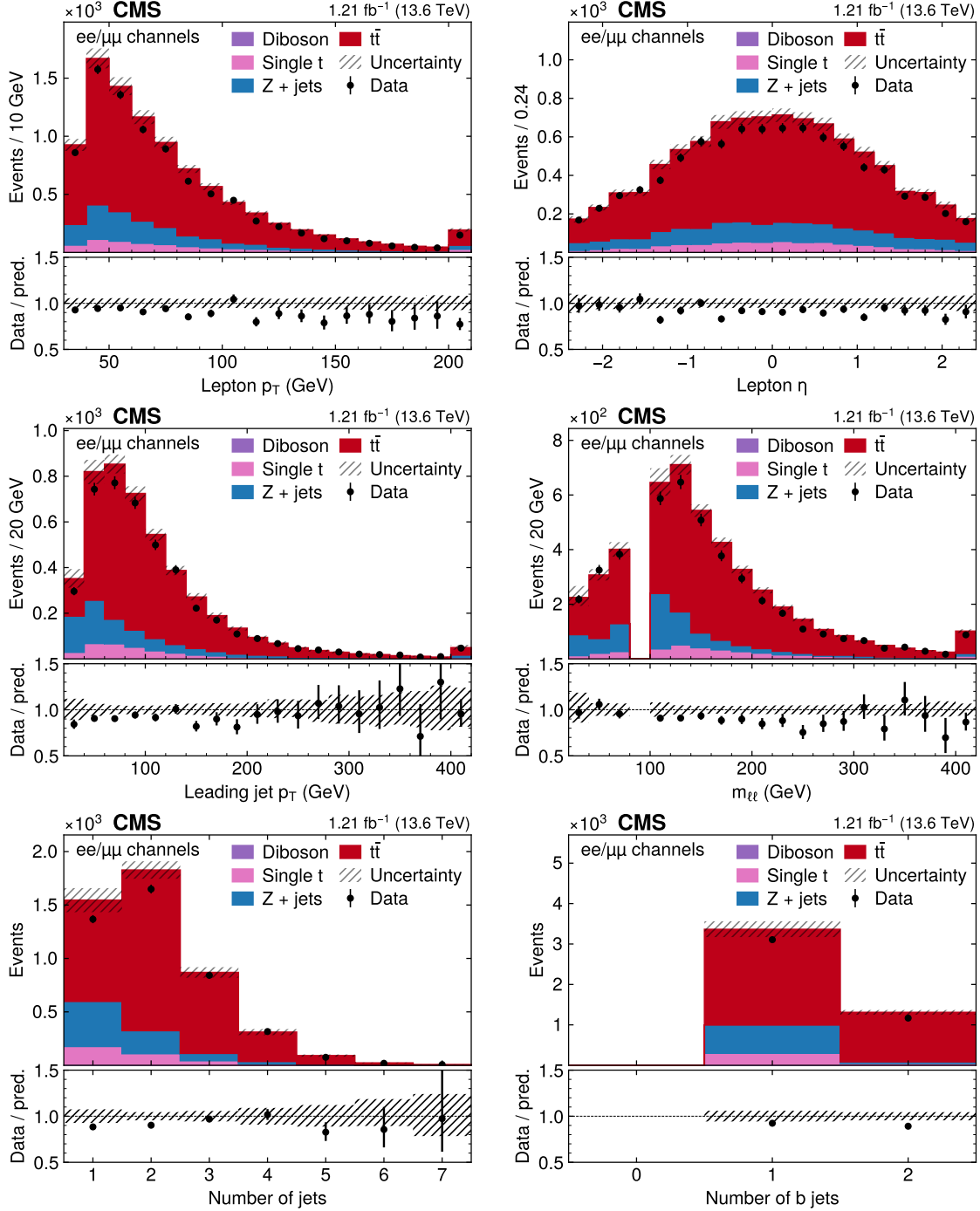


Figure 5.9: **Control distributions in the ee and $\mu\mu$ channels.** The distributions are shown in the same manner as in Fig. 5.8. *Figure taken from Ref. [5].*

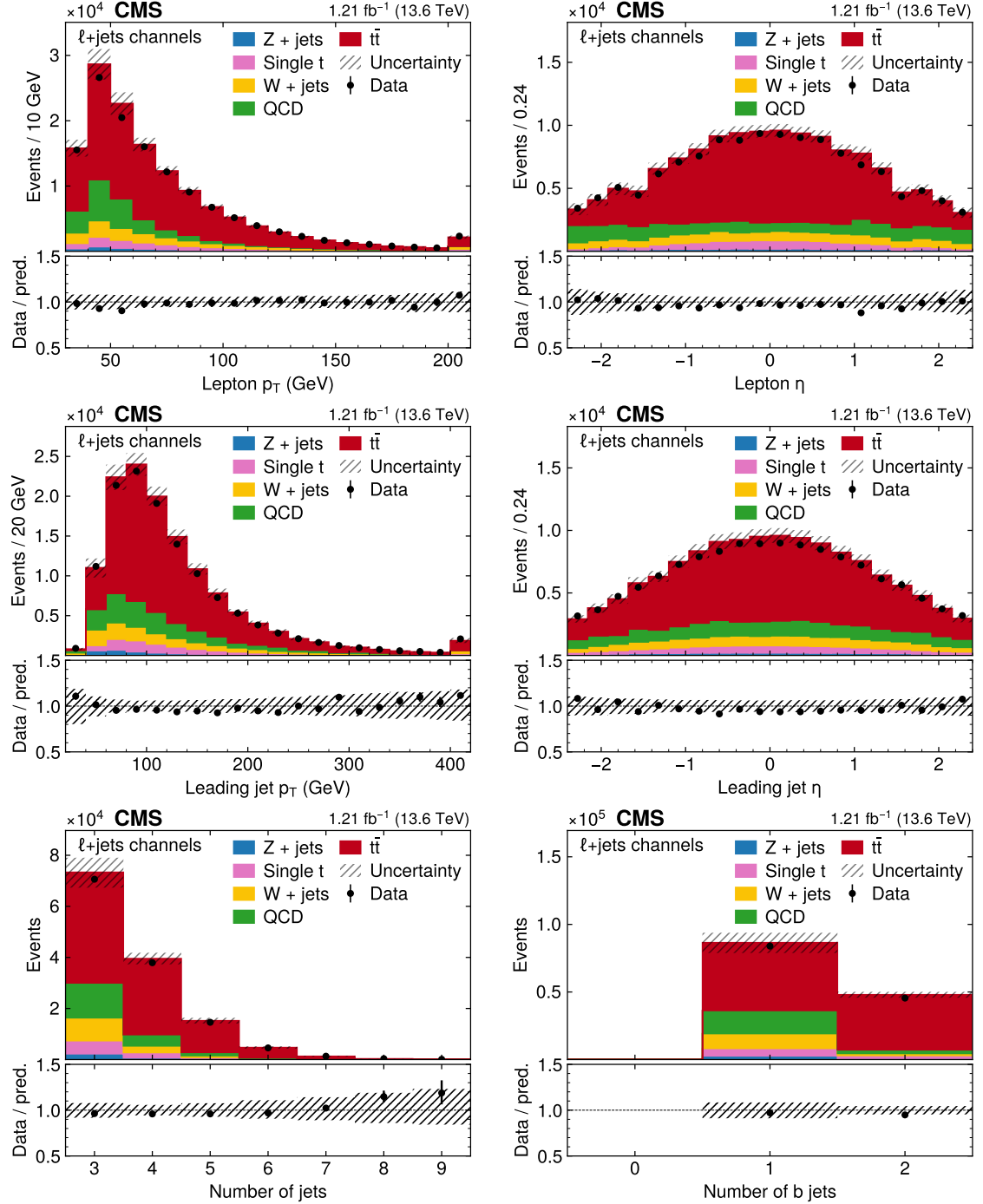


Figure 5.10: **Control distributions in the $\ell + \text{jets}$ channels.** The distributions are shown in the same manner as in Fig. 5.8, except for the center-right figure, which here shows $|\eta|$ of the leading jet. *Figure taken from Ref. [5].*

1582 Good agreement between data and simulation within the full uncertainties is seen
1583 in all distributions.

1584 5.5 Systematic uncertainties

1585 In order to translate the distribution of observed and expected events into a result
1586 for the inclusive $t\bar{t}$ cross section while taking into account all relevant sources of
1587 systematic uncertainties, a binned profile maximum likelihood fit as described in
1588 Sec. 4.4 is performed using the tool `combine` [132]. The parameter of interest (POI)
1589 used for this fit is the signal strength $r = \sigma_{t\bar{t}}/\sigma_{t\bar{t}}^{\text{pred}}$, i.e. the inclusive $t\bar{t}$ cross section
1590 normalized to its theoretical prediction. A linear signal model is used as defined in
1591 Eq. (4.3), and the $t\bar{t}$ cross section is extracted using its maximum likelihood estimate
1592 and uncertainty.

1593 This section describes the considered systematic uncertainties, which can be di-
1594 vided into experimental uncertainties, arising from incomplete knowledge of the
1595 details of the detector and resulting differences between data and simulation, and
1596 theoretical uncertainties, which concern imperfect modeling of the underlying phys-
1597 ical processes in the different event generators.

1598 All systematic uncertainties are included in the fit as nuisance parameters (NPs) as
1599 discussed in Sec. 4.4. In practice, NPs which encode shape effects on the considered
1600 observables are implemented using *template morphing*, i.e. a smooth polynomial
1601 interpolation between the nominal shape and the shapes encoding the variations
1602 by ± 1 standard deviations. NPs that encode only normalization effects are instead
1603 implemented as simple log-normal uncertainties. Both definitions can be found in
1604 detail in Ref. [132].

1605 Special attention is given in this section to some experimental uncertainties which
1606 are important to this measurement. This includes the luminosity, which is the
1607 dominating uncertainty, as well as the b tagging uncertainties due to the special
1608 way they are treated in the fit.

1609 **Luminosity uncertainty** In order to translate event yields into a result on any
1610 cross section, the total integrated luminosity is required as a calibration constant.
1611 Any experimental error on the luminosity will be directly transferred to the total
1612 error on the measurement, and thus minimizing the luminosity uncertainty is crucial
1613 for any cross section measurement.

1614 For the data set used in this analysis, the total integrated luminosity was mea-
1615 sured by the CMS Collaboration with an estimated uncertainty of 2.3%. Of this
1616 number, 2.1% is due to the calibration of the integrated luminosity, using the meth-
1617 ods presented in Ref. [100].

1618 The agreement in the absolute scale is checked by comparing different indepen-
1619 dently calibrated luminosity measurements. The integrated luminosity measured

with the hadronic forward calorimeter and the silicon pixel detector is found to agree at a level of better than 0.8%. Accounting for residual differences in time stability and linearity between the luminosity detectors results in a total uncertainty of 2.3%. This preliminary estimate of the integrated luminosity at the time of publication was further validated using the yield of reconstructed Z bosons decaying into muon pairs [148]. After correcting for efficiencies and normalizing to the fiducial cross section predicted at NNLO with next-to-NNLL corrections, good agreement was observed.¹

In contrast to all other uncertainties described below, the uncertainty in the integrated luminosity is not directly included in the likelihood fit, but rather treated as an external uncertainty and added in quadrature afterwards, since it is expected to factorize completely from all other uncertainties. The impact of varying the normalization of the backgrounds estimated from simulation by the integrated luminosity uncertainty was found to be negligible.

b tagging uncertainty As mentioned in Sec. 5.3.1, the efficiency for correctly identifying a jet originating from a b quark (b tagging) is expected to be different in data and simulation. At the time of this measurement, directly after the start of Run 3, no general-purpose b tagging studies had been available. Thus, the approach adopted here is to consider the b tagging efficiency in data to be completely unknown and measure it concurrently with the cross section in the likelihood fit.

For this purpose, the probability for an event with n_{jet} selected jets to have n_{btag} correctly identified b jets, depending on the assumed b tagging efficiency ϵ_b , is assumed to be a multinomial of the form

$$P(n_{\text{btag}}|n_{\text{jet}}) \propto \epsilon_b^{n_{\text{btag}}} (1 - \epsilon_b)^{n_{\text{no tag}}} \quad (5.14)$$

Here, $n_{\text{no tag}}$ is the number of true b jets in the event which fall into the acceptance of the selection, but fail to be tagged by DEEPJET. It is estimated from MC simulation.

By taking the ratio of eq. 5.14 in data and simulation, one can derive a per-event weight which corrects the number of b tags in MC:

$$w_b = \frac{(\epsilon_b^{\text{data}})^{n_{\text{btag}}} (1 - \epsilon_b^{\text{data}})^{n_{\text{no tag}}}}{(\epsilon_b^{\text{MC}})^{n_{\text{btag}}} (1 - \epsilon_b^{\text{MC}})^{n_{\text{no tag}}}} = (f_b)^{n_{\text{btag}}} \left(\frac{1 - f_b \epsilon_b^{\text{MC}}}{1 - \epsilon_b^{\text{MC}}} \right)^{n_{\text{no tag}}} \quad (5.15)$$

Here, $f_b = \epsilon_b^{\text{data}} / \epsilon_b^{\text{MC}}$ is the unknown b tagging scale factor. It is left freely floating in the likelihood fit. This is technically implemented by producing shape templates from MC with f_b varied up and down by a fixed value and interpolating in between. This shape template can be seen in Fig. 5.11, where it is evident that

¹Since publication of this result, a more precise luminosity measurement for 2022 data has become available in Ref. [149].

1652 the categorization in the number of b tags gives significant constraining power for
 1653 f_b . In the 1b categories, the shape with respect to the number of jets deviates
 1654 significantly from a flat variation proportional to f_b as naively expected. This is
 1655 because of out-of-acceptance jets, corresponding to the second factor in Eq. (5.15).

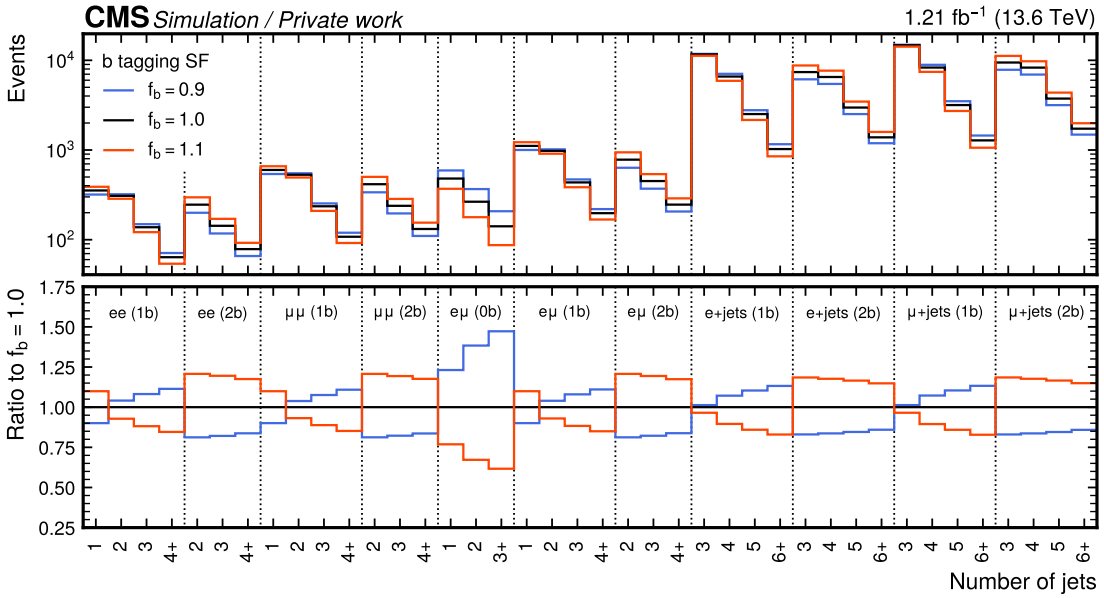


Figure 5.11: **b tagging scale factor variation.** The effect of varying the b tagging scale factor f_b in $t\bar{t}$ MC by an arbitrary value of ± 0.1 , shown for the number of jets in the 11 fit categories.

1656 Note that, since f_b is taken to be a single number, this method only corrects the
 1657 overall b jet efficiency and does not consider any dependence of ϵ_b on jet kinematics.
 1658 Because this measurement uses the same jet quality requirements (particularly the
 1659 same p_T cuts) in all channels, and assuming that the b jet p_T and η spectra in
 1660 the different channels are roughly similar, any kinematic dependence is effectively
 1661 integrated out in the overall efficiency scale factor f_b . The lack of corrections to the
 1662 spectrum is not considered problematic in this context, as the likelihood fit does not
 1663 rely directly on kinematic information.

1664 **Lepton identification uncertainty** The uncertainty assumed on the lepton iden-
 1665 tification scale factors comes from two different sources: First, an inherent uncer-
 1666 tainty originating in the tag-and-probe method (as described in Sec. 5.3.1) is con-
 1667 sidered. It consists of statistical uncertainties from both data and simulation, a
 1668 systematic uncertainty derived from a comparison with a different Z+jets simula-
 1669 tion sample produced at NLO in QCD, and another systematic uncertainty due
 1670 to the choice of fitting function. Together, they make up for an uncertainty of

1671 $\sim 0.8\%$ (0.5%) on the electron (muon) scale factors in the bulk of the phase space,
1672 and can rise up towards $\sim 5\%$ for high lepton p_T .

1673 Secondly, it is taken into account that the scale factor between data and simulation
1674 might be slightly different in the Z+jets selection used for the T&P method and
1675 the $t\bar{t}$ selection used for the measurement of the cross section. The most important
1676 reason for this is the requirement of (b tagged) jets in almost all considered cate-
1677 gories, as well as the requirement for at least three jets in the lepton+jets channels.
1678 This effect has been studied at CMS in the past and the difference found to be less
1679 then 0.5% for muons and 1.0% for electrons. Taking a conservative approach, these
1680 values are used as an additional component in the respective uncertainties.

1681 In the first, preliminary version of this measurement [134], the dedicated lepton
1682 efficiency scale factors as measured with the T&P method were not yet available,
1683 and a different approach was taken. Similar to the b tagging efficiency, the lepton
1684 efficiency scale factors were kept freely floating the likelihood fit. Due to the different
1685 dependency on the lepton efficiencies in the different lepton flavor channels, the fit
1686 was able to constrain the efficiencies to a precision of 2% [5]. The resulting scale
1687 factors were later found to be in good agreement with those obtained from the T&P
1688 method, serving as a valuable cross-check. However, this method ultimately led to
1689 less precision and was thus not used in the final result. **TODO decide on removing**
1690 **as Alexander suggested**

1691 **Pileup uncertainty** As described in Sec. 5.3.1, three different pileup-related vari-
1692 ables are employed to reweight the simulation to the observed data, and the average
1693 of the three weights is used as the nominal value. This method is repeated using
1694 only one of the variables - the number of good reconstructed vertices n_{PV} - and the
1695 difference in expected yields treated as an uncertainty. This procedure was com-
1696 pared to the usual estimation of pileup-related uncertainties in CMS. There, the
1697 theoretical expectation for the number of interactions is taken as the product of the
1698 instantaneous luminosity and the total inelastic cross proton-proton cross section
1699 of $69.2(32)$ mb at $\sqrt{s} = 13$ TeV [100]. It was found that the heuristic method used
1700 here leads to larger uncertainties than the one from the inelastic cross section, and
1701 can thus be considered more conservative.

1702 **Jet energy uncertainties** Uncertainties in the jet energy calibration are split
1703 into 26 different sources concerning different experimental and theoretical effects,
1704 following the standard CMS procedure outlined in Ref. [143]. 17 of these sources
1705 are found to be non-negligible and included in the fit, while the others are indis-
1706 tinguishable from fluctuations due to limited MC statistics. These sources include,
1707 among others, uncertainties due to jet p_T resolution and jet flavor composition,
1708 statistical uncertainties in the derivations of the energy corrections, and residual
1709 differences between data and simulation.

1710 **Trigger uncertainties** Since the trigger scale factors are derived using the tag-
1711 and-probe method in the same way as the lepton scale factors, similar uncertainties
1712 are applied, including the uncertainties of 0.5% for muons and 1.0% for electrons due
1713 to extrapolation between Z+jets and tt topologies. The only difference is that in the
1714 dilepton channels the uncertainties need to be propagated according to Eq. (5.2).
1715 This has the effect of greatly reducing the impact of the trigger uncertainties in
1716 those channels compared to the lepton ID uncertainties, since the nominal per-event
1717 trigger efficiency is already very close to one.

1718 **Matrix element scale uncertainties** The theoretical predictions of both sig-
1719 nal and background are calculated using matrix elements at either LO or NLO in
1720 perturbative QCD, matched to a parton shower. Since this effectively means trun-
1721 cating the perturbative expansion of the scattering amplitude at a given power in
1722 the strong coupling constant, the effect of higher-order terms is neglected in the
1723 calculation.

1724 At the same time, the necessity of renormalization of divergent diagrams and
1725 factorization of non-perturbative contributions introduces non-physical parameters
1726 into the prediction in the form of the renormalization and factorization scales μ_R
1727 and μ_F (cf. Sec. 3.1). These parameters are usually set to typical energy scales of
1728 the considered process, and might also depend on the event kinematics (dynamic
1729 scales).

1730 To estimate possible uncertainties due to these missing terms as well as due to the
1731 choice of scales, the scales μ_R and μ_F are varied separately by a factor of 2 up and
1732 down, and the resulting change in simulation is taken as an uncertainty in the form
1733 of shape templates [150]. To avoid double-counting uncertainties in the background
1734 cross section predictions (see below) while still accounting for possible rate variations
1735 due to acceptance effects, the templates are normalized to the nominal cross section
1736 values before applying any selection cuts.

1737 **PDF uncertainties** The PDFs used to evaluate the non-perturbative contribu-
1738 tion of the proton-proton collision have systematic uncertainties attached. They are
1739 estimated by independently reweighting the simulation to 100 different replicas of
1740 the used NNPDF 3.1 PDF set and taking the envelope of the resulting changes,
1741 following the recommendations of the PDF4LHC working group [151]. Additionally,
1742 the effect of the choice of the strong coupling constant in the PDF is assessed using
1743 a similar reweighting, and attached as a separate nuisance parameter. Analogously
1744 to the matrix element uncertainties, the resulting variations are normalized before
1745 any selection cuts to keep acceptance and shape effects while not double-counting
1746 cross section changes.

1747 **Parton shower uncertainties** The parton shower model used for the predictions
1748 is only accurate (at most) at LL and LC in QCD (cf. Sec. 3.2) and thus requires
1749 appropriate uncertainties. For this purpose, the scales at which the strong coupling
1750 constant is evaluated are varied up and down by a factor 2 separately for initial
1751 and final state radiation and for different processes, and the resulting changes are
1752 propagated to the fit as shape templates.

1753 **ME/PS matching uncertainty** For the simulation of the $t\bar{t}$ signal, an additional
1754 uncertainty concerning the matching between matrix element simulation in POWHEG
1755 and parton showering in PYTHIA is considered. This is done by varying the h_{damp}
1756 parameter in POWHEG controlling the amount of radiation generated at matrix
1757 element level, following Ref. [152].

1758 **Top quark p_T uncertainty** It has been shown in previous measurements of $t\bar{t}$
1759 differential cross sections that the p_T spectrum of the top quark is significantly
1760 softer in data than in the standard POWHEG MC simulation [153–155]. This effect
1761 is propagated to the p_T spectra of the top decay products and can thus lead to
1762 misestimation of the acceptance due to lepton and b jet p_T requirements. Fixed-
1763 order predictions at NNLO in QCD and NLO in EW are known to largely alleviate
1764 the discrepancy [156]. Thus, a common strategy is to reweight the top quark p_T
1765 spectrum in MC simulation to the one extracted from such fixed-order predictions.

1766 At the time of the measurement, fixed-order predictions at NNLO in QCD and
1767 NLO EW were available only for $\sqrt{s} = 13$ TeV and could not be directly applied to
1768 the MC simulation at $\sqrt{s} = 13.6$ TeV. Instead, the simulation is left uncorrected
1769 for the nominal prediction, and a variation is constructed by calculating the ratio
1770 of the fixed-order prediction from Ref. [156] and the POWHEG MC simulation at
1771 $\sqrt{s} = 13$ TeV, and applying it to the POWHEG MC simulation at $\sqrt{s} = 13.6$ TeV.
1772 The difference between uncorrected prediction and the variation is assigned as an
1773 additional uncertainty, which is one-sided by construction.

1774 **Background cross section uncertainties** For the cross sections of the different
1775 processes, log-normal rate uncertainties are assigned based on the process and order
1776 at which it was calculated. Separate 15% uncertainties are used for the t -channel
1777 single-top and tW backgrounds since they are generated at NLO with a NNLO
1778 prediction for the cross section, while for W+jets and Diboson, 30% is used since
1779 these samples are only generated at LO. For Z+jets, this is reduced to 20% due
1780 to the data-driven estimation of the normalization. Additionally, for the fully data-
1781 driven QCD background, two separate nuisance parameters for the e+jets and μ +jets
1782 channels are defined, covering a conservative uncertainty of 30% each.

1783 **Background statistical uncertainties** Finally, since the background in this
1784 measurement is estimated either using MC simulation or data-driven methods, an
1785 independent statistical uncertainty needs to be attached to each bin, reflecting the
1786 finite number of events it contains. This is done using the so-called *Barlow–Beeston*
1787 *light* method [157]. For MC backgrounds, these uncertainties are minuscule. How-
1788 ever, for the data-driven QCD background, they also contain the propagated statis-
1789 tical uncertainty due to the limited number of data events in the CRs, which is in
1790 general non-negligible.

1791 5.6 Fit results

1792 Performing the fit yields a $t\bar{t}$ signal strength of $r = 0.959 \pm 0.025$, where the un-
1793 certainty includes statistical and all systematic contributions, except for the 2.1%
1794 uncertainty on the luminosity. This corresponds to an inclusive $t\bar{t}$ cross section of

$$\sigma_{t\bar{t}} = 881 \pm 23 \text{ (stat+syst)} \pm 20 \text{ (lumi) pb.}$$

1795 The result is in good agreement with the standard model prediction of $\sigma_{t\bar{t}}^{\text{pred}} =$
1796 $924^{+32}_{-40} \text{ pb.}$

1797 Fig. 5.12 shows the agreement between data and simulation before and after the
1798 fit. It can be immediately seen that the fit greatly reduces the uncertainty on the
1799 prediction by constraining systematic uncertainties and simultaneously improves the
1800 agreement compared to the data.

1801 Of particular note here is the free-floating b tagging efficiency (compare sec. 5.5),
1802 whose effect can be directly read off from the categorization in the number of b jets:
1803 Before the fit (Fig. 5.12 top), the event yield for two or more b jets is overestimated in
1804 the simulation, while the yield for zero b jets is underestimated. This suggests that
1805 the b tagging efficiency is slightly lower in the data than assumed in the simulation.
1806 Indeed, the fit confirms this: the b tagging scale factor between data and simulation
1807 in the phase space of this measurement is measured to be $f_b = 0.980 \pm 0.009$. As a
1808 result, after the fit (Fig. 5.12 bottom), the event yields agree in all b jet categories.

1809 5.6.1 Statistical checks

1810 To better understand the sources of systematic uncertainty, as well as the contribu-
1811 tions of the different measurement channels, the fit is repeated twice, restricted to
1812 either the dilepton or the $\ell+\text{jets}$ channels. For both cases as well as the combination,
1813 the contribution of different groups of nuisance parameters is calculated by freezing
1814 the groups to their postfit values and repeating the fit, as explained in Sec. 4.4.
1815 It should be noted that this procedure does not take into account correlations be-
1816 tween the groups, and thus the sum in quadrature of the separate components will
1817 in general not add up to the total uncertainty.

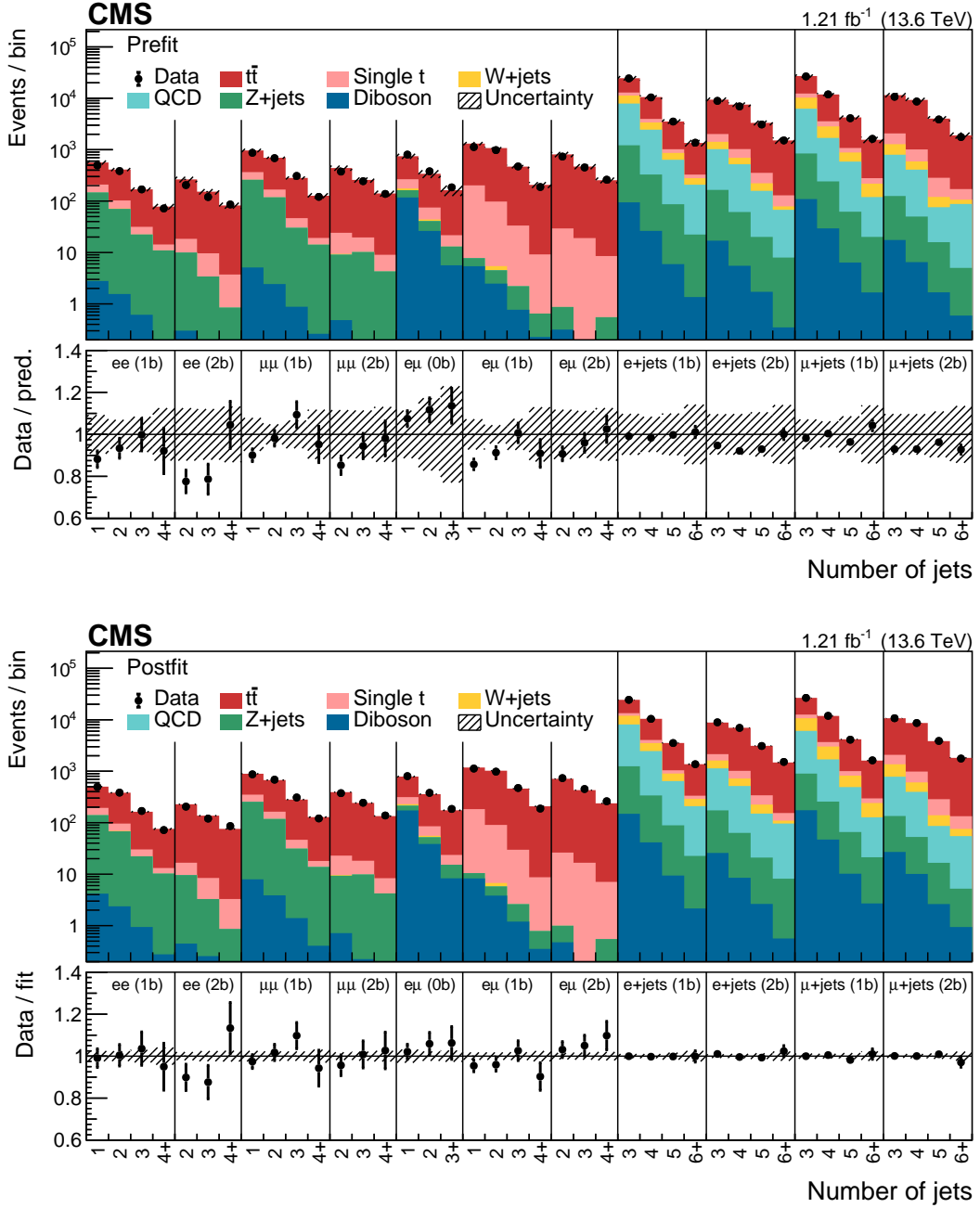


Figure 5.12: **Comparison of data and simulation before and after the fit.**

The distribution of the number of jets in the different fit categories is shown for data and simulation before (top) and after the likelihood fit (bottom). The fit greatly improves the agreement and strongly constrains the background uncertainties. *Figure taken from Ref. [5].*

Source	Full measurement	dilepton only	$\ell+$ jets only
Lepton ID efficiencies	1.6	2.2	1.0
Trigger efficiency	0.3	<0.1	0.5
JES	0.6	0.7	1.1
b tagging efficiency	1.1	0.8	2.1
Pileup reweighting	0.5	0.2	1.1
ME scale, $t\bar{t}$	0.5	0.4	0.5
ME scale, backgrounds	0.2	0.1	0.3
ME/PS matching	0.1	0.4	0.7
PS scales	0.3	0.5	0.4
PDF and α_S	0.3	0.4	0.4
Top quark p_T	0.5	0.3	0.5
tW background	0.7	1.0	0.4
t -channel single-t background	0.4	<0.1	0.5
Z+jets background	0.3	0.2	<0.1
W+jets background	<0.1	<0.1	0.2
Diboson background	0.6	0.6	<0.1
QCD multijet background	0.3	—	0.5
Statistical uncertainty	0.5	1.2	0.5
Combined uncertainty	2.6	3.4	3.3
Integrated luminosity	2.3	2.3	2.3

Table 5.3: **Sources of systematic uncertainty.** The relative per-cent contribution of different groups of sources of systematic uncertainty for the full measurement as well as for restrictions to the dilepton and $\ell+$ jets channels only. They are calculated according to Sec. 4.4 and do not take correlations between the different groups into account.

1818 The results can be found in Tab. 5.3, where it can be seen how the combination
 1819 of channels helps to reduce the total uncertainty: in the dilepton channels, the dom-
 1820 inating uncertainties are the lepton identification uncertainty, which enters twice
 1821 compared to the $\ell+$ jets channels, as well as the statistical uncertainty of the data
 1822 due to the relatively low branching ratio. In the $\ell+$ jets channels, b tagging, JES,
 1823 and pileup uncertainties dominate, reflecting the less clean selection and increased
 1824 importance of jets. When the channels are combined, the uncertainty contribution
 1825 of these groups lies inbetween the two separate numbers, showing how the chan-
 1826 nel combination represents a tradeoff between the advantages and disadvantages of
 1827 either channel.

1828 Furthermore, the nuisance parameter pulls, constraints and impacts, as defined in

Sec. 4.4, are shown in Fig. 5.13 for the channel combination. One can see how the electron identification scale factors, which are the leading impact, are constrained by the combination of channels, while the same is not true of the muon identification scale factors due to their lower prefit uncertainty.

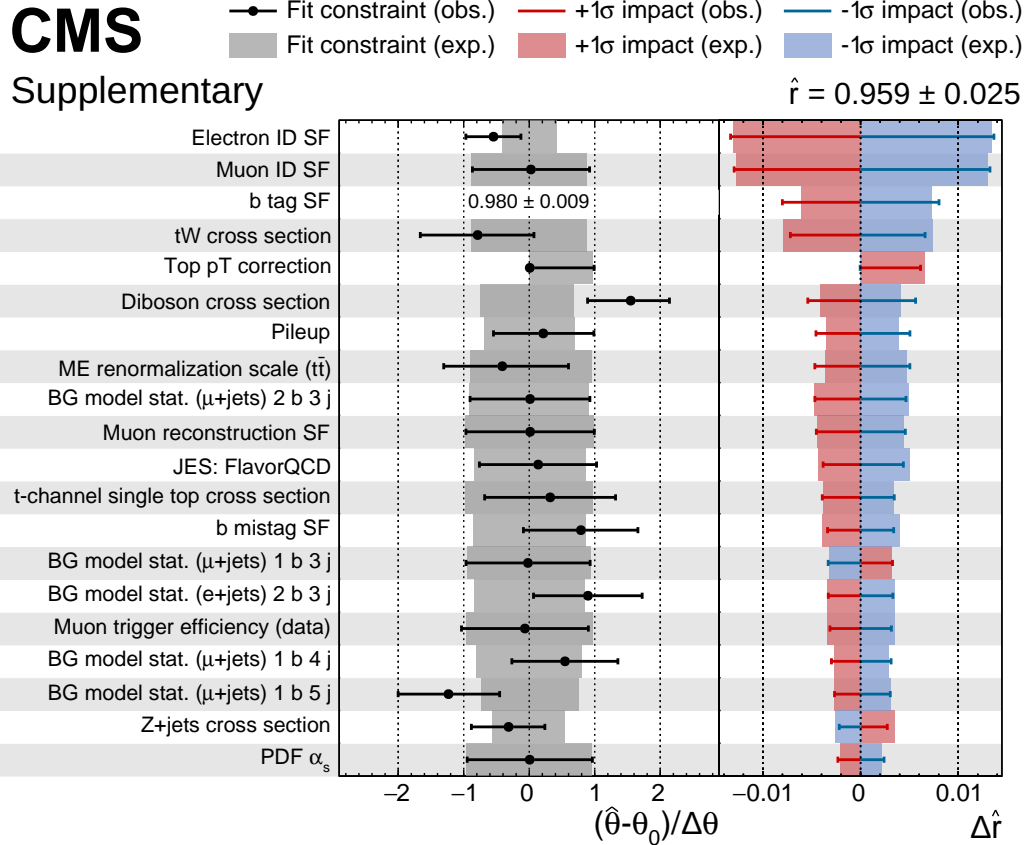


Figure 5.13: **Nuisance parameter pulls, constraints and impacts.** The expected and observed values are shown as shaded bands and error bars, respectively. Nuisance parameters are sorted by their observed impact on the signal strength r . For the b tagging scale factor, for which no prefit uncertainty is defined, the post-fit uncertainty is shown instead of the pull. *Figure taken from the supplementary material of Ref. [5].*

5.6.2 Top quark mass dependence

An additional source of uncertainty that has not been considered so far is the choice of top quark mass in the $t\bar{t}$ MC simulation. It affects the selection efficiency indirectly via the p_T cuts on leptons and jets, with higher top quark mass values leading to harder spectra and thus to larger efficiencies.

Contrary to other uncertainty sources, the top quark mass is not profiled in the likelihood fit. Instead, the dependence of the extracted $t\bar{t}$ cross section is explicitly quantified as a function of the top quark mass by shifting its value in simulation by ± 3 GeV from its default of $m_t = 172.5$ GeV. The extraction of $\sigma_{t\bar{t}}$ is then repeated and the dependence on m_t extracted through a simple linear fit. This strategy has been taken in previous CMS and ATLAS $t\bar{t}$ cross section measurements [158, 159], and thus facilitates comparison with previous results.

For an upwards shift of $\Delta m_t = 1$ GeV, the $t\bar{t}$ cross section is found to shift downwards by 8.5 pb, and vice versa. If one takes the current experimental uncertainty of 0.3 GeV [13] as an allowed range for m_t , this would lead to an additional uncertainty on $\sigma_{t\bar{t}}$ of 0.3%.

5.7 Summary and Outlook

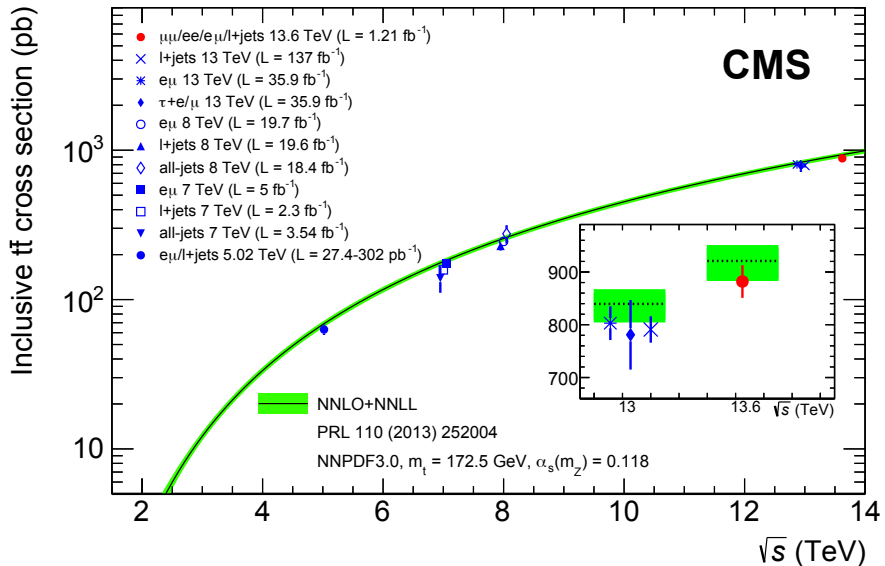


Figure 5.14: Summary of $\sigma_{t\bar{t}}$ measurements. An overview of inclusive $t\bar{t}$ cross section measurements at CMS at different center-of-mass energies [158, 160–166] as well as comparison to the SM prediction [167]. This measurement is displayed as the red dot. *Figure taken from Ref. [5].*

In this chapter, the inclusive $t\bar{t}$ cross section is measured for the first time at a center-of-mass energy of $\sqrt{s} = 13.6$ TeV. Data corresponding to an integrated luminosity of 1.21 fb^{-1} from the beginning of LHC Run 3 are analyzed. Despite this comparatively small amount of data, a total precision of ca. 3% with respect to the inclusive cross section is achieved.

1855 Fig. 5.14 compares the result of this chapter to other inclusive $t\bar{t}$ cross section
1856 measurements performed by CMS at other center-of-mass energies [158, 160–166],
1857 as well as to the SM prediction [167]. The precision is comparable to other measure-
1858 ments at $\sqrt{s} = 7, 8$, and 13 TeV, some of them with significantly higher integrated
1859 luminosities. All results are in agreement with the SM.

1860 This measurement was designed specifically for the earliest data of Run 3, in
1861 order to achieve high precision without relying on a full suite of calibrations being
1862 available. In particular, b tagging and lepton efficiencies can be constrained *in situ*
1863 using the combination of dilepton and $\ell + \text{jets}$ channels as well as the categorization
1864 by number of b-tagged jets. No large inconsistencies for any of the considered physics
1865 objects were found. The measurement was made public in September of 2022 just
1866 two months after the start of Run 3 and constituted the first public physics result
1867 of LHC Run 3. At the time, it provided a valuable first proof that CMS data taken
1868 in Run 3 were of high quality and ready for physics.

1869 The next step for this result would be to transfer the technique developed in this
1870 work to well-understood data and high integrated luminosities in order to achieve
1871 the highest precision possible for $\sigma_{t\bar{t}}$. Such a measurement will certainly be domi-
1872 nated by systematic uncertainties, most importantly the luminosity and the lepton
1873 identification efficiencies (as already partly the case here). The channel combination
1874 method developed here could potentially help reduce the latter uncertainty through
1875 an *in situ* constraint, while the former is independent of the analysis strategy and
1876 requires more precise luminosity measurements for improvement. In addition, a
1877 more detailed study of the individual sources of uncertainty will likely be necessary
1878 to assess whether some can be reduced through improved calibrations.

1879 Additionally, one could try to use such a high-precision $t\bar{t}$ cross section measure-
1880 ment to indirectly measure the top quark mass, one of the fundamental parameters
1881 of the Standard Model, by comparing the measured value of $\sigma_{t\bar{t}}$ to SM predictions
1882 for different top quark masses. For this purpose, it would be important to reduce
1883 the dependence on the top quark mass in simulation (c.f. Sec. 5.6.2), for example by
1884 reducing the p_T requirements on leptons and jets as much as experimentally feasible.
1885 All of this leaves multiple parts for future studies to tread, which will be exciting
1886 to follow in the coming years as larger parts of the Run 3 data set are analyzed at
1887 CMS.

1888 **6 Simulation of on- and off-shell $t\bar{t}$
1889 production with **bb41****

1890 **6.1 Introduction**

1891 The accurate modeling of top quark production processes at the LHC is of crucial
1892 importance for precision measurements of top quark properties. In particular, the
1893 fact the top quark is an unstable colored resonance with a short lifetime presents
1894 challenges for correctly modeling its mass line shape as used for top mass and width
1895 measurements [168–170]. Typically, the modeling is done with full NLO MC sim-
1896 ulations matched to a parton shower (NLO+PS), and multiple such generators are
1897 available with different features and degrees of accuracy.

1898 In this chapter, the predictions of some of these generators from the POWHEG
1899 framework [82, 83] are compared to each other, as well as to unfolded data mea-
1900 sured in Ref. [171], for different variables relevant to top mass and/or width mea-
1901 surements. A particular focus is the generator **bb41** [7], which specifically improves
1902 the treatment of the unstable top resonance and of the interference between $t\bar{t}$ and
1903 tW , and is described in detail in Sec. 6.2. In this work, **bb41** is implemented and
1904 validated for the first time in the CMS simulation setup. The comparison is done
1905 at the generator level, i.e. including parton showering and hadronization but not
1906 detector simulation and experimental reconstruction.

1907 The results of this work have been published in a CMS public note as Ref. [6].
1908 Since the publication of this note, a new version of **bb41** has been made avail-
1909 able [172]. In this thesis, updated results including both versions will be shown.

1910 **6.2 The Monte Carlo generator **bb41****

1911 **bb41** [7, 172] is a full NLO+PS MC generator for the process $pp \rightarrow b\bar{b}\ell^+\ell^-\nu_\ell\bar{\nu}_\ell$,
1912 including all off-shell contributions. This includes the dilepton decay channel of
1913 both $t\bar{t}$ and tW production, as well as non-resonant contributions involving Z or
1914 Higgs bosons, as shown in Fig. 6.1. Since these processes all lead to the same
1915 final state at NLO in QCD, they interfere with each other and cannot be easily
1916 separated. **bb41** includes this interference by construction since it computes the full
1917 amplitude including all diagrams at once.

1918 In addition, by considering the full amplitude instead of splitting it into pro-
1919 duction and decay, **bb41** treats the top quark as an unstable resonance without

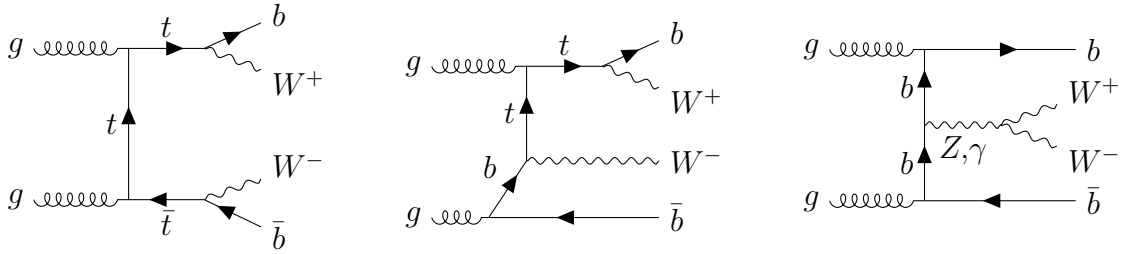


Figure 6.1: **Feynman diagrams for bb41.** Examples of Feynman diagrams for the $pp \rightarrow b\bar{b}W^+W^-$ process as described by bb41, including double-resonant (left), single-resonant (center) and non-resonant contributions (right). The decay of the W bosons into leptons is not shown for brevity.

approximations. It is implemented in the “resonance-aware” version of POWHEG, called POWHEG vRES [173], which includes the hardest QCD radiation also for unstable resonances - such as top quarks - in addition to the hardest initial state radiation always provided by POWHEG. As a result, an event generated by bb41 can have up to three hard emissions at matrix element level. The correct description of these FSR emissions is relevant e.g. for observables related to the mass of the top quark, and can be challenging for parton showers, leading to large uncertainties.

This work investigates two different versions of bb41. The first version is the one originally published in Ref. [7] and publicly available on the POWHEG website [174]. In the following, it will be referred to as bb41 v1.

The second version of bb41 was recently published in Ref. [172]. Its most prominent feature compared to the previous version is the addition of the lepton+jets decay channel of $t\bar{t}$, i.e. the $b\bar{b}\ell\nu_\ell q\bar{q}'$ final state. Moreover, it includes several improvements to the dilepton final state, such as avoidance of spurious finite width effects and improved resonance history projectors (see Ref. [172] for details). At the time of writing this thesis, the new code is not publicly available. A preview version was made available to the CMS collaboration by the authors, and the dilepton final state of this version - referred to as bb41 v2 - is shown in this work. The lepton+jets final state, on the other hand, was not ready for validation in the preview version, and so could not be included.

6.3 Other $t\bar{t}$ Monte Carlo generators

The distributions predicted by bb41 are compared to three other MC generators for the $t\bar{t}/tW$ final state, which are briefly presented in this section. All of these are implemented in POWHEG v2, and as such do not contain explicit treatment of radiation in unstable resonances.

1945 6.3.1 hvq

1946 **1945** `hvq` [85], standing for *heavy quark*, is the standard code used, at the time of writing,
1947 by both the ATLAS and CMS collaborations for producing $t\bar{t}$ MC events. It applies
1948 the narrow-width approximation (NWA) to generate stable $t\bar{t}$ pairs at NLO in QCD,
1949 with up to one additional ISR emission. The top quarks are then randomly smeared
1950 according to the top quark width, giving an approximate treatment of finite-width
1951 effects. Following this, the top quarks are decayed - in this case, in the dilepton
1952 channel for all lepton flavors - using internal POWHEG routines [175]. These rou-
1953 tines work at tree level at LO in QCD and preserve spin correlations. Further ISR
1954 emissions as well as all FSR emissions are provided by the parton shower.

1955 6.3.2 ST_wtch

1956 Since `hvq` generates only the double-resonant $t\bar{t}$ amplitude, a second generator has to
1957 be used alongside it for the single-resonant tW and $t\bar{t}/tW$ interference contributions.
1958 Here, `ST_wtch` [176] is used for this purpose. It works very similar to `hvq`, also
1959 generating a stable tW pair in the NWA, smearing with the top width and decaying
1960 the particles using the same routines.

1961 However, in order to at least approximately recover the full $b\bar{b}W^+W^-$ amplitude,
1962 it is necessary to select a scheme for the treatment of the $t\bar{t}/tW$ interference to
1963 prevent double-counting. Since the separation between $t\bar{t}$ and tW is not well defined
1964 at NLO, such schemes will to some degree always be ad-hoc and ambiguous. Two
1965 such schemes are implemented for `ST_wtch`, and both are compared in this work:
1966 in the first, called diagram removal (DR), all terms involving the square of double-
1967 resonant diagrams are simply removed from the squared amplitude. This is the
1968 most intuitive choice, but has the disadvantage of not being gauge invariant [177].
1969 The second method, diagram subtraction (DS), keeps double-resonant diagrams in
1970 the squared amplitude, and subtracts a gauge invariant counter-term to remove the
1971 double counting [176–178]. For both schemes, the prediction of `ST_wtch` is added
1972 to the one of `hvq` (together called $t\bar{t} + tW$) to produce distributions that can be
1973 compared to `bb41`.

1974 6.3.3 ttb_NLO_dec

1975 The generator `ttb_NLO_dec` [179], similar to `hvq`, works in the NWA and thus
1976 generates stable $t\bar{t}$ pairs with ad-hoc smearing. However, unlike `hvq`, it is fully
1977 NLO-accurate not only in the production, but also in the decay of the top quarks.
1978 This means that, like `bb41`, it generates up to one hard FSR emission per decaying
1979 top quark, leading to up to three hard emissions in the final state.

1980 It also provides an LO-accurate treatment of the $t\bar{t}/tW$ interference by reweighting
1981 the generated $t\bar{t}$ events to the full off-shell LO amplitude. Thus, like `bb41`, it can

Parameter	Value
POWHEG settings	
Top quark mass	172.5 GeV
Top quark width	1.33 GeV
h_{damp}	$1.38 m_t$ [152]
PDF set	NNPDF 3.1 [76]
PYTHIA settings	
PYTHIA version	8.307
PYTHIA tune	CP5 [94]
PowhegHooks settings [87]	
POWHEG:veto	on
POWHEG:pThard	0
POWHEG:pTdef	1

Table 6.1: **Generator settings.** An overview of the settings for POWHEG and PYTHIA, as well as the matching between them, for all considered generators.

1982 be used on its own and does not need to be added together with e.g. `ST_wtch`, but
 1983 is expected to work at a lower accuracy since it includes more approximations.

1984 6.4 Technical setup

1985 For all generators, LHE events were generated and then showered and hadronized
 1986 with the multi-purpose generator PYTHIA. Wherever possible, the same settings
 1987 were used for the different generators, an overview of which can be found in Tab. 6.1.
 1988 They are mostly identical to the default settings used by CMS for MC generation,
 1989 as discussed in Ref. [94].

1990 6.4.1 Parton shower matching

1991 Special care has to be taken regarding the matching of the POWHEG ME gener-
 1992 ators to the parton shower as provided by PYTHIA. For `hvq` and `ST_wtch`, this
 1993 is accomplished here using a shower veto as described in Sec. 3.2, and technically
 1994 implemented using the `PowhegHooks` module of PYTHIA. By default, this module
 1995 can only handle one ISR emission at matrix element level, and thus needs to be
 1996 extended for `bb41` and `ttb_NLO_dec`, which also contain FSR emissions in the top
 1997 decay. This was implemented by the `bb41` authors in the `PowhegHooksBB4L` module
 1998 as described in detail in Ref. [180]. An updated form of this module compatible
 1999 with `bb41` v2 is used here. Similarly to the ISR case, it is possible to directly start
 2000 the shower at the energy scale of the POWHEG emission, or alternatively employ a

2001 veto for emissions above this scale. The latter is used as the default option, and
2002 compared to the former in Sec. 6.5.2.

2003 6.4.2 Same-flavor leptons

2004 By default, both versions of `bb41` generate only dilepton final states with opposite-
2005 flavor leptons (electrons, muons or τ leptons). This is because, in principle, there
2006 are additional diagrams contributing to the $b\bar{b}\ell^+\ell^-\nu_\ell\bar{\nu}_\ell$ amplitude for same-flavor
2007 leptons, such as $b\bar{b}ZZ$ with $ZZ \rightarrow \ell^+\ell^-\nu_\ell\bar{\nu}_\ell$, that are not included in `bb41`.

2008 In practice, the effect of these diagrams will be small, especially in experimental
2009 analyses where a cut is applied to reject resonant same-flavor lepton pairs close to
2010 the Z boson mass (compare Sec. 5.2.3). To make sure that `bb41` can be used in CMS
2011 for experimental analyses involving all lepton flavors, a relabeling procedure already
2012 included in `bb41` is extended to also produce same-flavor lepton final states, neglect-
2013 ing the aforementioned diagrams. This procedure is used for all `bb41` distributions
2014 shown in this chapter.

2015 6.5 Results

2016 6.5.1 Comparison between generators

2017 In this section, the two `bb41` versions are compared against each other, as well as
2018 to the alternative generators introduced in Sec. 6.3, for different observables. All of
2019 these comparisons are done after parton showering and hadronization, but without
2020 any detector simulation.

2021 The package RIVET [181] was used to analyze the events. For some observables,
2022 publicly available analysis packages were employed, which is stated in the captions
2023 of the figures where applicable. Furthermore, some observables include distributions
2024 at the jet level, which are obtained by running an anti- k_T algorithm with distance
2025 parameter $\Delta R = 0.4$ (AK4) [124].

2026 **Lepton observables** To begin the comparison, events with at least two leptons of
2027 opposite sign satisfying $p_T > 20 \text{ GeV}$ and $|\eta| < 2.4$ are selected. Photons surround-
2028 ing the leptons in a small cone of $\Delta R < 0.1$, originating from photon radiation,
2029 are clustered together with the leptons (“dressed leptons”). The p_T distributions of
2030 the leading and subleading of these two leptons are shown in Fig. 6.2. They show
2031 good agreement between the generators within the renormalization and factorization
2032 scale uncertainties. $t\bar{t} + tW$ using the DR scheme predicts a slightly harder lepton
2033 spectrum than the others, while the DS scheme agrees with `bb41` and `ttb_NLO_dec`.

2034 The same trend can be seen in Fig. 6.3 for the invariant lepton mass $m_{\ell\ell}$, both
2035 inclusively and split by lepton flavor channels. The per-channel distributions are all

6 Simulation of on- and off-shell $t\bar{t}$ production with **bb41**

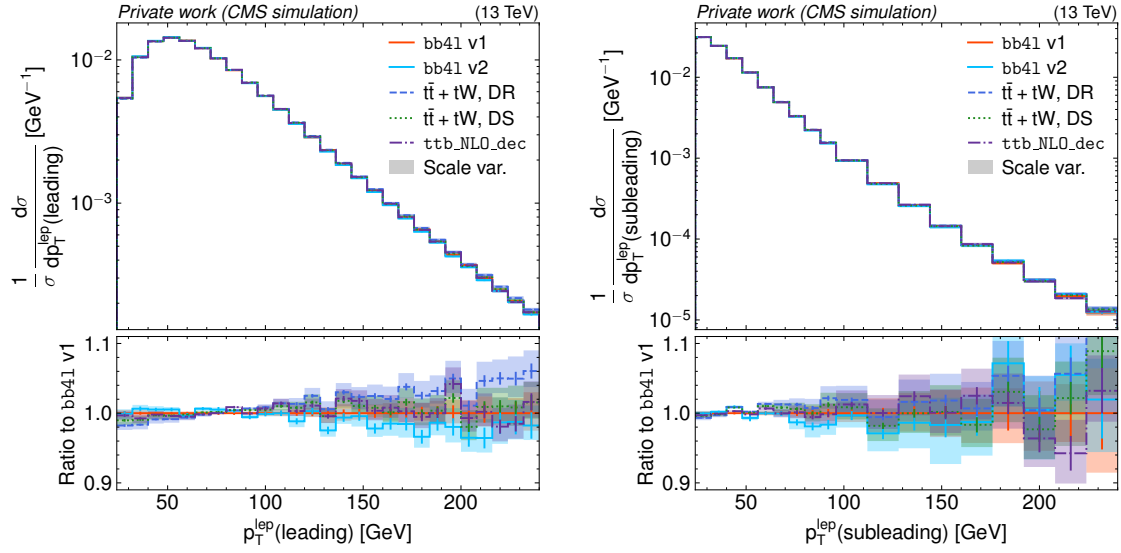


Figure 6.2: **Distributions of lepton p_T** of the leading (left) and subleading (right) lepton for **bb41** v1 (red), v2 (aqua), $t\bar{t} + tW$ with the DR (blue) and DS scheme (green), as well as **ttb_NLO_dec** (magenta). The shaded bands show the uncertainty due to scale variations, while the error bars show the statistical uncertainty. *Figure adapted from Ref. [6].*

2036 comparable within statistical uncertainties, which validates the extension to same-
2037 flavor leptons for **bb41** presented in Sec. 6.4.2.

2038 **Jet observables** Next, some selected AK4 jet observables are compared. Jets con-
2039 taining a B hadron are identified as b jets using a ghost association technique [182,
2040 183].

2041 Fig. 6.4 shows the inclusive jet multiplicity and the transverse momentum of the
2042 leading b jet for the different generator setups. Several differences can be observed,
2043 both between the two versions of **bb41** and between **bb41** and the other generators.
2044 For the jet multiplicity, the variations are largely covered by the scale uncertainties.
2045 However, for the leading b jet transverse momentum, a discrepancy remains at
2046 very low p_T that is not accounted for by these uncertainties. It is interesting to
2047 note that the number of jets agrees well between $t\bar{t} + tW$ and **bb41** v2, while **bb41**
2048 v1 and **ttb_NLO_dec** disagree and predict a larger number of jets. The origin of
2049 these discrepancies, especially between the **bb41** versions, is not yet understood and
2050 subject of discussion with the authors of the program.

2051 Next, Fig. 6.5 shows the b quark fragmentation, defined as the fraction of energy of
2052 the central B hadron in a jet compared to the total jet energy, as well as the average
2053 differential b jet shape $\langle \rho(R) \rangle$, which is the transverse momentum density of the
2054 particles making up the b jet as a function of its radius R . Both of these variables

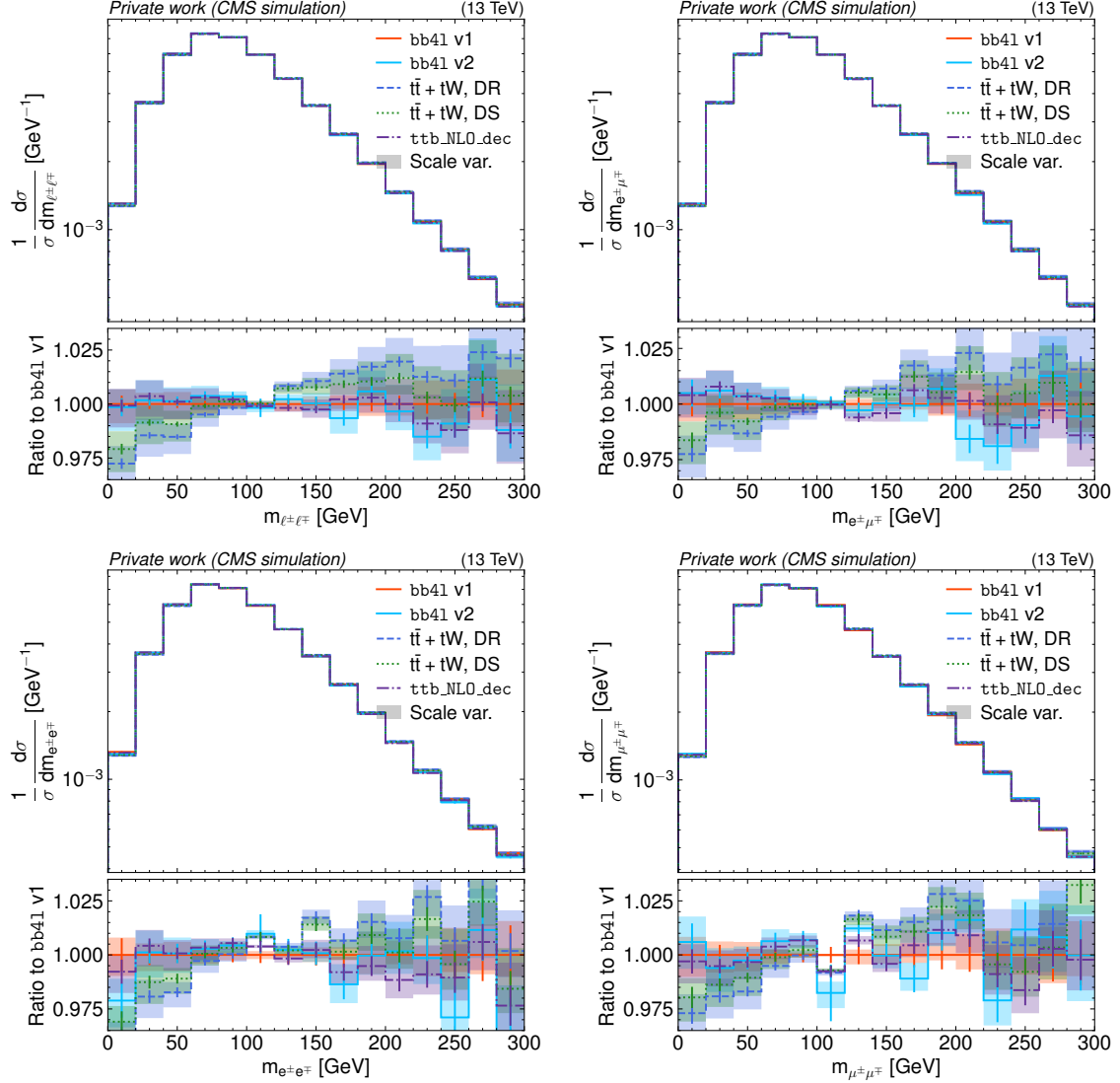


Figure 6.3: **Distributions of $m_{\ell\ell}$** for all lepton flavors combined (upper left) as well as in the $e\mu$ (upper right), ee (lower left) and $\mu\mu$ channels (lower right), shown in the same manner as in Fig. 6.2. *Figure adapted from Ref. [6].*

6 Simulation of on- and off-shell $t\bar{t}$ production with bb41

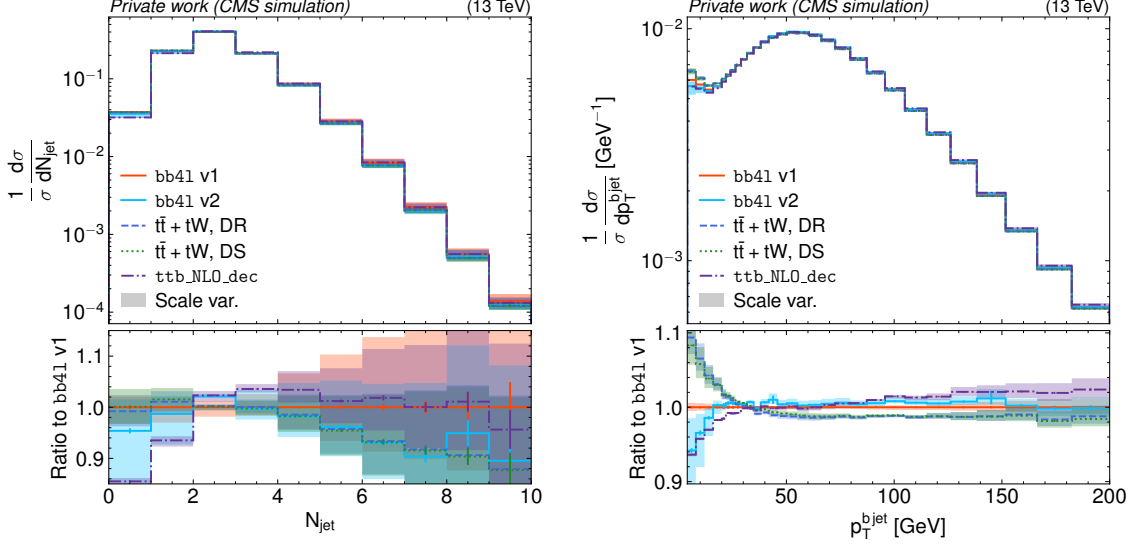


Figure 6.4: **Number of jets and b jet p_T .** Distributions of the inclusive number of AK4 jets (left) and the p_T of the leading b jet (right, RIVET analysis MC_HFJETS), shown in the same manner as in Fig. 6.2. *Figure adapted from Ref. [6].*

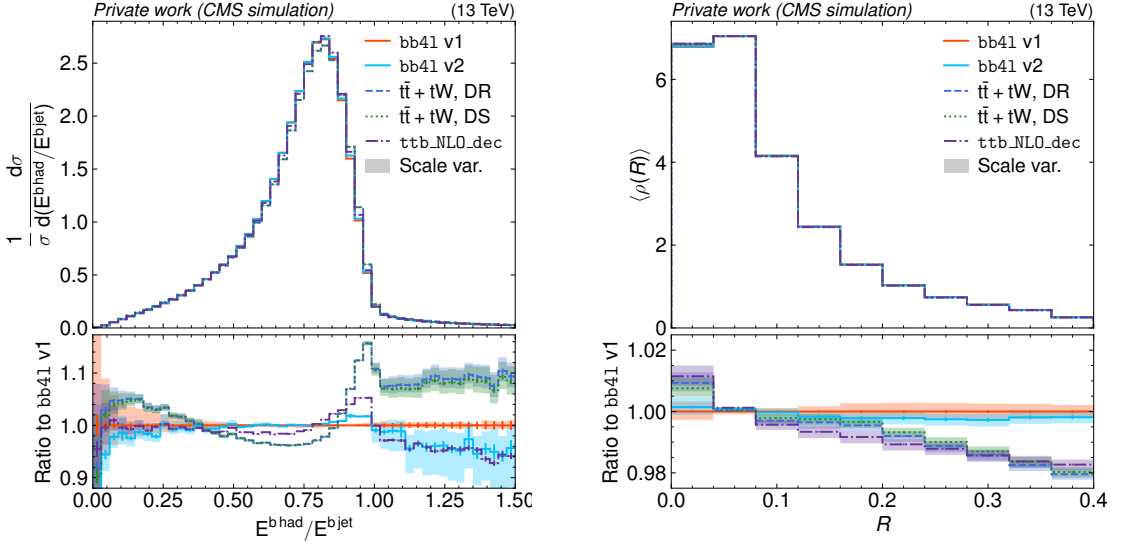


Figure 6.5: **b fragmentation and jet shape.** Distributions of the b quark fragmentation (left, RIVET analysis MC_HFJETS) and the average differential b jet shape (right, RIVET analysis MC_HFDECAYS), shown in the same manner as in Fig. 6.2. *Figure adapted from Ref. [6].*

2055 are sensitive to final-state radiation from the top decay, and are thus expected to be
 2056 affected by the full NLO calculation performed by `bb41`. It can be seen that both
 2057 versions of `bb41` predict softer b jet spectra and wider jets than both $t\bar{t} + tW$ and
 2058 `ttb_NLO_dec`, which can be interpreted as more FSR emissions being generated.
 2059 Notably, this effect cannot be solely due to the inclusion of hard FSR emissions in
 2060 `bb41` since these are also present in `ttb_NLO_dec`.

2061 In general, all of these trends for `bb41` (softer lepton and b jet spectra as well
 2062 as wider jets) agree with what was observed in Refs. [180, 184], but differ from the
 2063 results initially reported in Ref. [7].

2064 **Invariant $b\ell$ mass** A common proxy observable to use for measurements of the
 2065 top quark mass in dilepton events is the invariant mass of a b jet and a lepton, $m_{b\ell}$.
 2066 To do so, a procedure is needed to unambiguously assign the leptons and b jets (of
 2067 which there might be varying numbers per event depending on the event selection)
 2068 to each other. Here, exactly two b jets per event are required, and the so-called
 2069 minimax mass is used, defined as

$$m_{b\ell}^{\text{minimax}} = \min [\max(m_{b_1\ell_1}, m_{b_2\ell_2}), \max(m_{b_1\ell_2}, m_{b_2\ell_1})]. \quad (6.1)$$

2070 This prescription amounts to maximizing the invariant mass over the two $b\ell$ pairs
 2071 in the event, and then minimizing it over the two possible assignments of b jets and
 2072 leptons. It is notable in that, for double-resonant $t\bar{t}$ events, it shows a kinematic
 2073 cutoff at a value of $\sqrt{m_t^2 - m_W^2} \approx 150$ GeV. As a result, the tail above this cutoff is
 2074 sensitive to single-resonant tW events as well as $t\bar{t}/tW$ interference and thus to the
 2075 top quark width.

2076 Fig. 6.6 shows the distribution of $m_{b\ell}^{\text{minimax}}$, again for all considered cases. It can be
 2077 seen that both versions of `bb41` are in good agreement with each other, and are also
 2078 in agreement with `ttb_NLO_dec` except for the lowest bin. Unfolded ATLAS data
 2079 taken from Ref. [171] is overlaid on top of the predictions, and shows good agreement
 2080 for both `bb41` and `ttb_NLO_dec`. In the tail, the two interference handling schemes
 2081 for $t\bar{t} + tW$ show significant differences as expected, with `bb41` and `ttb_NLO_dec`
 2082 lying between them. Since `bb41` is expected to provide a more accurate prediction
 2083 of the interference than either scheme, this validates that using the difference of
 2084 the schemes as an uncertainty covers the true values, as is done in many CMS and
 2085 ATLAS measurements. Going forward, such uncertainties could be dropped from
 2086 future measurements by using `bb41` predictions directly.

2087 **Top quark reconstruction** Finally, in order to directly study the effects on top
 2088 quark observables, a simple generator-level top quark reconstruction is performed.
 2089 To do so, two dressed leptons and two b jets are selected as before, while the two
 2090 neutrinos in the dileptonic top decay are taken from truth-level information. The W
 2091 bosons are reconstructed from the neutrinos and charged leptons according to the

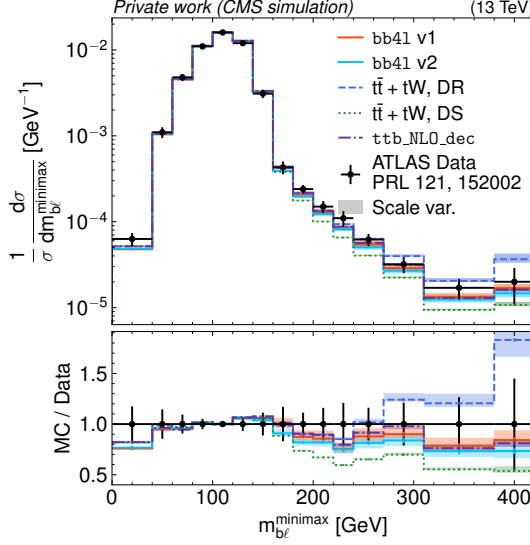


Figure 6.6: **Distribution of $m_{b\ell}^{\text{minimax}}$** , shown in the same manner as in Fig. 6.2. ATLAS data from Ref. [171] is overlaid as black dots, and the RIVET routine from said reference was used to obtain the distributions. *Figure adapted from Ref. [6].*

lepton charge, and then combined with the b jets by choosing the pairs for which the difference Δm_t between the invariant masses is minimal.

This reconstruction procedure is not equivalent to a full experimental reconstruction, in which neutrinos are measured only as missing transverse momentum and thus cannot be directly assigned to the leptons. It also does not include any detector resolution effects. However, it does take into account the effects of FSR in the top decay by considering the full b jets instead of parton-level b quarks, which is why it was chosen for the comparison.

Fig. 6.7 shows the resulting distributions for the top quark mass and p_T . It can be seen that the different generators show different line shapes for the top quark mass: **bb41** predicts a small shift towards lower values compared to $t\bar{t} + tW$ for both interference handling schemes as well as **ttb_NLO_dec**, and also predicts significantly lower amounts of off-shell tops with masses below the pole mass compared to $t\bar{t} + tW$. Both of these facts are important for precision top mass measurements, in which such shifts can influence the final fit results. The presence of these differences is expected: due to the use of the NWA for both $t\bar{t} + tW$ and **ttb_NLO_dec**, the top line shape can only be modeled approximately in these generators, while **bb41** provides a true NLO-accurate description. It can furthermore be seen that the two **bb41** versions are not in perfect agreement with each other, though the difference is within the scale uncertainties.

For the top quark p_T , on the other hand, any trend in the comparison between the

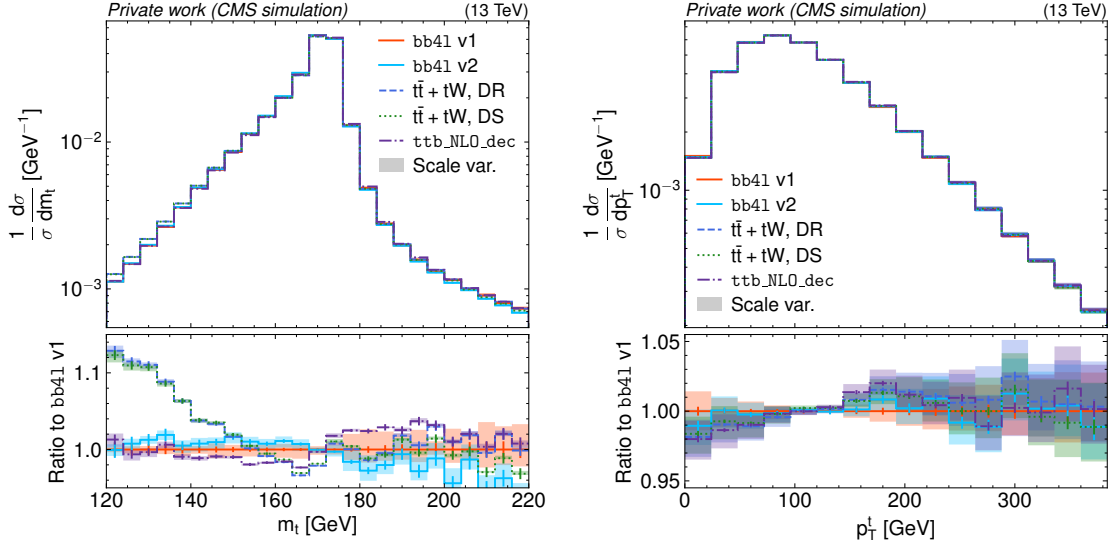


Figure 6.7: **Top quark line shape and p_T .** Distributions of the reconstructed top quark mass (left) and p_T (right), summed for both top and antitop quark, shown in the same manner as in Fig. 6.2. *Figure adapted from Ref. [6].*

generators is covered by the scale uncertainties, though **bb41** does seem to again predict softer p_T spectra than the other generators, consistent with the trends observed for the lepton p_T and $m_{\ell\ell}$.

Lastly, the invariant mass and p_T distributions of the $t\bar{t}$ system as a whole are shown in Fig. 6.8. For $m_{t\bar{t}}$, no clear trend can be seen for any of the considered generators. The p_T of the $t\bar{t}$ system, on the other hand, shows significant differences both between the two **bb41** versions and between **bb41** and the other generators (which agree with each other). It should be noted that, since the initial state of the $pp \rightarrow t\bar{t}$ process has no p_T ¹, this variable is exactly zero at LO in QCD, and consequently determined only by emissions at NLO and beyond. As a result, it is expected to be sensitive to the NLO calculation and matching between matrix element and parton shower.

6.5.2 Comparison of FSR matching settings

Complementary to the previous generator comparisons, this section investigates the effect of the matching between matrix element and parton shower for FSR in **bb41**. As explained in Sec. 6.4.1, two principal options are available to match **bb41** to PYTHIA in the used module PowhegHooksBB4L: In the first and nominal approach

¹Non-zero p_T of the incoming partons can be modeled with transverse momentum distributions [185], but this is not considered here.

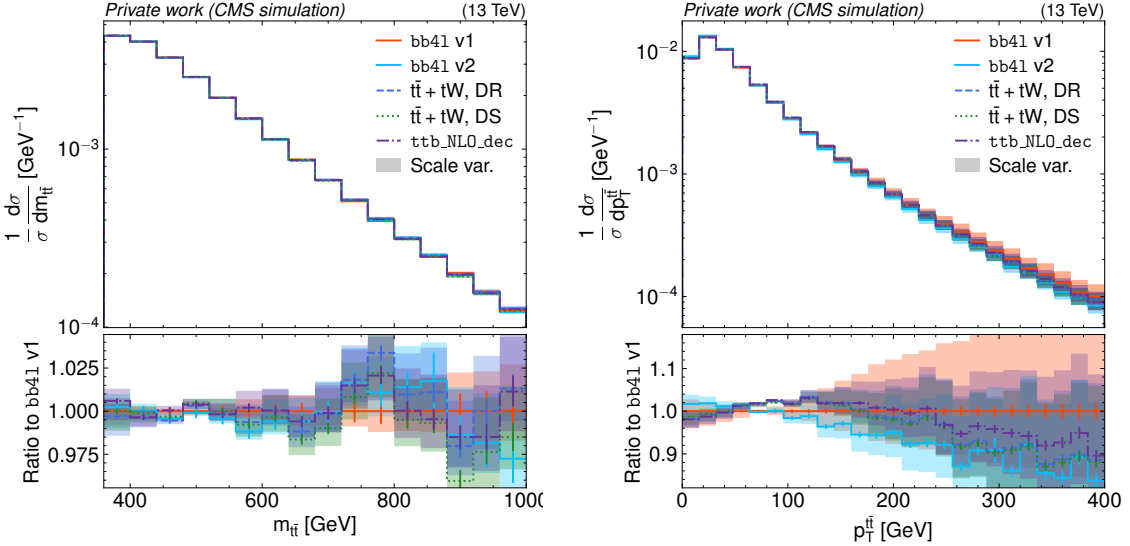


Figure 6.8: **Kinematics of the $t\bar{t}$ system.** Distributions of the reconstructed invariant mass (left) and p_T (right) of the $t\bar{t}$ system, shown in the same manner as in Fig. 6.2. *Figure adapted from Ref. [6].*

(denoted “FSR veto”), the parton shower is started at the kinematic limit, and FSR emissions that lie above the POWHEG energy scale of the relevant emission from the top decay as generated by POWHEG are vetoed.

In the second approach (“Res. scale”), the shower is directly started at the energy scale of the POWHEG FSR emission. This neglects the fact that the hardness scale definitions used in POWHEG and PYTHIA as ordering variables are similar but do not match exactly. When the PYTHIA emission is only slightly softer (by the PYTHIA definition) than the POWHEG emission, it is thus possible that it is in fact harder than the POWHEG emission by the POWHEG definition, leading to double-counting. Similarly, an emission that is only slightly harder by the PYTHIA definition and is thus not generated might in fact be softer by the POWHEG definition, leading to under-counting.

In order to demonstrate the importance of correct parton shower matching, a third case (“Kin. limit”) is considered, in which the parton shower for FSR emissions is started naively at the kinematic limit without any veto procedure specifically directed at **bb41**. This approach is thus expected to double-count FSR emissions.

The comparison in this section has been performed with **bb41 v1**. The matching for ISR emissions, done by **PowhegHooks**, is left identical between the three cases, as given in Tab. 6.1.

Fig. 6.9 shows the distributions of the top quark mass, reconstructed the same as before, and the b fragmentation for the different matching choices. Both of these observables were chosen for their sensitivity to FSR effects. It can be seen that

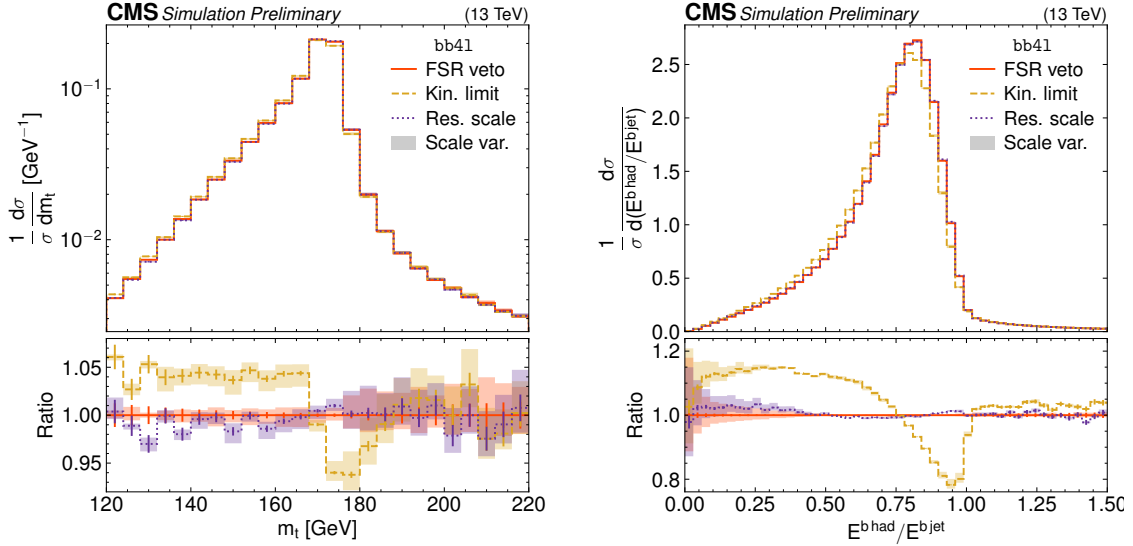


Figure 6.9: **Comparison of FSR matching settings.** Distributions of the reconstructed top quark mass (left, same as in Fig. 6.7) and the b quark fragmentation (right, same as in Fig. 6.5), for bb41 with different FSR matching settings as explained in the text (Sec. 6.5.2). The shaded bands show scale uncertainties. *Figure taken from Ref. [6].*

the options “FSR veto” and “Res. scale” agree reasonably well with each other, with the top mass line shape showing a small shift between them within the scale uncertainties. This implies that the mismatch between the POWHEG and PYTHIA energy scale definitions has a subleading effect in practice. On the other hand, the naive “Kin. limit” approach shows a large discrepancy due to its double-counting of FSR emissions, highlighting the importance of correct FSR matching procedures for NLO generators.

6.5.3 Recoil in top decay

In the simple parton shower in PYTHIA, there is a well-known problem affecting the virtualities of heavy unstable colored resonances, such as the top quark, in the treatment of FSR emissions in the resonance decay [186]. In particular, when performing a gluon emission off the decaying top quark and thus changing a $t \rightarrow Wb$ configuration to $t \rightarrow Wbg$, there is an ambiguity on how to distribute the recoil imposed by the gluon between the top decay products (W and b quark) such that the four-momentum of the Wbg system is conserved.

PYTHIA 8.307, which is the version used for the previous studies in this chapter, offers two different treatments for this problem, which amount to assigning the recoil to only the W (“recoil to W”) or only to the b quark (“recoil to b”). Both of these

2170 are approximations, since a true treatment would distribute the recoil between the
 2171 W and b quark in some form. CMS, and thus the studies previously shown in this
 2172 chapter, use the “recoil to b” option.

2173 Since PYTHIA 8.310, a third option (“recoil to top”) has been made available
 2174 via the setting `TimeShower:recoilStrategyRF`. For this option, the W is chosen
 2175 as the recoiler at first, but the emissions are then reweighted in such a way as to
 2176 approximate the radiation pattern expected in a true resonance-aware shower [186].
 2177 It has been found in Ref. [187] that the difference between this improved method
 2178 and the old ones can have a substantial impact on top mass proxy observables and
 2179 consequently measured top mass values, and there have been discussions on whether
 2180 such a difference should be included as a systematic uncertainty.

2181 This problem, in its core, is an issue of the parton shower and not the ME gen-
 2182 erator. Nonetheless, **bb41** is expected to alleviate some of the ambiguities since it
 2183 always includes the hardest gluon emission in each top decay at the ME level, where
 2184 no question of assigning the recoil is raised. For subsequent and thus subleading
 2185 emissions, the issue in principle still persists.

2186 To estimate the effect of the top recoil in **bb41** and compare it to $t\bar{t} + tW$, events
 2187 from both generators are re-showered in PYTHIA 8.310 with the two choices of setting

```
TimeShower:recoilStrategyRF = 1 ("recoil to b") and
TimeShower:recoilStrategyRF = 2 ("recoil to top").
```

2188 **bb41** v2 is used for this comparison, and all other settings are kept at the nominal.
 2189 For $t\bar{t} + tW$, only the DR scheme is considered for the interference handling.

2190 The results are shown in Fig. 6.10 for the reconstructed top mass and the b
 2191 quark fragmentation. Large differences are visible between the two recoil strategies
 2192 for $t\bar{t} + tW$, as expected from Refs. [186, 187]. For **bb41**, on the other hand, the
 2193 differences are very small, and lie within the scale uncertainties for the top quark
 2194 mass. This implies that the effect of the recoil in subleading emissions is negligible
 2195 in **bb41** for the shown observables. As a result, **bb41** circumvents the problem of
 2196 top recoil that can otherwise be significant for $t\bar{t}$ analyses. **TODO** After discussion
 2197 with Afiq I am not really convinced whether these results are actually correct... In
 2198 particular, are we sure that the recoil strategy option in pythia works correctly when
 2199 matched to bb4l? Simone is unfortunately no longer around to ask. Should I remove
 2200 it?

2201 6.6 Summary and Outlook

2202 In this chapter, several generator-level studies of the MC generator **bb41**, which
 2203 generates the full $b\bar{b}\ell^+\ell^-\nu_\ell\bar{\nu}_\ell$ final state including $t\bar{t}/tW$ interference and off-shell
 2204 top effects at NLO in QCD, have been presented. **bb41** has been compared to

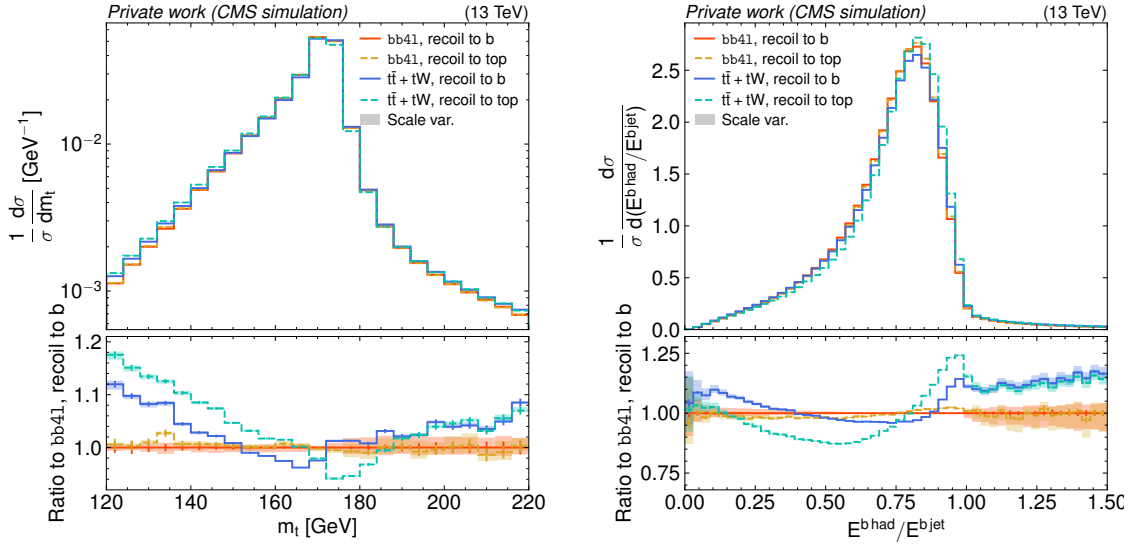


Figure 6.10: **Comparison of top recoil strategies.** Distributions of the reconstructed top quark mass (left, same as in Fig. 6.7) and the b quark fragmentation (right, same as in Fig. 6.5), for bb41 and $t\bar{t} + tW$ with two different recoil treatments, as defined in the text (Sec. 6.5.3). The shaded bands show scale uncertainties.

other common $t\bar{t}$ generators, namely `hvq`, `ST_wtch` (with two interference handling schemes) and `ttb_NLO_dec`, for different lepton, (b) jet and reconstructed top quark observables. For m_{bl}^{minimax} , `bb41` agrees well with ATLAS data from Ref. [171], improving greatly upon the two interference handling schemes DR and DS for $t\bar{t} + tW$. For the reconstructed top quark mass, `bb41` shows a significant shift compared to $t\bar{t} + tW$. In addition, two different `bb41` versions have been compared, finding slight differences within scale uncertainties, and the matching of ME and parton shower as well as the treatment of the top recoil in `bb41` have been studied further.

These studies represent valuable information for the choice of $t\bar{t}$ MC generator in upcoming CMS measurements. For analyses in which $t\bar{t}$ and tW are major backgrounds, `bb41` can help reduce uncertainties originating in the $t\bar{t}/tW$ interference treatment, and provide a more accurate description when off-shell regions of phase space are probed. This is briefly explored in Sec. 7.5.4 in the context of a search for $t\bar{t}$ bound state effects, which are naturally located in an off-shell-region. Furthermore, `bb41` will be crucial for a simultaneous top mass and width measurement using MC templates, as originally proposed in Ref. [180], in CMS. Alternatively, one might perform an differential $t\bar{t} + tW$ cross section measurement, where `bb41` could be used to unfold the data to generator level.

2223 **7 Search for heavy scalar or pseudoscalar
2224 bosons in $t\bar{t}$ final states**

2225 **7.1 Introduction**

2226 Additional spin-0 particles are predicted in many attractive extensions of the Stan-
2227 dard Model, and can be searched for in $t\bar{t}$ final states at the LHC if the new states are
2228 heavy (i.e. have a mass larger than $2m_t$), electrically neutral, and exhibit Yukawa-
2229 like couplings to fermions (see Sec. 2.3.1). A generic model for such states with either
2230 pseudoscalar (A) or scalar (H) couplings to top quarks was given in Eq. (2.18).

2231 In addition, $t\bar{t}$ bound state effects are expected in the SM in several calculations,
2232 with a pseudoscalar component dominating at the LHC as discussed in Sec. 2.2.3.
2233 Since additional BSM particles and bound state effects are expected to lead to
2234 similar experimental signatures, it makes sense to search for them for using the
2235 same methods.

2236 This chapter presents such a search for new spin-0 states with either scalar or
2237 pseudoscalar interactions with the top quark, using the full Run 2 data set with an
2238 integrated luminosity of 138 fb^{-1} at the CMS experiment. It follows up on a similar
2239 search done using only 35.9 fb^{-1} of data taken in 2016 [20]. Similar searches have
2240 also been published by ATLAS, one with 20.3 fb^{-1} of data taken at $\sqrt{s} = 8\text{ TeV}$ [188]
2241 and one with 140 fb^{-1} of data taken at $\sqrt{s} = 13\text{ TeV}$ [189].

2242 The work done as part of this thesis focused on the dilepton decay channel of $t\bar{t}$,
2243 which is thus described in detail in Secs. 7.2 to 7.6. A significant excess of events
2244 is observed at invariant masses close to the $t\bar{t}$ threshold, which is interpreted either
2245 as a pseudoscalar $t\bar{t}$ bound state (Secs. 7.7.1 to 7.7.3) or as an additional scalar or
2246 pseudoscalar boson (Sec. 7.7.4). For the latter interpretation, exclusion limits for a
2247 large mass range are also presented in Sec. 7.8. Following this, the dilepton channel
2248 is combined with a similar analysis of the $\ell+\text{jets}$ decay channel, which is discussed
2249 in Sec. 7.9, and exclusion regions are provided for the presence of either one or
2250 two additional bosons. The results of this work are briefly compared in Sec. 7.10
2251 to preliminary ATLAS results in Ref. [190] which confirmed this measurement, to
2252 earlier ATLAS results in Ref. [189] in which no excess was observed, and to other
2253 $t\bar{t}$ measurements. Finally, a summary and outlook are given in Sec. 7.11.

2254 The results presented here were first made public as a Physics Analysis Sum-
2255 mary [191], and later submitted to *Reports on Progress in Physics* in an updated
2256 form in two parts: first in Ref. [8] focusing solely on the interpretation of a $t\bar{t}$ bound

state, and second in Ref. [9] focusing on the interpretation in terms of additional bosons. They build upon the framework developed in Ref. [192], with this work consisting of the implementation of matrix element reweighting for the signal simulation (Sec. 7.4), the simulation and scrutinization of the $t\bar{t}$ bound state signal (Sec. 2.2.3), the comparison with other MC generators for the $t\bar{t}$ continuum (Sec. 7.5.4), the interpretation of the observed excess in terms of $t\bar{t}$ bound states or additional bosons including all corresponding cross-checks (Sec. 7.7), the combination with the $\ell+\text{jets}$ channel (Sec. 7.9), the comparison to other results (Sec. 7.10), and the preparation of the results for publication in Refs. [9] and [8].

2266 7.2 Analysis setup

2267 This section describes the analysis strategy in the dilepton channels, consisting of
2268 the considered data sets, object definitions, event selection criteria, corrections and
2269 reconstruction algorithms.

2270 7.2.1 Data sets

2271 **Experimental data** The analysis is performed using the full CMS Run 2 ultra-
2272 legacy (UL) data set, which is the final, re-reconstructed and recalibrated data set
2273 recommended by CMS for physics analyses. It is split into the three data taking
2274 years of Run 2: 2016, 2017 and 2018, where 2016 is further split into two parts,
2275 denoted “2016pre” and “2016post”, because of a modification of the APV readout
2276 chip settings that affects the efficiency of the track hit reconstruction during the
2277 2016 data-taking period [193].

2278 A similar combination of dilepton and single-lepton triggers as in Sec. 5.2.1 is
2279 used for all years, with the p_T thresholds varying slightly between data taking eras,
2280 as shown in Tab. 7.1.

2281 **Background simulation** Since the final state of the signals considered in this
2282 analysis are the same as in the SM $t\bar{t}$ background, it is clear that a large irreducible
2283 background is expected. As a result, it is essential that the SM Monte Carlo sim-
2284 ulation is as both theoretically precise and has sufficient statistics, and that any
2285 remaining imprecisions are covered by the systematic uncertainty model.

2286 The SM $t\bar{t}$ background is again simulated at NLO in QCD with the $h\nu q$ process
2287 from the MC generator package POWHEG v2 and interfaced to PYTHIA 8 for show-
2288 ering. Equivalent settings as in Sec. 5.2.1 and Sec. 6.4, corresponding to the CMS
2289 defaults, have been used. To achieve the necessary precision, the NLO simulation is
2290 reweighted to higher orders in both QCD and electroweak (EW) processes, which is
2291 described in Sec. 7.3.

Trigger	Year	Lepton p_T requirement
single-e	2016	$e (p_T > 27 \text{ GeV})$
	2017	$e (p_T > 35 \text{ GeV})$
	2018	$e (p_T > 32 \text{ GeV})$
single- μ	2016	$\mu (p_T > 24 \text{ GeV})$
	2017	$\mu (p_T > 27 \text{ GeV})$
	2018	$\mu (p_T > 24 \text{ GeV})$
ee	all	$e_1 (p_T > 23 \text{ GeV}) \text{ and } e_2 (p_T > 12 \text{ GeV})$
$\mu\mu$	all	$\mu_1 (p_T > 17 \text{ GeV}) \text{ and } \mu_2 (p_T > 8 \text{ GeV})$

Table 7.1: **Trigger p_T thresholds.** Overview of the used triggers in the three data taking years, as well as their lepton p_T thresholds.

In addition, several minor backgrounds are included, a summary of which can be found in Tab. 7.2. Of note here is the Z+jets background, which is simulated at NNLO in QCD using the MiNNLO method in POWHEG v2 [194, 195]. It was found here that the higher-order corrections are relevant to the analysis especially for low values of the invariant dilepton mass $m_{\ell\ell}$. Most processes are normalized to cross sections predicted at higher orders of QCD where available, which can be found in Tab. 7.3.

Signal simulation The signal for the general A/H model described in Sec. 7.1 is generated at LO in QCD using MG5_AMC@NLO with a custom Universal FeynRules Output (UFO) model. The $pp \rightarrow A/H \rightarrow t\bar{t}$ resonance and the A/H-SM interference are simulated separately, and both are again showered with PYTHIA 8. In order to cover the phase space of the A/H model, the signals are generated for all combinations of the following values of the A/H masses and widths:

$$\begin{aligned} m_{A/H} &\in \{365, 400, 500, 600, 800, 1000\} \text{ GeV} \\ \Gamma_{A/H}/m_{A/H} &\in \{2.5, (5), 10, 25\} \% \end{aligned} \quad (7.1)$$

Samples with a width of 5%, indicated by the bracket, were generated only for a mass of 400 GeV, which leads to 38 signal points total. In addition, samples for the pseudoscalar case only were generated with

$$m_A \in \{450, 550, 700, 900\} \text{ GeV}, \quad \Gamma_A/m_A = 9 \%. \quad (7.2)$$

All of these samples were combined and reweighted at matrix element level to obtain phase space points between these mass and width values, as described further

Process	QCD order	ME Generator
$t\bar{t}$	NLO	POWHEG v2 (hvq)
tW	NLO	POWHEG v2 (ST_wtch)
$Z/\gamma^* + \text{jets}$	NNLO	POWHEG v2 (Zj MiNNLO)
t -channel single top	NLO	POWHEG v2 (ST_tch) + MADSPIN
s -channel single top	NLO	MG5_AMC@NLO
$t\bar{t}W$	NLO	MG5_AMC@NLO
$t\bar{t}Z$	NLO	MG5_AMC@NLO
WW, WZ & ZZ	LO	PYTHIA 8.2
A/H signal	LO	MG5_AMC@NLO
η_t signal	LO	MG5_AMC@NLO

Table 7.2: **Simulated background and signal samples.** An overview of the different background and signal processes considered, as well as the theoretical order in QCD and the ME generator used to simulate them. For all samples, PYTHIA 8.2 is used for showering and hadronization.

Process	Cross section (pb)	Order	Program / reference
$t\bar{t}$	833.9	NNLO+NNLL	Top++
tW	71.7	NNLO (approx.)	[140]
t -channel single top	217.0	NLO	Hathor [196, 197]
s -channel single top	10.3	NLO	Hathor [196, 197]
$t\bar{t}W$	0.64	NLO	MG5_AMC@NLO
$t\bar{t}Z$	0.75	NLO	MG5_AMC@NLO
$Z/\gamma^* + \text{jets} \rightarrow \ell\ell, m_{\ell\ell} > 10 \text{ GeV}$	24.7×10^3	NNLO	FEWZ [198, 199]
WW	118.7	NNLO	[200]
WZ	471.3	NLO	MCFM [201]
ZZ	165.2	NLO	MCFM [201]

Table 7.3: **Cross sections for background processes.** The cross sections used for the normalization of background processes, as well as the orders in QCD at which they were computed. Where applicable, cross sections are given as the sum of the process and its charge conjugate.

2310 in Sec. 7.4.

2311 Furthermore, signal samples for possible $t\bar{t}$ bound state effects are generated us-
 2312 ing the color-singlet η_t and χ_t models as defined in Sec. 2.2.3, using custom UFO
 2313 models implemented in MG5_AMC@NLO and again showered with PYTHIA. The
 2314 branching ratio of $W \rightarrow \ell\nu$ is taken to be 11.1%, corresponding to the default value
 2315 used by MG5_AMC@NLO.

2316 For all signal and background samples, the detector response is simulated with
 2317 GEANT 4 and the full CMS simulation and reconstruction chain as described in
 2318 Sec. 3.6 is performed.

2319 7.2.2 Object definition

2320 **Leptons** All electrons and muons are required to have $p_T > 20\text{ GeV}$ and $|\eta| < 2.4$.
 2321 Similar to Sec. 5.2.2, electrons in the transition region between barrel and endcaps
 2322 in the ECAL, corresponding to $1.44 < |\eta_{\text{SC}}| < 1.57$, are removed, and additional ID
 2323 criteria are applied for both types of leptons.

2324 For electrons, the multivariate classifier (MVA)-based ID described in Ref. [113] is
 2325 used at a working point giving 90 % background rejection. This ID already includes
 2326 an isolation requirement as part of the MVA training, and no further requirement
 2327 is applied.

2328 For muons, the same cut-based ID from Ref. [141] as in Sec. 5.2.2, also at the tight
 2329 working point, is used, and the same I_{rel} requirement using a cone size of $\Delta R < 0.4$
 2330 is applied in addition.

2331 **Jets** Jets are again reconstructed using the anti- k_T algorithm [124] with a distance
 2332 parameter of 0.4. They are required to fulfill $p_T > 20\text{ GeV}$, $|\eta| < 2.4$, and have a
 2333 minimum distance of $\Delta R > 0.4$ from all leptons passing the above criteria in the
 2334 event. The Charged Hadron Subtraction (CHS) method [122] is used to remove
 2335 hadrons that originate from pileup from the jet clustering.

2336 Additional ID criteria are applied to reject jets originating in detector noise and
 2337 reconstruction failures [99]. They consist of requirements on the multiplicities of
 2338 the different jet constituents (charged hadrons, neutral hadrons, and electrons or
 2339 photons) as well as their energy fractions relative to the total jet energy. The
 2340 required values are centrally provided depend on the jet $|\eta|$ as well as on the analysis
 2341 era. In total, a genuine jet efficiency of about 99 % is achieved, while about 99.9 %
 2342 of noise jets are rejected in the relevant $|\eta|$ range [99].

2343 The DEEPJET algorithm [125], same as in Sec. 5.2.2, is used to identify jets
 2344 originating from the showering and hadronization of b quarks. The medium working
 2345 point of DEEPJET in CMS is chosen, which has a b jet identification efficiency of
 2346 77 %, as well as a misidentification rate of 15 % for c quark jets and of 2 % for light
 2347 quark and gluon jets [142].

Missing transverse momentum In the dileptonic decay of $t\bar{t}$, the two neutrinos cannot be measured experimentally, and escape the detector unseen. However, their presence can be inferred from momentum conservation: In a proton-proton collision, the longitudinal component of the incoming partons in the hard scattering process is unknown, while the transverse component can be assumed to be close to zero. Thus, the missing transverse momentum \vec{p}_T^{miss} can be inferred as the negative vectorial sum of all reconstructed objects (jets, leptons and photons) [126]. As with the jets, hadrons likely to originate from pileup are removed from the calculation of \vec{p}_T^{miss} using the CHS method [122]. Along with the leptons and jets, \vec{p}_T^{miss} will be used to reconstruct the $t\bar{t}$ system.

7.2.3 Event selection

Events are selected with exactly two leptons of opposite electric charge and sorted into three channels (ee , $e\mu$ and $\mu\mu$) by lepton flavor, similar to Sec. 5.2.3. The two leptons need to fulfill $p_T > 25 \text{ GeV}$ and $p_T > 20 \text{ GeV}$ for the leading and subleading lepton, respectively, and their invariant mass is required to be $m_{\ell\ell} > 20 \text{ GeV}$ in order to reject background from $\gamma^* + \text{jets}$ production and low-mass resonances.

In all channels, at least two jets with $p_T > 30 \text{ GeV}$ are required, of which at least one needs to be b-tagged. Furthermore, in the same-flavor lepton channels (ee and $\mu\mu$), additional cuts are applied to reject $Z + \text{jets}$ background: Events with $|m_{\ell\ell} - m_Z| < 15 \text{ GeV}$, i.e. close to the Z boson mass peak, are discarded (again just as in Sec. 5.2.3), and the magnitude of the missing transverse momentum is required to be $\vec{p}_T^{\text{miss}} > 40 \text{ GeV}$.

The effect of all selection cuts is summarized in Tab. 7.4.

7.2.4 Experimental corrections

Similar as in Sec. 5.3, several corrections are applied to the MC simulation in order to achieve good agreement with the data. In contrast to the $t\bar{t}$ cross section measurement, where most of these corrections were derived as part of this work, many of the experimental corrections used in this chapter were provided centrally by the CMS collaboration. These will only be described very briefly; more details can be found in the associated references.

Trigger scale factors The selection efficiency of the triggers from Tab. 7.1 needs to be corrected in simulation to the one measured in data. This is done via scale factors, which were centrally derived by CMS as a function of the p_T of the two leptons using the so-called cross-trigger method: Events are selected using a different set of triggers - here, a combination of jet and \vec{p}_T^{miss} triggers - which is assumed to be fully orthogonal to the lepton triggers used for the main selection. Thus, the event sample is unbiased with respect to the lepton triggers, and the lepton trigger

Cut	Data yield/ 10^3			$t\bar{t} \rightarrow \ell\ell$ MC	
	ee	e μ	$\mu\mu$	efficiency (%)	purity (%)
Triggers	3504932			64.4	0.4
Two OC leptons	65589	2240	108363	20.6	1.4
Lepton p_T	65189	2169	106112	20.3	1.4
$m_{\ell\ell} > 20$ GeV	64746	2081	103276	19.8	1.4
Z window (ee/ $\mu\mu$)	5795	2081	9367	17.6	12.7
At least 2 jets	1235	1287	1947	15.4	43.2
Jet p_T	644	999	985	12.9	59.2
At least one b tag	319	853	489	11.7	84.6
p_T^{miss} (ee/ $\mu\mu$)	234	853	354	10.7	88.9

Table 7.4: **Selection cuts and event yields.** The data yield in all analysis eras after successively applying all selection cuts, separately for the three lepton flavor channels. The second-to-last column shows the selection efficiency of $t\bar{t} \rightarrow \ell\ell$ events ($\ell = e, \mu, \tau$), and the last column shows the purity, defined as the fraction of $t\bar{t} \rightarrow \ell\ell$ events and total event yield. Both efficiency and purity are evaluated using simulation.

efficiency can be measured as the fraction of the events who pass the lepton triggers in addition to the jet/ p_T^{miss} triggers. This is done independently for all data taking years. The resulting scale factor can differ from unity by up to 5 % for leptons with $p_T \approx 20$ GeV and less then 1 % for higher p_T values.

Lepton scale factors Differences in the efficiency for a lepton to pass the identification and isolation criteria as defined in Sec. 7.2.2 are measured using the tag-and-probe method, as in Sec. 5.3, and applied to simulation using scale factors binned in p_T and $|\eta|$ of the lepton. The scale factor typically differs from unity by about 1-5 %, with the magnitude increasing for high $|\eta|$. For more details on this method see Refs. [113, 141].

Pileup reweighting In contrast to the data-driven reweighting method used for the inclusive $t\bar{t}$ cross section measurement (Sec. 5.3), the mean number of pileup interactions per bunch crossing in simulation is reweighted to year-dependent distributions provided centrally by CMS. These have been derived from measurements of the instantaneous luminosity combined with a total inelastic proton-proton cross section of $69.2(32)$ mb at $\sqrt{s} = 13$ TeV [100].

Jet energy and p_T^{miss} corrections The difference in the jet energy response of the detector (JES) as well as the jet energy resolution (JER) in data and simulation was corrected in the same way as described in Sec. 5.3, using centrally derived jet

energy corrections (JECs) as described in Ref. [143]. These corrections are further propagated to the calculation of \vec{p}_T^{miss} [126]. Possible additional corrections to the x and y components of \vec{p}_T^{miss} were investigated, but found to not be required for good description of the observables considered in this analysis.

b-tagging scale factors The identification efficiency of the DEEPJET b-tagging algorithm was calibrated using events with jets containing a muon, likely originating from the semileptonic decay of a B hadron, following the methodology described in Ref. [142]. Note that the calibration done on dileptonic $t\bar{t}$ events presented in the same reference is not used as an input here, since it was derived in part on the same data set and would thus lead to double-counting. However, similar to the discussion in Sec. 5.6, it is expected that the b-tagging efficiency will be constrained from the data during the likelihood fit.

ECAL L1 pre-firing In the 2016 and 2017 data-taking years, the L1 trigger of the electromagnetic calorimeter was affected by a gradual shift in the timing of the inputs in the forward region ($|\eta| > 2.0$) [119]. This effect, called L1 pre-firing, is corrected for using simulation scale factors computed from data.

Z+jets background normalization In the same-flavor lepton channels (ee and $\mu\mu$), Z+jets events constitute a minor but important background. Since this analysis is sensitive to small shape effects, it is necessary to precisely model this background both in shape and normalization. An NNLO Monte Carlo simulation (see Tab. 7.2) is used for this purpose, which generates up to two additional partons (including b quarks) in the final state, as required by the event selection of at least two jets and at least one b tag. Still, in order to be certain of the Z+jets rate, the same data-driven estimation as presented in Sec. 5.3.2, using a control region with $|m_{\ell\ell} - m_Z| < 15 \text{ GeV}$ and a sideband with zero b-tagged jets, is performed. The resulting ratios of Z+jets yields compared to the prediction of the original simulation can be found in Tab. 7.5.

	2016pre	2016post	2017	2018
ee	0.96 ± 0.010	0.97 ± 0.008	0.87 ± 0.006	0.88 ± 0.005
$e\mu$	0.96 ± 0.007	0.97 ± 0.005	0.88 ± 0.004	0.89 ± 0.003
$\mu\mu$	0.96 ± 0.009	0.97 ± 0.006	0.90 ± 0.005	0.90 ± 0.004

Table 7.5: Z+jets scale factors. Ratio of the Z+jets event yields estimated in data using the method described in Sec. 5.3.2 to the prediction by the MC simulation for the four data-taking periods. The results in the $e\mu$ channel are the geometric means of those in the ee and $\mu\mu$ channels. Uncertainties are statistical only.

2430 7.2.5 Reconstruction of the $t\bar{t}$ system

2431 Having identified the relevant objects - leptons, jets and \vec{p}_T^{miss} - in an event, the next
2432 step consists of reconstructing the $t\bar{t}$ system, i.e. the four-momenta of the top and
2433 antitop quark. The presence of two neutrinos in dileptonic $t\bar{t}$ decays, which escape
2434 detection except through missing transverse momentum, leads to a significant loss
2435 of information. As a result, reconstructing the full event kinematics is non-trivial
2436 and requires several assumptions. In this work, a variation of the algorithm first
2437 presented in Ref. [202] is used, which is briefly outlined in this section.

2438 The algorithm works in two steps, starting with the assignment of jets to the b
2439 and \bar{b} quarks originating from the $t\bar{t}$ decay. To do so, pairs of jets are selected from
2440 all jets in the event (passing the requirements outlined in Sec. 7.2.2) depending on
2441 the number n_b of b-tagged jets: For events with $n_b \geq 2$, all permutations of two
2442 b-tagged jets each are considered as candidate pairs, while for events with $n_b = 1$,
2443 the candidate pairs are formed by pairing the single b-tagged jet with all other jets
2444 in the event.

2445 From these candidates, the best pair is now chosen based on the invariant masses
2446 $m_{\ell+b}$ and $m_{\ell-\bar{b}}$ of the b/ \bar{b} candidate and the corresponding (anti)lepton. First, the
2447 expected truth-level distribution of $m_{\ell b}$ is determined from MC simulation, which
2448 can be seen in Fig. 7.1. Then, in each event, the likelihoods to observe the respective
2449 values of $m_{\ell+b}$ and $m_{\ell-\bar{b}}$ for each candidate pair are computed from the expected
2450 distribution. The candidate pair that maximizes the product of the two likelihoods
2451 for $m_{\ell+b}$ and $m_{\ell-\bar{b}}$ is chosen for the remainder of the reconstruction.

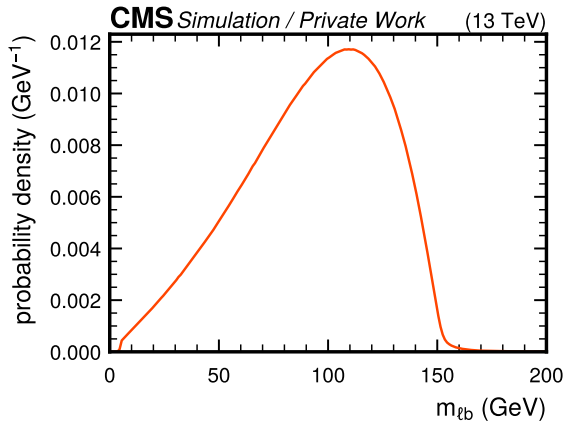


Figure 7.1: **Probability distribution of $m_{\ell b}$.** The truth-level probability distribution of $m_{\ell b}$, as calculated from $t\bar{t}$ MC simulation and used for assigning the b/ \bar{b} candidates as well as for the weighted average over the smeared solutions. *Figure reproduced from Ref. [192].*

2452 Next, the four-momenta of the top and antitop quark are reconstructed using the

2453 momentum conservation equations. That is, one demands

$$\begin{aligned} p_t &= p_{W^+} + p_b = p_{\ell^+} + p_{\nu_\ell} + p_b \\ p_{\bar{t}} &= p_{W^-} + p_{\bar{b}} = p_{\ell^-} + p_{\bar{\nu}_\ell} + p_{\bar{b}} \end{aligned} \quad (7.3)$$

2454 where all variables are understood as four-momenta. The lepton and b-quark
 2455 momenta are experimentally measured, while the neutrino momenta are unknowns.
 2456 Demanding them to be massless, i.e. $p_{\nu_\ell}^2 = p_{\bar{\nu}_\ell}^2 = 0$, yields the six components of the
 2457 two neutrino three-momenta as free parameters.

2458 To resolve the ambiguities, several assumptions need to be made. First, it is
 2459 assumed that all of the missing transverse momentum in the event stems from the
 2460 neutrinos, i.e.

$$p_{\nu_\ell,x} + p_{\bar{\nu}_\ell,x} = p_x^{\text{miss}}, \quad p_{\nu_\ell,y} + p_{\bar{\nu}_\ell,y} = p_y^{\text{miss}} \quad (7.4)$$

2461 Additionally, it is assumed that both the top quarks and W bosons are exactly
 2462 on-shell, that is

$$p_{W^+}^2 = m_W^2, \quad p_{W^-}^2 = m_W^2 \quad (7.5)$$

2463 and

$$p_t^2 = m_t^2, \quad p_{\bar{t}}^2 = m_t^2 \quad (7.6)$$

2464 where m_t and m_W are the pole masses of the top quark and W boson, respectively.
 2465 Applying these six constraints leads to a system of quartic equations for the neutrino
 2466 three-momenta \vec{p}_{ν_ℓ} and $\vec{p}_{\bar{\nu}_\ell}$, which was solved in Ref. [203]. From these, the top and
 2467 antitop quark four-momenta can then be calculated. Since the quartic equation
 2468 can in general have up to four solutions, the solution with the lowest value of the
 2469 invariant $t\bar{t}$ mass $m_{t\bar{t}}$ is chosen. This was found in Ref. [204] to minimize the bias
 2470 in $m_{t\bar{t}}$ especially for low- $m_{t\bar{t}}$ events.

2471 In practice, however, this method will often not give a solution even for those b
 2472 jets which are correctly assigned to the truth-level b quarks. This is because the
 2473 experimental inputs to the method - the jet and lepton four-momenta as well as
 2474 \vec{p}_T^{miss} - will deviate from their truth-level values within the experimental resolution
 2475 of the detectors and object reconstruction. In addition, the constraints will not
 2476 be fulfilled exactly: There might be additional p_T^{miss} in the event because of e.g.
 2477 neutrinos produced in τ lepton or B hadron decays, and the W bosons and top
 2478 quarks might be off-shell with respect to their pole masses within their respective
 2479 widths.

2480 To alleviate this, several of the input variables are randomly smeared to model
 2481 the experimental resolution. For both the b jets and leptons, the energies are varied
 2482 while keeping their masses constant, and the directions of their three-momenta are

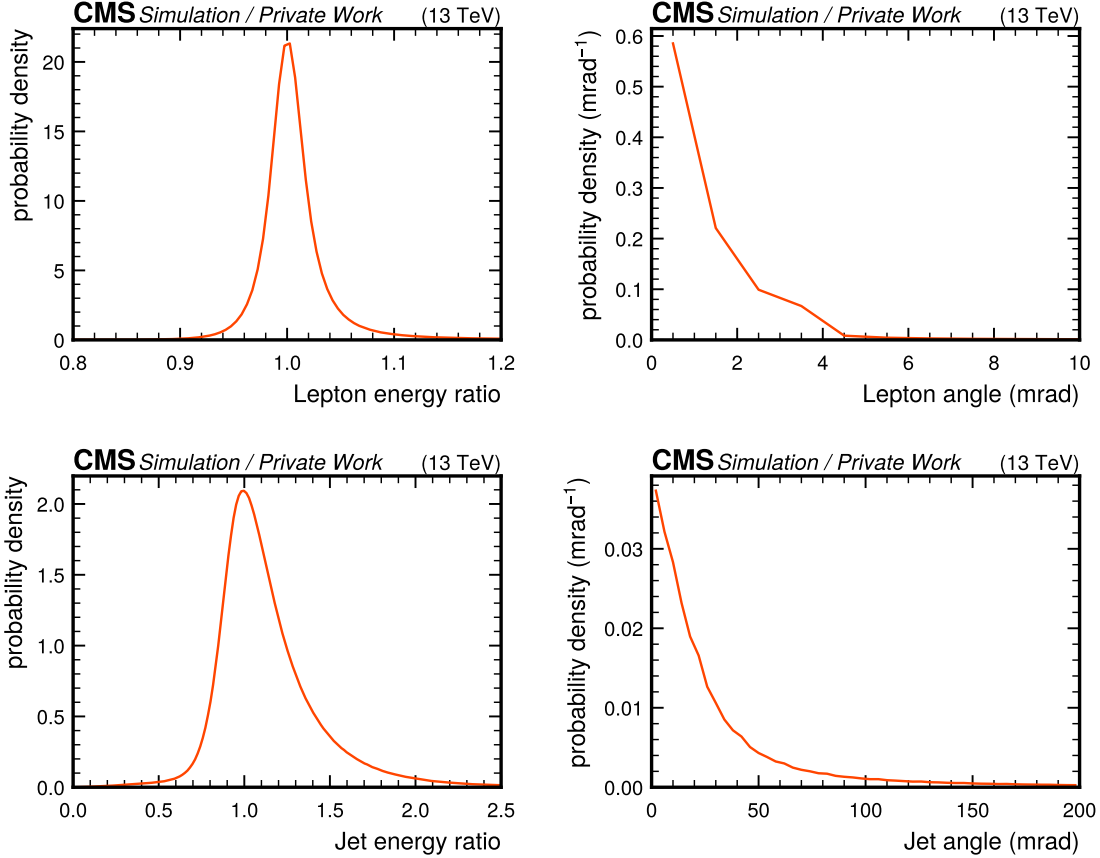


Figure 7.2: **Probability distributions used in the smearing of jets and leptons.** The probability distributions for the ratio of measured and truth-level energies (left) as well as the angular difference between measured and truth-level three-momenta (right) for leptons (top) and jets (bottom). All distributions were calculated using $t\bar{t}$ MC simulation. *Figure reproduced from Ref. [192].*

varied in a uniformly random direction. For both of these cases, the variations are randomly sampled from distributions obtained by comparing the measured and truth-level four-momentum in the nominal $t\bar{t}$ MC simulation, as shown in Fig. 7.2. The smearing of the jets is also propagated to the calculation of $\vec{p}_{T\text{miss}}$. Additionally, the values of m_W used for the constraints on p_{W+} and p_{W-} are randomly sampled from a relativistic Breit-Wigner distribution corresponding to the W boson width Γ_W . This smearing procedure is repeated 100 times per event with different random values, resulting in up to 100 reconstructed $t\bar{t}$ systems per event, depending on the number of cases where there is no real solution.

Finally, one unambiguous solution per event is constructed by again using the

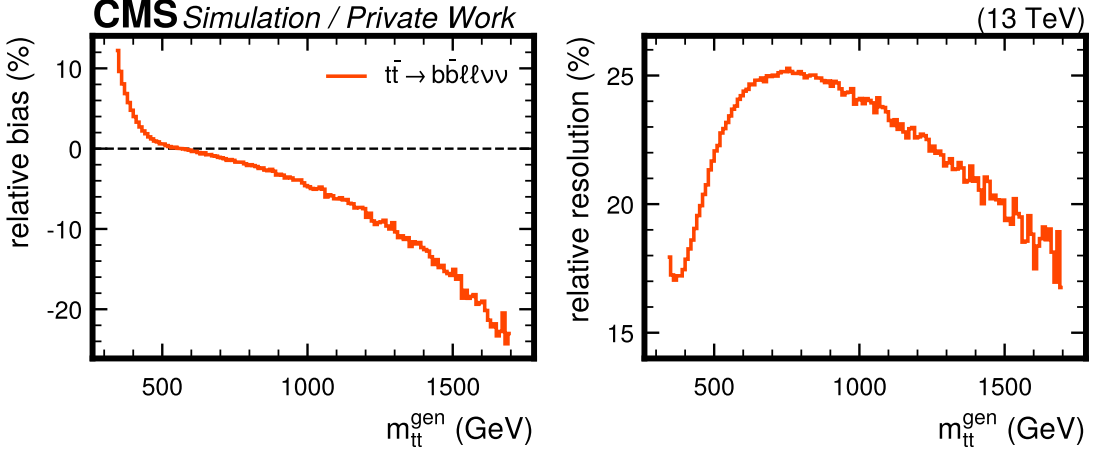


Figure 7.3: **Bias and resolution of $m_{t\bar{t}}$.** Relative bias and resolution of the $t\bar{t}$ reconstruction algorithm, defined in Eq. (7.8), as a function of truth-level $m_{t\bar{t}}$ and evaluated in MC simulation of dileptonic $t\bar{t}$.

invariant lepton-b quark masses and their truth-level likelihoods. For each iteration of the smearing procedure that yielded a real solution, a weight is defined as the product of the likelihoods for obtaining the smeared values of $m_{\ell+b}$ and $m_{\ell-\bar{b}}$, i.e.

$$w = \mathcal{P}(m_{\ell+b}) \cdot \mathcal{P}(m_{\ell-\bar{b}}) \quad (7.7)$$

The final solution for the reconstructed top and antitop four-momenta is defined as the weighted average over all real solutions, using the weight as given in Eq. (7.7).

For $t\bar{t} \rightarrow b\bar{b}\ell\ell\nu\nu$ events passing all previous selection steps, the efficiency of the full reconstruction algorithm is ca. 90%, as evaluated in MC simulation. To assess the accuracy of the reconstruction relative to the truth-level top quarks, defined after parton showering, a per-event relative deviation is defined as

$$\Delta m_{t\bar{t}} = \frac{m_{t\bar{t}}^{\text{reco}} - m_{t\bar{t}}^{\text{gen}}}{m_{t\bar{t}}^{\text{gen}}}, \quad (7.8)$$

where $m_{t\bar{t}}^{\text{reco}}$ and $m_{t\bar{t}}^{\text{gen}}$ stand for the reconstructed and truth-level $m_{t\bar{t}}$, respectively. The mean and standard deviation of $\Delta m_{t\bar{t}}$ are then the relative bias and resolution of the reconstruction algorithm. They are evaluated in simulation of dileptonic $t\bar{t}$ and shown in Fig. 7.3 as a function of truth-level $m_{t\bar{t}}$. The method shows a bias towards high $m_{t\bar{t}}$ for events with $m_{t\bar{t}}^{\text{gen}} \lesssim 500$ GeV and towards low $m_{t\bar{t}}$ for $m_{t\bar{t}}^{\text{gen}} \gtrsim 600$ GeV, with resolutions in the range of 17 – 25%. It should be noted here that this bias relative to the truth level is by itself not problematic, since it is expected to be the same in both simulation and data and e.g. no unfolding of the reconstructed distributions to the truth level is attempted.

2511 7.2.6 Sensitive observables

2512 To distinguish the A/H and η_t signals from the background, three sensitive ob-
2513 servables are considered. The first is the invariant $t\bar{t}$ mass $m_{t\bar{t}}$, defined with the
2514 reconstruction procedure as explained in the last section. As shown in Fig. 2.7,
2515 an A/H signal is expected to result in a peak-dip structure in $m_{t\bar{t}}$, where the zero
2516 crossing between peak and dip should be in the vicinity of the A/H mass. The mag-
2517 nitude as well as ratio of the peak and the dip depend non-linearly on the coupling
2518 modifier. The η_t signal, on the other hand, is expected to peak slightly below the
2519 $t\bar{t}$ production threshold at $m_{t\bar{t}} \simeq 2m_t - 2$ GeV as discussed in Sec. 2.2.3 and shown
2520 in Fig. 2.5. In practice, due to the limited detector resolution, the exact position of
2521 this peak will not be observable, and the signal will result in a generic enhancement
2522 of the yield for very low values of $m_{t\bar{t}}$.

2523 In addition, the two spin correlation observables c_{hel} and c_{han} , as defined in
2524 Eq. (2.4) and Eq. (2.10), are used to gain further sensitivity. Both variables are
2525 again defined using the $t\bar{t}$ system reconstruction as described in the previous sec-
2526 tion. As discussed in Sec. 2.2.2, they are ideal for separating spin-singlet and spin-
2527 triplet states, respectively. Thus, A and η_t signals, producing singlet states, will
2528 have enhanced contributions at high values of c_{hel} , while H signals, producing 3P_0
2529 triplet states, will be enhanced at low values of c_{han} . This allows not only for better
2530 discrimination between signal and background, but also to probe the \mathcal{CP} structure
2531 of a possible observed signal.

2532 To combine all three variables, three-dimensional templates are created with $20 \times$
2533 3×3 bins in the three observables $m_{t\bar{t}}$, c_{hel} and c_{han} . For $m_{t\bar{t}}$, an irregular binning
2534 is chosen to account for the decrease in production cross section at high values. An
2535 example can be seen in Fig. 7.4 for SM $t\bar{t}$ and three different signals (A, H and η_t).

2536 7.3 Higher-order corrections in $t\bar{t}$

2537 In this analysis, the SM $t\bar{t}$ background is irreducible - after all, it leads to the exact
2538 same final state as the signal. As a result, it is crucial to model it as precisely as
2539 possible: a mismodeling of the $t\bar{t}$ kinematic distribution, especially in $m_{t\bar{t}}$, might
2540 otherwise be confused for a signal and lead to bias.

2541 The MC simulation used for the SM $t\bar{t}$ background is performed at NLO in QCD
2542 using the POWHEG v2 subprocess `hvq`, as studied also in Chapter 6. On top of
2543 this, two different sets of corrections are applied to include missing higher orders,
2544 namely NNLO QCD and NLO electroweak (EW) corrections. Both of these are
2545 estimated by comparing the MC simulation, which is matched to a parton shower,
2546 to fixed-order predictions. The simulation is then reweighted using scale factors
2547 binned two-dimensionally in $m_{t\bar{t}}$ and $\cos\theta_t^*$, where the latter is the cosine of the
2548 scattering angle of the top quark to the beam axis in the $t\bar{t}$ rest frame. These two

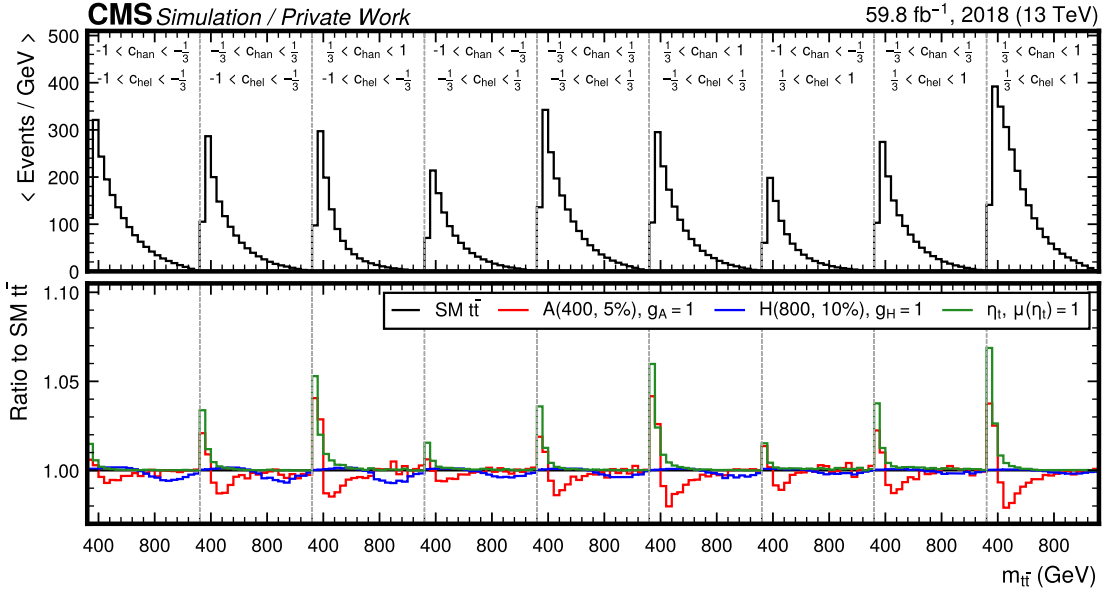


Figure 7.4: **3D template for $m_{t\bar{t}} \times c_{\text{hel}} \times c_{\text{han}}$** for SM $t\bar{t}$ (top) as well as three different example signals (bottom, shown as the ratio to SM $t\bar{t}$), corresponding to the luminosity taken in 2018 only.

variables fully define the kinematics of the top quarks in the $t\bar{t}$ rest frame, save for FSR emissions.

7.3.1 NNLO QCD corrections

The NNLO QCD predictions are obtained with the program MATRIX [139]. They are computed at the level of stable top quarks with a dynamic scale choice of

$$\mu_R = \mu_F = \frac{1}{2} \left(\sqrt{mt^2 + p_{T,t}^2} + \sqrt{m_{\bar{t}}^2 + p_{T,\bar{t}}^2} \right), \quad (7.9)$$

where $p_{T,t}$ and $p_{T,\bar{t}}$ are the transverse momenta of the top and antitop. Fig. 7.5 shows the resulting effect on the 3D $m_{t\bar{t}} \times c_{\text{hel}} \times c_{\text{han}}$ distribution at the detector level as the black line. They are on the order of 1 – 2%.

7.3.2 NLO EW corrections

The NLO corrections in the electroweak coupling α_{EW} are computed with the HATHOR code [196, 205–207] using a dynamic scale choice of $\mu_R = \mu_F = \frac{1}{2}m_{t\bar{t}}$. Of particular interest here is a class of diagrams which contain an exchange of a virtual SM Higgs boson, an example of which is seen in Fig. 7.6. The matrix element

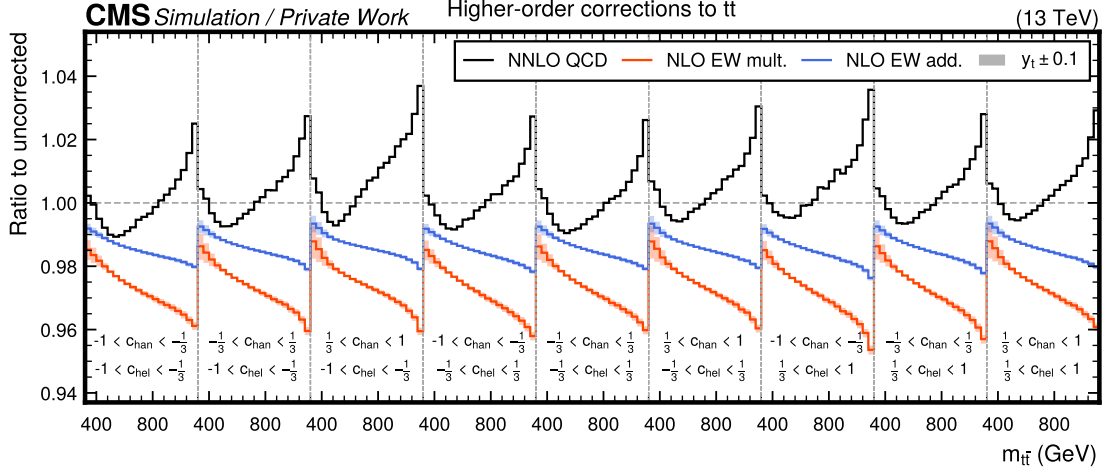


Figure 7.5: **Effect of NNLO QCD and NLO EW corrections** on the 3D $m_{t\bar{t}} \times c_{hel} \times c_{han}$ distribution after reconstruction in the form of ratios to the uncorrected distributions. The NNLO QCD corrections are shown as the solid black line, while the NLO EW corrections are shown in orange for the multiplicative scheme and in blue for the additive scheme. The effect of varying y_t by ± 0.1 in the NLO EW corrections is shown as the shaded bands.

for this diagram is proportional to the square of the SM Higgs-top Yukawa coupling y_t , giving a y_t^2 -dependent correction to $t\bar{t}$ distributions from the interference with LO diagrams. This correction is sizable mostly for low $m_{t\bar{t}}$ values, and is important for this analysis because the SM Higgs exchange might change the $t\bar{t}$ spin state and thus c_{hel} and c_{han} . To accurately account for this, the correction is derived separately for the different initial states (gg , $q\bar{q}$ and gq) of $t\bar{t}$ production.

The results obtained with HATHOR are accurate only to LO in α_S , i.e. $\mathcal{O}(\alpha_S^2)$, and as of the time of writing no full calculation including both NLO QCD and EW effects exists. Thus, there is an ambiguity on how the NLO-accurate (in QCD) MC simulation and the NNLO-accurate corrections presented in the previous section should be combined with the EW corrections.

Formally, the differential cross section as predicted by Powheg can be decomposed as

$$d\sigma_{\text{POWHEG}} = \alpha_S^2 d\sigma_{\text{LO}} + \alpha_S^3 d\sigma_{\text{NLO}} \quad (7.10)$$

where additional terms beyond $\mathcal{O}(\alpha_S^3)$ due to additional radiation in Powheg and Pythia are not written for simplicity. On the other hand, HATHOR predicts

$$d\sigma_{\text{HATHOR}} = \alpha_S^2 d\sigma_{\text{LO}} + \alpha_S^2 \alpha_{\text{EW}} d\sigma_{\text{EW}}. \quad (7.11)$$

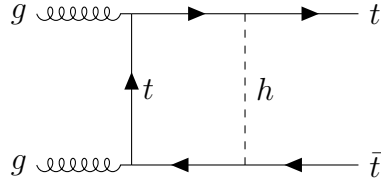


Figure 7.6: **EW correction involving a SM Higgs boson.** An example Feynman diagram for NLO EW corrections to $t\bar{t}$ production involving the exchange of a virtual SM Higgs boson h .

2577 One possible way to combine the calculations is the additive scheme, given by

$$\begin{aligned} d\sigma_{\text{add.}} &= d\sigma_{\text{POWHEG}} + d\sigma_{\text{HATHOR}} - \alpha_S^2 d\sigma_{\text{LO}} \\ &= \alpha_S^2 d\sigma_{\text{LO}} + \alpha_S^3 d\sigma_{\text{NLO}} + \alpha_S^2 \alpha_{\text{EW}} d\sigma_{\text{EW}} \end{aligned} \quad (7.12)$$

2578 which is formally accurate to $\mathcal{O}(\alpha_S^3)$ and $\mathcal{O}(\alpha_S^2 \alpha_{\text{EW}})$. This approach does not include
2579 any cross terms of order $\mathcal{O}(\alpha_S^3 \alpha_{\text{EW}})$, which are not fully calculated by either Powheg
2580 or HATHOR. However, it is reasonable to assume that these cross terms factorize
2581 approximately, leading to the alternative multiplicative scheme [207]

$$\begin{aligned} d\sigma_{\text{mult.}} &= d\sigma_{\text{POWHEG}} \times \frac{d\sigma_{\text{HATHOR}}}{\alpha_S^2 d\sigma_{\text{LO}}} \\ &= \alpha_S^2 d\sigma_{\text{LO}} + \alpha_S^3 d\sigma_{\text{NLO}} + \alpha_S^2 \alpha_{\text{EW}} d\sigma_{\text{EW}} + \alpha_S^3 \alpha_{\text{EW}} \frac{d\sigma_{\text{NLO}} d\sigma_{\text{EW}}}{d\sigma_{\text{LO}}} \end{aligned} \quad (7.13)$$

2582 The difference between the two schemes is in the last term of order $\mathcal{O}(\alpha_S^3 \alpha_{\text{EW}})$,
2583 which is an approximation to the QCD-EW cross terms. In this work, the multi-
2584 plicative approach is used for all nominal results, while the difference to the additive
2585 approach is included as a systematic uncertainty. In both cases, the needed term
2586 $\alpha_S^2 d\sigma_{\text{LO}}$ is computed with MG5_AMC@NLO.

2587 The effect of both approaches on the 3D $m_{t\bar{t}} \times c_{\text{hel}} \times c_{\text{han}}$ distribution at the
2588 detector level after parton showering can be seen in Fig. 7.5 for different values of
2589 y_t . The multiplicative scheme leads to a larger correction of roughly 2 – 4%, while
2590 the additive scheme only gives 1 – 2%. Notably, the effect of varying y_t modifies not
2591 only the $m_{t\bar{t}}$ distribution close to the $t\bar{t}$ threshold, but also the distribution of c_{hel} .
2592 As a result, such a variation in data could potentially be confused for a pseudoscalar
2593 signal. It is thus important to include it as a systematic uncertainty, as described
2594 in Sec. 7.5.

2595 7.4 Matrix element reweighting for A/H signals

2596 In order to probe the full phase space of the generic A/H model as described in
 2597 Sec. 7.1, predictions at different A/H masses and widths with a sufficiently small
 2598 spacing are required so that interpolation between the points is possible. However,
 2599 generating a separate MC sample for each mass and width point is computationally
 2600 very expensive.

2601 7.4.1 Principle of the method

2602 As an alternative, it is possible to re-use existing samples for different mass and
 2603 width points via matrix element reweighting. This method works by noting that a
 2604 given MC sample can be seen as a random sample, drawn from a PDF of the form

$$\mathcal{P}(x_i^{\text{ME}}, x_j^{\text{reco}}) = \mathcal{P}^{\text{ME}}(x_i^{\text{ME}}) \cdot \mathcal{P}^{\text{rem}}(x_j^{\text{reco}} | x_i^{\text{ME}}) \quad (7.14)$$

2605 Here, x_i^{ME} are all variables defining the event at the matrix element (ME) level,
 2606 i.e. at the level of the hard interaction, and x_j^{reco} are all variables after detector
 2607 simulation and object reconstruction. For the case of the A/H signals, which are
 2608 generated at LO in QCD, x_i^{ME} is given by the four-momenta and helicities of the
 2609 final-state particles (leptons, neutrinos and b quarks) in the hard process. The x_j^{reco}
 2610 consist of all possible reconstruction-level variables that are relevant to the analysis,
 2611 such as e.g. jet and lepton four-momenta, lepton identification criteria or $\vec{p}_{\text{T}}^{\text{miss}}$.

2612 $\mathcal{P}^{\text{ME}}(x_i^{\text{ME}})$ refers to the probability density of the ME-level variables as predicted
 2613 by the ME generator, which will be proportional to the absolute square of the matrix
 2614 element. This function will depend on the chosen scenario of the A/H model, i.e.
 2615 $m_{\text{A}/\text{H}}$ and $\Gamma_{\text{A}/\text{H}}$. Meanwhile, the conditional probability density $\mathcal{P}^{\text{rem}}(x_j^{\text{reco}} | x_i^{\text{ME}})$
 2616 encodes the effects of all other components of the simulation chain, such as the
 2617 parton shower, hadronization, detector simulation and reconstruction. It gives the
 2618 probability to observe reconstruction-level variables x_j^{reco} for an event with ME-level
 2619 variables x_i^{ME} .

2620 The principal assumption of the method is now that \mathcal{P}^{rem} , and thus the whole
 2621 simulation chain except for the matrix element, is independent of the underlying
 2622 A/H signal scenario ($m_{\text{A}/\text{H}}$ and $\Gamma_{\text{A}/\text{H}}$). This assumption is certainly true for the
 2623 detector simulation and reconstruction, while care must be taken for the parton
 2624 shower, which in general needs to be matched to the matrix element and can this
 2625 way have a residual dependence. The validity of the assumption will be discussed
 2626 in more detail below.

2627 If the assumption is fulfilled, a given A/H MC sample generated with parameters
 2628 $m_{\text{A}/\text{H}}^0$ and $\Gamma_{\text{A}/\text{H}}^0$ can now be reweighted to a different A/H scenario with parameters
 2629 $\hat{m}_{\text{A}/\text{H}}$ and $\hat{\Gamma}_{\text{A}/\text{H}}$ by applying to each event i a weight

$$w_i = \frac{\mathcal{P}^{\text{ME}}(x_i^{\text{ME}} | \hat{m}_{\text{A}/\text{H}}, \hat{\Gamma}_{\text{A}/\text{H}})}{\mathcal{P}^{\text{ME}}(x_i^{\text{ME}} | m_{\text{A}/\text{H}}^0, \Gamma_{\text{A}/\text{H}}^0)} \quad (7.15)$$

2630 The quantities in the denominator and nominator are the ME-level probability
 2631 densities for each event, evaluated at the original and target A/H parameters, respec-
 2632 tively. When this weight is inserted into Eq. (7.14), the original probability cancels,
 2633 giving the correct probability density for the target scenario $\hat{m}_{\text{A}/\text{H}}$ and $\hat{\Gamma}_{\text{A}/\text{H}}$.

2634 In practice, this method will only work if the MC sample used for the reweighting
 2635 has sufficient phase space overlap with the target A/H scenario, i.e. if the two
 2636 probabilities in Eq. (7.15) are not too different from each other for the majority of
 2637 the events. Otherwise, the weights will become very small in some regions of the
 2638 phase space and very large in others, resulting in poor statistics for the reweighted
 2639 sample.

2640 The method was implemented by directly evaluating the squared matrix elements
 2641 for the different A/H hypotheses, using the standalone reweighting interface pro-
 2642 vided by MG5_AMC@NLO and the same UFO model as for the signal generation.

2643 7.4.2 Combination of multiple origin samples

2644 At the time of this analysis, a set of signal samples for different A/H scenarios
 2645 (as given in Sec. 7.2.1) was already available. These samples were used as origin
 2646 samples for the reweighting. To maximize the statistical power of the method and to
 2647 mitigate problems from poor phase space overlap, subsets of the available samples
 2648 were combined during reweighting and ranked with an average event weight.

2649 In detail, this procedure works as follows: First, a set of several samples j (the
 2650 origin samples) with different parameters $m_{\text{A}/\text{H}}$ and $\Gamma_{\text{A}/\text{H}}$ are all reweighted sepa-
 2651 rately to the same target parameters $\hat{m}_{\text{A}/\text{H}}$ and $\hat{\Gamma}_{\text{A}/\text{H}}$ with per-event weights $w_{i,j}$ as
 2652 given in Eq. (7.15). These need to be multiplied with a possible generator weight
 2653 of the origin sample $u_{i,j}$, giving the total per-event weight $\hat{w}_{i,j} = w_{i,j}u_{i,j}$. For fully
 2654 unweighted origin samples, $u_{i,j} = 1$.

2655 Then, the different samples are weighted with a per-sample weight v_j proportional
 2656 to

$$v_j \propto \langle \hat{w}_{i,j} \rangle^{-1} = \frac{\sum_i \hat{w}_{i,j}}{\sum_i \hat{w}_{i,j}^2} \quad (7.16)$$

2657 where the sums run over all the events i in the considered sample j . This expression is
 2658 the inverse of the average ME weight for sample j . It is chosen such that samples with
 2659 large phase space overlap with the target A/H scenario - and thus small ME weights
 2660 $w_{i,j}$ - are assigned a large weight v_j in the combination of samples. Similarly, samples
 2661 with poor phase space overlap, and thus large average ME weights, get assigned
 2662 small weights and contribute less strongly to the combined sample. Finally, the total

2663 combined sample is normalized to the expected cross section for the target scenario,
2664 which is calculated independently. It is shown in App. C.1 that this procedure
2665 minimizes the total statistical error of the combined sample.

2666 In practice, all available masses and parities (A and H) are combined for each tar-
2667 get A/H mass. Resonance and interference contributions are treated separately from
2668 each other. Furthermore, it was found that, for the resonance contribution only,
2669 it is necessary to split the combination of different A/H widths into two halves:
2670 those with $\Gamma_{A/H}/m_{A/H}$ less or greater than 10%. This is due to an interplay of
2671 MG5_AMC@NLO and the PYTHIA shower leading to a dependency on the A/H
2672 width in the matrix element, which is not taken into account in the reweighting. For
2673 $\Gamma_{A/H}/m_{A/H} < 10\%$ (narrow resonance), MG5_AMC@NLO includes the interme-
2674 diate A/H particle in the event record, which is then treated by PYTHIA as a unstable
2675 resonance and its virtuality as predicted by the matrix element is preserved. For
2676 $\Gamma_{A/H}/m_{A/H} \geq 10\%$ (broad resonance), the A/H particle is not included in the event
2677 record, and its virtuality is thus not preserved. This leads to slight differences in
2678 distributions affected by the parton showering. The choice of 10% for the transition
2679 between the two modes is an arbitrary parameter, and thus not necessarily physical.
2680 Nonetheless, it was decided in this analysis to not mix the two width ranges in the
2681 reweighting in order to obtain full closure with a standalone generation.

2682 7.4.3 Validation

2683 The combined reweighting is validated for two masses of $m_{A/H} = 400$ and 800 GeV
2684 as well as widths of 2.5 and 10%. For each of these points, the reweighting is
2685 performed as stated above, but leaving out A/H scenarios with the same mass from
2686 the combination of origin samples since otherwise the weights would be trivially
2687 one. The reweighted $m_{t\bar{t}}$ distributions at generator level are then compared to the
2688 standalone samples at the same $m_{A/H}$ and $\Gamma_{A/H}$.

2689 The resulting comparisons and residuals can be seen in Fig. 7.7 for A and H,
2690 separated into the resonance and interference contributions. It can be seen that
2691 the closure between reweighting and standalone generation is excellent within the
2692 statistical uncertainties.

2693 7.5 Systematic uncertainties

2694 Similar to Sec. 5.5, systematic uncertainties affect the distributions of both SM
2695 background and signal processes. They are listed in this section, split into theory
2696 (Sec. 7.5.1) and experimental uncertainties (Sec. 7.5.2).

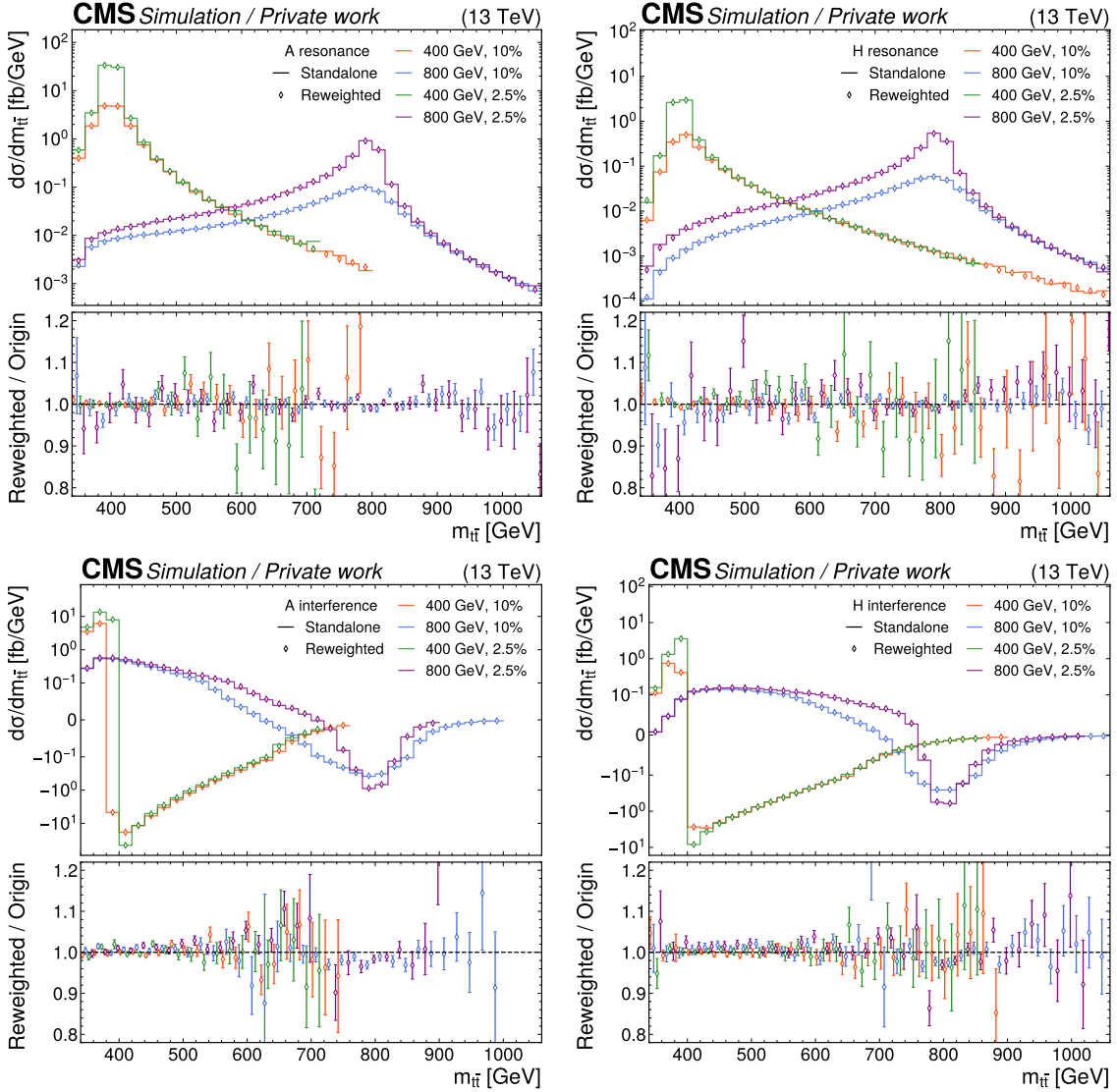


Figure 7.7: Validation of the ME reweighting. Comparison of standalone generated (lines) and reweighted (diamond markers) $m_{t\bar{t}}$ distributions for different values of $m_{A/H}$ and $\Gamma_{A/H}$. From top left to bottom right: A resonance, H resonance, A interference, H interference. The lower panel shows the ratio of reweighted and standalone distributions. The error bars give the combined statistical uncertainty of the reweighted and standalone sample.

²⁶⁹⁷ 7.5.1 Theory uncertainties

²⁶⁹⁸ **Scale uncertainties** Uncertainties due to missing higher orders in the matrix el-
²⁶⁹⁹ ement as well as the parton shower are included separately for the SM $t\bar{t}$, tW , and
²⁷⁰⁰ $Z+jets$ backgrounds as well as all considered signals by varying the associated scales
²⁷⁰¹ by a factor 2 up and down independently, same as in Sec. 5.5. Only the shape
²⁷⁰² components of the ME scales are taken from the respective ME generators, while
²⁷⁰³ the normalization uncertainty is treated externally, as described below. For A and
²⁷⁰⁴ H, the uncertainties are considered uncorrelated between the resonance and inter-
²⁷⁰⁵ ference components, which is found to be conservative. For η_t , the renormalization
²⁷⁰⁶ scale uncertainty is not included since the considered model does not encode any
²⁷⁰⁷ dependence on either μ_R or α_S .

²⁷⁰⁸ **PDF uncertainties** For the SM $t\bar{t}$ background, the uncertainty due to the PDF
²⁷⁰⁹ is again included based on the 100 provided eigenvalues of the NNPDF 3.1 PDF
²⁷¹⁰ set. However, it is not sufficient to simply take the envelope of these variations since
²⁷¹¹ this would capture only the change in $t\bar{t}$ normalization, while this analysis is mostly
²⁷¹² sensitive to shape variations.

²⁷¹³ Instead, a principal component analysis (PCA) is performed on the final 3D
²⁷¹⁴ $m_{t\bar{t}} \times c_{\text{hel}} \times c_{\text{han}}$ templates obtained from the different eigenvalues, thus finding those
²⁷¹⁵ linear combinations that have a noticeable shape effect. Only the first eigenvector
²⁷¹⁶ (corresponding to the largest eigenvalue) is non-negligible, and this variation is con-
²⁷¹⁷ sidered as the PDF uncertainty. For more details on this procedure, see Ref. [192].
²⁷¹⁸ Independently of this, another uncertainty based on the value of α_S in the PDF is
²⁷¹⁹ considered similarly to Sec. 5.5.

²⁷²⁰ **EW correction uncertainties** As described in Sec. 7.3.2, two independent un-
²⁷²¹ certainties are attached to the NLO electroweak correction of SM $t\bar{t}$: First, the
²⁷²² value of the SM top-Higgs Yukawa coupling is allowed to vary in the range $y_t =$
²⁷²³ $1.00^{+0.11}_{-0.11}$, with the range given by the uncertainty of the experimental measurement
²⁷²⁴ in Ref. [208]. Second, the difference between the additive and multiplicative appli-
²⁷²⁵ cation scheme (Eqs. (7.12) and (7.13)) is considered as a separate uncertainty, as
²⁷²⁶ recommended in Ref. [207], and symmetrized around the nominal.

²⁷²⁷ **Top quark mass uncertainty** The top quark mass uncertainty in SM $t\bar{t}$ is es-
²⁷²⁸ timated by varying it from its nominal value of $m_t = 172.5$ GeV by ± 3 GeV in the
²⁷²⁹ POWHEG simulation, and then scaling down the resulting relative deviation by a
²⁷³⁰ factor 1/3, leading to a ± 1 GeV uncertainty. This is done since the variation, ob-
²⁷³¹ tained from an independent MC sample, is otherwise plagued by large statistical
²⁷³² uncertainties. Furthermore, the top mass is also varied in all considered signal sam-
²⁷³³ ples directly by ± 1 GeV through an ME reweighting method similar to Sec. 7.4.
²⁷³⁴ The chosen range of ± 1 GeV is conservative with respect to the most precise top

2735 mass measurements at the time of writing, which have uncertainties on the order of
2736 0.4 GeV [18, 209]. The top mass uncertainties between background and signals are
2737 considered as fully correlated.

2738 **Further uncertainties in SM $t\bar{t}$** Additionally, separate SM $t\bar{t}$ samples are used
2739 to evaluate uncertainties due to ME/PS matching (same as in Sec. 5.5), the under-
2740 lying event tune [94], and the color reconnection model in PYTHIA [98, 210]. All of
2741 these effects are found to be small.

2742 **Background cross section uncertainties** For the SM $t\bar{t}$ background, the shift
2743 in the predicted NNLO+NNLL $t\bar{t}$ cross section due to the ME scale variations as
2744 well as the top quark mass is calculated with Top++ [136] in the same manner as
2745 the nominal cross section. The resulting shifts in the cross section are $^{+20.5}_{-17.9}$ pb for a
2746 variation of μ_F by a factor two up and down, $^{+30.1}_{-9.6}$ pb for a similar variation of μ_R ,
2747 and $^{+22.5}_{-23.5}$ pb for a top mass variation in the range ± 1 GeV. These three variations are
2748 treated as fully correlated with the respective shape uncertainties obtained at NLO
2749 from the POWHEG simulation as described above, so that no additional nuisance
2750 parameter for the $t\bar{t}$ normalization is introduced.

2751 For minor backgrounds, explicit uncertainties of 15% for tW and t-channel single
2752 top [211–213], 30% for diboson and $t\bar{t} + X$ [214, 215], and 5% for the data-driven
2753 Z/γ^* + jets normalization [216] are considered, which are all based on the precision
2754 of relevant cross section measurements.

2755 **Background statistical uncertainties** Again similar to Sec. 5.5, per-bin back-
2756 ground statistical uncertainties for all simulated processes are included following
2757 Ref. [157].

2758 7.5.2 Experimental uncertainties

2759 **Jet and p_T^{miss} uncertainties** The uncertainty on the calibration of the jet p_T
2760 detector response is assessed through the “reduced” set of subsources provided by
2761 the CMS Collaboration, which encompasses seven different subsources. Of these,
2762 five subsources are found to be relevant for this analysis, while two subsources af-
2763 fecting mainly the endcaps and hadronic forward calorimeter are negligible. The
2764 five relevant subsources are:

- 2765 • The absolute scale uncertainty, referring to the constant term in the jet p_T
2766 response (“Absolute”). It is split into a statistical component (uncorrelated
2767 between years) and a systematic component (correlated), the latter encoding
2768 e.g. corrections due to FSR and ISR in the JEC derivation.

- 2769 • The relative scale uncertainty in the barrel and first part of the endcaps
2770 ($|\eta| < 2.5$), encoding the p_T dependence of the jet p_T response (“**BBEC1**”).
2771 It is similarly split into an uncorrelated statistical and a correlated systematic
2772 component.
- 2773 • An uncertainty due to residual differences in the η dependence between JECs
2774 derived in dijet, Z+jets, and γ +jets selections (“**RelativeSample**”), consid-
2775 ered uncorrelated between years.
- 2776 • An uncertainty due to residual differences between different methods of deriv-
2777 ing the JECs (“**RelativeBal**”), considered fully correlated between years.
- 2778 • An uncertainty due to the difference in jet flavor response in PYTHIA and
2779 HERWIG, considered separately for b quark jets (“**FlavorPureBottom**”) and
2780 non-b quark jets (“**FlavorQCD**”) and fully correlated between years.

2781 Furthermore, the uncertainty in the jet p_T resolution is considered separately,
2782 again uncorrelated between years. All jet uncertainties are fully propagated to the
2783 calculation of p_T^{miss} , and an additional p_T^{miss} uncertainty based on soft, unclustered
2784 hadronic activity is also considered.

2785 **b tagging uncertainties** Similarly, the uncertainty on the b tagging efficiency
2786 is split into 17 subsources, corresponding e.g. to different parton shower modeling,
2787 the treatment of leptons in the jet, or the propagation of the jet p_T scale uncer-
2788 tainties [142]. One component represents the statistical uncertainty and is thus
2789 considered uncorrelated, while all others are correlated among years. Moreover, an
2790 uncertainty on mistagging of light-flavor jets is included, also split into a statistical
2791 and a systematic component.

2792 **Lepton and trigger uncertainties** Uncertainties on the lepton reconstruction,
2793 identification, and isolation efficiencies, as measured centrally in CMS using the tag-
2794 and-probe method, are considered separately for muons and electrons [113, 141].
2795 For the muons, the uncertainty is split into a statistical component (uncorrelated
2796 between the analysis years) and a systematic component (correlated), which is based
2797 on e.g. the requirements applied to the tag muon or the choice of function used for
2798 the tag-and-probe fit. Similarly, the dilepton trigger efficiency uncertainties are
2799 considered uncorrelated between years and lepton flavor channels. Finally, in data
2800 taken in 2016 or 2017, an additional uncertainty is assigned due to an inefficiency
2801 in the ECAL L1 trigger [119], as described in Sec. 7.2.4.

2802 **Luminosity uncertainty** The uncertainty on the total integrated luminosity is
2803 included following Refs. [100, 217, 218], leading to a total luminosity uncertainty of

2804 1.6%, split into a total of seven components that encode the correlations between
 2805 the years. Similar as in Sec. 5.5, the largest single contributions to the uncertainty
 2806 come from factorization between the x and y axes during scans used for the lumi-
 2807 nosity calibration as well as due to residual differences between different luminosity
 2808 detectors [100].

2809 **Pileup uncertainty** To estimate the uncertainty on the amount of pileup per pp
 2810 bunch crossing, the effective inelastic proton-proton cross section used for pileup
 2811 reweighting in the simulation is varied by 4.6% from its nominal value [219].

2812 7.5.3 Uncertainty smoothing

2813 Several of the considered uncertainty sources, e.g. the top quark mass in SM $t\bar{t}$, are
 2814 estimated by comparing to separate MC samples, which causes the relative deviation
 2815 due to the source to be affected by large statistical noise. A similar problem appears
 2816 for uncertainties which effectively vary the cuts applied on MC events, such as e.g.
 2817 the jet p_T scale uncertainties by way of jet acceptances. If left untreated, fitting
 2818 these noisy shape templates to the data could lead to erroneous constraints in the
 2819 likelihood fit.

2820 To prevent this, a smoothing procedure based on the algorithm LOWESS (short
 2821 for *locally weighted scatterplot smoothing*) [220, 221] is applied to these sources.
 2822 The procedure follows Ref. [31] and is described briefly in the following. First, the
 2823 relative deviation of the respective source is defined as $r^\pm = (N^\pm - N^0)/N^0$, where
 2824 N^0 , N^+ , and N^- are the event yields for the nominal template, the up variation,
 2825 and the down variation. They are considered three-dimensionally (3D) as a function
 2826 of the sensitive observables $\vec{x} = (m_{t\bar{t}}, c_{\text{hel}}, c_{\text{han}})$. To avoid artifacts from the choice
 2827 of binning in the analysis, the number of bins along each direction of \vec{x} is doubled
 2828 for the purpose of the smoothing.

2829 Second, for each bin in \vec{x} , a 3D hyperplane is fitted to r^\pm using a least-squares fit.
 2830 The fit is performed in a 3D *sliding window* with a fixed size of $2h_i$ in each direction,
 2831 where h_i with $i = 1, 2, 3$ is the *bandwidth* along each axis. This means that only
 2832 bins close to the bin that is being evaluated enter in the fit. Furthermore, the bins
 2833 enter the fit with a weight depending on their distance to the bin being evaluated.
 2834 If \vec{x} denotes the bin being evaluated, the weight of bin \vec{y} is given by [31]

$$w(\vec{x}, \vec{y}) = (1 - d(\vec{x}, \vec{y})^3)^3, \quad d(\vec{x}, \vec{y}) = \sqrt{\sum_i \left(\frac{x_i - y_i}{2h_i} \right)^2}. \quad (7.17)$$

2835 The function $w(\vec{x}, \vec{y})$ equals 1 for $\vec{x} = \vec{y}$, i.e. each bin enters with maximal weight
 2836 1 in its own fit, and falls off to 0 when \vec{y} tends towards the edge of the sliding
 2837 window as given by h_i . This local weighting thus favors points close to the bin being

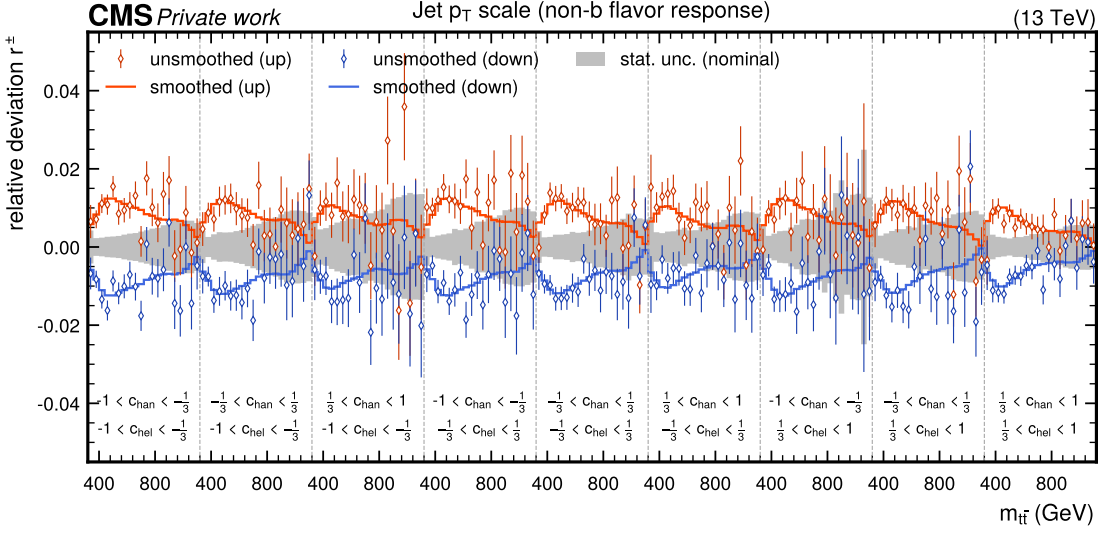


Figure 7.8: **Uncertainty smoothing.** The smoothed (solid lines) and unsmoothed (diamond markers) relative deviations in $m_{t\bar{t}} \times c_{\text{hel}} \times c_{\text{han}}$, shown for the example of the JEC subsource encoding the flavor response of non-b quark jets. The MC statistical uncertainty of the nominal sample is shown in grey.

evaluated.

The bandwidths h_i are free parameters of the method and are chosen using *leave-one-out cross validation* for each uncertainty source separately. In this method, the events making up the templates are randomly split into 10 batches, and nine of these batches are combined into the *training set* while the last is considered the *testing set*. The smoothing is applied to the relative deviation as computed from the training set, where the three bandwidths are scanned in fixed grids given by $h_i \in (0.1, 0.2, 0.5, 0.7, 1.0)$ for $m_{t\bar{t}}$ and $h_i \in (0.33, 0.50, 0.83, 1.0)$ for c_{hel} and c_{han} , all understood as relative to the total bin range in the respective axis. The resulting smoothed template is compared to the unsmoothed template in the testing set, and a χ^2 is computed taking into account the statistical uncertainty of the testing set. This procedure is repeated with each of the ten batches as the testing set, and it is further repeated 50 times with different random partitions. For each choice of bandwidths, the average χ^2 from all repetitions is computed, and the set of bandwidths which minimizes the average χ^2 is chosen for the smoothing.

To further prevent the algorithm from erroneously interpreting statistical noise as shape information, each relative deviation is also fitted using a constant line. The χ^2 is again calculated, and if it is found to be smaller than the χ^2 obtained from the smoothing, the uncertainty source in question is replaced by a pure normalization uncertainty as given by the constant line fit. In practice, this is relevant for some

2858 of the minor backgrounds as well as the signals due to the small statistics of their
2859 samples, but never occurs for the SM $t\bar{t}$ background.

2860 The results of the smoothing for the optimal bandwidth are shown for the example
2861 of the JEC subsource encoding the flavor response of non- b quark jets (the largest of
2862 the JEC subsources) in Fig. 7.8. The noise visible in the unsmoothed distributions
2863 is fully mitigated by the smoothing procedure.

2864 7.5.4 Differences between MC generators

2865 It has been observed that the theoretical uncertainties collected in Sec. 7.5.1 do not
2866 necessarily cover the differences in the predictions of different MC generators for
2867 $t\bar{t}$ [29, 30, 171, 222]. To assess the size of these effects, the standard $t\bar{t}$ prediction
2868 as computed using POWHEG hvq matched to PYTHIA is compared to alternate
2869 generator setups.

2870 The first of these is the same POWHEG hvq matrix element matched to the
2871 multi-purpose event generator HERWIG instead of PYTHIA. The angular-ordered
2872 parton shower in HERWIG is used (as opposed to the p_T -ordered dipole shower in
2873 PYTHIA) together with the CMS CH3 tune [223]. Furthermore, HERWIG uses a clus-
2874 ter hadronization model [224] instead of the string hadronization model of PYTHIA
2875 as described in Sec. 3.4.

2876 Figure 7.9 shows the ratios of the predictions from HERWIG and PYTHIA for the
2877 reconstructed $m_{t\bar{t}}$ distribution, as well as for the c_{hel} distribution close to the $t\bar{t}$
2878 threshold (i.e. where the η_t signal is located) and in the $t\bar{t}$ continuum. Besides a
2879 significantly lower $t\bar{t}$ acceptance, HERWIG predicts an increase of events at the $t\bar{t}$
2880 threshold similar to η_t . This appears concerning at first glance since, should the data
2881 follow the prediction from HERWIG instead of PYTHIA, this enhancement could be
2882 confused with an η_t signal if PYTHIA is used as the baseline prediction. However, as
2883 seen in Fig. 7.9 in the center, HERWIG at the same predicts a flatter slope in c_{hel} than
2884 PYTHIA at the $t\bar{t}$ threshold, equivalent to a reduction of $t\bar{t}$ spin correlations¹. This is
2885 in contrast to the η_t signal, in which the $t\bar{t}$ spins are maximally anti-correlated. The
2886 inclusion of the spin correlation variable c_{hel} in the analysis thus makes it possible
2887 to separate the differences between POWHEG and HERWIG with respect to η_t .

2888 The second alternative generator is bb41 matched to PYTHIA, as studied exten-
2889 sively in Chapter 6. Here, particularly the off-shell effects included in bb41 might be
2890 of interest for the extraction of η_t since the latter is located below the $t\bar{t}$ threshold.
2891 The setup denoted as “bb41 v2” in Sec. 6.2, corresponding to Ref. [172], is used, and
2892 compared to the sum of the POWHEG hvq $t\bar{t}$ and tW predictions for consistency.

2893 A caveat here is presented by the corrections to NNLO QCD and NLO EW as
2894 described in Sec. 7.3. These are derived from fixed-order corrections assuming stable
2895 top quarks, and are not available for the full $b\bar{b}\ell\ell\nu\nu$ final state. To still be able to

¹This effect was also seen in the context of Ref. [30].

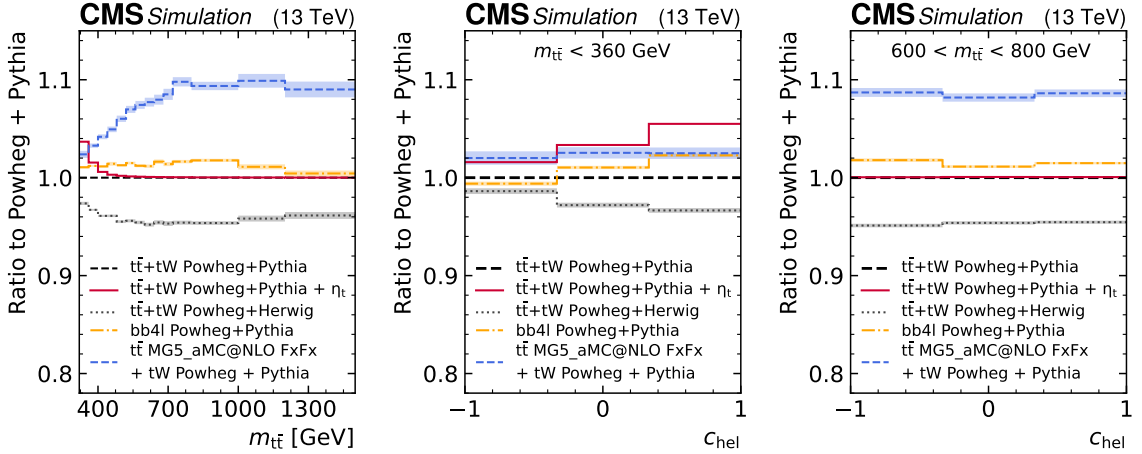


Figure 7.9: **Comparison between MC generators for $t\bar{t} + tW$.** The predictions of different MC setups, namely POWHEG $t\bar{t} + tW$ matched to HERWIG (grey), bb4l matched to PYTHIA (orange), and MG5_AMC@NLO matched to PYTHIA (blue), all shown as the ratio to the prediction of POWHEG $t\bar{t} + tW$ matched to PYTHIA, for the inclusive reconstructed $m_{t\bar{t}}$ distribution (left) as well as the reconstructed c_{hel} distribution, restricted to $m_{t\bar{t}} < 360 \text{ GeV}$ (center) and to $600 < m_{t\bar{t}} < 800 \text{ GeV}$ (right). The effect of the η_t signal is also shown in red for comparison. *Figure taken from Ref. [8].*

apply them to bb4l predictions, the bb4l sample is split into a $t\bar{t}$ and a tW part in an ad-hoc way by using the matrix element history projectors implemented in bb4l v2 [172]. The corrections are then applied to the $t\bar{t}$ part only, in the same manner as to POWHEG hvq.

The ratios of the predictions are also shown in Fig. 7.9. It can be seen that bb4l does not predict major differences in the reconstructed $m_{t\bar{t}}$ spectrum even at its lower edge. However, it results in a significantly steeper slope in reconstructed c_{hel} close to the threshold. This increase in slope is of similar magnitude as the effect expected due to η_t .

The source of this difference is not yet fully understood. bb4l contains NLO QCD corrections to the top decay which are not present in hvq (though they are approximated through the matrix element corrections in PYTHIA). However, NLO corrections to spin correlations are expected to not only be small, but reduce the spin correlation instead of enhancing it [21].

It is possible that the effect instead originates in the $t\bar{t}/tW$ interference: For the tW contribution, where one of the leptons is not actually the decay product of a top quark, $t\bar{t}$ spin correlation is not truly definable. The slope of the reconstructed c_{hel} distribution, obtained under the assumption that the events contain a $t\bar{t}$ system,

will thus be arbitrary with no clear *a priori* expectation, and in general different to the slope in SM $t\bar{t}$. The same holds for the $t\bar{t}/tW$ interference. Since **bb41** now gives a true (though effectively LO) prediction of the $t\bar{t}/tW$ interference instead of the ad-hoc treatment of the DR and DS schemes (cf. Sec. 6.3), it is expected that the magnitude of the interference contribution in **bb41** will be different. Thus, it is possible that the total c_{hel} slope, arising from the combination of $t\bar{t}$, tW , and $t\bar{t}/tW$ interference, will be different as well.

A third alternative prediction is provided by $t\bar{t} + \text{jets}$ production simulated with **MG5_AMC@NLO**, matched to **PYTHIA** with the FxFx scheme [90]. While this prediction is formally also NLO-accurate in QCD in the NWA, and thus comparable to **POWHEG hvq**, it has been observed in past measurements that **MG5_AMC@NLO** does not agree as well with data as **POWHEG** for $t\bar{t}$ production. Indeed it shows a large slope in the $m_{t\bar{t}}$ distribution, as also seen in Fig. 7.9. As a result, **MG5_AMC@NLO** is given less focus compared to the other two predictions here.

In this work, **POWHEG hvq + PYTHIA** is considered for the nominal background prediction in all cases. A comparison to **POWHEG hvq + HERWIG**, **MG5_AMC@NLO + PYTHIA**, and **bb41 + PYTHIA** is shown in Sec. 7.7.3 in the context of measuring the η_t cross section. Furthermore, the effect of including the differences to **POWHEG hvq + HERWIG** and **bb41 + PYTHIA** as two additional shape-based nuisance parameters in the fit is similarly given in Sec. 7.7.3. Note that in Ref. [8], these nuisance parameters were considered as part of the main result in order to be conservative with respect to the total uncertainty.

7.6 Pre-fit distributions

The agreement between the total MC prediction, including all corrections described in Secs. 7.2.4 and 7.3, and the observed data are presented in this section. Shown observables are lepton p_T , η , and $\Delta\phi_{\ell\ell}$ (Fig. 7.10); jet p_T , η , and number of jets (Fig. 7.11); as well as p_T^{miss} , the invariant mass of the two leptons $m_{\ell\ell}$, and the invariant mass of the two leptons and two b-tagged jets $m_{b\bar{b}\ell\ell}$ (Fig. 7.12). All of them are shown after all lepton, jet, b tag and p_T^{miss} requirements, but before the $t\bar{t}$ reconstruction, summed over all analysis years, and separately for the same-flavor (ee and $\mu\mu$) and opposite-flavor ($e\mu$) channels, since the latter have different backgrounds and cuts.

Furthermore, different distributions resulting from the $t\bar{t}$ reconstruction are shown in Fig. 7.13, this time summed also over lepton flavor. They consist of top quark p_T , η , and scattering angle $\cos\theta^*$, as well as the three observables used for the fit $m_{t\bar{t}}$, c_{hel} , and c_{han} .

It can be seen that there is a slight but consistent over-prediction of the background normalization compared to the data in almost all distributions. Furthermore, there is a slight slope in the ratio of data and simulation yields in the p_T of leptons,

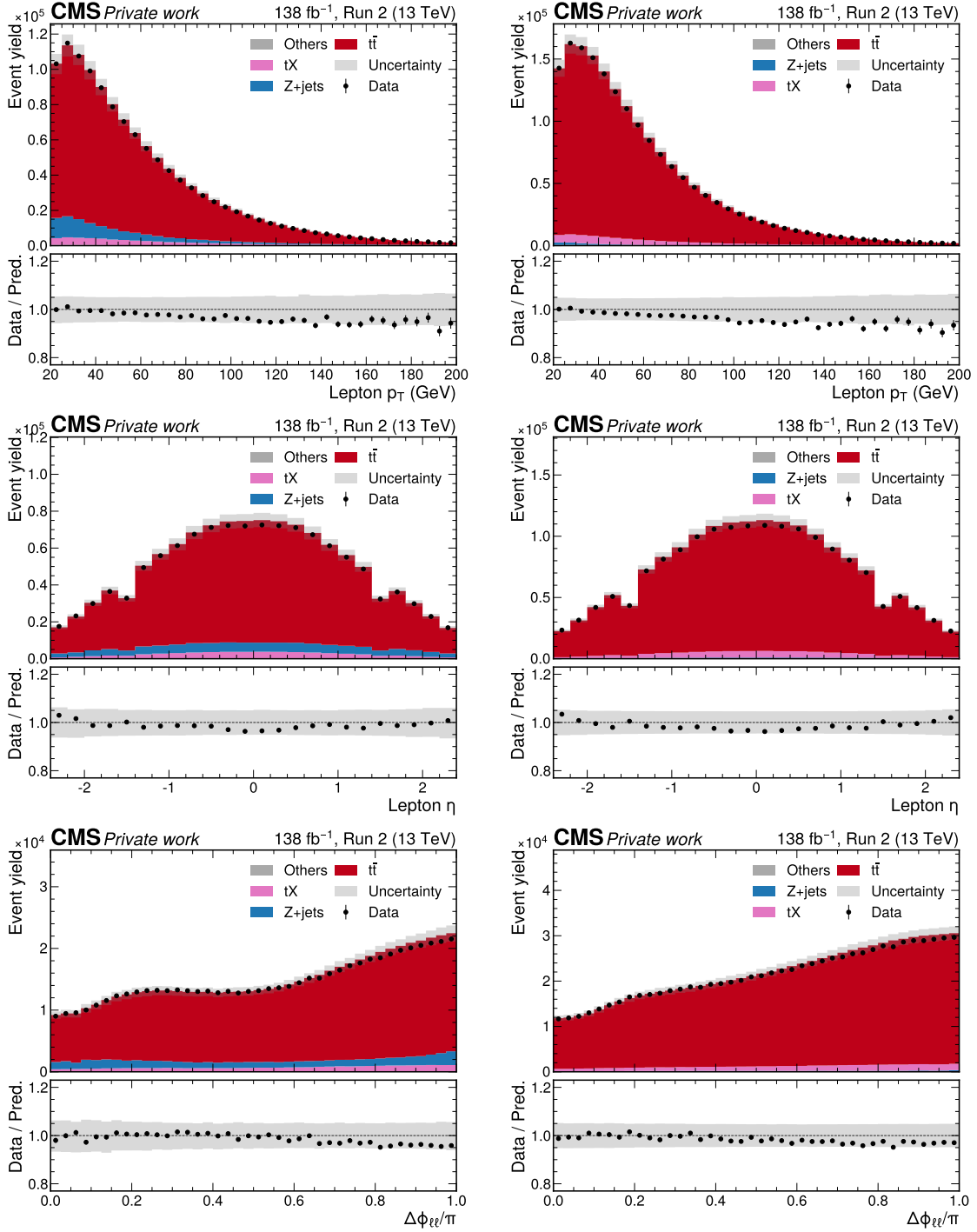


Figure 7.10: Control distributions. Shown are the distributions of p_T of both leptons (top), η of both leptons (center), and the azimuthal angle $\Delta\phi_{ll}$ between the leptons (bottom) in the $e\bar{e}/\mu\bar{\mu}$ (left) and $e\mu/\bar{\mu}\bar{\mu}$ channels (right). All figures show both data (black dots) and different simulated background processes (colored bars), as well as the total systematic uncertainty (gray band).

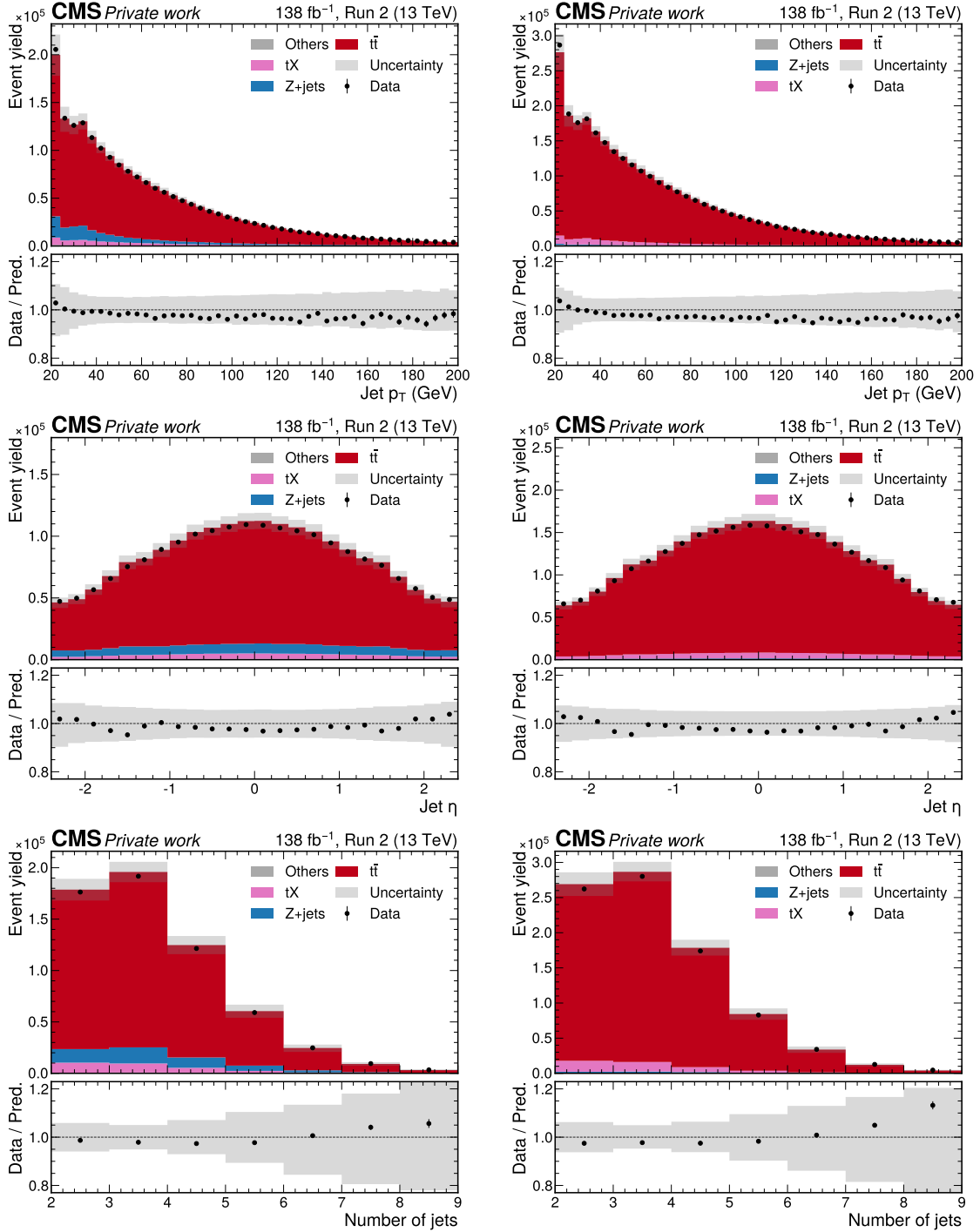


Figure 7.11: **Control distributions.** Shown are the distributions of p_T of all jets (top), η of all jets (center), and the number of jets (bottom) in the ee/ $\mu\mu$ (left) and e μ channels (right). All figures show both data (black dots) and different simulated background processes (colored bars), as well as the total systematic uncertainty (gray band).

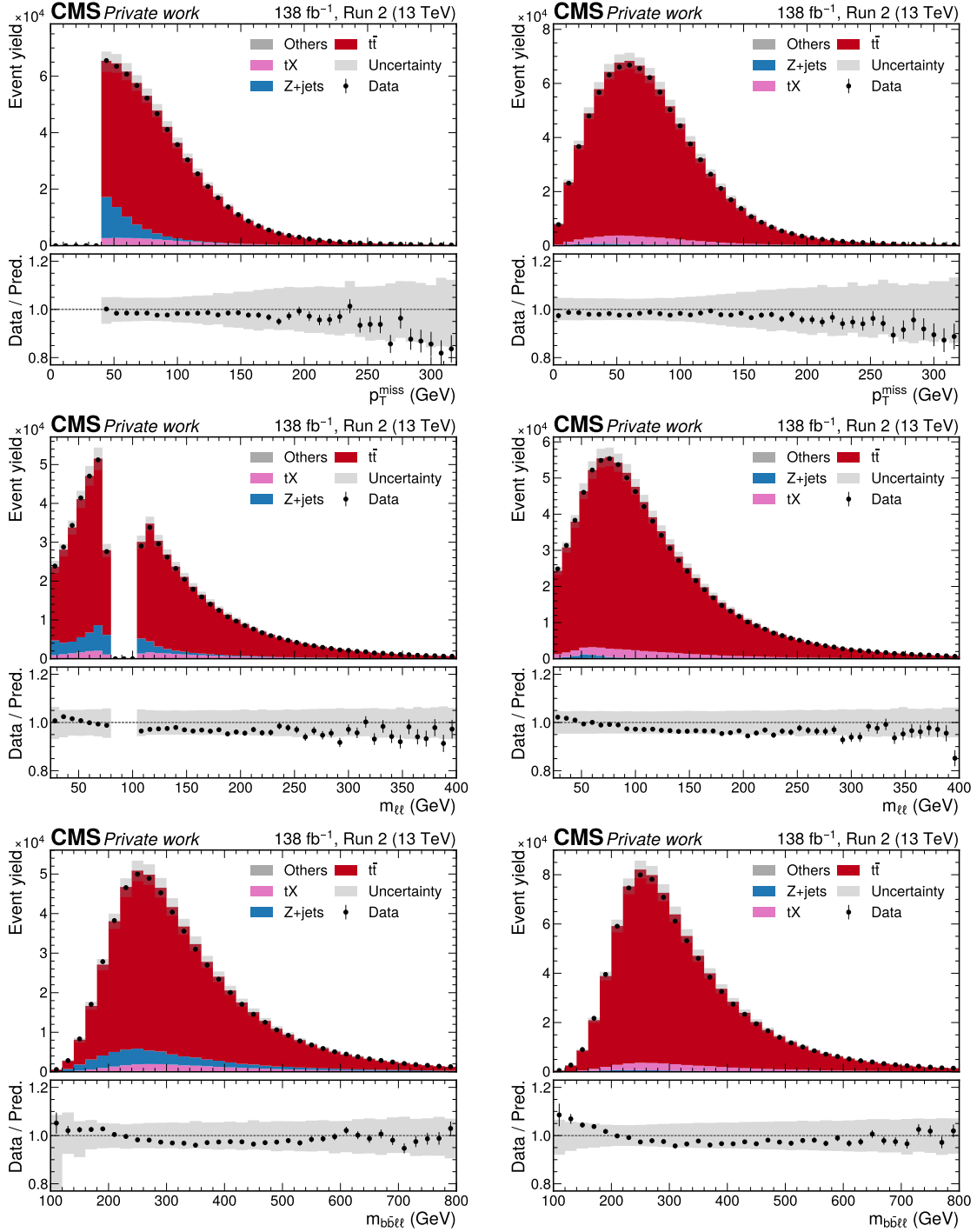


Figure 7.12: Control distributions. Shown are the distributions of p_T^{miss} (top), $m_{\ell\ell}$ (center), and the invariant mass $m_{bb\ell\ell}$ of both b candidates and both leptons (bottom) in the ee/ $\mu\mu$ (left) and e μ channels (right). All figures show both data (black dots) and different simulated background processes (colored bars), as well as the total systematic uncertainty (gray band).

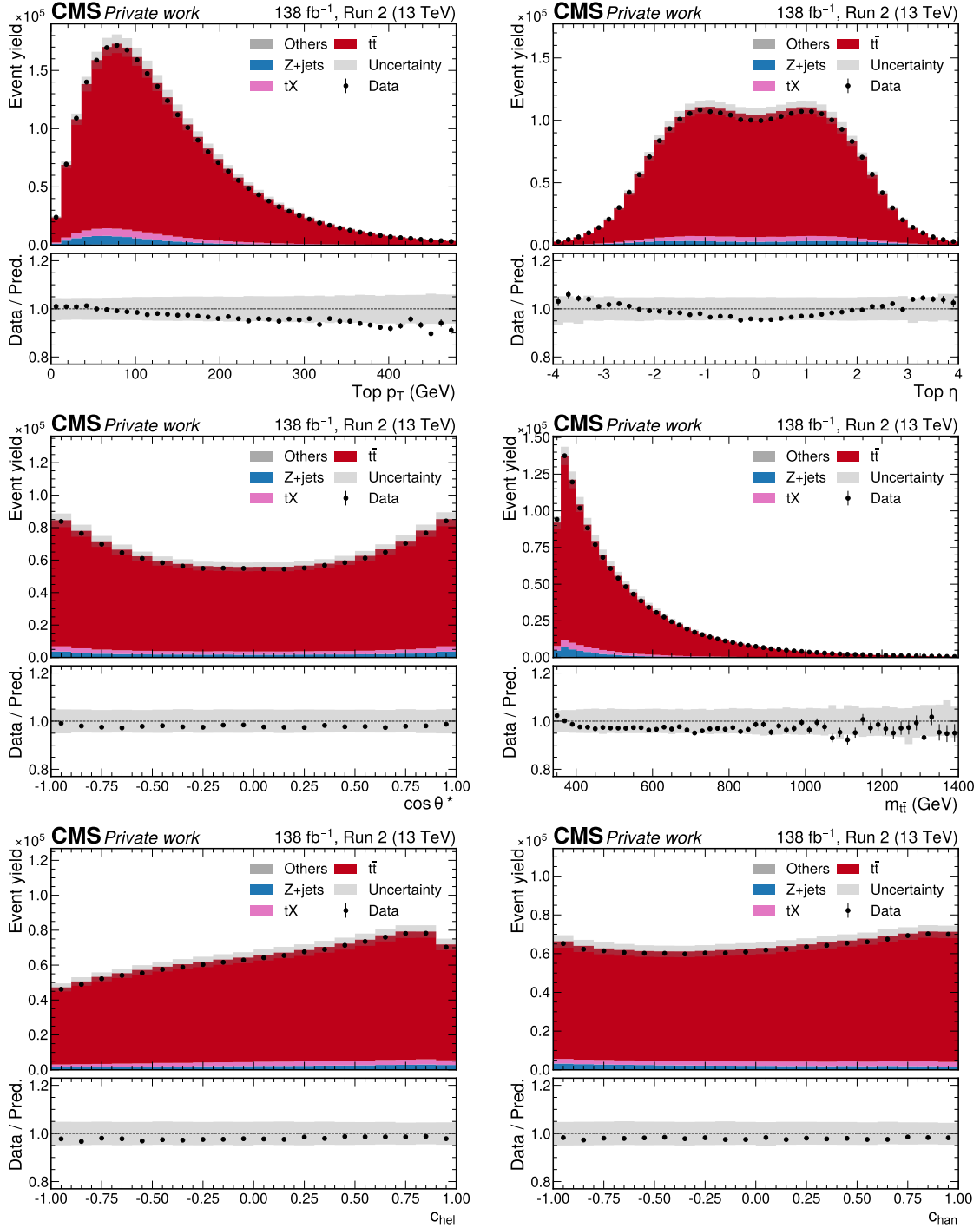


Figure 7.13: **Control distributions after $t\bar{t}$ reconstruction.** Shown are (from top left to bottom right) the distributions of the top quark p_T , top quark η , $m_{t\bar{t}}$, $\cos \theta^*$, c_{hel} and c_{chan} for the sum of all dilepton channels. All figures show both data (black dots) and different simulated background processes (colored bars), as well as the total systematic uncertainty (gray band).

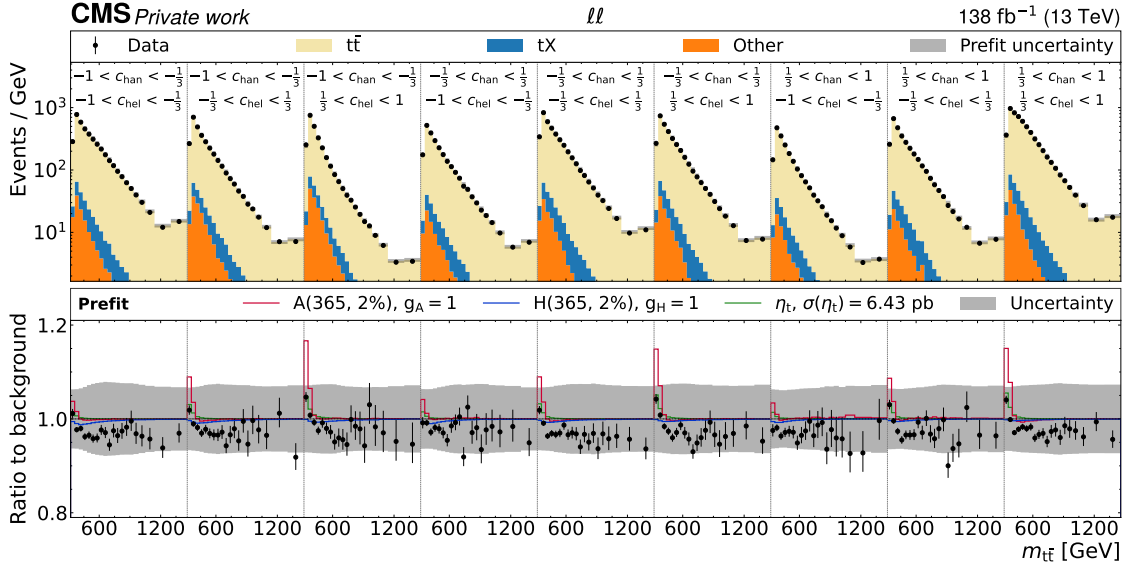


Figure 7.14: **Prefit distributions of $m_{t\bar{t}} \times c_{\text{hel}} \times c_{\text{han}}$.** The unrolled three-dimensional distribution in $m_{t\bar{t}}$, c_{hel} and c_{han} as used for statistical analysis before the fit to the data, summed over all years and lepton flavors. The upper panel shows the sum of the background simulation (colored bars) and the observed data (black dots), while the lower panel shows the ratio of the data to the prediction, with different signals overlaid: A (red) and H (blue), both for $m_{A/H} = 365$ GeV and $\Gamma_{A/H}/m_{A/H} = 2\%$, and η_t (green). *Figure adapted from Ref. [9].*

2953 jets or the reconstructed top quarks. This is likely a result of the well-known top
 2954 quark p_T mismodeling at the LHC, which is not fully removed by NNLO QCD cor-
 2955 rections as used here [153, 155]. Further discrepancies are found for high values of $|\eta|$
 2956 and for large number of jets, both of which are covered by systematic uncertainties.

2957 Finally, the three-dimensional $m_{t\bar{t}} \times c_{\text{hel}} \times c_{\text{han}}$ distribution used for the statistical
 2958 analysis is shown before the fit, including all systematic uncertainties, in Fig. 7.14.
 2959 A notable excess of the data compared to the prediction is observed for low val-
 2960 ues of $m_{t\bar{t}}$, consistent with the excess seen in the one-dimensional $m_{t\bar{t}}$ distribution
 2961 (Fig. 7.13) and in the related observables $m_{\ell\ell}$ and $m_{b\bar{b}\ell\ell}$ (Fig. 7.12). The excess is
 2962 stronger for large values of c_{hel} as seen from the multi-dimensional binning, while
 2963 no trend can be seen by eye regarding c_{han} .

2964 7.7 Interpretation of the excess

2965 7.7.1 Extraction of $t\bar{t}$ bound state effects

2966 The prefit excess visible in Fig. 7.14 is interpreted in terms of a pseudoscalar $t\bar{t}$
 2967 bound state by performing a signal+background fit with η_t as the signal, as defined
 2968 in Sec. 2.2.3. The POI in the fit is $\sigma(\eta_t)$, the cross section of the η_t model, which can
 2969 be understood as the difference between the data and the fixed-order perturbative
 2970 QCD (FO pQCD) background prediction. It is measured to be

$$\sigma(\eta_t) = 8.7 \pm 0.5(\text{stat}) \pm 1.0(\text{syst}) \text{ pb} = 8.7 \pm 1.1 \text{ pb}. \quad (7.18)$$

2971 The statistical and systematic component of the uncertainty are estimated as
 2972 described in Sec. 4.4. The significance of the result compared to a background-only
 2973 hypothesis, i.e. without a bound state, is more than five standard deviations.

2974 The result is in good agreement with the prediction of 6.4 pb given in Ref. [40],
 2975 obtained by fitting the results of an NRQCD calculation from Ref. [36], though
 2976 this result is not one-to-one comparable since it considers only the range of $m_{t\bar{t}} \in$
 2977 [338, 350] GeV. It should be noted that the results of Ref. [36] (as well as the newer
 2978 ones in Ref. [38]) were obtained by using NLO hard functions for the NRQCD
 2979 calculations, and moving to NNLO might give a significant increase in cross section,
 2980 by analogy to the difference in NNLO and NLO cross sections for the $t\bar{t}$ continuum.
 2981 Furthermore, the NRQCD approach employed in these calculations considers only
 2982 the ground state wavefunction of the bound $t\bar{t}$ system, and independent calculations
 2983 have shown that including contributions from excited states could increase the cross
 2984 section by orders of 15–20% [225, 226].

2985 The postfit $m_{t\bar{t}} \times c_{\text{hel}} \times c_{\text{han}}$ distribution can be seen in Fig. 7.15. The data,
 2986 including the excess at low $m_{t\bar{t}}$, is described well by the η_t model combined with the
 2987 FO pQCD background. To illustrate this further, one-dimensional projections of the
 2988 $m_{t\bar{t}} \times c_{\text{hel}} \times c_{\text{han}}$ template into inclusive $m_{t\bar{t}}$, as well as into c_{hel} for both low and high
 2989 $m_{t\bar{t}}$, are shown in Fig. 7.16. One can clearly see that the data at the $t\bar{t}$ threshold
 2990 shows a stronger slope in data than in the FO pQCD prediction, consistent with the
 2991 η_t signal, while no such slope is seen at high $m_{t\bar{t}}$, i.e. in the $t\bar{t}$ continuum.

2992 7.7.2 Parity of the excess

2993 To investigate whether the observed excess is \mathcal{CP} -odd (pseudoscalar) or \mathcal{CP} -even
 2994 (scalar) in nature, a simultaneous fit is performed with both η_t and χ_t , as defined in
 2995 Sec. 2.2.3, as freely floating signals. These correspond to pure 1S_0 and 3P_0 $t\bar{t}$ states,
 2996 respectively, both localized at the $t\bar{t}$ threshold.

2997 The result is shown in Fig. 7.17 in the form of compatibility contours. Consistent
 2998 with the result of the η_t -only fit, a non-zero η_t contribution is preferred by the fit by
 2999 more than 5 standard deviations. By contrast, the measured χ_t cross section, which

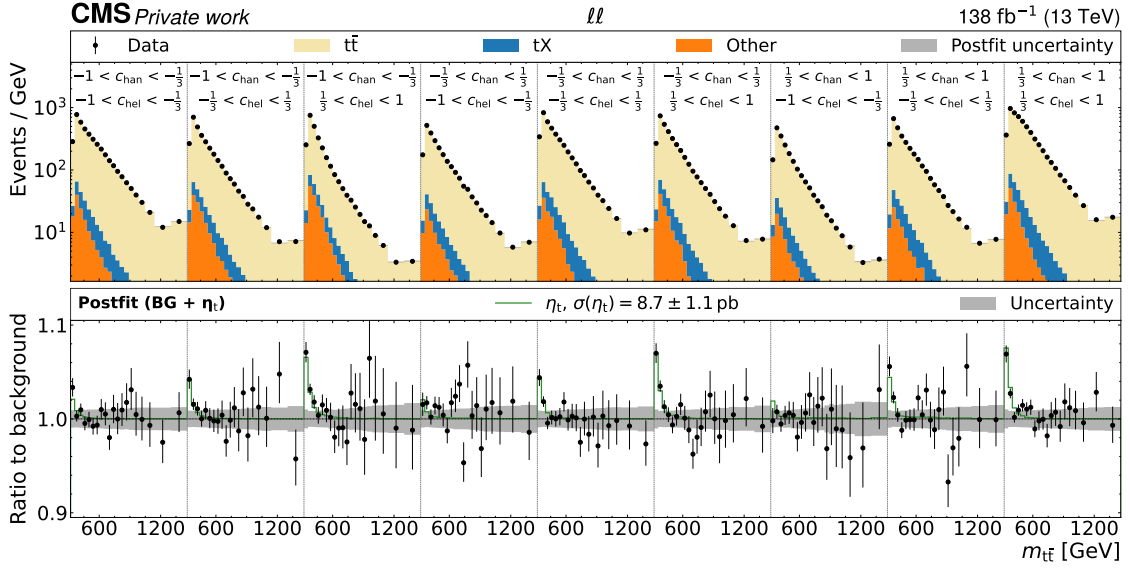


Figure 7.15: **Postfit distributions of $m_{t\bar{t}} \times c_{\text{hel}} \times c_{\text{han}}$ for the η_t fit.** The unrolled three-dimensional distribution in $m_{t\bar{t}}$, c_{hel} and c_{han} as after the fit to data with η_t as the signal, summed over all years and lepton flavors. The upper panel shows the sum of the background simulation (colored bars) and the observed data (black dots), while the lower panel shows the ratio of the data to the prediction with the postfit η_t signal overlaid. *Figure adapted from Ref. [8].*

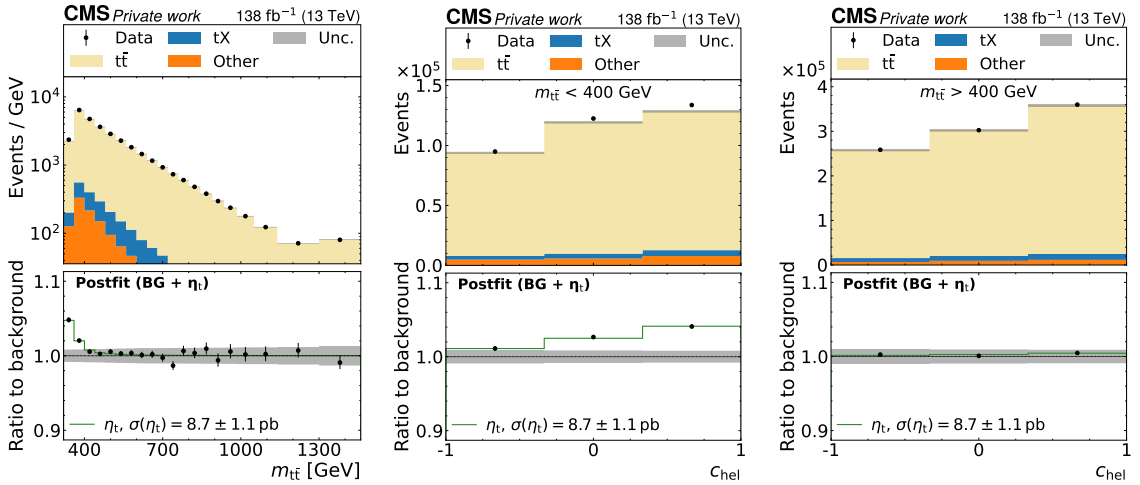


Figure 7.16: **Postfit distributions of $m_{t\bar{t}}$ and c_{hel} for the η_t fit.** One-dimensional distributions of inclusive $m_{t\bar{t}}$ (left), c_{hel} for $m_{t\bar{t}} < 400$ GeV (center), and c_{hel} for $m_{t\bar{t}} > 400$ GeV (right), projected from the $m_{t\bar{t}} \times c_{\text{hel}} \times c_{\text{han}}$ template in Fig. 7.15 with the same notations. *Figure adapted from Ref. [8].*

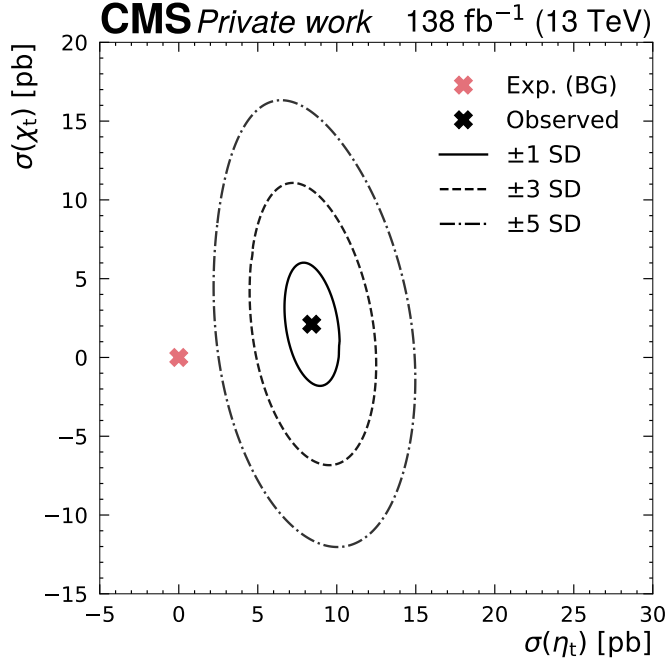


Figure 7.17: Parity of the excess. Observed compatibility contours in a simultaneous fit of η_t (corresponding to ${}^1\text{S}_0$) and χ_t (corresponding to ${}^3\text{P}_0$). The best-fit point is shown as the black cross, while the BG-only expectation (i.e. $\sigma(\eta_t) = \sigma(\chi_t) = 0$) is marked in pink. *Figure adapted from Ref. [8].*

can be seen as the ${}^3\text{P}_0$ component of the excess, is compatible with zero within one standard deviation. Based on this, it can be said that the observed excess is dominated by a pseudoscalar or ${}^1\text{S}_0$ spin state.

7.7.3 Checks of the result

Nuisance parameter pulls and impacts In Fig. 7.18, nuisance parameter pulls, constraints and impacts for the η_t extraction fit are presented, following the definitions in Sec. 4.4. The most impactful nuisances are all related to the modeling of the $t\bar{t}$ background. In particular, the value of the top Yukawa coupling y_t in the EW corrections is the leading uncertainty. This is notably one of the few uncertainties which can lead to a steeper c_{hel} slope in the $t\bar{t}$ prediction and could thus to some degree be confused for η_t , as discussed in Sec. 7.3.2.

Further important modeling uncertainties are the FSR scales in the $t\bar{t}$ parton shower as well as the top quark mass. The latter is constrained to a postfit uncertainty of ± 0.4 GeV, and fully compatible with the nominal value of 172.5 GeV. This strong constraint is similar in size to the current most precise direct top quark mass

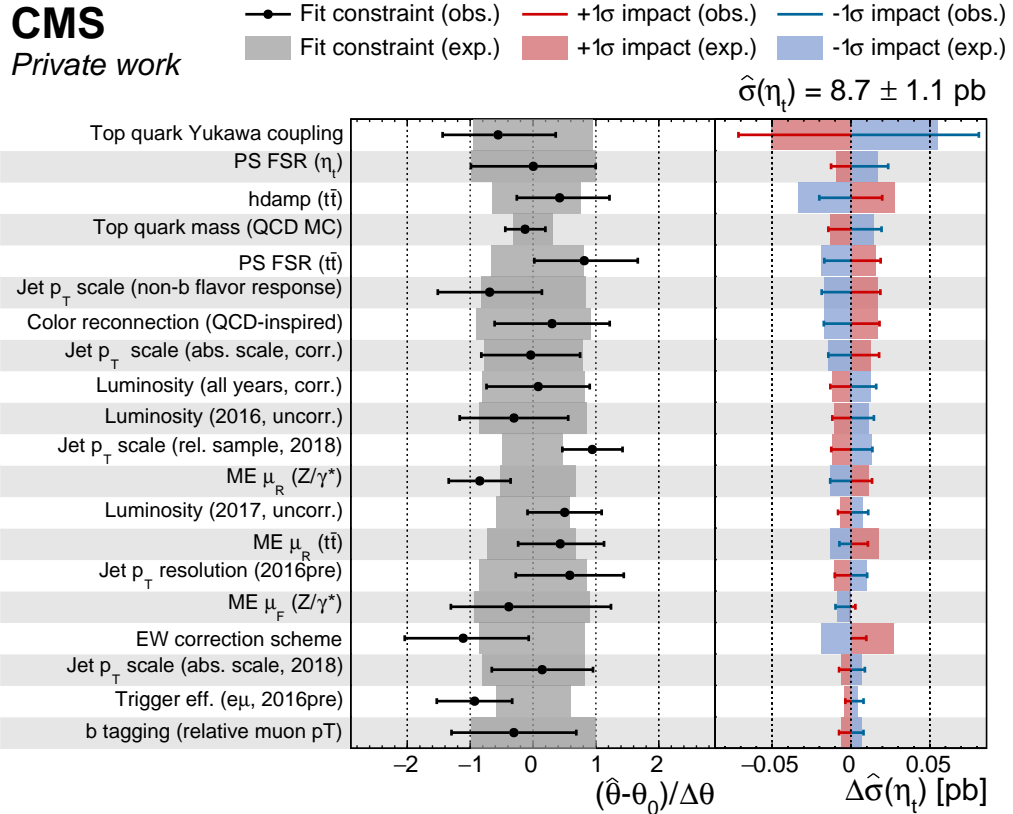


Figure 7.18: **Nuisance parameter pulls and impacts.** Expected and observed pulls, constraints, and impacts on the η_t cross section for the most impactful nuisance parameters in the η_t -only fit. *Figure adapted from Ref. [8].*

measurements [18, 209]. While it is expected that the $m_{t\bar{t}}$ distribution is strongly sensitive to the top quark mass, it is still surprising that the constraint competes with dedicated top quark mass measurements.

To verify that the constraint does not lead to an underestimation of the uncertainty on $\sigma(\eta_t)$, the top quark mass nuisance parameter is decorrelated in two different ways: either by splitting it into three regions defined by $m_{t\bar{t}} < 400 \text{ GeV}$, $400 < m_{t\bar{t}} < 600 \text{ GeV}$, and $m_{t\bar{t}} > 600 \text{ GeV}$, or by decorrelating it between the nine c_{hel} and c_{han} bins used for the measurements. In both cases, similar constraints are found on at least some of the resulting nuisance parameters, and the extracted η_t cross section is compatible with the nominal result.

A strong pull of around -1 is further observed in the EW correction scheme uncertainty. This uncertainty effectively encodes missing knowledge from NLO QCD-NLO EW cross terms in the higher-order corrections to $t\bar{t}$ as discussed in Sec. 7.3.2, with a nuisance parameter value of $+1$ corresponding to no cross terms (the addi-

tive scheme) and 0 corresponding to approximated cross terms (the multiplicative scheme). A pull of -1 could thus imply that the cross terms are underestimated by this approximation, though this is speculation as no full computation of the cross terms has been performed at the time of writing.

Experimental nuisances like the jet energy scales, on the other hand, influence mostly $m_{t\bar{t}}$ and thus do not have a large impact on the POI. Of note here are the pulls and constraints in nuisance parameters which influence only one of the four analysis eras, namely a subsource of the jet p_T scale in 2018, the uncorrelated component of the integrated luminosity in 2017, and the $e\mu$ trigger efficiency in 2016pre. The pulls imply that there are small inconsistencies (within one standard deviation) between the eras that are not accounted for in the MC simulation. Since this measurement is performed in a high-statistics region of phase space and with a large luminosity, it is expected to constrain ratios between normalization effects in different years, while of course the overall normalization (i.e. the total integrated luminosity) should be not pulled or significantly constrained. The exact source of the per-year differences is not clear; however, due to the small impact on the POI, this is not considered a problem.

In total, no pulls much larger than one prefit standard deviation are observed, indicating that the uncertainty model accommodates the data well.

Fit using $m_{b\bar{b}\ell\ell}$ instead of $m_{t\bar{t}}$ The three observables $m_{t\bar{t}}$, c_{hel} and c_{han} are all obtained from the kinematic reconstruction as described in Sec. 7.2.5. This procedure assumes, among others, that the top quarks are exactly on-shell with a fixed mass of 172.5 GeV. For η_t , which is located below the $t\bar{t}$ threshold, this assumption is clearly violated. Since the same kinematic reconstruction procedure is applied to simulation and data, this is in principle not a problem as long as the virtuality of the top quarks is well described by simulation and residual differences covered by systematic uncertainties. However, since the modeling of η_t in particular is rather uncertain, it is still important to check whether this assumption in the kinematic reconstruction introduces any bias.

This is done by repeating the fit with the observable $m_{t\bar{t}}$ replaced by $m_{b\bar{b}\ell\ell}$ (as shown also in Fig. 7.12), thus removing kinematic information obtained via the reconstruction from the fit. The kinematic reconstruction is still performed, however, to obtain c_{hel} and c_{han} ².

The resulting $m_{b\bar{b}\ell\ell} \times c_{\text{hel}} \times c_{\text{han}}$ postfit distribution can be found in Figs. 7.19 and 7.20. It can be seen that the excess is still clearly present, though with a wider spread due to the coarser resolution of $m_{b\bar{b}\ell\ell}$ compared to $m_{t\bar{t}}$. An η_t cross section of $\sigma(\eta_t) = 7.5 \pm 1.8 \text{ pb}$ is extracted, which is in agreement with the nominal result within one standard deviation.

²It has separately been checked that the requirement for events to pass the kinematic reconstruction does not bias the result, either.

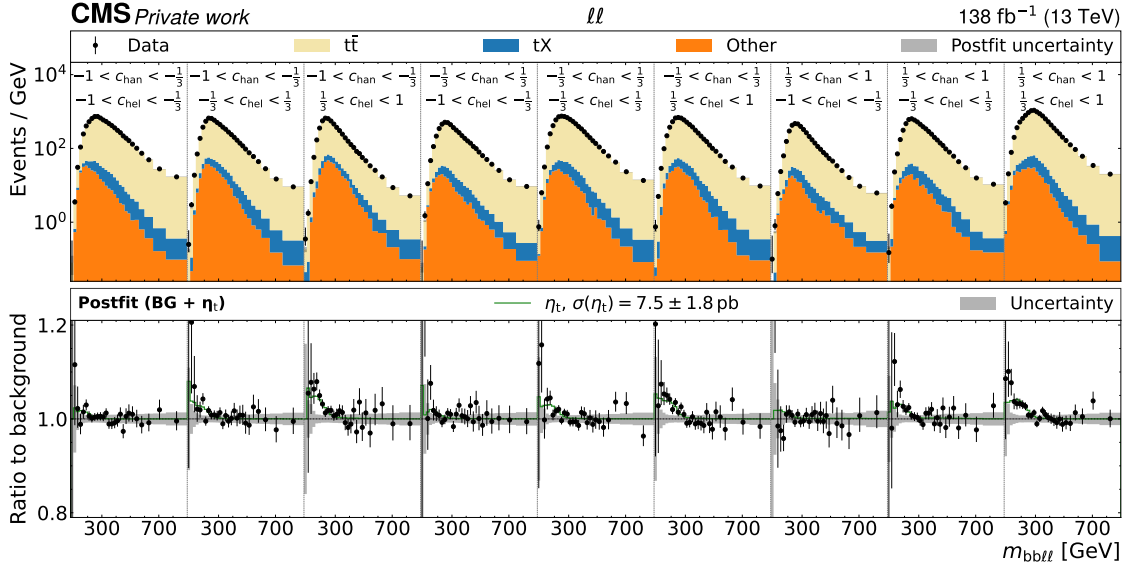


Figure 7.19: **Postfit distributions of $m_{bb\ell\ell} \times c_{hel} \times c_{han}$ for the η_t fit.** The unrolled three-dimensional distribution in $m_{bb\ell\ell}$, c_{hel} and c_{han} after the fit to data with η_t as the signal using $m_{bb\ell\ell}$ instead of $m_{t\bar{t}}$, summed over all years and lepton flavors. The first $m_{bb\ell\ell}$ bin in each $c_{hel} \times c_{han}$ slice is an underflow bin containing events with $m_{bb\ell\ell} < 80$ GeV. Otherwise, notations are as in Fig. 7.15.

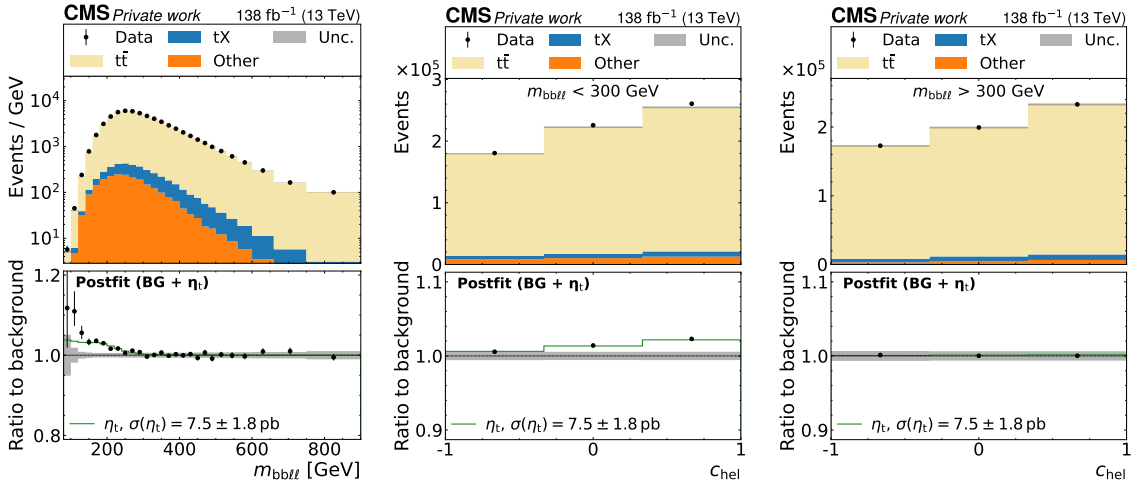


Figure 7.20: **Postfit distributions of $m_{bb\ell\ell}$ and c_{hel} for the η_t fit.** One-dimensional distributions of inclusive $m_{bb\ell\ell}$ (left), c_{hel} for $m_{bb\ell\ell} < 300$ GeV (center), and c_{hel} for $m_{bb\ell\ell} > 300$ GeV (right), projected from a 3D template of $m_{bb\ell\ell} \times c_{hel} \times c_{han}$. The first $m_{bb\ell\ell}$ bin in the left figure is an underflow bin containing events with $m_{bb\ell\ell} < 80$ GeV. Otherwise, notations are as in Fig. 7.15. *Figure adapted from Ref. [8].*

3067 **Alternate generator setups** The influence of the choice of generator setup for
 3068 the $t\bar{t}$ prediction is further quantified by repeating the η_t extraction fit with alternate
 3069 setups. Besides the nominal setup from POWHEG `hvq` matched to PYTHIA, the three
 3070 setups introduced in Sec. 7.5.4 are considered: POWHEG `hvq` matched to HERWIG,
 3071 MG5_AMC@NLO matched to PYTHIA with the FxFx scheme, and `bb41` matched
 3072 to PYTHIA.

Generator setup	$\sigma(\eta_t)$ [pb]
POWHEG <code>hvq</code> + PYTHIA (nominal)	8.7 ± 1.1
POWHEG <code>hvq</code> + HERWIG	8.6 ± 1.1
MG5_AMC@NLO FxFx + PYTHIA	9.8 ± 1.3
POWHEG <code>bb41</code> + PYTHIA	6.6 ± 1.4

Table 7.6: **Results for alternate generators.** Results for $\sigma(\eta_t)$ obtained with different simulated event samples for the FO pQCD $t\bar{t}+tW$ prediction.

3073 The results can be found in Tab. 7.6. The results from PYTHIA and HERWIG are
 3074 fully in agreement with each other, while MG5_AMC@NLO results in a higher η_t
 3075 cross section by about one standard deviation, and `bb41` results in a lower η_t cross
 3076 section by about ~ 1.5 standard deviations.

3077 As an additional check, the differences between the predictions from POWHEG `hvq`
 3078 + HERWIG and POWHEG `hvq` + PYTHIA as well as between `bb41` and $t\bar{t} + tW$ are
 3079 included in the fit as additional nuisance parameters. In both cases, the POWHEG
 3080 `hvq` + PYTHIA prediction is considered the nominal, and the alternate prediction
 3081 is considered the $+1\sigma$ template. The -1σ template is constructed by symmetrizing
 3082 the relative difference around the nominal, and intermediate values are obtained by
 3083 interpolation.

3084 The resulting η_t cross section with these nuisance parameters included is $\sigma(\eta_t) =$
 3085 $8.8^{+1.2}_{-1.4}$ pb³. This figure is fully compatible with the nominal result with an asymmet-
 3086 rically increased uncertainty. The reason for the increase can be seen in Fig. 7.21,
 3087 showing the nuisance parameter pulls and impacts: The nuisance parameter encod-
 3088 ing the difference between `bb41` and $t\bar{t} + tW$ represents the leading impact on the
 3089 η_t cross section and is asymmetric. This is understandable from the steeper slope
 3090 in c_{hel} for `bb41` as seen in Fig. 7.9, which is similar to the η_t signal, and is also in
 3091 agreement with the reduced η_t cross section for a `bb41` background prediction shown
 3092 in Tab. 7.6. It is furthermore significantly constrained towards zero, i.e. towards the
 3093 default $t\bar{t} + tW$ prediction, implying that the data prefers the NWA approach over
 3094 the *a priori* superior `bb41` prediction. The reason for this is not readily apparent.
 3095 One possible cause could be the fact that the NLO EW and NNLO QCD correc-
 3096 tions are applied to `bb41` in a necessarily ad-hoc manner, and might thus spoil the

³This figure is considered the nominal result in Ref. [8]

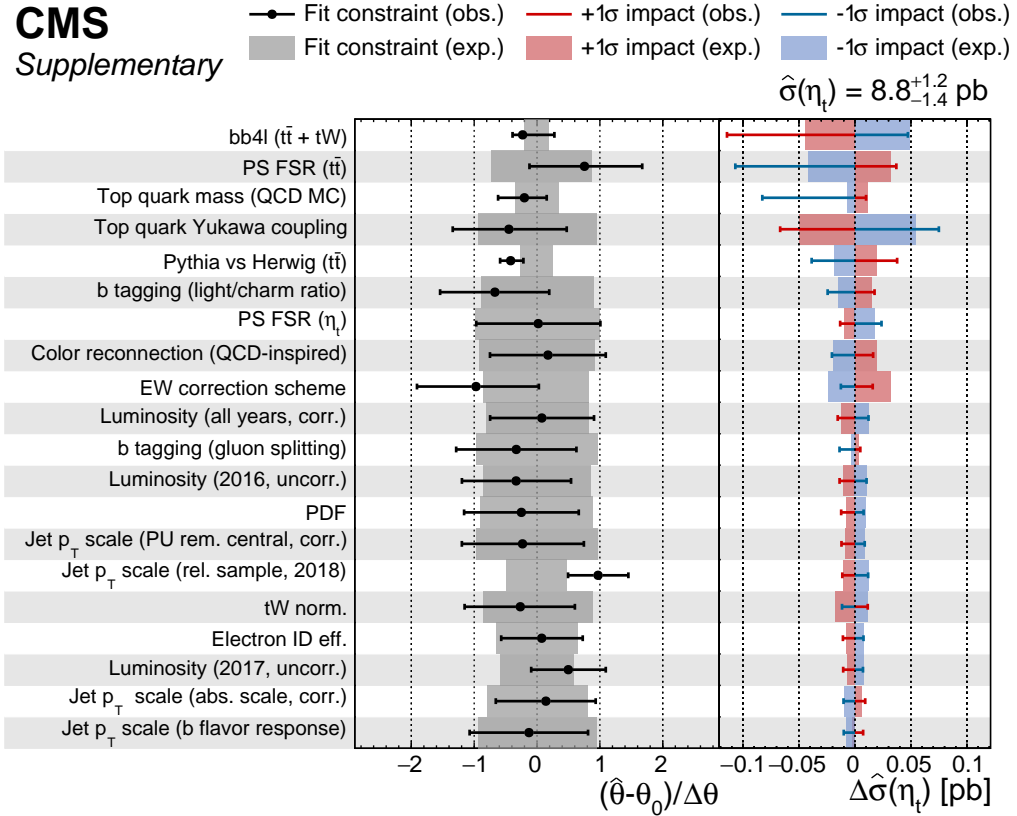


Figure 7.21: **Nuisance parameter pulls and impacts including alternate generators.** Expected and observed pulls, constraints, and impacts on the η_t cross section for the most impactful nuisance parameters in the η_t -only fit where the differences between the predictions from POWHEG hvq + HERWIG and bb4l + PYTHIA compared to POWHEG hvq + PYTHIA are included as additional nuisance parameters. *Figure adapted from Ref. [8].*

3097 agreement with the data (cf. Sec. 7.5.4). However, in the scope of this work, this
 3098 remains speculation.

3099 On the other hand, the nuisance parameter encoding the difference of PYTHIA
 3100 and HERWIG is less impactful, consistent with the results for HERWIG in Tab. 7.6,
 3101 and similarly strongly constrained. This is likely because the difference between
 3102 PYTHIA and HERWIG can be distinguished from η_t based on the combination of $m_{t\bar{t}}$
 3103 and c_{hel} information, as expanded upon in Sec. 7.5.4.

3104 7.7.4 Interpretation in terms of A and H

3105 While a $t\bar{t}$ bound state is the conceptually simplest explanation of the enhancement
 3106 at the $t\bar{t}$ threshold in the sense that it is predicted in the SM and does not invoke any
 3107 further (BSM) degrees of freedom, it is also possible to perform an interpretation
 3108 in terms of the generic spin-0 bosons A and H as introduced in Sec. 2.3.1. For this
 3109 purpose, fits allowing the presence of both A and H at the same time are performed.
 3110 The two independent POIs are the A/H-top coupling modifiers $g_{A\bar{t}\bar{t}}$ and $g_{H\bar{t}\bar{t}}$, and the
 3111 interference with the SM is fully taken into account through a parameterization in
 3112 terms of $g_{A/H\bar{t}\bar{t}}^2$ and $g_{A/H\bar{t}\bar{t}}^4$ (cf. Eq. (2.19)), thus allowing negative A/H contributions
 3113 with respect to the SM.

3114 A scan is performed over all pairs of considered A/H masses and widths (see
 3115 Sec. 7.2.1), and the pair with the largest difference in logarithmic likelihood $\Delta \ln L$
 3116 is identified as the best-fit point. This results in $m_A = 365 \text{ GeV}$, $\Gamma_A/m_A = 2\%$ for
 3117 A and $m_H = 925 \text{ GeV}$, $\Gamma_H/m_H = 3\%$ for H. It should be noted here that 365 GeV is
 3118 the lowest mass point considered in the available signals for A and H, while η_t and
 3119 χ_t are located at a lower value of 343 GeV. It is possible that considering a lower
 3120 value of m_A would lead to an even better fit; however, close to the $t\bar{t}$ threshold,
 3121 modeling the interference with the SM is difficult due to large corrections at higher
 3122 orders in QCD, and current models are not reliable enough [227, 228]. In particular,
 3123 the LO-to-NNLO K-factor for the A/H resonance cross section can become very
 3124 large for masses close to the threshold, suggesting large higher-order QCD effects
 3125 for both the resonance and interference with the SM.

3126 Figure 7.22 shows the postfit $m_{t\bar{t}} \times c_{\text{hel}} \times c_{\text{han}}$ distribution, and Fig. 7.23 shows
 3127 the allowed region for the two couplings $g_{A\bar{t}\bar{t}}$ and $g_{H\bar{t}\bar{t}}$ as obtained from a likelihood
 3128 scan. From the latter, the best-fit values and uncertainties at 68 % confidence level
 3129 for the coupling modifiers are found to be

$$g_{A\bar{t}\bar{t}} = 0.79^{+0.04}_{-0.05} \quad \text{and} \quad g_{H\bar{t}\bar{t}} = 1.47^{+0.17}_{-0.30}. \quad (7.19)$$

3130 The same excess close to the $t\bar{t}$ threshold already seen in Sec. 7.7.1 manifests
 3131 as a non-zero value of $g_{A\bar{t}\bar{t}}$, which Fig. 7.23 shows is preferred by more than five
 3132 standard deviations, similar as for the interpretation in terms of η_t . It is important
 3133 to stress that this result does not constitute any observation of a new BSM particle,
 3134 since a low-mass A and η_t cannot be conclusively distinguished, as discussed in the
 3135 following section.

3136 In addition, there is also a preference for a non-zero value of $g_{H\bar{t}\bar{t}}$, though this is
 3137 significant only at about 2 standard deviations and could thus be a simple statistical
 3138 fluctuation⁴. It should be noted that both of these values are local significances, i.e.

⁴The uncertainty ranges on $g_{A\bar{t}\bar{t}}$ and $g_{H\bar{t}\bar{t}}$ given in Eq. (7.19) are non-linear with respect to the confidence level due to the quadratic and quartic dependence of the event yield on $g_{A/H\bar{t}\bar{t}}$, as also seen in Fig. 7.23. At 95 % confidence level, the uncertainty ranges are $^{+0.07}_{-0.08}$ for $g_{A\bar{t}\bar{t}}$ and

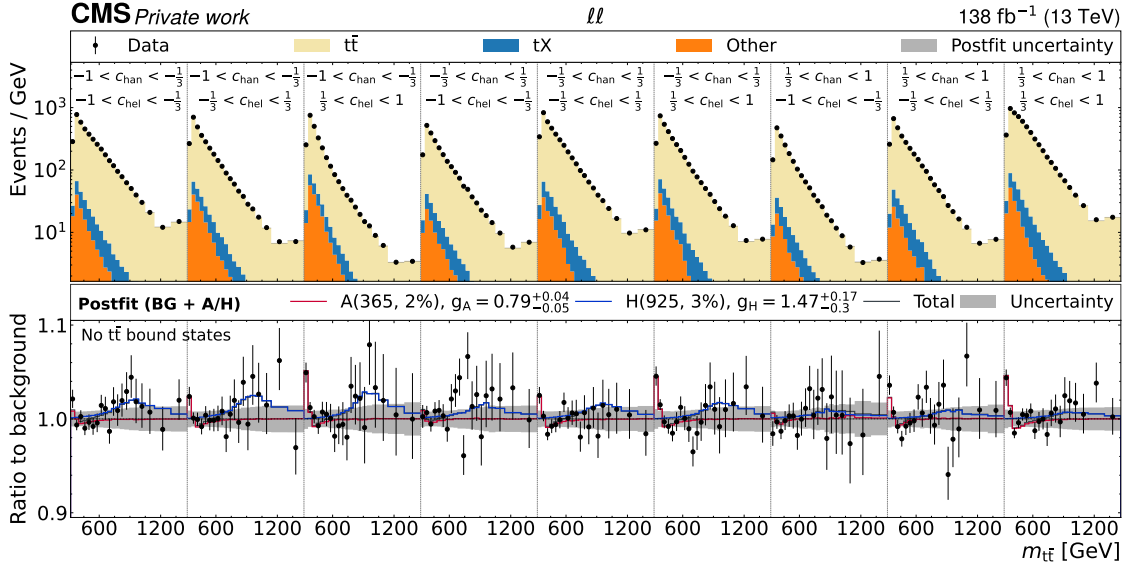


Figure 7.22: **Postfit distributions of $m_{t\bar{t}} \times c_{hel} \times c_{han}$ for the A+H fit.** The unrolled three-dimensional distribution in $m_{t\bar{t}}$, c_{hel} and c_{han} as after the fit to data with A and H as signals, summed over all years and lepton flavors. The A/H signals correspond to the best-fit masses and widths of $m_A = 365$ GeV, $\Gamma_A/m_A = 2\%$ for A and $m_H = 925$ GeV, $\Gamma_H/m_H = 3\%$ for H. The upper panel shows the sum of the background simulation (colored bars) and the observed data (black dots), while the lower panel shows the ratio of the data to the prediction with the postfit A and H signals, as well as their sum, overlaid.

they do not account for the look-elsewhere effect. The source of this preference is again evident from Fig. 7.22: it is due to a mild, broad excess in events compared to the prediction around $m_{t\bar{t}} \approx 900$ GeV, which is more pronounced in the low c_{han} bins compared to the others as would be expected for a scalar particle H.

7.7.5 Comparison of η_t and A interpretations

To compare the interpretations of the excess close to the $t\bar{t}$ threshold in terms of either η_t or a low-mass A, the prefit templates as a function of $m_{t\bar{t}}$ are shown in Fig. 7.24 left for the best-fit points of the two interpretations: $m_A = 365$ GeV, 2 % width, and $g_{At\bar{t}} = 0.79$ for A, as well as $\sigma(\eta_t) = 8.7$ pb for η_t . The shapes of the two templates look different: the effect of η_t is a simple enhancement in expected events close to the threshold, while A shows the characteristic peak-dip structure. The difference between the two templates is comparable in size to the normalized

^{+0.26}_{-1.47} for $g_{Ht\bar{t}}$, i.e. the data are compatible with $g_{Ht\bar{t}} = 0$ within two standard deviations.

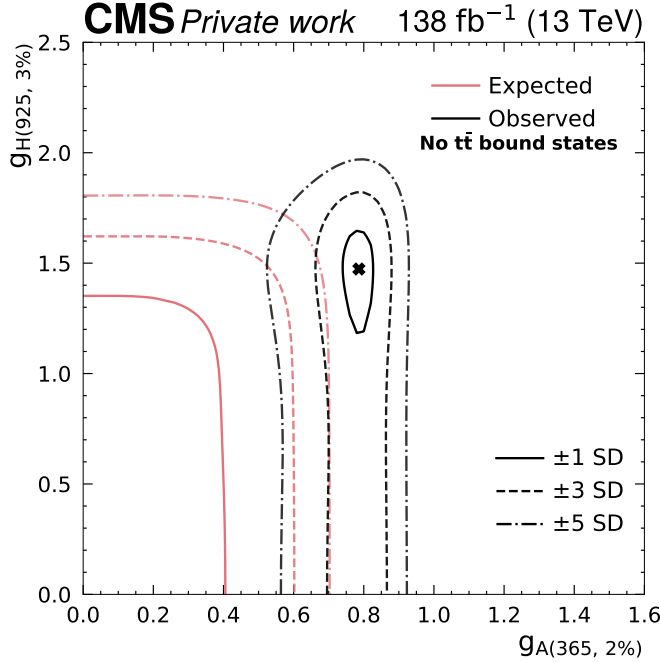


Figure 7.23: **Allowed coupling region in the A+H fit.** The two-dimensional allowed region for the coupling modifiers $g_{A\bar{t}\bar{t}}$ and $g_{H\bar{t}\bar{t}}$ in the A+H fit, for the best-fit A/H masses and widths of $m_A = 365 \text{ GeV}$, $\Gamma_A/m_A = 2\%$ for A and $m_H = 925 \text{ GeV}$, $\Gamma_H/m_H = 3\%$ for H, obtained through a scan of the profiled likelihood. The observed region is shown in black, while the SM expectation is shown in pink.

prefit systematic uncertainty for one standard deviation, shown in grey.

In Fig. 7.24 right, a scan of the profiled logarithmic likelihood with $g_{A\bar{t}\bar{t}}$ and $\sigma(\eta_t)$ as simultaneous POIs is performed. No H production is considered for this scan. From the observed allowed region, η_t is preferred over A at the level of one standard deviation. However, at two or more standard deviations, possible combinations of A and η_t including only A are allowed as well. The presence of neither A or η_t , on the other hand, is excluded. The expected allowed region, assuming $\sigma(\eta_t) = 8.7 \text{ pb}$ in the pseudodata, is also shown and is similar to the observed one.

It is important to stress that η_t represents a simplified model of a $t\bar{t}$ bound state, and its exact shape in $m_{t\bar{t}}$ is thus not precisely known. Furthermore, the $m_{t\bar{t}}$ shape of A might change when considering masses below the lower bound of $m_A = 365 \text{ GeV}$ considered in this analysis. Together with the only mild preference of η_t over A in the fit at the level of one standard deviation, it is clear that at the current level of precision the $t\bar{t}$ bound state η_t and a BSM pseudoscalar A cannot be conclusively distinguished.

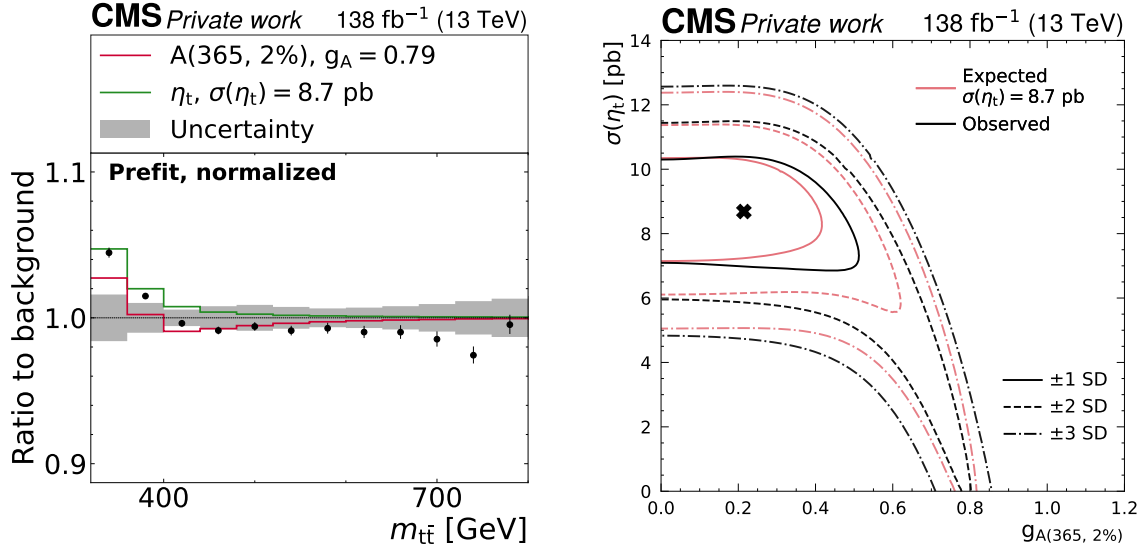


Figure 7.24: **Comparison of low-mass A and η_t .** Left: the normalized prefit $m_{t\bar{t}}$ distributions for A at $m_A = 365 \text{ GeV}$, 2 % width, and the best-fit coupling of $g_{A\bar{t}} = 0.79$ (red) as well as η_t at the best-fit cross section of $\sigma(\eta_t) = 8.7 \text{ pb}$ (green), with the data overlaid (black markers). The normalized prefit uncertainty is shown as the grey band. Right: the two-dimensional allowed region as a function of $g_{A\bar{t}}$ and $\sigma(\eta_t)$, obtained through a scan of the profiled likelihood. The observed region is shown in black, while the expected region assuming $\sigma(\eta_t) = 8.7 \text{ pb}$ is shown in pink.

³¹⁶⁶ 7.8 Limits on A/H bosons

³¹⁶⁷ Having discussed the excess seen at the $t\bar{t}$ threshold and its possible interpretations,
³¹⁶⁸ in this section exclusion limits on A/H bosons in the full considered mass range are
³¹⁶⁹ presented. This is done for two different scenarios: In the first scenario, denoted
³¹⁷⁰ “A/H only”, the SM $t\bar{t}$ background is described by the FO pQCD prediction from
³¹⁷¹ POWHEG + PYTHIA reweighted to NLO EW and NNLO QCD, same as for the η_t
³¹⁷² extraction in Sec. 7.7.1 and for the A+H fit in Sec. 7.7.4. The observed excess is thus
³¹⁷³ expected to manifest in the limits in the form of a weaker observed than expected
³¹⁷⁴ limit for low A/H masses.

³¹⁷⁵ In the second scenario, denoted “A/H + η_t ”, the observed excess is assumed to
³¹⁷⁶ originate solely from a $t\bar{t}$ bound state, which is further assumed to be well described
³¹⁷⁷ by the η_t model. Under this assumption, the η_t contribution is added to the $t\bar{t}$
³¹⁷⁸ background prediction, where the normalization of η_t is an additional free-floating
³¹⁷⁹ nuisance parameter. A and/or H contributions are then considered as signals on top
³¹⁸⁰ of this background.

In both scenarios, the limits are calculated with the CL_s prescription as introduced in Sec. 4.4. However, a complication arises from the non-linearity of the A/H signal as a function of $g_{A/\text{H}t\bar{t}}$, which means that the distribution of the test statistic is not necessarily χ^2 -distributed. As a result, the p -values p_{s+b} and p_b cannot be easily computed. To avoid having to perform computationally expensive toy experiments, a *raster scan* method is used in the same way as in Ref. [20]. For a given A/H mass and width point, the coupling modifier $g_{A/\text{H}t\bar{t}}$ is scanned in the range 0–5. For each value of $g_{A/\text{H}t\bar{t}}$, the total signal contribution is computed as the sum of the resonant signal, scaling with $g_{A/\text{H}t\bar{t}}^4$, and the SM-signal interference, scaling with $g_{A/\text{H}t\bar{t}}^2$. An auxiliary linear signal strength μ is then introduced, so that the total signal contribution becomes

$$s(\mu) = \mu \left(g_{A/\text{H}t\bar{t}}^4 s_{\text{res}} + g_{A/\text{H}t\bar{t}}^2 s_{\text{int}} \right) \quad (7.20)$$

where s_{res} and s_{int} are the resonance and interference contributions, respectively, and $g_{A/\text{H}t\bar{t}}$ is held fixed. $\mu = 1$ corresponds to the probed A/H signal, while $\mu = 0$ corresponds to the SM. Intermediate values of μ are in principle unphysical since they do not correspond to any value of $g_{A/\text{H}t\bar{t}}$.

Since the A/H signal now scales linearly with μ , the usual asymptotic approximation can be used to obtain the CL_s value for $\mu = 1$. It has been shown as a part of Ref. [20] that the distribution of the test statistic obtained in this way approximates well the true test statistic for $g_{A/\text{H}t\bar{t}}$ as evaluated using toy experiments. This procedure is repeated for all values of $g_{A/\text{H}t\bar{t}}$, and a value of $g_{A/\text{H}t\bar{t}}$ is, as usual, excluded at 95% confidence level when the CL_s value drops below 0.05.

The resulting observed and expected limits for all considered A and H masses and six representative width choices are shown in Figs. 7.25 and 7.26 for the “A/H only” scenario and in Figs. 7.27 and 7.28 for the “A/H + η_t ” scenario. The expected limits are mostly stronger for low masses since the signal cross sections fall off with rising A/H masses. An exception are H bosons with masses close to the threshold, for which the decay to $t\bar{t}$ is suppressed because the 3P_0 spin state requires one unit of orbital angular momentum, which in turn requires top quarks with non-zero velocity. This also leads to low cross sections for $\text{pp} \rightarrow \text{H} \rightarrow t\bar{t}$.

For low A/H widths, the rise of the expected limit with the mass is roughly linear. For higher widths, however, there is a jump in the limit in the mass range 650–750 GeV, coinciding with inflated uncertainty bands. The reason for this is a cancellation between the A/H resonance and A/H-SM interference components: At the $g_{A/\text{H}t\bar{t}}$ values relevant for the expected limits, the cross sections of resonance and interference approximately cancel, and because of the large width the peak-dip structure is not resolvable. Thus, the overall deviation from the SM and thus the sensitivity are small.

In the observed limits, the excess at the $t\bar{t}$ threshold is visible in the “A/H only” scenario at low A/H masses as expected. It is stronger for the pseudoscalar A

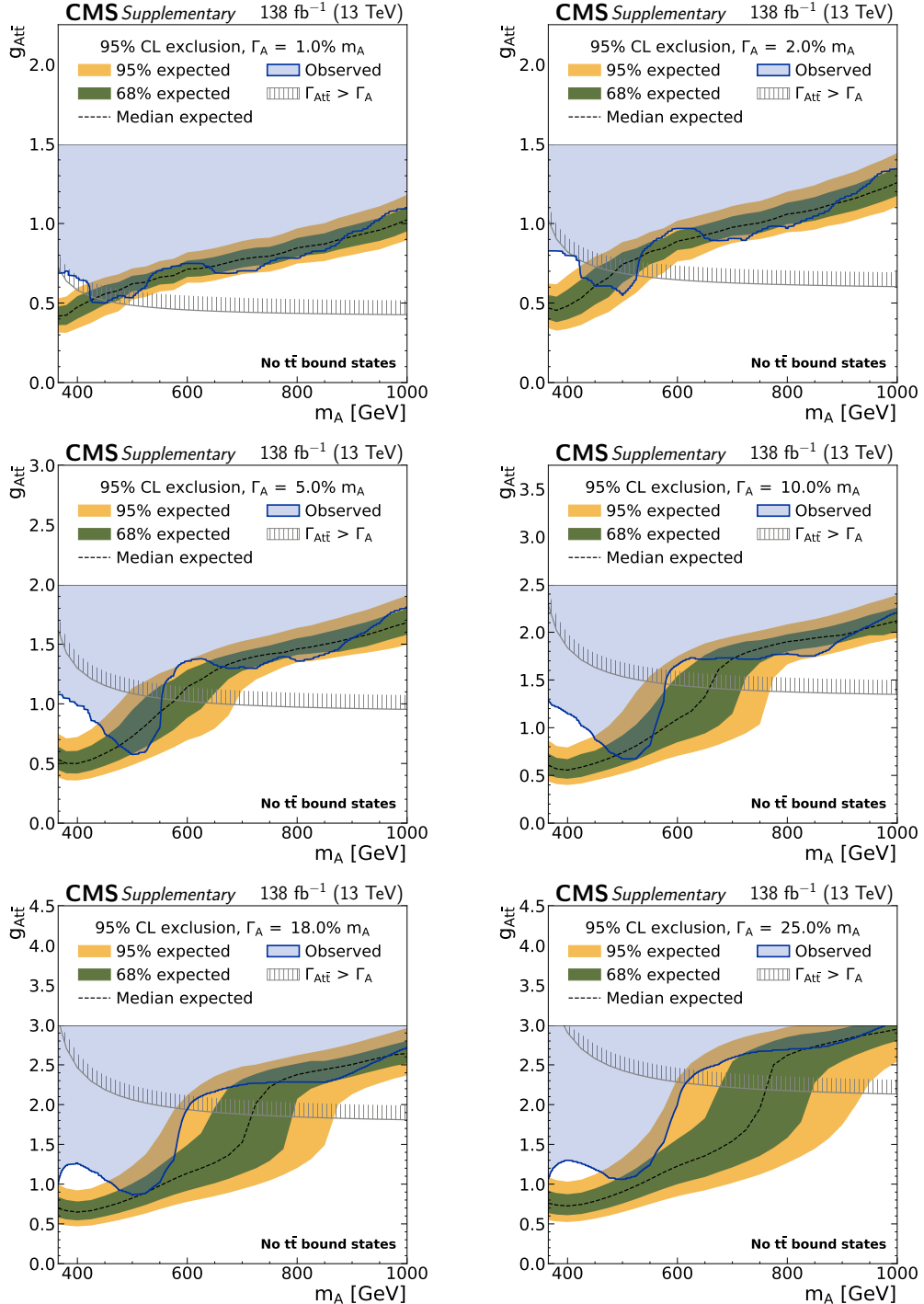


Figure 7.25: **Exclusion limits on $g_{A\bar{t}\bar{t}}$ in the “A only” scenario** in the dilepton channels as a function of the mass of the A boson for several relative widths. The observed limits are indicated by the blue shaded area, and the green and yellow bands indicate the regions containing 68 and 95% of limits expected under the SM hypothesis. The unphysical region of phase space in which the partial width $\Gamma_{A\rightarrow t\bar{t}}$ becomes larger than the total width of A is indicated by the hatched line.

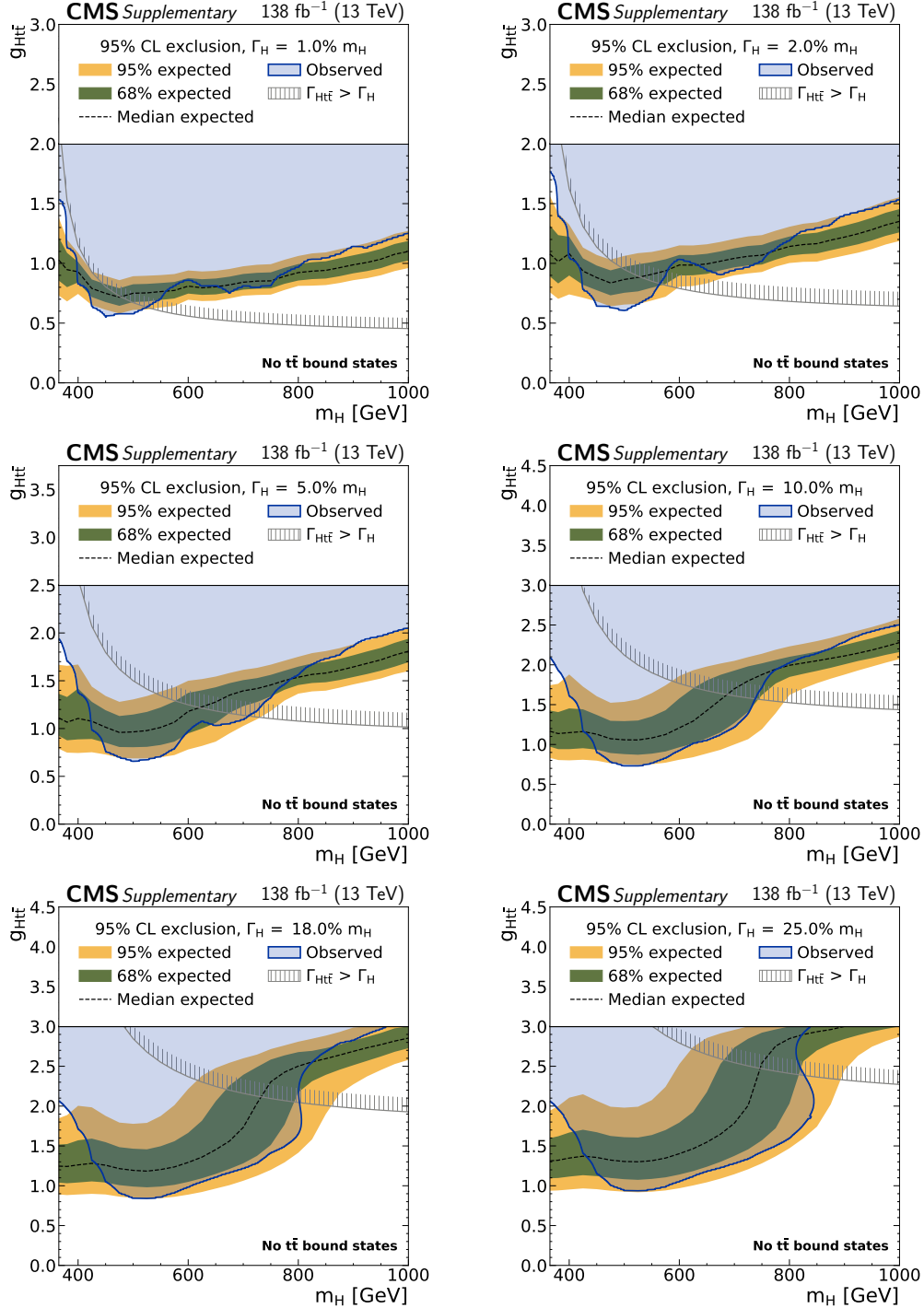


Figure 7.26: **Exclusion limits on g_{Htt} in the “H only” scenario** in the dilepton channels as a function of the mass of the H boson. Notations are equivalent to Fig. 7.25.

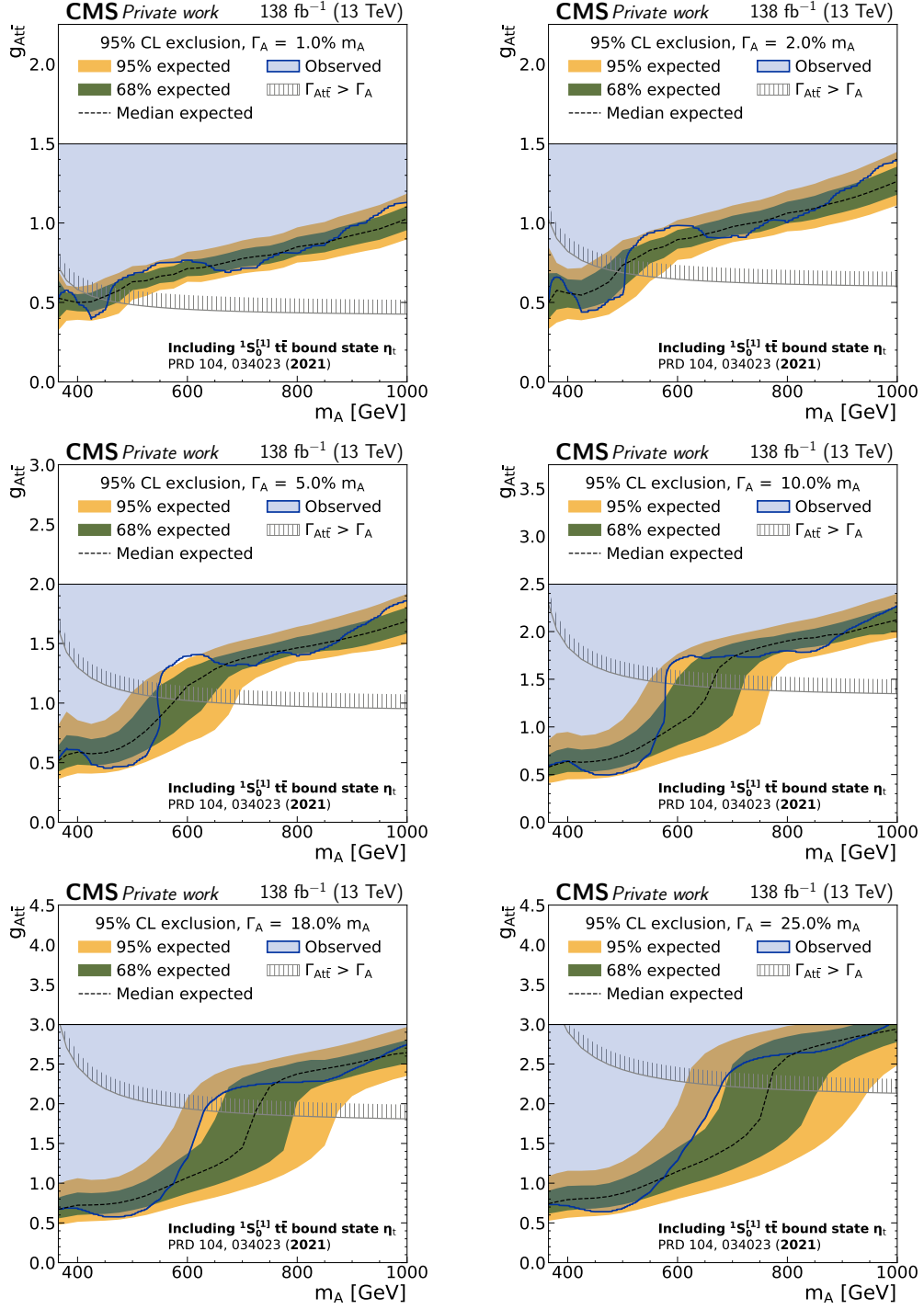


Figure 7.27: **Exclusion limits on $g_{A t\bar{t}}$ in the “A + η_t ” scenario** in the dilepton channels as a function of the mass of the A boson. Notations are equivalent to Fig. 7.25.

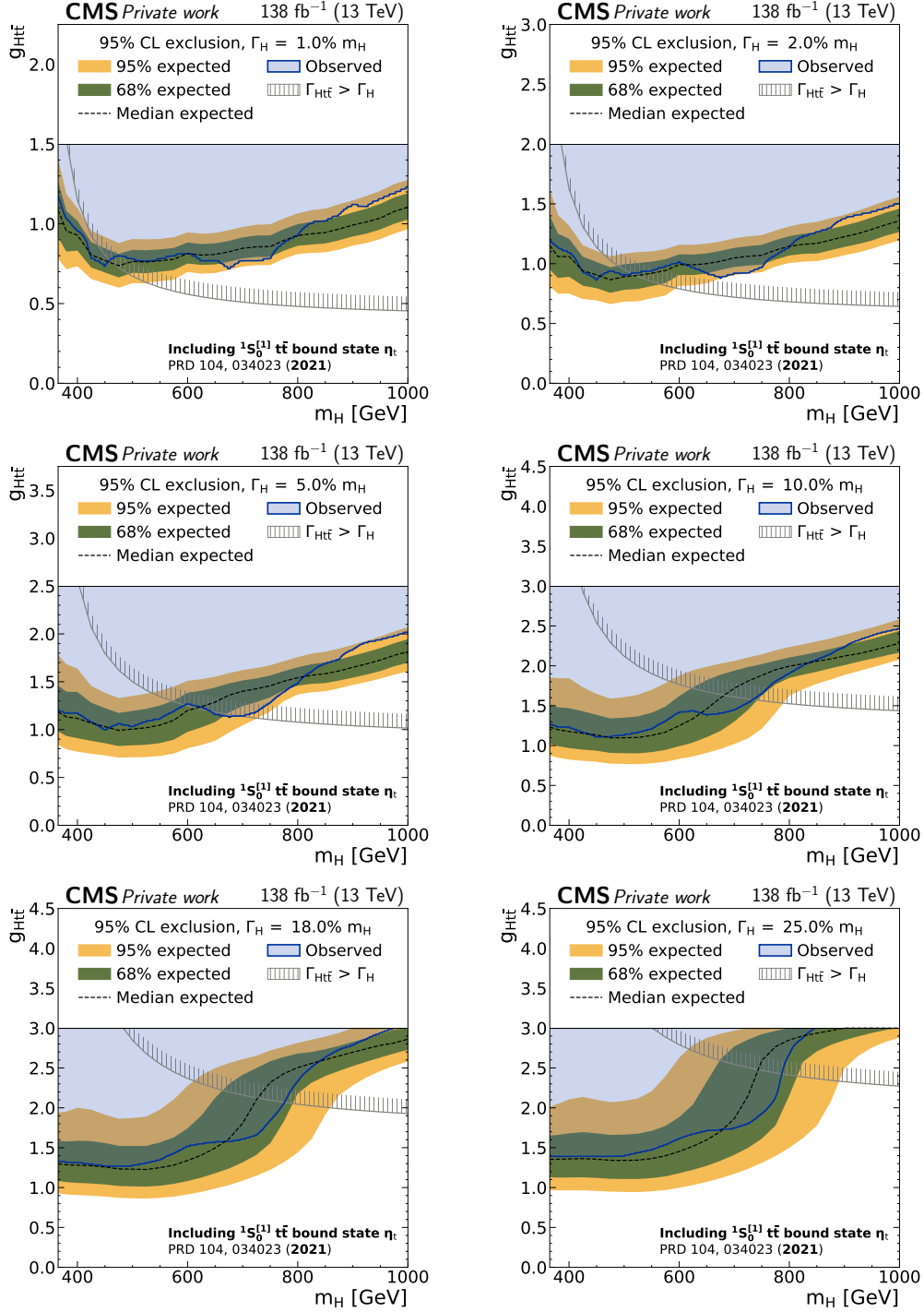


Figure 7.28: **Exclusion limits on g_{Htt} in the “ $H + \eta_t$ ” scenario** in the dilepton channels as a function of the mass of the H boson. Notations are equivalent to Fig. 7.25.

than for the scalar H, consistent with the results in Sec. 7.7.2. In the “A/H + η_t ” scenario, the excess is fully absorbed by the η_t contribution, and the observed and expected limits at low A/H masses agree. This is consistent with the slight preference of η_t over a low-mass A in the fit, as discussed in Sec. 7.7.5. By contrast, since the expected limits are calculated using pseudodata without η_t contribution, they change little between the scenarios.

Furthermore, the mild excess for H at high masses as seen in Fig. 7.23 is reproduced in the limits on $g_{Ht\bar{t}}$ in both scenarios in the approximate range of $900 < m_H < 1000$ GeV.

7.9 Combination with the ℓ +jets channels

So far, all results in this section have covered only the dilepton decay channel of $t\bar{t}$, which was analyzed as part of this thesis. In Ref. [9], the results on A/H bosons are combined with a separate analysis of the ℓ +jets decay channel. The combination (but not the ℓ +jets analysis) was also performed as part of this thesis, and is presented in this chapter. The ℓ +jets analysis strategy is roughly outlined in the following, for a more complete description, see Ref. [9].

7.9.1 Analysis strategy in the ℓ +jets channel

In the ℓ +jets channel, events with exactly one lepton and at least three jets are selected, of which at least two need to be b tagged. In addition to the criteria outlined in Sec. 7.2.2, both the lepton and the jets are required to fulfill $p_T > 30$ GeV to account for the higher single-lepton trigger thresholds. Furthermore, the cut-based identification criteria for electrons, as described in Ref. [113], are applied instead of MVA-based criteria. Similar as in the dilepton channel, the events are categorized by the flavor of the lepton into the e+jets and μ +jets channels.

The algorithm described in Ref. [229] is used to reconstruct the neutrino from the leptonic top decay. It enforces mass constraints on the W boson and leptonically decaying top quark and then minimizes the distance $D_\nu = |p_T^\nu - p_T^{\text{miss}}|$ between the neutrino p_T and the missing transverse momentum. In events with four or more jets, the same distance D_ν is then also used to assign the jets to the b and \bar{b} candidates as well as to the decay products of the hadronically decaying W boson. From this, the $t\bar{t}$ system can then be reconstructed. In events with exactly three jets, where information has been lost due to either an out-of-acceptance jet or the merger of two jets into one, additional steps have to be taken. The procedure described in Ref. [230] is applied to these events, which involves applying an energy correction factor to the four-momentum of the hadronically decaying top quark, depending on its reconstructed mass. Since the resolution of this procedure is necessarily worse than for events where all jets are available, events with three jets and four or more

3257 jets are treated as separate categories in the fit.

3258 A two-dimensional template is constructed from the reconstructed value of $m_{t\bar{t}}$
 3259 as well as $|\cos \theta_\ell^*|$, where θ_ℓ^* is the scattering angle of the leptonically decaying top
 3260 quark with respect to the direction of flight of the $t\bar{t}$ system in the laboratory frame.
 3261 This variable probes the total angular momentum J of the $t\bar{t}$ system, and is thus
 3262 sensitive to the spin of a possible mediator in $t\bar{t}$ production: For spin-0 mediators
 3263 like A/H ($J = 0$), the top quarks are emitted isotropically in the $t\bar{t}$ rest frame,
 3264 leading to a flat distribution of $|\cos \theta_\ell^*|$. By contrast, SM $t\bar{t}$ production consists of
 3265 a mixture of different J states. At the $t\bar{t}$ threshold, gg initial states with $J = 0$
 3266 dominate, leading to only small deviations from a flat $|\cos \theta_\ell^*|$ distribution and low
 3267 discriminating power. However, for high $m_{t\bar{t}}$, $q\bar{q}$ initial states with $J = 1$ are more
 3268 important, leading to a peak for high $|\cos \theta_\ell^*|$.⁵ Furthermore, $|\cos \theta_\ell^*|$ not sensitive
 3269 to the \mathcal{CP} structure of the mediator, in contrast to c_{hel} and c_{han} .

3270 The $t\bar{t}$ and tW background predictions as well as the A/H signals are estimated
 3271 using the same MC simulation as in the dilepton channels. Additionally, there is a
 3272 significant background contribution from QCD multijet production with a fake or
 3273 non-prompt lepton as well as EW processes such as W+jets production. These are
 3274 difficult to model using MC, and are instead estimated together by a data-driven
 3275 approach (cf. Sec. 5.3.2). A sideband in which the b tagging requirement on the
 3276 jets is inverted is used for this purpose; details can be found in Ref. [9].

3277 The dilepton and ℓ +jets channels are directly combined by performing a simu-
 3278 taneous likelihood fit to all categories. All systematic uncertainties described in
 3279 Sec. 7.5 are applied in both channels as long as they are applicable, and the chan-
 3280 nels are always treated as fully correlated whenever an uncertainty is applicable in
 3281 both. Furthermore, in the ℓ +jets channel, additional uncertainties related to the
 3282 single-lepton trigger efficiencies and to the data-driven EW+QCD background es-
 3283 timation are applied [9]. An overview over all systematic uncertainties is given in
 3284 Tab. 7.7.

3285 Again, both the “A/H only” and “A/H + η_t ” scenarios are considered. For the
 3286 latter, the ℓ +jets analysis uses a slightly different η_t model, in which the width of
 3287 the bound state is set to $\Gamma(\eta_t) = 7 \text{ GeV}$ and a cut on the invariant mass $m_{WWb\bar{b}}$
 3288 is applied, as described in Sec. 2.2.3. For the sake of consistency, the same model
 3289 is also used in the dilepton channels when performing the combination only. The
 3290 resulting impact on the limits from the choice of η_t model is expected to be small.

3291 7.9.2 A/H limits

3292 The resulting observed and expected limits for the combination of both channels
 3293 are found in Figs. 7.29 to 7.32 for both scenarios. It can be seen that the large

⁵ $q\bar{q}$ initial states with $J = 0$ are forbidden at LO in QCD since the production proceeds through a spin-1 gluon in the s channel.

Uncertainty	Processes	Channels
Jet energy scale	all	all
Jet energy resolution	all	all
Unclustered p_T^{miss}	all	all
b tagging efficiency	all	all
b tagging misidentification	all	all
Single-electron trigger	all	e+jets
Single-muon trigger	all	$\mu+$ jets
Dilepton triggers	all	dilepton
Electron ID	all	e+jets, ee, e μ
Muon ID	all	$\mu+$ jets, e μ , $\mu\mu$
ECAL L1 trigger inefficiency	all	all
Pileup	all	all
Integrated luminosity	all	all
Top quark Yukawa coupling	$t\bar{t}$	all
EW correction scheme	$t\bar{t}$	all
Top quark mass	$t\bar{t}$, A/H, η_t	all
Matrix element scales	$t\bar{t}$, A/H, η_t , single t, Z+jets	all
Parton shower scales	$t\bar{t}$, A/H, η_t , single t, Z+jets	all
Color reconnection	$t\bar{t}$	all
ME-PS matching (h_{damp})	$t\bar{t}$	all
Underlying event tune	$t\bar{t}$	all
PDF	$t\bar{t}$	all
Single top normalization	single t	all
EW+QCD normalization	EW+QCD	$\ell+$ jets
EW+QCD shape	EW+QCD	$\ell+$ jets
$t\bar{t} + X$ normalization	$t\bar{t} + X$	dilepton
Z+jets normalization	Z+jets	dilepton
Diboson normalization	Diboson	dilepton

Table 7.7: **Systematic uncertainties in the channel combination.** An overview of the systematic uncertainties in the channel combination, including the processes and channels considered. All uncertainties that are applicable to both dilepton and $\ell+$ jets channels, as given in the rightmost column, are considered correlated between them.

³²⁹⁴ excess for low A/H masses is still present in the channel combination in the “A/H only” scenario, and is again stronger for the pseudoscalar A. The mild excess for ³²⁹⁵ the scalar H at $m_H \approx 925$ GeV, on the other hand, is not confirmed in the channel ³²⁹⁶ combination.
³²⁹⁷

³²⁹⁸ To assess the impact of the different channels, the expected limits for the dilepton

and ℓ +jets channels alone are also shown in red and orange, respectively. For most of the phase space, the ℓ +jets channel leads to stronger limits than the dilepton channel, which is mostly due to the higher branching ratio and thus higher available statistics as well as the better $m_{t\bar{t}}$ resolution in the ℓ +jets channel especially at high $m_{t\bar{t}}$. The difference is large at high A and H masses, where the contribution from the dilepton channels is rather small, while the dilepton channel becomes much more important for low masses, i.e. close to the $t\bar{t}$ threshold. This is because of the lack of sensitivity of $|\cos \theta_\ell^*|$ close to the $t\bar{t}$ threshold, while c_{hel} and c_{han} do not suffer from such a problem. For H at low masses in particular, the dilepton channel in fact gives stronger limits than ℓ +jets due to the sensitivity of c_{han} to scalar mediators.

7.9.3 Simultaneous A+H exclusion contours

In many possible BSM scenarios, multiple additional spin-0 states are expected at the same time, such as A and H in e.g. the 2HDM (cf. Sec. 2.3.2). Often, the masses of these scalars are close together since they originate from new physics at the same energy scale, in which case their signatures would not easily factorize. It is thus useful for future interpretations of the results to show exclusion contours not only for either A or H, but for the simultaneous presence of both.

To do so, simultaneous fits are performed with both A and H as freely floating signals as in Sec. 7.7.4. Frequentist exclusion contours are set with the Feldman–Cousins prescription [231, 232], in which the test statistic is numerically evaluated using toy experiments at each point in the $g_{A\bar{t}t}\text{-}g_{H\bar{t}t}$ plane. This procedure is fully correct in the Frequentist sense and does not rely on approximations of the test statistic, which are not guaranteed to hold for two non-linear signals, but is computationally expensive.

Due to this, combined with the large four-dimensional phase space of possible signals, only a few example mass and width points are shown in this work, and only for the dilepton and ℓ +jets combination in the “A/H + η_t ” scenario. They can be found in Fig. 7.33 for the case of identical A and H masses as well as in Fig. 7.34 for differing A and H masses. Alternatively, a coarse scan of the negative log-likelihood of the full span is available online as part of the HepData record [233].

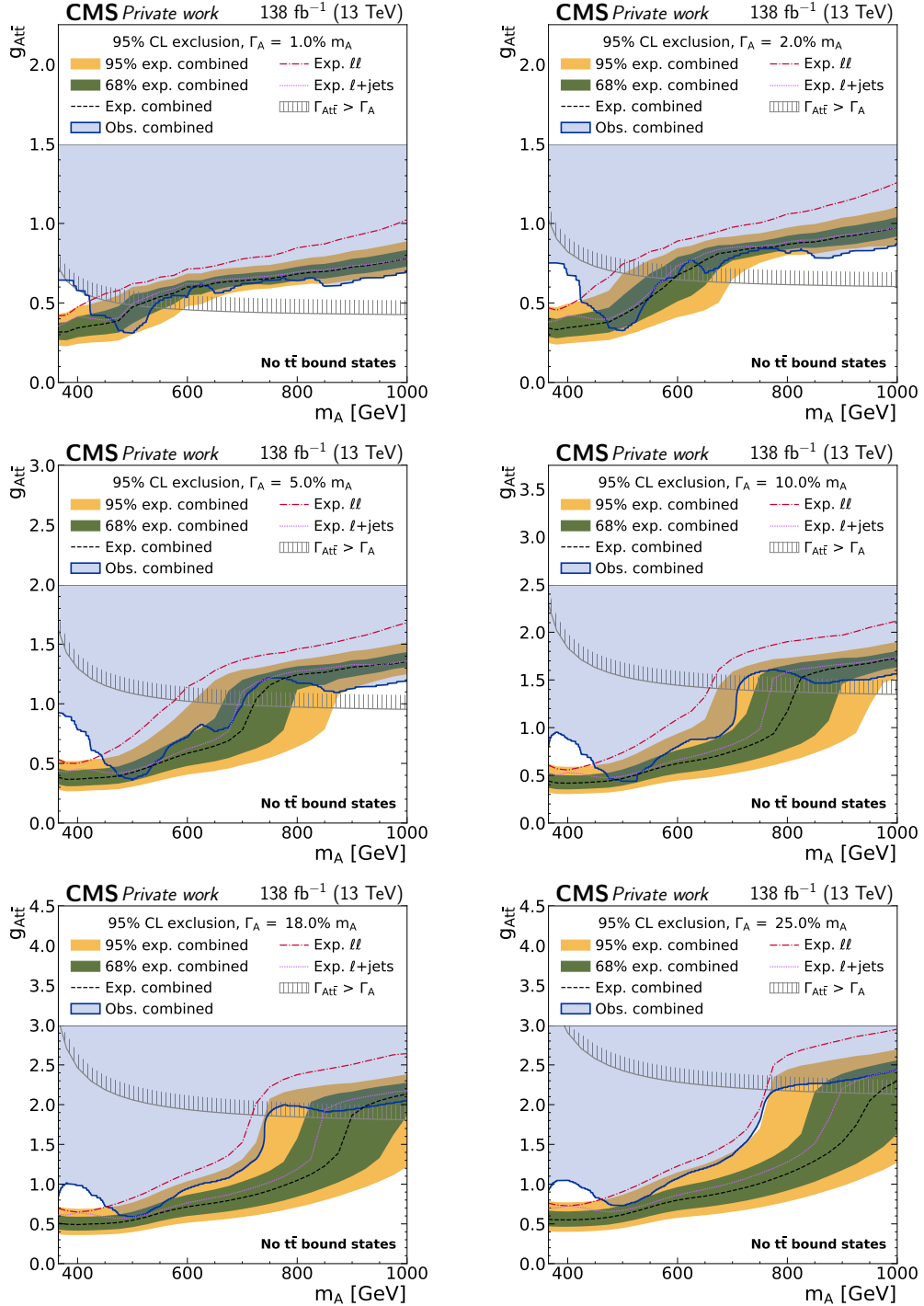


Figure 7.29: **Combined exclusion limits on $g_{At̄}$ in the “A only” scenario** in the dilepton and $\ell+jets$ channels as a function of the mass of the A boson. The expected limits in the dilepton and $\ell+jets$ channels alone are shown as the red and purple lines for comparison. Otherwise, notations are equivalent to Fig. 7.25. *Figure adapted from Ref. [9].*

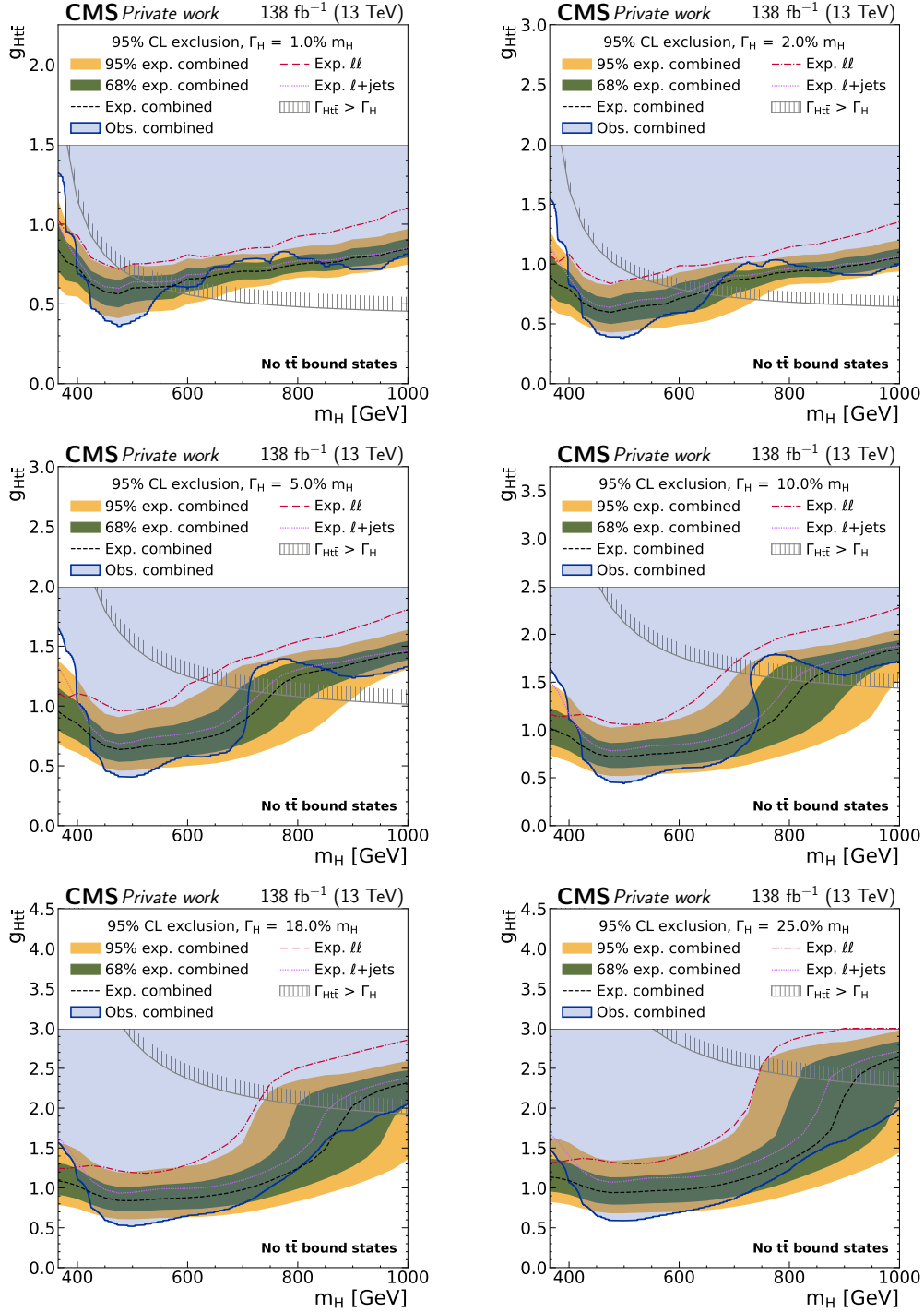


Figure 7.30: **Combined exclusion limits on $g_{H\bar{t}}$ in the “H only” scenario** in the dilepton and ℓ +jets channels as a function of the mass of the H boson. Notations are equivalent to Fig. 7.29. *Figure adapted from Ref. [9].*

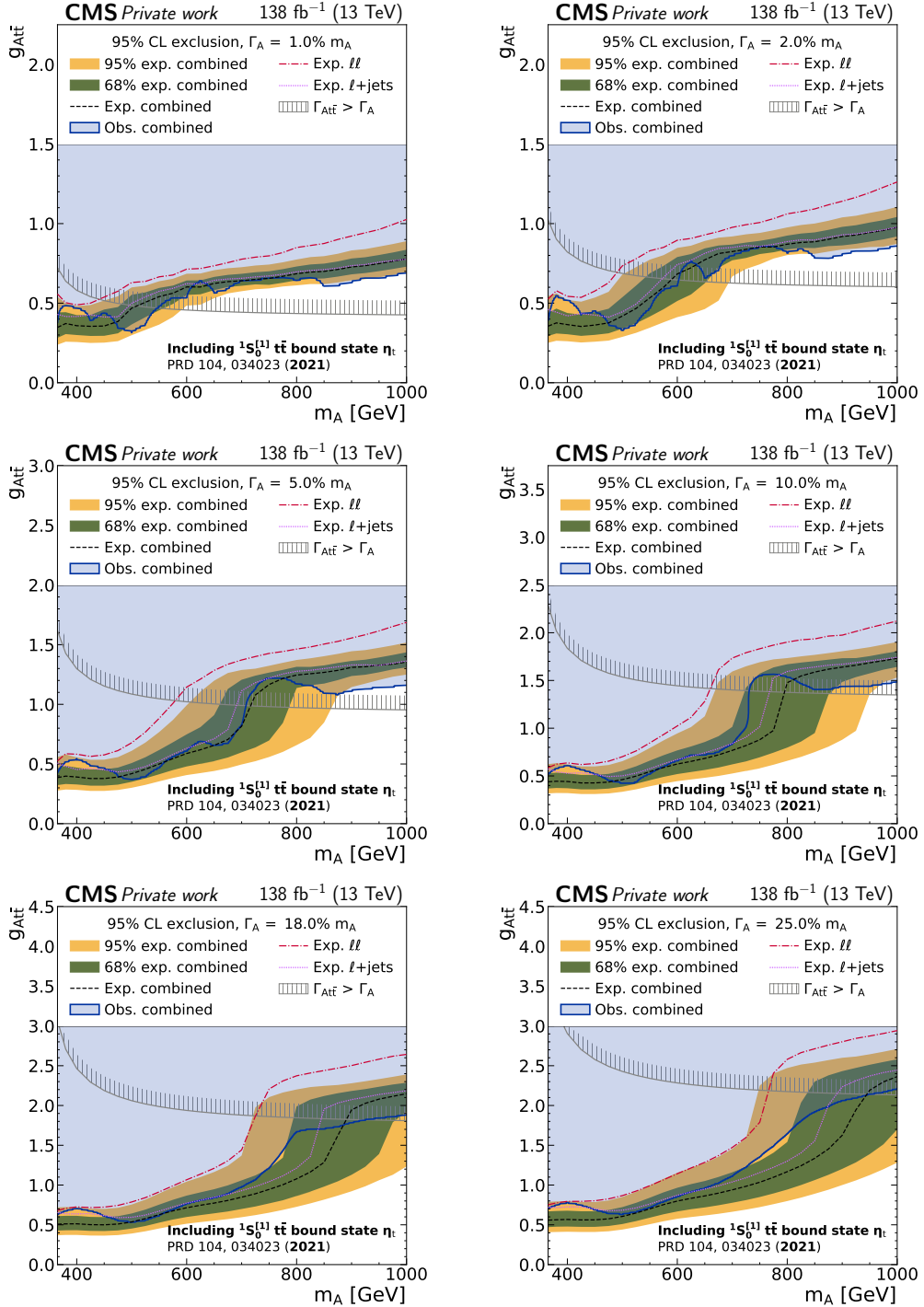


Figure 7.31: **Combined exclusion limits on $g_{A\bar{t}\bar{t}}$ in the “A + η_t ” scenario** in the dilepton and $\ell+jets$ channels as a function of the mass of the A boson. Notations are equivalent to Fig. 7.29. *Figure adapted from Ref. [9].*

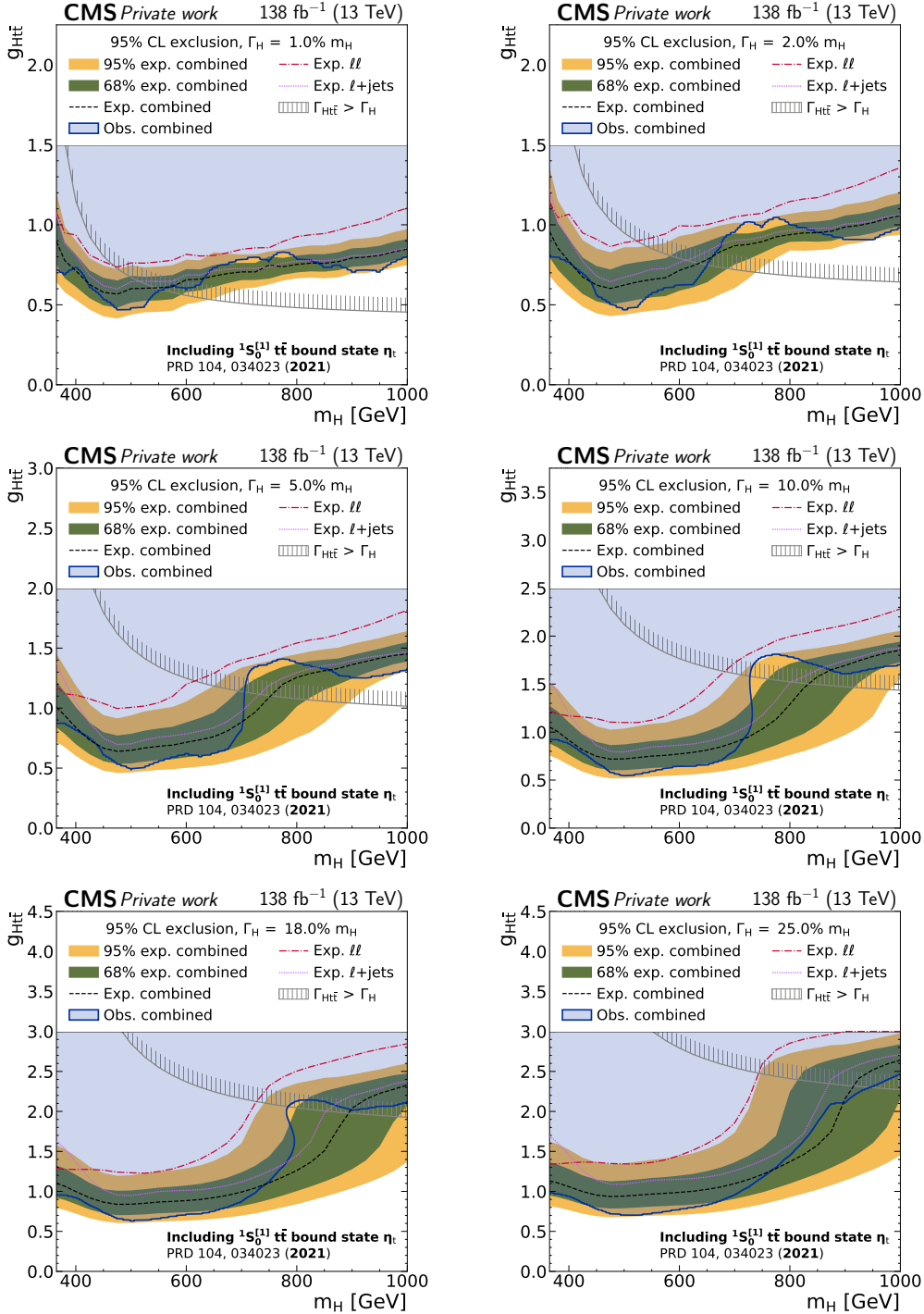


Figure 7.32: **Combined exclusion limits on $g_{Ht\bar{t}}$ in the “H + η_t ” scenario** in the dilepton and ℓ +jets channels as a function of the mass of the H boson. Notations are equivalent to Fig. 7.29. *Figure adapted from Ref. [9].*

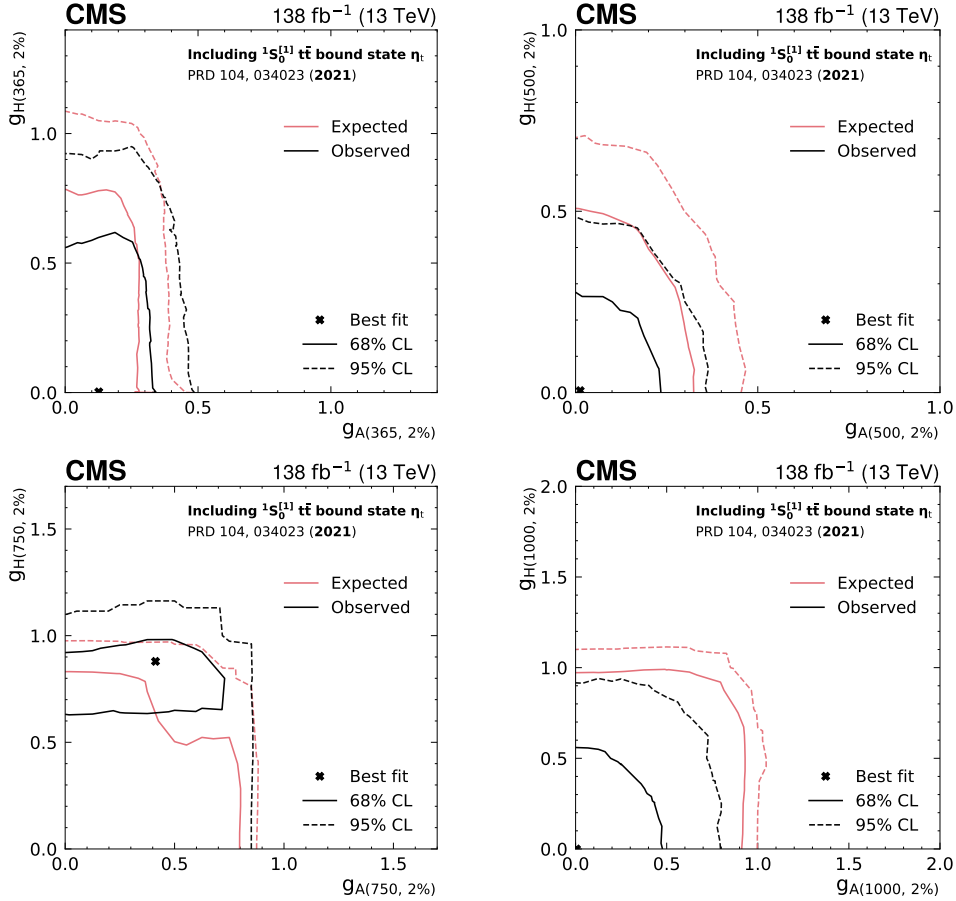


Figure 7.33: **Frequentist 2D exclusion contours for $g_{A t\bar{t}}$ and $g_{H t\bar{t}}$** for four different signal hypotheses with identical A and H masses of 365 GeV (upper left), 500 GeV (upper right), 750 GeV (lower left) and 1000 GeV (lower right), all assuming a width of 2%. In all cases, η_t production is added to the background. *Figure taken from Ref. [9].*

3329 7.10 Comparison to other results

3330 7.10.1 ATLAS $t\bar{t}$ threshold measurement

3331 After this work was made public, the ATLAS Collaboration presented preliminary
 3332 results for a similar measurement at the $t\bar{t}$ threshold in Ref. [190], which confirmed
 3333 the presence of a pseudoscalar excess over the $t\bar{t}$ continuum prediction.

3334 The ATLAS result uses a very similar setup as presented in this work. It like-
 3335 wise considers only the dilepton decay channel of $t\bar{t}$, uses the full Run 2 dataset
 3336 (corresponding to 140 fb^{-1} for ATLAS), reconstructs the $t\bar{t}$ system using a similar
 3337 algorithm, and finally bins in $m_{t\bar{t}}$, c_{hel} and c_{han} to extract the $t\bar{t}$ bound state compo-

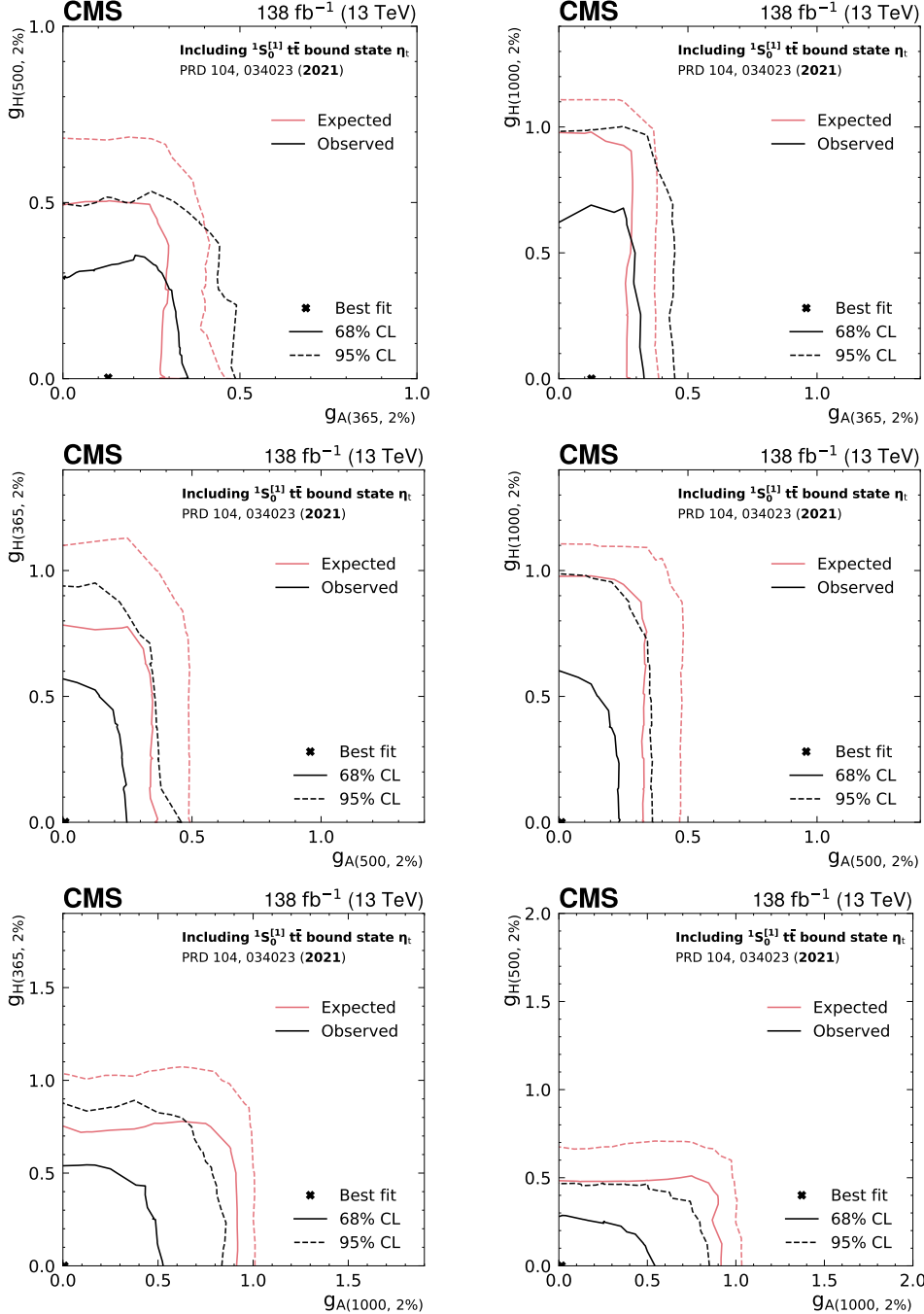


Figure 7.34: **Frequentist 2D exclusion contours for $g_{A\bar{t}\bar{t}}$ and $g_{H\bar{t}\bar{t}}$** for six different signal hypotheses with differing A and H masses, corresponding to combinations of 365 GeV, 500 GeV and 1000 GeV, all assuming a width of 2%. In all cases, η_t production is added to the background. *Figure taken from Ref. [9].*

3338 nent using a simplified model. The binning in c_{hel} and c_{han} is identical to this work,
 3339 while in $m_{t\bar{t}}$ only four bins of 50 GeV width around the $t\bar{t}$ threshold are considered.
 3340 Events with high values of $m_{t\bar{t}}$ are rejected. In the following, some further significant
 3341 differences between the CMS and ATLAS results are briefly described.

3342 First, ATLAS considers two additional sets of control regions (CRs) which are
 3343 directly included in the likelihood fit. One is defined by requiring $m_{\ell\ell}$ to be within the
 3344 vicinity of the Z boson mass, similar to the Z+jets scale factor estimation described
 3345 in Secs. 5.3.2 and 7.2.4, and serves the same purpose of correcting the yield of the
 3346 Z+jets simulation after the b tagging requirement. The other set of CRs targets
 3347 fake or non-prompt leptons and is defined by requiring the two selected leptons to
 3348 have the same charge. The dominant contribution here comes from $t\bar{t} \rightarrow \ell + \text{jets}$
 3349 events with an additional fake or non-prompt lepton. Such a CR is not included
 3350 in the CMS result; it has however been internally checked using a similar selection
 3351 that the data is well-described by the $t\bar{t} \rightarrow \ell + \text{jets}$ MC simulation.

3352 Second, ATLAS employs a different systematics model, in particular for uncer-
 3353 tainties related to the modeling of the $t\bar{t}$ continuum. Notable differences are:

- 3354 • the ME scale uncertainties are estimated at NNLO by varying the scales in
 3355 the reweighting to NNLO QCD and NLO EW (which is performed using the
 3356 same tools as used here);
- 3357 • no uncertainty due to a variation of the top-SM Higgs Yukawa coupling is
 3358 considered;
- 3359 • two-point uncertainties comparing the **hvq** + PYTHIA prediction to **hvq** +
 3360 herwig as well as to **bb41** + PYTHIA are included in the nominal result, similar
 3361 as in Ref. [8] and in Sec. 7.7.3; these uncertainties are treated as partially (50%)
 3362 decorrelated between the nine bins of c_{hel} and c_{han} ;
- 3363 • an additional ME-PS matching uncertainty is defined by varying the parameter
 3364 p_T^{hard} in PYTHIA [87];
- 3365 • an additional uncertainty due to the top recoil scheme in PYTHIA (cf. Sec. 6.5.3)
 3366 is considered.

3367 In total, this results in significantly more degrees of freedom in the fit used by
 3368 ATLAS than the one used by CMS.

3369 Third, the nominal model used by ATLAS to probe $t\bar{t}$ bound state effects is based
 3370 on Ref. [42], which includes a matrix-element level reweighting to an NRQCD cal-
 3371 culation. As discussed in Sec. 2.2.3, this model could not be sufficiently scrutinized
 3372 for inclusion in the results of this work, and particularly the modeling of spin corre-
 3373 lations and the matching to the $t\bar{t}$ continuum is under question. Using this model,
 3374 ATLAS extracts a cross section of $9.0 \pm 1.3 \text{ pb}$ [190].

3375 However, ATLAS also provides results using the same η_t model considered in
3376 this work, using the same values for the η_t mass and width, which gives $\sigma(\eta_t) =$
3377 $13.4 \pm 1.9 \text{ pb}$ [190]. This figure is more appropriate to compare to the result of this
3378 work, $\sigma(\eta_t) = 8.7 \pm 1.1 \text{ pb}$. The results are thus in tension with each other at the
3379 level of ca. 2 standard deviations. Since the ATLAS results are preliminary and
3380 very recent at the time of writing, the source of this tension is not yet known. It
3381 will be the task of future studies and comparisons between the experiments to shed
3382 further light on this topic.

3383 7.10.2 ATLAS A/H $\rightarrow t\bar{t}$ search

3384 Before the appearance of this result and Ref. [190], the ATLAS collaboration pre-
3385 sented a similar search for heavy pseudoscalar or scalar bosons in $t\bar{t}$ events using
3386 the full LHC Run 2 data set in Ref. [189], and observed no excess at the $t\bar{t}$ thresh-
3387 old. To decide whether that result contradicts the one presented here as well as the
3388 preliminary ATLAS result of Ref. [190], it is necessary to understand the differences
3389 between the analyses.

3390 Ref. [189] combines the dilepton and ℓ +jets decay channels of $t\bar{t}$, similar to the
3391 combination presented in Sec. 7.9 for A and H, though the definitions of the chan-
3392 nels are different: In the ℓ +jets channel, ATLAS does not consider events with only
3393 three jets as described in Sec. 7.9.1, but instead includes events with only one b
3394 tag in addition to events with two or more b tags. Furthermore, ATLAS defines an
3395 additional category with ℓ +jets events in which the decay products of the hadroni-
3396 cally decaying top quark are merged, though this is expected to contribute mostly
3397 at high $m_{t\bar{t}}$.

3398 In the dilepton channels, Ref. [189] uses a fundamentally different strategy than
3399 the one presented in this work. Instead of performing an explicit $t\bar{t}$ reconstruction,
3400 thus giving access to $m_{t\bar{t}}$ and the spin correlation observables c_{hel} and c_{han} , Ref. [189]
3401 uses the invariant mass $m_{b\bar{b}\ell\ell}$ of the visible decay products as well as $\Delta\phi_{\ell\ell}$, the
3402 azimuthal distance between the two leptons in the laboratory frame. The former
3403 can be considered a proxy for $m_{t\bar{t}}$, though with significant smearing due to the loss
3404 of information from the two neutrinos, as also studied in Sec. 7.7.3. The latter has
3405 indirect sensitivity to the $t\bar{t}$ spin correlation, but this sensitivity is intermixed with
3406 kinematic information due to the boosts of the leptons from their top quark parents.
3407 As a result, it is known to be hard to model accurately and affected by theoretical
3408 uncertainties [27, 234].

3409 Combining all these differences, it is expected that the dilepton channels in
3410 Ref. [189] give only subdominant sensitivity compared to the ℓ +jets channels. In
3411 this work, while the situation is similar for high $m_{t\bar{t}}$, the dilepton channels contribute
3412 significantly close to the $t\bar{t}$ threshold. Furthermore, the direct use of spin corre-
3413 lation information means that the effect of many systematic uncertainties which only
3414 affect the kinematics is lessened greatly, as elaborated on in Sec. 7.7.3. It has been

checked internally that adopting the strategy employed in Ref. [189] for the dilepton channels in this work would lead to a greatly lessened sensitivity at the $t\bar{t}$ threshold, and likely no claims of a significant excess.

A further cause of differences could be the different treatment of systematic uncertainties, similar as in Ref. [190]. Ref. [189] considers additional nuisance parameters for the modeling of the $t\bar{t}$ continuum regarding the choice of parton shower (PYTHIA vs. HERWIG), the choice of calculation for the top quark decay (POWHEG vs. MADSPIN), and the choice of PDF in the calculation of the NNLO QCD and NLO EW corrections. The first of these has been studied here in Sec. 7.5.4, and found to not influence the results strongly in the dilepton channels due to the effect of c_{hel} . However, the important uncertainties due to the top quark Yukawa coupling and the EW correction scheme are not included in Ref. [189], since the EW corrections are calculated in a different manner. Moreover, several significant uncertainties are treated as decorrelated between different bins of the angular variables $\cos\theta^*$ and $\Delta\phi_{\ell\ell}$, which could reduce the sensitivity gained from these variables.

Since no explicit signal model for a $t\bar{t}$ bound state is considered in Ref. [189], the expected sensitivities to η_t cannot be directly compared. Instead, the closest considered signal is the generic pseudoscalar A at a mass of 400 GeV, higher than the minimum of 365 GeV considered here. Since a non-negligible excess is still present at that value both in the dilepton channels alone (Fig. 7.25) and in the combination with $\ell+\text{jets}$ (Fig. 7.29), while no such excess is visible in Fig. 15 of Ref. [189], the choice of signals is not the cause of the differences on its own. However, the shape difference between A at 400 GeV including the SM interference and η_t is not negligible. It is conceivable that, if the excess truly originates from a $t\bar{t}$ bound state manifesting as a narrow peak at the $t\bar{t}$ threshold, fitting the non-matching A signal to the data will worsen the issues due to modeling and systematic uncertainties as described in the previous paragraphs.

Even with all this information, it is not fully clear whether the result of this work and the preliminary ATLAS result in Ref. [190] on the one hand and the ATLAS result in Ref. [189] on the other hand should be considered in conflict with each other or not. Together with the cross-checks performed in Sec. 7.7.3, it seems likely that the $t\bar{t}$ kinematic reconstruction in the dilepton channels, in particular the access to spin correlation, is the most important difference.

7.10.3 Other $t\bar{t}$ measurements

While this work constitutes the first time that an excess consistent with a $t\bar{t}$ bound state has been observed with a large significance, there have been hints for such an effect in other $t\bar{t}$ measurements. First, several measurements of unfolded $t\bar{t}$ differential cross sections have observed excesses in data compared to MC predictions of the $t\bar{t}$ continuum at low invariant masses, such as $m_{t\bar{t}}$ in dilepton events [235], $m_{\ell\ell}$ in $e\mu$ events [236], and $m_{t\bar{t}}$ in $\ell+\text{jets}$ events [222]. The significances of these

3455 excesses vary depending on the MC generator the data is compared to, and are also
 3456 strongly influenced by systematic uncertainties for the two $m_{t\bar{t}}$ measurements.

3457 Secondly, the measurements of quantum entanglement in $t\bar{t}$ pairs in the dilepton
 3458 channel presented in Refs. [29, 30] measure as a sensitive observable the value of
 3459 D , i.e. the slope of c_{hel} (cf. Sec. 2.2.1), for low $m_{t\bar{t}}$ events. This is very similar
 3460 in spirit to the observables $m_{t\bar{t}}$ and c_{hel} used in the dilepton channel of this work,
 3461 though the measurement is only performed one-dimensionally in c_{hel} instead of the
 3462 3D $m_{t\bar{t}} \times c_{\text{hel}} \times c_{\text{han}}$ template used here. In both Refs. [29, 30], a smaller (i.e. more
 3463 negative) value of D is observed in data compared to MC $t\bar{t}$ continuum predictions,
 3464 though the significance is only at the level of one SD. This can be interpreted as
 3465 a hint for the presence of an additional pseudoscalar contribution from a $t\bar{t}$ bound
 3466 state, consistent with the results of this work.

3467 7.11 Summary and Outlook

3468 In this chapter, a generic search for spin-0 states in $t\bar{t}$ events with the full data of
 3469 LHC Run 2 was presented, targeting the dilepton decay channel of $t\bar{t}$. In addition
 3470 to the invariant mass $m_{t\bar{t}}$, it uses the spin correlation variables c_{hel} and c_{han} to probe
 3471 the spin and \mathcal{CP} structure of $t\bar{t}$ and possible new particles.

3472 A statistically significant excess was observed in data for low $m_{t\bar{t}}$ events, close to
 3473 the $t\bar{t}$ production threshold, showing spin correlations consistent with a pseudoscalar
 3474 state. This excess is interpreted as a pseudoscalar $t\bar{t}$ quasi-bound state η_t , which is
 3475 expected to be present in the SM according to NRQCD calculations. A simplified
 3476 model for the production of η_t is used to measure its cross section, yielding $\sigma(\eta_t) =$
 3477 $8.7 \pm 1.1 \text{ pb}$. Several cross-checks of this result, relaxing assumptions on the $t\bar{t}$
 3478 kinematic reconstruction as well as considering alternative MC generator setups,
 3479 validate the observed excess. This result represents the first observation of η_t .

3480 Alternatively, the excess could be interpreted as an additional pseudoscalar boson
 3481 A , with mass close to the $t\bar{t}$ threshold. While the explanation as a $t\bar{t}$ bound state
 3482 might be favored *a priori* as it is part of the SM and does not invoke any new
 3483 physics, experimentally the two interpretations cannot be distinguished with the
 3484 current resolution. In addition to the interpretation of the excess, exclusion limits
 3485 are set on new pseudoscalar or scalar bosons A/H through their coupling strengths
 3486 to the top quark, allowing for either one or both of these bosons simultaneously.
 3487 They are presented for two scenarios, where the observed excess is either assumed
 3488 to be fully described by the bound state η_t or fully by the new boson A . These limits
 3489 are further combined with a separate analysis targeting the $\ell+\text{jets}$ decay channel of
 3490 $t\bar{t}$.

3491 It is clear that much remains to be studied about the excess observed in this
 3492 work. Firstly, the interpretation in terms of η_t presented here is performed only
 3493 in the dilepton channels. In the preliminary results of Ref. [191], the combination

with the ℓ +jets channels was also performed for the measurement of the η_t cross section; however, since the ℓ +jets analysis used was not optimized for signals at the $t\bar{t}$ threshold, little sensitivity could be gained compared to the dilepton channels alone. Instead, a separate ℓ +jets analysis optimized for a $t\bar{t}$ bound state should be performed in the future. In particular, spin correlation variables analogous to c_{hel} and c_{han} could be defined also in the ℓ +jets channel, as has already been done in Ref. [28] through ML-based identification of the decay products of the hadronically decaying top quark. Further sensitivity in both channels could possibly be gained from leveraging color flow observables [237, 238] to distinguish the color-singlet η_t and A/H from the dominant color-octet $t\bar{t}$ contribution.

By contrast, in the dilepton channel, the most pressing targets of improvement are the kinematic reconstruction and the $t\bar{t}$ modeling uncertainties. For the former, it would again be useful to investigate ML-based reconstruction techniques, for which several proof-of-concept studies have already been performed [192, 239], in a realistic setup. For the latter, the differences between different generator setups, as briefly studied in Sec. 7.5.4, needs to be understood more deeply. It would be ideal to cover the difference between predictions by a set of well-motivated nuisance parameters with clear physical meaning, as has been recently used by CMS in the measurement of the W boson mass [78, 240]. Extending this approach to the $t\bar{t}$ process however requires many theoretical advancements, and is likely to lie far in the future for now. In a similar fashion, it will be required to obtain a more precise prediction for the $t\bar{t}$ bound state itself. A possible approach here, involving the reweighting of $t\bar{t}$ events by the ratio of Green's functions, is presented in Ref. [42], though this remains to be validated.

To further sidestep the issue of imperfect modeling of both η_t and the $t\bar{t}$ continuum, one could attempt to observe the $t\bar{t}$ bound state in other decay channels, the most promising being the decay to two photons, $\eta_t \rightarrow \gamma\gamma$. This final state is experimentally extremely clean and does not require MC modeling of the $\gamma\gamma$ background. Instead, a possible signal could be extracted using a parametric fit of a peak over a falling background, similar to the measurement of the SM Higgs boson in the $h \rightarrow \gamma\gamma$ channel. The most important obstacle in such a project would be the small branching ratio of η_t to $\gamma\gamma$. Extrapolations of the partial width to $\gamma\gamma$ from $b\bar{b}$ and $c\bar{c}$ bound states [241], combined with an expected total width of $\Gamma(\eta_t) \approx 2m_t$, predict a branching ratio of $\approx 2 \times 10^{-5}$, though this is a rough estimate that could be wrong by as much as an order of magnitude. If this prediction holds, it might be possible to probe this decay channel with the full statistics collected in Runs 2 and 3 of the LHC. Moreover, a measurement of the ratio of branching fractions to $\gamma\gamma$ and $t\bar{t}$ could help distinguish a bound state from possible BSM scenarios.

It is further necessary, of course, to repeat the analysis presented here with the data of LHC Run 3, ideally combining the results. While the η_t cross section, and similarly A/H limits at low masses, are dominated by systematic effects, especially the sensitivity at high A and H masses is limited by the statistics of the data. The

increase in center-of-mass energy from 13 to 13.6 TeV will also help increase the cross section of high-mass signals, together making it possible to extend the probed A/H mass range to higher values.

Furthermore, concerning the limits on A and H derived here, the next step is to include these generic exclusion limits into concrete bounds on BSM models of interest. A particular such model, the production of heavy Axion-Like Particles coupling to top quarks, is studied on a phenomenological basis in the following chapter.

3544 **8 Investigation of Axion-Like Particles**
3545 **decaying to $t\bar{t}$**

3546 **8.1 Introduction**

3547 Following the results of Chapter 7 including the interpretations as generic scalar or
3548 pseudoscalar bosons and $t\bar{t}$ bound states, this chapter is dedicated to Axion-Like
3549 Particles decaying to $t\bar{t}$. As explained in Sec. 2.3.3, the coupling structure of ALPs
3550 to top quarks is identical to those of the generic pseudoscalar A, such as e.g. in
3551 the 2HDM, if the basis for the ALP is chosen appropriately (cf. Eq. (2.23)). The
3552 difference comes from the gluon interaction term, which is absent for the model used
3553 for A in Chapter 7, and which results in an additional diagram where the ALP is
3554 produced through a contact interaction with the gluons.

3555 If the coefficient $c_{\tilde{G}}$ of the ALP-gluon interaction term in Eq. (2.23) vanishes, the
3556 forms of the Lagrangians for ALP and A become identical, and the limits for A
3557 shown in Chapter 7 can be directly recasted. This is done in Sec. 8.2. If on the
3558 other hand $c_{\tilde{G}} \neq 0$, the kinematic distributions of the ALP will differ from those of
3559 A, and the experimental results are not easily translatable. This case is addressed in
3560 the scope of this work through an phenomenological study on simulation only. The
3561 technical setup of this study is described in Sec. 8.3, after which the distributions
3562 of ALP and A are compared for different benchmark points in Sec. 8.4. Projected
3563 exclusion limits for the $c_{\tilde{G}} \neq 0$ case are presented in Sec. 8.5, and a short summary
3564 is given in Sec. 8.6.

3565 The results of this chapter have been originally published in *JHEP* as Ref. [10].
3566 Since the results of Chapter 7 (Refs. [8, 191]) were not yet public at the time, the
3567 previous CMS result from Ref. [20] was used as a baseline. For this thesis, the
3568 translation of limits in Sec. 8.2 has been updated to reflect the results of Chapter 7.

3569 All results presented in this chapter have been obtained as part of this thesis,
3570 except for the comparison to other final states in Sec. 8.5, which was performed by
3571 the coauthors of Ref. [10] as indicated.

3572 **8.2 Translation of experimental limits**

3573 In the basis of Eq. (2.23), the ALP Lagrangian is identical in form to the Lagrangian
3574 of the generic pseudoscalar A given in Eq. (2.18) as long as the gluon interaction

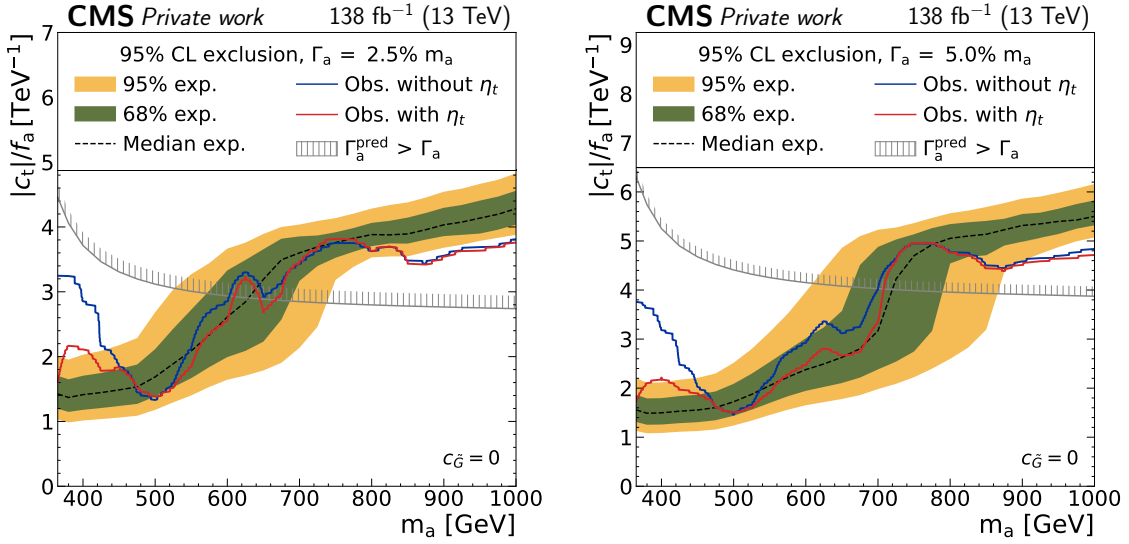


Figure 8.1: **ALP limits for $c_{\tilde{G}} = 0$.** Expected and observed limits on the ALP-top coupling c_t/f_a as a function of the ALP mass for the case $c_{\tilde{G}} = 0$ for the combined dilepton and $\ell+\text{jets}$ decay channels, translated from the results of Chapter 7. The expected limit (black line) is shown without contribution from $t\bar{t}$ bound states in the background modeling, while the observed limit is shown both without $t\bar{t}$ bound states (blue) and with η_t included in the background (red). *Figure adapted from Ref. [10].*

3575 coefficient $c_{\tilde{G}}$ vanishes. For this case, one finds by comparing the coefficients that
 3576 the phenomenology will be identical if

$$\frac{c_t}{f_a} = \frac{g_{A t \bar{t}}}{v} \quad (8.1)$$

3577 where $v = 246$ GeV is the SM Higgs vacuum expectation value. Thus, the experi-
 3578 mental results of Chapter 7, particularly the limits on $g_{A t \bar{t}}$ from the combination of
 3579 dilepton and $\ell+\text{jets}$ decay channels as presented in Sec. 7.9.2, can be recasted into
 3580 limits on the ALP coupling c_t/f_a for the case $c_{\tilde{G}} = 0$. This is shown in Fig. 8.1 for
 3581 two different (fixed) ALP widths. The observed limits are shown with and without
 3582 a $t\bar{t}$ bound state contribution, corresponding to the two scenarios in Fig. 7.29 and
 3583 Fig. 7.31, and the same excess as in Chapter 7 is seen for at low ALP masses when
 3584 the η_t contribution is not included.

3585 In a similar fashion, the best-fit point for A as presented in Eq. (7.19) can be
 3586 translated to an ALP for the case of $c_{\tilde{G}} = 0$, giving

$$m_a = 365 \text{ GeV}, \quad \Gamma_a/m_a = 2\%, \quad \text{and} \quad \frac{c_t}{f_a} = 3.2 \pm 0.2 \text{ TeV}^{-1}.$$

This represents a third alternative interpretation of the excess besides a $t\bar{t}$ bound state or a generic pseudoscalar A . The same caveats as for the A interpretation, as outlined in Sec. 7.7.4, apply; in particular, the mass of 365 GeV is the lowest mass point considered in the signal samples, and it is possible that lower masses closer to the $t\bar{t}$ threshold would result in a better fit.

8.3 Phenomenological setup

The remainder of this chapter is dedicated to exploring an ALP decaying to $t\bar{t}$ for the case $c_{\tilde{G}} \neq 0$, for which the results of Chapter 7 are not easily translatable since the distributions are expected to differ in shape. Due to time constraints, it was not possible as part of this work to investigate this case experimentally in the same fashion as done in Chapter 7. Instead, a phenomenological study is performed on MC simulation only, using a setup that approximates the workflow in Chapter 7.

To do so, MC samples for the signal are generated at LO in QCD with MG5_AMC@NLO for two different ALP masses (400 GeV and 800 GeV). For the ALP, an UFO model taken from Ref. [242] is used and modified to include the top quark loop form factor, considering finite mass effects, according to the expressions given in Ref. [243]. Both possible production diagrams, as shown in Fig. 2.8, as well as their interference with the SM are considered. A similar ME reweighting technique as in Sec. 7.4 is used to obtain samples for different widths and $c_{\tilde{G}}$ values. For the generic pseudoscalar A as well as the SM $t\bar{t}$ background, the same generators as in Sec. 7.2.1 are used (MG5_AMC@NLO and POWHEG v2 hvq, respectively). For all samples, the NNPDF 3.1 PDF set [76] is used, and PYTHIA 8.2 is used to simulate initial and final state radiation [86].

Since the ALP always has a \mathcal{CP} -odd coupling to top quarks (cf. Eq. (2.23)), it is expected to decay to a $t\bar{t}$ system in the 1S_0 state, identically to A . This is true irrespective of the gluon coupling $c_{\tilde{G}}$ since the latter only affects the production, not the decay, and the ALP as a colorless, spinless particle has no internal degrees of freedom. Thus, $m_{t\bar{t}}$ and c_{hel} are good discriminating variables, again similar to A , while c_{han} (optimal for \mathcal{CP} -even couplings) does not offer much additional discrimination and is not considered here. Because c_{hel} is easily experimentally available only in the dilepton decay channel of $t\bar{t}$, only this decay channel is considered here.

No detector simulation is performed. Instead, the truth-level top quarks and leptons after parton showering are used, and efficiency, acceptance, and resolution corrections are applied to the $m_{t\bar{t}}$ distribution. The resolution correction is performed via a Gaussian smearing on a per-event basis, the standard deviation of which is derived from full detector simulation. Since this study was performed before the results of Chapter 7 were public, its predecessor Ref. [20] is used to extract the resolution by fitting to the $m_{t\bar{t}}$ distributions displayed therein. The result is $\sigma(m_{t\bar{t}})/m_{t\bar{t}} = 15\%$, which is somewhat lower than the widths found using the full

3626 detector simulation in Sec. 7.2.5 (c.f. Fig. 7.3). However, it should be cautioned that
 3627 since the true $m_{t\bar{t}}$ smearing in the full detector simulation is not perfectly Gaussian,
 3628 the results are not one-to-one comparable.

3629 The experimental acceptance and efficiency, defined as the fraction of $t\bar{t} \rightarrow \ell\ell$ (ℓ
 3630 being electrons, muons or leptonically decaying taus) events to survive all trigger and
 3631 selection requirements, is estimated to be 10.6% for both signal and $t\bar{t}$ background,
 3632 also based on Ref. [20]. This is lower compared to the updated analysis presented
 3633 in Chapter 7, where values of 15–16% are achieved, varying slightly with the data-
 3634 taking period. Thus, the projections in this chapter should be considered somewhat
 3635 conservative.

3636 For simplicity, instead of a multi-dimensional binning in $m_{t\bar{t}}$ and c_{hel} like in Chap-
 3637 ter 7, a one-dimensional binning in $m_{t\bar{t}}$ only is used, and events are required to have
 3638 $c_{\text{hel}} > 0.6$ to enhance the ALP signal over the background. A simplified version of
 3639 the likelihood model from Chapter 7 is used, implemented in `pyhf` [133], in order to
 3640 estimate projected significances and limits. Only sources of systematic uncertainty
 3641 arising from theory are considered, namely:

- 3642 • Missing higher orders in the matrix element, estimated from varying renor-
 3643 malization and factorization scale by factors of 2,
- 3644 • The PDF uncertainty, estimated as the envelope of 100 pseudo-Hessian NNPDF 3.1
 3645 replicas [76],
- 3646 • The total $t\bar{t}$ background production cross section, taken as a log-normal un-
 3647 certainty of 6% following Ref. [20],
- 3648 • The top quark mass in the $t\bar{t}$ background, varied in the range $m_t = 172.5 \pm$
 3649 1 GeV.

3650 It is clear that this simple treatment of systematic uncertainties can only give a
 3651 rough estimate of the full likelihood as used in Chapter 7, which is sensitive mostly to
 3652 the differences in shapes induced by the various systematic sources. In particular,
 3653 like in the experimental result, the variation of the top quark mass is important
 3654 especially for ALPs with masses close to the $t\bar{t}$ threshold.

3655 To illustrate the dependence on the likelihood model, the significances in the fol-
 3656 lowing results will be quoted for three different setups including different systematic
 3657 uncertainties, namely all of the above, all of the above except for the top quark
 3658 mass, and statistical uncertainties only. By comparing to the expected significance
 3659 given in Ref. [20] for the best-fit point of the pseudoscalar A , it is found that the
 3660 full setup overestimates the uncertainty, while the setup without the top quark mass
 3661 slightly underestimates it.

$c_t/f_a [\text{TeV}^{-1}]$	$c_{\tilde{G}}/f_a [\text{TeV}^{-1}]$	A	$(\sigma^{\text{tot}} - \sigma^{\text{SM}}) [\text{pb}]$
3.0	+0.015	0.95	+6.7
3.0	-0.015	0.43	-2.7
1.0	+0.025	0.75	-1.7
1.0	-0.025	0.87	+2.0

Table 8.1: **Benchmark points for comparing ALP and A.** In addition to the ALP couplings c_t/f_a and $c_{\tilde{G}}/f_a$ for the benchmark points, also the difference in integrated cross section to the SM is shown, as well as a value of $g_{A\bar{t}\bar{t}}$ corresponding to a generic pseudoscalar A with the same integrated cross section.

3662 8.4 Comparison of ALP and A

3663 To investigate the differences and possible discrimination between ALP and A, four
 3664 different ALP benchmark points with $c_{\tilde{G}} \neq 0$ are defined for a mass of 400 GeV and
 3665 a width of 2.5%. Each of the benchmarks is compared to a generic pseudoscalar A
 3666 with its coupling $g_{A\bar{t}\bar{t}}$ chosen such that the total integrated cross section of ALP and
 3667 A are identical, i.e. that they cannot be distinguished by cross section information
 3668 alone. The chosen couplings and resulting cross sections can be found in Tab. 8.1.

3669 The expected $m_{t\bar{t}}$ distributions, including the smearing and acceptance described
 3670 in Sec. 8.3, for the four benchmark points are shown in Fig. 8.2, together with the
 3671 expected statistical uncertainty for both Run 2 and the HL-LHC.

3672 It can be seen that the shapes of the distributions differ qualitatively for the differ-
 3673 ent benchmarks: For example, the case $c_t/f_a = 3.0 \text{ TeV}^{-1}$ and $c_{\tilde{G}}/f_a = 0.015 \text{ TeV}^{-1}$
 3674 (top left) shows a clear peak-dip structure similar to the A case, and as a result will
 3675 likely not be distinguishable from it. In contrast, e.g. the case $c_t/f_a = 1.0 \text{ TeV}^{-1}$
 3676 and $c_{\tilde{G}}/f_a = -0.025 \text{ TeV}^{-1}$ (bottom right) shows a dip-peak structure instead, which
 3677 cannot be reproduced by A. This is possible because of the relative sign of the two
 3678 couplings in this case, i.e. $c_t c_{\tilde{G}} < 0$, which flips the sign of the interference between
 3679 the gluon interaction diagram in Fig. 2.8 and the SM.

3680 By comparing the distributions to the expected statistical uncertainty, one can
 3681 already estimate roughly whether discrimination of the signals with respect to the
 3682 SM or with respect to each other is possible. To quantify this further, the expected
 3683 significance to reject the SM-only hypothesis under the benchmark scenarios are
 3684 reported in Tab. 8.2. They are computed with the likelihood model as defined in
 3685 Sec. 8.3, and quoted both for the three different described uncertainty setups as
 3686 well as for three different eras of the LHC, corresponding to different (expected)
 3687 integrated luminosities: full Run 2 (138 fb^{-1}), Run 2+3 (300 fb^{-1}), and the HL-
 3688 LHC (3 ab^{-1}). For the latter case, all systematic uncertainties are halved to account

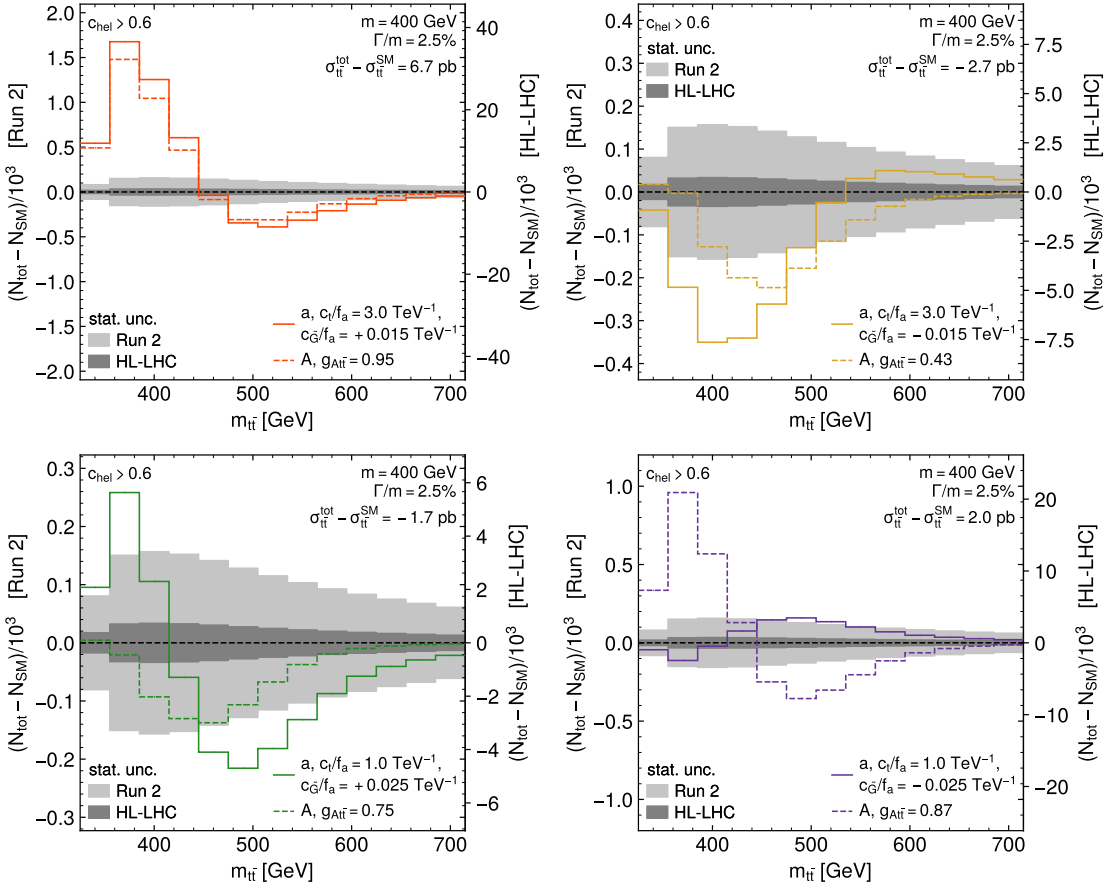


Figure 8.2: **Expected $m_{t\bar{t}}$ distributions for $pp \rightarrow a/A \rightarrow t\bar{t}$.** Shown are both ALP and A at a mass of 400 GeV for four benchmark points, with the SM subtracted. The couplings for A and a are adjusted such that the inclusive cross section is identical. The gray bands show the expected statistical uncertainty for Run 2 and HL-LHC. *Figure taken from Ref. [10].*

for the expected increase in data reconstruction quality and reduction in theoretical uncertainty.

Tab. 8.2 shows that all considered benchmark scenarios can be expected to be distinguished from the SM with $> 5\sigma$ significance if the top quark mass uncertainty is not considered in the model, that is, if experimentally it can be significantly reduced from the estimate used in this study.

If one such signal would be discovered in the future, it would be important to ascertain the particle it originates from. The $m_{t\bar{t}}$ distribution could then be used to distinguish between an ALP, exhibiting both couplings to top quarks and gluons, and the more restrictive case of A, in which only a top quark coupling is allowed. To quantify this, Tab. 8.3 now shows, for the four benchmark points, the expected

		a	Luminosity	Significance (a vs. SM)		
c_t/f_a [TeV $^{-1}$]	$c_{\tilde{G}}/f_a$ [TeV $^{-1}$]	all syst.		no m_t	stats only	
3.0	+0.015	Run 2	3.9	> 10	> 10	
		Run 2+3	5.2	> 10	> 10	
		HL-LHC	> 10	> 10	> 10	
3.0	-0.015	Run 2	2.1	2.2	4.4	
		Run 2+3	3.0	3.0	6.5	
		HL-LHC	8.7	8.8	> 10	
1.0	+0.025	Run 2	1.1	2.6	4.0	
		Run 2+3	1.4	3.2	5.9	
		HL-LHC	3.9	8.2	> 10	
1.0	-0.025	Run 2	0.7	1.7	2.8	
		Run 2+3	0.9	2.2	4.1	
		HL-LHC	2.3	5.5	> 10	

Table 8.2: **Significances for detecting an ALP** with a mass of 400 GeV and a width of 2.5% for the benchmark scenarios considered in Fig. 8.2. Three different treatments of the uncertainties as defined in Sec. 8.3 are shown. For the HL-LHC projection, all systematic uncertainties are scaled by a factor of 0.5.

significances for rejecting the A hypothesis assuming that the corresponding ALP model is realized in nature. Again, the three different uncertainty models and three LHC eras are considered. It can be seen that for all benchmarks, the HL-LHC data would make it possible to distinguish the two scenarios with $> 5\sigma$ significance in the case of an observation.

8.5 Projected limits for ALPs

In case that no (additional) signal is seen in either Run 3 or at the HL-LHC, one would quantify the exclusion of ALP models based on limits in the plane of c_t/f_a and $c_{\tilde{G}}/f_a$. Projections for such expected 95% exclusion limits are presented in Fig. 8.3 for the three different considered luminosities as well as for ALP masses of 400 and 800 GeV. All systematic uncertainties save for the top quark mass are considered here, same as in the “no m_t ” column in Tabs. 8.2 and 8.3.

The figures show that strong limits can be set for values of $|c_{\tilde{G}}|/f_a \gtrsim 0.05$ TeV $^{-1}$ where the gluon-ALP interaction dominates and leads to signals with large cross sections, while the limits are weaker close to $c_{\tilde{G}} = 0$. Notably, the smallest signals are obtained for slightly negative values of $c_{\tilde{G}}/f_a$ due to destructive interference between the two production diagrams, leading to a slight tilt of the curve in the left panel of Fig. 8.3. Of the four considered benchmark points for a 400 GeV ALP,

c_t/f_a [TeV $^{-1}$]	a	$c_{\tilde{G}}/f_a$ [TeV $^{-1}$]	A	Luminosity	Significance (a vs. A)		
					all syst.	no m_t	stats only
3.0	+0.015	0.95	Run 2 Run 2+3 HL-LHC	Run 2	1.3	1.9	3.3
				Run 2+3	1.8	2.3	4.9
				HL-LHC	5.3	5.7	> 10
3.0	−0.015	0.43	Run 2 Run 2+3 HL-LHC	Run 2	1.2	1.9	3.3
				Run 2+3	1.7	2.4	4.9
				HL-LHC	5.0	6.0	> 10
1.0	+0.025	0.75	Run 2 Run 2+3 HL-LHC	Run 2	1.5	2.3	2.7
				Run 2+3	2.0	3.1	3.9
				HL-LHC	5.8	8.8	> 10
1.0	−0.025	0.87	Run 2 Run 2+3 HL-LHC	Run 2	3.7	9.0	> 10
				Run 2+3	4.6	> 10	> 10
				HL-LHC	> 10	> 10	> 10

Table 8.3: **Significances for the discrimination of an ALP and A** for the benchmark scenarios considered in Fig. 8.2. The uncertainties are treated as in Tab. 8.2.

3718 all can be safely expected to be excluded with HL-LHC data, while those with
 3719 $c_t/f_a = 3 \text{ TeV}^{-1}$ might already be excluded by the combination of Run 2 and 3.

3720 As part of the work of the coauthors in Ref. [10], the projected limits for Run 2
 3721 were compared with limits derived from existing analyses in other search channels,
 3722 using `HiggsTools` [244]. These are reproduced briefly in the following in order to
 3723 provide a point of reference; details can be found in Ref. [10]. The following search
 3724 channels were found to be of relevance:

- 3725 • $pp \rightarrow a \rightarrow \gamma\gamma$, from a generic narrow-resonance search in ATLAS [245],
- 3726 • $pp \rightarrow a \rightarrow Zh$, from a search for pseudoscalars decaying into a Z boson and a
 3727 SM Higgs boson in ATLAS [246],
- 3728 • $pp \rightarrow t\bar{t}a \rightarrow t\bar{t}t\bar{t}$, from the CMS measurement of the four-top production cross
 3729 section [247],
- 3730 • interference effects between the ALP effective Lagrangian and SM Effective
 3731 Field Theory (SMEFT), which would induce non-zero Wilson coefficients of
 3732 SMEFT operators in electroweak precision observables such as e.g. the W
 3733 boson mass, leading to indirect limits [248].

3734 The comparison of all these limits to the projected limits from $pp \rightarrow a \rightarrow t\bar{t}$ de-
 3735 rived in this work is shown in Fig. 8.4 in the c_t - $c_{\tilde{G}}$ plane for a 400 GeV ALP.
 3736 For almost all points, $pp \rightarrow a \rightarrow t\bar{t}$ leads to stronger limits than all other direct

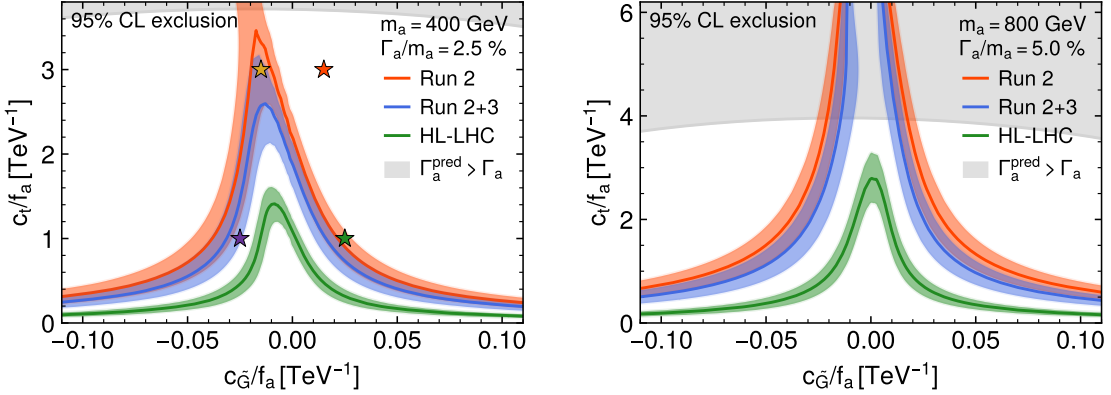


Figure 8.3: **Projected ALP limits.** Projected 95% exclusion limits in the plane of $c_{\tilde{G}}/f_a$ and c_t/f_a for a mass of 400 GeV and a width of 2.5% (left) as well as 800 GeV and 5.0% (right). The limits are shown for three different integrated luminosities, corresponding to Run 2, Run 2+3, and the HL-LHC, where for the latter the systematic uncertainties are halved. *Figure taken from Ref. [10].*

3737 search channels. Furthermore, for $|c_{\tilde{G}}|/f_a \gtrsim 0.03 \text{ TeV}^{-1}$ the projected limits are also
 3738 stronger than the indirect ones from ALP-SMEFT interference, while this is not
 3739 the case for smaller $|c_{\tilde{G}}|/f_a$. It should however be noted that the indirect limits are
 3740 subject to more assumptions, in particular, that the ALP is the only new physics
 3741 contribution at the ALP scale ($\approx f_a$). For a more detailed discussion, see again
 3742 Ref. [10].

3743 8.6 Summary and Outlook

3744 In this chapter, the $t\bar{t}$ final state is found to be an excellent channel for searching
 3745 for heavy ALPs coupling to top quarks. Depending on the value of the explicit
 3746 gluon-ALP coupling $c_{\tilde{G}}$, two scenarios are considered. For $c_{\tilde{G}} = 0$, the results of the
 3747 experimental search for a generic pseudoscalar presented in Chapter 7, including the
 3748 excess observed there, are directly translated into limits on the ALP-top coupling
 3749 c_t/f_a .

3750 For $c_{\tilde{G}} \neq 0$, on the other hand, a phenomenological study targeting the dilepton
 3751 decay channel of $t\bar{t}$ is performed on simulation only, comparing ALPs to a generic
 3752 pseudoscalar A which does not couple directly to gluons. It is found that ALP
 3753 and A can lead to drastically different $m_{t\bar{t}}$ distributions depending on the coupling
 3754 values, and could possibly be distinguished at the HL-LHC if a signal is observed.
 3755 Furthermore, projected expected limits in the plane of the ALP couplings c_t/f_a and
 3756 $c_{\tilde{G}}/f_a$ are set for different integrated luminosities. They are more sensitive than

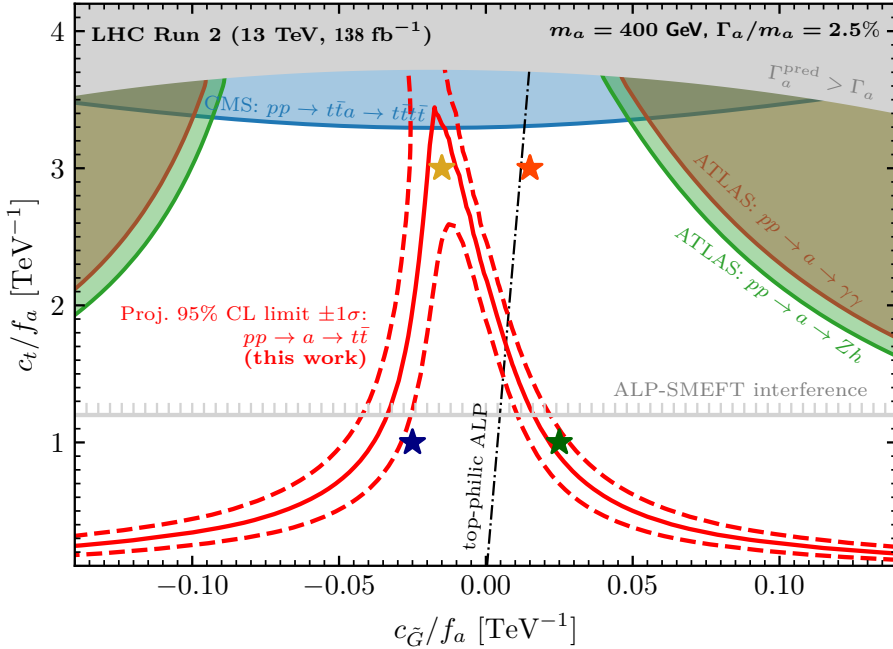


Figure 8.4: **Comparison of limits from different search channels.** 95% exclusion limits in the plane of $c_{\tilde{G}}/f_a$ and c_t/f_a for a mass of 400 GeV and a width of 2.5% (left) from different search channels. The projected limits from this work are overlaid in red. *Figure taken from Ref. [10].*

3757 other possible direct search channels in almost the whole parameter space.

3758 The obvious continuation of this work would be to include the ALP signals for
 3759 the $c_{\tilde{G}} \neq 0$ case into an experimental search like the one performed in Chapter 7.
 3760 For the purpose of this thesis, this was not possible within the time constraints, and
 3761 needs to be postponed to the future. Alternatively, one could investigate how the
 3762 parameter space considered in this work - in particular, the very large ALP mass
 3763 and comparatively strong top coupling - match to possible UV completions of the
 3764 ALP effective Lagrangian.

3765 9 Summary and Conclusions

3766 In this work, various aspects of top quark pair ($t\bar{t}$) production with the CMS detector
3767 at the Large Hadron Collider (LHC) were studied. First, a measurement of the
3768 inclusive $t\bar{t}$ production cross section at a center-of-mass energy of $\sqrt{s} = 13.6$ TeV was
3769 performed, using 1.21 fb^{-1} of early LHC Run 3 data. By combining the dilepton and
3770 $\ell + \text{jets}$ decay channels of $t\bar{t}$ for the first time and categorizing the events by their
3771 number of b-tagged jets, the analysis is capable of constraining lepton and b tagging
3772 efficiencies directly *in situ*.

3773 The result of $\sigma_{t\bar{t}} = 881 \pm 23 \text{ (stat+syst)} \pm 20 \text{ (lumi)} \text{ pb}$ is compatible with the SM
3774 prediction within one standard deviation. The measurement became public only
3775 two months after the analyzed data set was recorded, constituting the first physics
3776 result of LHC Run 3. Despite the small luminosity, the precision of the result is
3777 comparable with previous $\sigma_{t\bar{t}}$ measurements. At the time, it served as an important
3778 validation of the quality of CMS Run 3 data.

3779 Second, off-shell $t\bar{t}$ production as well as interference between $t\bar{t}$ and tW produc-
3780 tion was studied in simulation using the Monte Carlo (MC) generator **bb41**, which
3781 generates the full $\text{pp} \rightarrow b\bar{b}\ell\ell\nu\nu$ amplitude at next-to-leading order (NLO) in quan-
3782 tum chromodynamics (QCD). In this work, **bb41** matched to the parton shower in
3783 PYTHIA is implemented and validated in the CMS software stack for the first time
3784 and compared to several other $t\bar{t}$ MC generators. Good agreement between **bb41**
3785 and unfolded ATLAS data is found for the variable $m_{b\ell}^{\min\max}$, which is sensitive to
3786 the $t\bar{t}/\text{tW}$ interference. Significant shifts in the reconstructed top mass line shape
3787 compared to other generators are observed. Additionally, a brief investigation of the
3788 matching procedure between **bb41** and PYTHIA is presented. These studies repre-
3789 sent the starting point for future precision $t\bar{t}$ analyses in CMS using **bb41**, such as
3790 measurements of the top mass and width.

3791 Finally, a search for spin-0 states decaying to $t\bar{t}$ in the dilepton channel has
3792 been presented. The search uses the full CMS Run 2 data set, corresponding to
3793 138 fb^{-1} and $\sqrt{s} = 13$ TeV, and employs the invariant $t\bar{t}$ mass ($m_{t\bar{t}}$) as well as two $t\bar{t}$
3794 spin correlation observables to gain sensitivity to the \mathcal{CP} structure of possible new
3795 intermediate states. An excess compared to the $t\bar{t}$ continuum prediction is observed
3796 for low $m_{t\bar{t}}$ events, consistent with spin correlations as expected from a pseudoscalar
3797 state. This excess is interpreted as a pseudoscalar $t\bar{t}$ bound state η_t , as predicted
3798 by several calculations in non-relativistic QCD (NRQCD). The production cross
3799 section of η_t is measured using a simplified η_t model, resulting in $\sigma(\eta_t) = 8.7 \pm$
3800 1.1 pb , which is of the same order of magnitude as NRQCD-based estimates. The

3801 uncertainty is dominated by its systematic component, in particular the challenging
3802 modeling of the $t\bar{t}$ continuum. Several detailed cross-checks, such as bypassing
3803 the experimental $t\bar{t}$ reconstruction as well as using different MC generators, are
3804 discussed, and all confirm the presence of the excess. The significance of the result
3805 exceeds five standard deviations.

3806 Alternatively, the same search is interpreted in terms of new, generic pseudoscalar
3807 (A) or scalar (H) particles coupling to top quarks, as expected e.g. in Two-Higgs
3808 Doublet models (2HDMs). The interference between the new particles and the SM
3809 is taken into account. Besides an interpretation of the same excess at low $m_{t\bar{t}}$,
3810 exclusion limits on the couplings to the top quark are presented in two scenarios,
3811 assuming the excess to be either fully described by A and H or fully by a $t\bar{t}$ bound
3812 state. These limits are combined with a similar search in the ℓ +jets decay channels
3813 of $t\bar{t}$, and exclusion regions are also provided for the simultaneous presence of A and
3814 H.

3815 For a third interpretation, Axion-Like Particles (ALPs) decaying to $t\bar{t}$ are consid-
3816 ered. In the case of vanishing tree-level couplings between ALP and gluons $c_{\tilde{G}}$, the
3817 results for the generic pseudoscalar A are directly translatable, and experimental
3818 limits on the coupling between ALP and top quark are presented. The more generic
3819 case of $c_{\tilde{G}} \neq 0$ is studied using simulated events, and projected significances and
3820 exclusion limits on such ALPs decaying to $t\bar{t}$ are derived for various phases of the
3821 LHC. It is found that at the high-luminosity LHC, ALPs and other pseudoscalars
3822 as e.g. in the 2HDM could be distinguishable based on their $m_{t\bar{t}}$ distribution. The
3823 resulting limits are expected to improve on limits from other final states in large
3824 areas of phase space.

3825 Branching out from the different aspects of this work, many directions of further
3826 study could be pursued. The most pressing one is certainly a further investigation
3827 of the excess at the $t\bar{t}$ production threshold observed here. Since the ATLAS ex-
3828 periment has confirmed the excess in a preliminary result, it would now be of great
3829 interest to determine the origin of the excess - in particular, whether it is purely the
3830 result of a SM bound state or whether it originates in BSM physics - though this will
3831 likely be challenging. Searches at the same invariant mass in other decay channels,
3832 in particular $\gamma\gamma$, as well as measurements of other kinematic distributions for low $m_{t\bar{t}}$
3833 events could represent first steps towards this goal. It is also in general important
3834 to improve the experimental $t\bar{t}$ reconstruction techniques e.g. with modern machine
3835 learning approaches, which would also greatly contribute to precision measurements
3836 of top quark properties. From the theoretical perspective, more precise calculations
3837 of the $t\bar{t}$ threshold region are required, for which this work will hopefully serve as a
3838 motivation.

3839 It is not every day that such an excess is observed in high energy physics. Regard-
3840 less of its origin, its study marks the begin of a new chapter in top quark physics.

3841

A Bibliography

- 3842 [1] ATLAS Collaboration, “Observation of a new particle in the search for the
3843 standard model Higgs boson with the ATLAS detector at the LHC”, *Phys.
3844 Lett. B*, vol. 716, p. 1, 2012. DOI: 10.1016/j.physletb.2012.08.020. arXiv:
3845 1207.7214 [hep-ex].
- 3846 [2] CMS Collaboration, “Observation of a new boson at a mass of 125 GeV with
3847 the CMS experiment at the LHC”, *Phys. Lett. B*, vol. 716, p. 30, 2012. DOI:
3848 10.1016/j.physletb.2012.08.021. arXiv: 1207.7235 [hep-ex].
- 3849 [3] CMS Collaboration, “Observation of a new boson with mass near 125 GeV
3850 in pp collisions at $\sqrt{s} = 7$ and 8 TeV”, *JHEP*, vol. 06, p. 081, 2013. DOI:
3851 10.1007/JHEP06(2013)081. arXiv: 1303.4571 [hep-ex].
- 3852 [4] CMS Collaboration, “The CMS Experiment at the CERN LHC”, *JINST*,
3853 vol. 3, S08004, 2008. DOI: 10.1088/1748-0221/3/08/S08004.
- 3854 [5] CMS Collaboration, “First measurement of the top quark pair production
3855 cross section in proton-proton collisions at $\sqrt{s} = 13.6$ TeV”, *JHEP*, vol. 08,
3856 p. 204, 2023. DOI: 10.1007/JHEP08(2023)204. arXiv: 2303.10680 [hep-ex].
- 3857 [6] CMS Collaboration, “Simulation of on- and off-shell $t\bar{t}$ production with the
3858 Monte Carlo generator b_bbar_4l at CMS”, CERN, Geneva, Tech. Rep.,
3859 2023. [Online]. Available: <https://cds.cern.ch/record/2884265>.
- 3860 [7] T. Ježo, J. M. Lindert, P. Nason, C. Oleari, and S. Pozzorini, “An NLO+PS
3861 generator for $t\bar{t}$ and Wt production and decay including non-resonant and
3862 interference effects”, *Eur. Phys. J. C*, vol. 76, p. 691, 2016. DOI: 10.1140/
3863 epjc/s10052-016-4538-2. arXiv: 1607.04538 [hep-ph].
- 3864 [8] CMS Collaboration, “Observation of a pseudoscalar excess at the top quark
3865 pair production threshold”, 2025, submitted to *Rep. Prog. Phys.* arXiv: 2503.
3866 22382 [hep-ex].
- 3867 [9] CMS Collaboration, “Search for heavy pseudoscalar and scalar bosons decaying
3868 to a top quark pair in proton-proton collisions at $\sqrt{s} = 13$ TeV”, 2025,
3869 submitted to *Rep. Prog. Phys.* arXiv: 2507.05119 [hep-ex].
- 3870 [10] A. Anuar et al., “ALP-ine quests at the LHC: hunting axion-like particles
3871 via peaks and dips in $t\bar{t}$ production”, *JHEP*, vol. 24, p. 197, 2024. DOI: 10.
3872 1007/JHEP12(2024)197. arXiv: 2404.19014 [hep-ph].
- 3873 [11] B. R. Martin and G. Shaw, *Particle Physics*. Wiley, 2008, ISBN: 978-0-470-
3874 03294-7.

- 3875 [12] M. D. Schwartz, *Quantum Field Theory and the Standard Model*. Cambridge
3876 University Press, Mar. 2014, ISBN: 978-1-107-03473-0, 978-1-107-03473-0.
- 3877 [13] R. L. Workman et al., “Review of Particle Physics”, *PTEP*, vol. 2022, p. 083C01,
3878 2022. DOI: 10.1093/ptep/ptac097.
- 3879 [14] P. W. Higgs, “Broken symmetries, massless particles and gauge fields”, *Phys.*
3880 *Lett.*, vol. 12, pp. 132–133, 1964. DOI: 10.1016/0031-9163(64)91136-9.
- 3881 [15] F. Englert and R. Brout, “Broken Symmetry and the Mass of Gauge Vector
3882 Mesons”, *Phys. Rev. Lett.*, vol. 13, J. C. Taylor, Ed., pp. 321–323, 1964. DOI:
3883 10.1103/PhysRevLett.13.321.
- 3884 [16] CDF Collaboration, “Observation of top quark production in $\bar{p}p$ collisions”,
3885 *Phys. Rev. Lett.*, vol. 74, pp. 2626–2631, 1995. DOI: 10.1103/PhysRevLett.
3886 74.2626. arXiv: hep-ex/9503002.
- 3887 [17] D0 Collaboration, “Observation of the top quark”, *Phys. Rev. Lett.*, vol. 74,
3888 pp. 2632–2637, 1995. DOI: 10.1103/PhysRevLett.74.2632. arXiv: hep-
3889 ex/9503003.
- 3890 [18] ATLAS and CMS Collaborations, “Combination of Measurements of the Top
3891 Quark Mass from Data Collected by the ATLAS and CMS Experiments at
3892 $\sqrt{s} = 7$ and 8 TeV”, *Phys. Rev. Lett.*, vol. 132, no. 26, p. 261902, 2024. DOI:
3893 10.1103/PhysRevLett.132.261902. arXiv: 2402.08713 [hep-ex].
- 3894 [19] Y. Kats and D. Uzan, “Prospects for measuring quark polarization and spin
3895 correlations in $b\bar{b}$ and $c\bar{c}$ samples at the LHC”, *JHEP*, vol. 03, p. 063, 2024.
3896 DOI: 10.1007/JHEP03(2024)063. arXiv: 2311.08226 [hep-ph].
- 3897 [20] CMS Collaboration, “Search for heavy Higgs bosons decaying to a top quark
3898 pair in proton-proton collisions at $\sqrt{s} = 13$ TeV”, *JHEP*, vol. 04, p. 171, 2020,
3899 [Erratum: JHEP 03, 187 (2022)]. DOI: 10.1007/JHEP04(2020)171. arXiv:
3900 1908.01115 [hep-ex].
- 3901 [21] W. Bernreuther, A. Brandenburg, Z. G. Si, and P. Uwer, “Top quark pair
3902 production and decay at hadron colliders”, *Nucl. Phys. B*, vol. 690, pp. 81–
3903 137, 2004. DOI: 10.1016/j.nuclphysb.2004.04.019. arXiv: hep-ph/
3904 0403035.
- 3905 [22] F. Maltoni, C. Severi, S. Tentori, and E. Vryonidou, “Quantum detection of
3906 new physics in top-quark pair production at the LHC”, *JHEP*, vol. 03, p. 099,
3907 2024. DOI: 10.1007/JHEP03(2024)099. arXiv: 2401.08751 [hep-ph].
- 3908 [23] K. Cheng, T. Han, and M. Low, “Optimizing entanglement and Bell inequality
3909 violation in top antitop events”, *Phys. Rev. D*, vol. 111, no. 3, p. 033004,
3910 2025. DOI: 10.1103/PhysRevD.111.033004. arXiv: 2407.01672 [hep-ph].

- [3911] [24] A. Czarnecki, M. Jezabek, and J. H. Kuhn, “Lepton Spectra From Decays
[3912] of Polarized Top Quarks”, *Nucl. Phys. B*, vol. 351, pp. 70–80, 1991. DOI:
[3913] 10.1016/0550-3213(91)90082-9.
- [3914] [25] W. Bernreuther, A. Brandenburg, Z. G. Si, and P. Uwer, “Spin properties of
[3915] top quark pairs produced at hadron colliders”, *Acta Phys. Polon. B*, vol. 34,
[3916] K. Fialkowski, M. Jezabek, and M. Rozanska, Eds., pp. 4477–4490, 2003.
[3917] arXiv: hep-ph/0304244.
- [3918] [26] CMS Collaboration, “Measurements of t t-bar spin correlations and top quark
[3919] polarization using dilepton final states in pp collisions at sqrt(s) = 8 TeV”,
[3920] *Phys. Rev. D*, vol. 93, no. 5, p. 052007, 2016. DOI: 10.1103/PhysRevD.93.
[3921] 052007. arXiv: 1601.01107 [hep-ex].
- [3922] [27] CMS Collaboration, “Measurement of the top quark polarization and t t-bar spin
[3923] correlations using dilepton final states in proton-proton collisions at $\sqrt{s} =$
[3924] 13 TeV”, *Phys. Rev. D*, vol. 100, no. 7, p. 072002, 2019. DOI: 10.1103/
[3925] PhysRevD.100.072002. arXiv: 1907.03729 [hep-ex].
- [3926] [28] CMS Collaboration, “Measurements of polarization and spin correlation and
[3927] observation of entanglement in top quark pairs using lepton+jets events from
[3928] proton-proton collisions at $\sqrt{s} = 13$ TeV”, *Phys. Rev. D*, vol. 110, no. 11,
[3929] p. 112016, 2024. DOI: 10.1103/PhysRevD.110.112016. arXiv: 2409.11067
[3930] [hep-ex].
- [3931] [29] CMS Collaboration, “Observation of quantum entanglement in top quark
[3932] pair production in proton–proton collisions at $\sqrt{s} = 13$ TeV”, *Rept. Prog.
[3933] Phys.*, vol. 87, no. 11, p. 117801, 2024. DOI: 10.1088/1361-6633/ad7e4d.
[3934] arXiv: 2406.03976 [hep-ex].
- [3935] [30] ATLAS Collaboration, “Observation of quantum entanglement with top quarks
[3936] at the ATLAS detector”, *Nature*, vol. 633, no. 8030, pp. 542–547, 2024. DOI:
[3937] 10.1038/s41586-024-07824-z. arXiv: 2311.07288 [hep-ex].
- [3938] [31] A. A. Anuar, “Top Quark Spin and Polarization Properties in Searches for
[3939] New Phenomena with the CMS Detector at the LHC”, PhD thesis, DESY,
[3940] Hamburg, 2019.
- [3941] [32] W. Bernreuther, P. Galler, Z.-G. Si, and P. Uwer, “Production of heavy Higgs
[3942] bosons and decay into top quarks at the LHC. II: Top-quark polarization and
[3943] spin correlation effects”, *Phys. Rev. D*, vol. 95, no. 9, p. 095012, 2017. DOI:
[3944] 10.1103/PhysRevD.95.095012. arXiv: 1702.06063 [hep-ph].
- [3945] [33] W. Bernreuther, D. Heisler, and Z.-G. Si, “A set of top quark spin correlation
[3946] and polarization observables for the LHC: Standard Model predictions and
[3947] new physics contributions”, *JHEP*, vol. 12, p. 026, 2015. DOI: 10.1007/
[3948] JHEP12(2015)026. arXiv: 1508.05271 [hep-ph].

- 3949 [34] V. S. Fadin, V. A. Khoze, and T. Sjöstrand, “On the threshold behaviour
3950 of heavy top production”, *Z. Phys. C*, vol. 48, p. 613, 1990. DOI: 10.1007/BF01614696.
- 3951
- 3952 [35] Y. Kiyo, J. H. Kuhn, S. Moch, M. Steinhauser, and P. Uwer, “Top-quark
3953 pair production near threshold at LHC”, *Eur. Phys. J. C*, vol. 60, pp. 375–
3954 386, 2009. DOI: 10.1140/epjc/s10052-009-0892-7. arXiv: 0812.0919
3955 [hep-ph].
- 3956 [36] Y. Sumino and H. Yokoya, “Bound-state effects on kinematical distributions
3957 of top quarks at hadron colliders”, *JHEP*, vol. 09, p. 034, 2010, [Erratum:
3958 *JHEP* 06, 037 (2016)]. DOI: 10.1007/JHEP09(2010)034. arXiv: 1007.0075
3959 [hep-ph].
- 3960 [37] W.-L. Ju, G. Wang, X. Wang, X. Xu, Y. Xu, and L. L. Yang, “Top quark
3961 pair production near threshold: single/double distributions and mass deter-
3962 mination”, *JHEP*, vol. 06, p. 158, 2020. DOI: 10.1007/JHEP06(2020)158.
3963 arXiv: 2004.03088 [hep-ph].
- 3964 [38] M. V. Garzelli, G. Limatola, S. Moch, M. Steinhauser, and O. Zenaiev, “Up-
3965 dated predictions for toponium production at the LHC”, Dec. 2024. arXiv:
3966 2412.16685 [hep-ph].
- 3967 [39] F. Maltoni, C. Severi, S. Tentori, and E. Vryonidou, “Quantum tops at circu-
3968 lar lepton colliders”, *JHEP*, vol. 09, p. 001, 2024. DOI: 10.1007/JHEP09(2024)
3969 001. arXiv: 2404.08049 [hep-ph].
- 3970 [40] B. Fuks, K. Hagiwara, K. Ma, and Y.-J. Zheng, “Signatures of toponium
3971 formation in LHC run 2 data”, *Phys. Rev. D*, vol. 104, no. 3, p. 034023,
3972 2021. DOI: 10.1103/PhysRevD.104.034023. arXiv: 2102.11281 [hep-ph].
- 3973 [41] J. A. Aguilar-Saavedra, “Toponium hunter’s guide”, *Phys. Rev. D*, vol. 110,
3974 no. 5, p. 054032, 2024. DOI: 10.1103/PhysRevD.110.054032. arXiv: 2407.
3975 20330 [hep-ph].
- 3976 [42] B. Fuks, K. Hagiwara, K. Ma, and Y.-J. Zheng, “Simulating toponium for-
3977 mation signals at the LHC”, *Eur. Phys. J. C*, vol. 85, no. 2, p. 157, 2025.
3978 DOI: 10.1140/epjc/s10052-025-13853-3. arXiv: 2411.18962 [hep-ph].
- 3979 [43] T. Barnes, S. Godfrey, and E. S. Swanson, “Higher charmonia”, *Phys. Rev.*
3980 *D*, vol. 72, p. 054026, 2005. DOI: 10.1103/PhysRevD.72.054026. arXiv:
3981 hep-ph/0505002.
- 3982 [44] G. Bertone, D. Hooper, and J. Silk, “Particle dark matter: Evidence, candi-
3983 dates and constraints”, *Phys. Rept.*, vol. 405, pp. 279–390, 2005. DOI: 10.
3984 1016/j.physrep.2004.08.031. arXiv: hep-ph/0404175.

- 3985 [45] T. A. Porter, R. P. Johnson, and P. W. Graham, “Dark Matter Searches with
3986 Astroparticle Data”, *Ann. Rev. Astron. Astrophys.*, vol. 49, pp. 155–194, 2011.
3987 DOI: 10.1146/annurev-astro-081710-102528. arXiv: 1104.2836 [astro-
3988 ph.HE].
- 3989 [46] A. Arbey and F. Mahmoudi, “Dark matter and the early Universe: a review”,
3990 *Prog. Part. Nucl. Phys.*, vol. 119, p. 103865, 2021. DOI: 10.1016/j.ppnp.
3991 2021.103865. arXiv: 2104.11488 [hep-ph].
- 3992 [47] A. de Gouv  a, “Neutrino Mass Models”, *Ann. Rev. Nucl. Part. Sci.*, vol. 66,
3993 pp. 197–217, 2016. DOI: 10.1146/annurev-nucl-102115-044600.
- 3994 [48] A. Dev, “Neutrino Oscillations and Mass Models”, Oct. 2023. arXiv: 2310.
3995 17685 [hep-ph].
- 3996 [49] P. Nelson, “Naturalness in Theoretical Physics”, *American Scientist*, vol. 73,
3997 no. 1, pp. 60–67, 1985.
- 3998 [50] S. Koren, “New Approaches to the Hierarchy Problem and their Signatures
3999 from Microscopic to Cosmic Scales”, Ph.D. dissertation, UC Santa Barbara,
4000 2020. arXiv: 2009.11870 [hep-ph].
- 4001 [51] N. Craig, “Naturalness: past, present, and future”, *Eur. Phys. J. C*, vol. 83,
4002 no. 9, p. 825, 2023. DOI: 10.1140/epjc/s10052-023-11928-7. arXiv:
4003 2205.05708 [hep-ph].
- 4004 [52] R. D. Peccei and H. R. Quinn, “CP Conservation in the Presence of In-
4005 stantons”, *Phys. Rev. Lett.*, vol. 38, pp. 1440–1443, 1977. DOI: 10.1103/
4006 PhysRevLett.38.1440.
- 4007 [53] R. D. Peccei and H. R. Quinn, “Constraints Imposed by CP Conservation in
4008 the Presence of Instantons”, *Phys. Rev. D*, vol. 16, pp. 1791–1797, 1977. DOI:
4009 10.1103/PhysRevD.16.1791.
- 4010 [54] CMS Collaboration, “Search for dark matter produced in association with
4011 a single top quark or a top quark pair in proton-proton collisions at $\sqrt{s} =$
4012 13 TeV”, CERN, Geneva, Tech. Rep., 2024. [Online]. Available: <https://cds.cern.ch/record/2895470>.
- 4013
- 4014 [55] T. D. Lee, “A Theory of Spontaneous T Violation”, *Phys. Rev. D*, vol. 8, G.
4015 Feinberg, Ed., pp. 1226–1239, 1973. DOI: 10.1103/PhysRevD.8.1226.
- 4016 [56] G. C. Branco, P. M. Ferreira, L. Lavoura, M. N. Rebelo, M. Sher, and
4017 J. P. Silva, “Theory and phenomenology of two-Higgs-doublet models”, *Phys.
4018 Rept.*, vol. 516, pp. 1–102, 2012. DOI: 10.1016/j.physrep.2012.02.002.
4019 arXiv: 1106.0034 [hep-ph].
- 4020 [57] H. E. Haber and G. L. Kane, “The Search for Supersymmetry: Probing
4021 Physics Beyond the Standard Model”, *Phys. Rept.*, vol. 117, pp. 75–263,
4022 1985. DOI: 10.1016/0370-1573(85)90051-1.

- 4023 [58] J. E. Kim, “Light Pseudoscalars, Particle Physics and Cosmology”, *Phys.
4024 Rept.*, vol. 150, pp. 1–177, 1987. DOI: 10.1016/0370-1573(87)90017-2.
- 4025 [59] S. Weinberg, “A New Light Boson?”, *Phys. Rev. Lett.*, vol. 40, pp. 223–226,
4026 1978. DOI: 10.1103/PhysRevLett.40.223.
- 4027 [60] F. Wilczek, “Problem of Strong P and T Invariance in the Presence of In-
4028 stantons”, *Phys. Rev. Lett.*, vol. 40, pp. 279–282, 1978. DOI: 10.1103/
4029 PhysRevLett.40.279.
- 4030 [61] L. Di Luzio, M. Giannotti, E. Nardi, and L. Visinelli, “The landscape of
4031 QCD axion models”, *Phys. Rept.*, vol. 870, pp. 1–117, 2020. DOI: 10.1016/
4032 j.physrep.2020.06.002. arXiv: 2003.01100 [hep-ph].
- 4033 [62] J. M. Pendlebury et al., “Revised experimental upper limit on the electric
4034 dipole moment of the neutron”, *Phys. Rev. D*, vol. 92, no. 9, p. 092003, 2015.
4035 DOI: 10.1103/PhysRevD.92.092003. arXiv: 1509.04411 [hep-ex].
- 4036 [63] C. Abel et al., “Measurement of the Permanent Electric Dipole Moment
4037 of the Neutron”, *Phys. Rev. Lett.*, vol. 124, no. 8, p. 081803, 2020. DOI:
4038 10.1103/PhysRevLett.124.081803. arXiv: 2001.11966 [hep-ex].
- 4039 [64] J. E. Kim, “Weak Interaction Singlet and Strong CP Invariance”, *Phys. Rev.
4040 Lett.*, vol. 43, p. 103, 1979. DOI: 10.1103/PhysRevLett.43.103.
- 4041 [65] M. A. Shifman, A. I. Vainshtein, and V. I. Zakharov, “Can Confinement En-
4042 sure Natural CP Invariance of Strong Interactions?”, *Nucl. Phys. B*, vol. 166,
4043 pp. 493–506, 1980. DOI: 10.1016/0550-3213(80)90209-6.
- 4044 [66] M. Dine, W. Fischler, and M. Srednicki, “A Simple Solution to the Strong
4045 CP Problem with a Harmless Axion”, *Phys. Lett. B*, vol. 104, pp. 199–202,
4046 1981. DOI: 10.1016/0370-2693(81)90590-6.
- 4047 [67] A. R. Zhitnitsky, “On Possible Suppression of the Axion Hadron Interac-
4048 tions”, *Sov. J. Nucl. Phys.*, vol. 31, p. 260, 1980.
- 4049 [68] H. Georgi, D. B. Kaplan, and L. Randall, “Manifesting the Invisible Axion at
4050 Low-energies”, *Phys. Lett. B*, vol. 169, pp. 73–78, 1986. DOI: 10.1016/0370-
4051 2693(86)90688-X.
- 4052 [69] V. A. Rubakov, “Grand unification and heavy axion”, *JETP Lett.*, vol. 65,
4053 pp. 621–624, 1997. DOI: 10.1134/1.567390. arXiv: hep-ph/9703409.
- 4054 [70] B. Holdom and M. E. Peskin, “Raising the Axion Mass”, *Nucl. Phys. B*,
4055 vol. 208, pp. 397–412, 1982. DOI: 10.1016/0550-3213(82)90228-0.
- 4056 [71] S. Dimopoulos, A. Hook, J. Huang, and G. Marques-Tavares, “A collider ob-
4057 servable QCD axion”, *JHEP*, vol. 11, p. 052, 2016. DOI: 10.1007/JHEP11(2016)
4058 052. arXiv: 1606.03097 [hep-ph].

- 4059 [72] T. Gherghetta, N. Nagata, and M. Shifman, “A Visible QCD Axion from an
4060 Enlarged Color Group”, *Phys. Rev. D*, vol. 93, no. 11, p. 115010, 2016. DOI:
4061 10.1103/PhysRevD.93.115010. arXiv: 1604.01127 [hep-ph].
- 4062 [73] M. E. Peskin and D. V. Schroeder, *An Introduction to quantum field theory*.
4063 Reading, USA: Addison-Wesley, 1995, ISBN: 978-0-201-50397-5, 978-0-429-
4064 50355-9, 978-0-429-49417-8. DOI: 10.1201/9780429503559.
- 4065 [74] G. Altarelli and G. Parisi, “Asymptotic Freedom in Parton Language”, *Nucl.
4066 Phys. B*, vol. 126, pp. 298–318, 1977. DOI: 10.1016/0550-3213(77)90384-4.
- 4067 [75] P. Skands, “Introduction to QCD”, in *Searching for New Physics at Small
4068 and Large Scales*, 2013, pp. 341–420. DOI: 10.1142/9789814525220_0008.
4069 arXiv: 1207.2389 [hep-ph].
- 4070 [76] R. D. Ball et al., “Parton distributions from high-precision collider data”,
4071 *Eur. Phys. J. C*, vol. 77, p. 663, 2017. DOI: 10.1140/epjc/s10052-017-
4072 5199-5. arXiv: 1706.00428 [hep-ph].
- 4073 [77] F. Maltoni and T. Stelzer, “MadEvent: Automatic event generation with
4074 MadGraph”, *JHEP*, vol. 02, p. 027, 2003. DOI: 10.1088/1126-6708/2003/
4075 02/027. arXiv: hep-ph/0208156.
- 4076 [78] F. J. Tackmann, “Beyond Scale Variations: Perturbative Theory Uncertain-
4077 ties from Nuisance Parameters”, Nov. 2024. arXiv: 2411.18606 [hep-ph].
- 4078 [79] P. Nason and B. Webber, “Next-to-Leading-Order Event Generators”, *Ann.
4079 Rev. Nucl. Part. Sci.*, vol. 62, pp. 187–213, 2012. DOI: 10.1146/annurev-
4080 nucl-102711-094928. arXiv: 1202.1251 [hep-ph].
- 4081 [80] J. Alwall et al., “The automated computation of tree-level and next-to-
4082 leading order differential cross sections, and their matching to parton shower
4083 simulations”, *JHEP*, vol. 07, p. 079, 2014. DOI: 10.1007/JHEP07(2014)079.
4084 arXiv: 1405.0301 [hep-ph].
- 4085 [81] C. Degrande, C. Duhr, B. Fuks, D. Grellscheid, O. Mattelaer, and T. Re-
4086 iter, “UFO - The Universal FeynRules Output”, *Comput. Phys. Commun.*,
4087 vol. 183, pp. 1201–1214, 2012. DOI: 10.1016/j.cpc.2012.01.022. arXiv:
4088 1108.2040 [hep-ph].
- 4089 [82] P. Nason, “A new method for combining NLO QCD with shower Monte Carlo
4090 algorithms”, *JHEP*, vol. 11, p. 040, 2004. DOI: 10.1088/1126-6708/2004/
4091 11/040. arXiv: hep-ph/0409146.
- 4092 [83] S. Frixione, P. Nason, and C. Oleari, “Matching NLO QCD computations
4093 with parton shower simulations: The POWHEG method”, *JHEP*, vol. 11,
4094 p. 070, 2007. DOI: 10.1088/1126-6708/2007/11/070. arXiv: 0709.2092
4095 [hep-ph].

- 4096 [84] S. Alioli, P. Nason, C. Oleari, and E. Re, “A general framework for imple-
 4097 menting NLO calculations in shower Monte Carlo programs: The POWHEG
 4098 BOX”, *JHEP*, vol. 06, p. 043, 2010. DOI: 10.1007/JHEP06(2010)043. arXiv:
 4099 1002.2581 [hep-ph].
- 4100 [85] S. Frixione, G. Ridolfi, and P. Nason, “A positive-weight next-to-leading-
 4101 order Monte Carlo for heavy flavour hadroproduction”, *JHEP*, vol. 09, p. 126,
 4102 2007. DOI: 10.1088/1126-6708/2007/09/126. arXiv: 0707.3088 [hep-ph].
- 4103 [86] T. Sjöstrand et al., “An introduction to PYTHIA8.2”, *Comput. Phys. Com-
 4104 mun.*, vol. 191, p. 159, 2015. DOI: 10.1016/j.cpc.2015.01.024. arXiv:
 4105 1410.3012 [hep-ph].
- 4106 [87] C. Bierlich et al., “A comprehensive guide to the physics and usage of PYTHIA
 4107 8.3”, *SciPost Phys. Codeb.*, vol. 2022, p. 8, 2022. DOI: 10.21468/SciPostPhysCodeb.
 4108 8. arXiv: 2203.11601 [hep-ph].
- 4109 [88] S. Frixione and B. R. Webber, “Matching NLO QCD computations and par-
 4110 ton shower simulations”, *JHEP*, vol. 06, p. 029, 2002. DOI: 10.1088/1126-
 4111 6708/2002/06/029. arXiv: hep-ph/0204244.
- 4112 [89] M. L. Mangano, M. Moretti, F. Piccinini, and M. Treccani, “Matching matrix
 4113 elements and shower evolution for top-quark production in hadronic colli-
 4114 sions”, *JHEP*, vol. 01, p. 013, 2007. DOI: 10.1088/1126-6708/2007/01/013.
 4115 arXiv: hep-ph/0611129.
- 4116 [90] R. Frederix and S. Frixione, “Merging meets matching in MC@NLO”, *JHEP*,
 4117 vol. 12, p. 061, 2012. DOI: 10.1007/JHEP12(2012)061. arXiv: 1209.6215
 4118 [hep-ph].
- 4119 [91] J. Bellm et al., “HERWIG7.0/HERWIG++3.0 release note”, *Eur. Phys. J.*
 4120 *C*, vol. 76, p. 196, 2016. DOI: 10.1140/epjc/s10052-016-4018-8. arXiv:
 4121 1512.01178 [hep-ph].
- 4122 [92] M. Bähr et al., “HERWIG++ physics and manual”, *Eur. Phys. J. C*, vol. 58,
 4123 p. 639, 2008. DOI: 10.1140/epjc/s10052-008-0798-9. arXiv: 0803.0883
 4124 [hep-ph].
- 4125 [93] P. Skands, S. Carrazza, and J. Rojo, “Tuning PYTHIA 8.1: the Monash 2013
 4126 Tune”, *Eur. Phys. J. C*, vol. 74, no. 8, p. 3024, 2014. DOI: 10.1140/epjc/
 4127 s10052-014-3024-y. arXiv: 1404.5630 [hep-ph].
- 4128 [94] CMS Collaboration, “Extraction and validation of a new set of CMS Pythia
 4129 8 tunes from underlying-event measurements”, *Eur. Phys. J. C*, vol. 80, p. 4,
 4130 2020. DOI: 10.1140/epjc/s10052-019-7499-4. arXiv: 1903.12179 [hep-
 4131 ex].

- 4132 [95] B. Andersson, G. Gustafson, G. Ingelman, and T. Sjostrand, “Parton Frag-
4133 mentation and String Dynamics”, *Phys. Rept.*, vol. 97, pp. 31–145, 1983. DOI:
4134 10.1016/0370-1573(83)90080-7.
- 4135 [96] T. Sjostrand, “Jet Fragmentation of Nearby Partons”, *Nucl. Phys. B*, vol. 248,
4136 pp. 469–502, 1984. DOI: 10.1016/0550-3213(84)90607-2.
- 4137 [97] S. Argyropoulos and T. Sjöstrand, “Effects of color reconnection on $t\bar{t}$ final
4138 states at the LHC”, *JHEP*, vol. 11, p. 043, 2014. DOI: 10.1007/JHEP11(2014)
4139 043. arXiv: 1407.6653 [hep-ph].
- 4140 [98] J. R. Christiansen and P. Z. Skands, “String Formation Beyond Leading
4141 Colour”, *JHEP*, vol. 08, p. 003, 2015. DOI: 10.1007/JHEP08(2015)003.
4142 arXiv: 1505.01681 [hep-ph].
- 4143 [99] CMS Collaboration, “Pileup mitigation at CMS in 13 TeV data”, *JINST*,
4144 vol. 15, no. 09, P09018, 2020. DOI: 10.1088/1748-0221/15/09/P09018.
4145 arXiv: 2003.00503 [hep-ex].
- 4146 [100] CMS Collaboration, “Precision luminosity measurement in proton-proton
4147 collisions at $\sqrt{s} = 13$ TeV in 2015 and 2016 at CMS”, *Eur. Phys. J. C*,
4148 vol. 81, no. 9, p. 800, 2021. DOI: 10.1140/epjc/s10052-021-09538-2.
4149 arXiv: 2104.01927 [hep-ex].
- 4150 [101] S. Agostinelli et al., “GEANT4 — a simulation toolkit”, *Nucl. Instrum. Meth.*
4151 *A*, vol. 506, p. 250, 2003. DOI: 10.1016/S0168-9002(03)01368-8.
- 4152 [102] “LHC Design Report Vol.1: The LHC Main Ring”, O. S. Bruning et al., Eds.,
4153 Jun. 2004. DOI: 10.5170/CERN-2004-003-V-1.
- 4154 [103] ATLAS Collaboration, “The ATLAS Experiment at the CERN Large Hadron
4155 Collider”, *JINST*, vol. 3, S08003, 2008. DOI: 10.1088/1748-0221/3/08/
4156 S08003.
- 4157 [104] LHCb Collaboration, “The LHCb Detector at the LHC”, *JINST*, vol. 3,
4158 S08005, 2008. DOI: 10.1088/1748-0221/3/08/S08005.
- 4159 [105] ALICE Collaboration, “The ALICE experiment at the CERN LHC”, *JINST*,
4160 vol. 3, S08002, 2008. DOI: 10.1088/1748-0221/3/08/S08002.
- 4161 [106] I. Zurbano Fernandez et al., “High-Luminosity Large Hadron Collider (HL-
4162 LHC): Technical design report”, vol. 10/2020, I. Béjar Alonso, O. Brüning,
4163 P. Fessia, L. Rossi, L. Tavian, and M. Zerlauth, Eds., Dec. 2020. DOI: 10.
4164 23731/CYRM-2020-0010.
- 4165 [107] CMS Collaboration, “Technical Proposal for the Phase-II Upgrade of the
4166 CMS Detector”, Geneva, Tech. Rep., 2015. DOI: 10.17181/CERN.VU8I.D59J.
4167 [Online]. Available: <https://cds.cern.ch/record/2020886>.

- 4168 [108] CMS Collaboration, “Development of the CMS detector for the CERN LHC
4169 Run 3”, *JINST*, vol. 19, P05064, 2024. DOI: 10.1088/1748-0221/19/05/
4170 P05064. arXiv: 2309.05466 [physics.ins-det].
- 4171 [109] CMS Collaboration, *CMS Detector Slice*, 2016. [Online]. Available: <https://cds.cern.ch/record/2120661>.
- 4173 [110] CMS Collaboration, “Description and performance of track and primary-
4174 vertex reconstruction with the CMS tracker”, *JINST*, vol. 9, P10009, 2014.
4175 DOI: 10.1088/1748-0221/9/10/P10009. arXiv: 1405.6569 [physics.ins-
4176 det].
- 4177 [111] W. Adam et al., “The CMS Phase-1 Pixel Detector Upgrade”, *JINST*, vol. 16,
4178 no. 02, P02027, 2021. DOI: 10.1088/1748-0221/16/02/P02027. arXiv:
4179 2012.14304 [physics.ins-det].
- 4180 [112] “The CMS electromagnetic calorimeter project: Technical Design Report”,
4181 Tech. Rep., 1997.
- 4182 [113] CMS Collaboration, “Electron and photon reconstruction and identification
4183 with the CMS experiment at the CERN LHC”, *JINST*, vol. 16, no. 05,
4184 P05014, 2021. DOI: 10.1088/1748-0221/16/05/P05014. arXiv: 2012.06888
4185 [hep-ex].
- 4186 [114] “The CMS hadron calorimeter project: Technical Design Report”, Tech. Rep.,
4187 1997.
- 4188 [115] “CMS Technical Design Report for the Phase 1 Upgrade of the Hadron
4189 Calorimeter”, Tech. Rep., Sep. 2012. DOI: 10.2172/1151651.
- 4190 [116] “The CMS muon project: Technical Design Report”, Tech. Rep., 1997.
- 4191 [117] N. Pozzobon, “The CMS Muon System performance during the LHC Run-2”,
4192 CERN, Geneva, Tech. Rep., 2019. DOI: 10.1088/1748-0221/14/11/C11031.
4193 [Online]. Available: <https://cds.cern.ch/record/2701333>.
- 4194 [118] V. Khachatryan et al., “The CMS trigger system”, *JINST*, vol. 12, no. 01,
4195 P01020, 2017. DOI: 10.1088/1748-0221/12/01/P01020. arXiv: 1609.02366
4196 [physics.ins-det].
- 4197 [119] CMS Collaboration, “Performance of the CMS Level-1 trigger in proton-
4198 proton collisions at $\sqrt{s} = 13$ TeV”, *JINST*, vol. 15, no. 10, P10017, 2020.
4199 DOI: 10.1088/1748-0221/15/10/P10017. arXiv: 2006.10165 [hep-ex].
- 4200 [120] W. Adam et al., “The CMS high level trigger”, *Eur. Phys. J. C*, vol. 46,
4201 pp. 605–667, 2006. DOI: 10.1140/epjc/s2006-02495-8. arXiv: hep-ex/
4202 0512077.
- 4203 [121] S. Varghese, “CMS High Level Trigger Performance for Run 3”, *PoS*, vol. EPS-
4204 HEP2023, p. 517, 2023. DOI: 10.22323/1.449.0517.

- 4205 [122] CMS Collaboration, “Particle-flow reconstruction and global event descrip-
4206 tion with the CMS detector”, *JINST*, vol. 12, P10003, 2017. DOI: 10.1088/
4207 1748-0221/12/10/P10003. arXiv: 1706.04965 [physics.ins-det].
- 4208 [123] D. Bertolini, P. Harris, M. Low, and N. Tran, “Pileup Per Particle Identifica-
4209 tion”, *JHEP*, vol. 10, p. 059, 2014. DOI: 10.1007/JHEP10(2014)059. arXiv:
4210 1407.6013 [hep-ph].
- 4211 [124] M. Cacciari, G. P. Salam, and G. Soyez, “The anti- k_t jet clustering algo-
4212 rithm”, *JHEP*, vol. 04, p. 063, 2008. DOI: 10.1088/1126-6708/2008/04/063.
4213 arXiv: 0802.1189 [hep-ph].
- 4214 [125] E. Bols, J. Kieseler, M. Verzetti, M. Stoye, and A. Stakia, “Jet Flavour
4215 Classification Using DeepJet”, *JINST*, vol. 15, no. 12, P12012, 2020. DOI:
4216 10.1088/1748-0221/15/12/P12012. arXiv: 2008.10519 [hep-ex].
- 4217 [126] CMS Collaboration, “Performance of missing transverse momentum recon-
4218 struction in proton-proton collisions at $\sqrt{s} = 13$ TeV using the CMS detec-
4219 tor”, *JINST*, vol. 14, no. 07, P07004, 2019. DOI: 10.1088/1748-0221/14/
4220 07/P07004. arXiv: 1903.06078 [hep-ex].
- 4221 [127] G. Cowan, K. Cranmer, E. Gross, and O. Vitells, “Asymptotic formulae for
4222 likelihood-based tests of new physics”, *Eur. Phys. J. C*, vol. 71, p. 1554, 2011,
4223 [Erratum: Eur.Phys.J.C 73, 2501 (2013)]. DOI: 10.1140/epjc/s10052-011-
4224 1554-0. arXiv: 1007.1727 [physics.data-an].
- 4225 [128] S. S. Wilks, “The large-sample distribution of the likelihood ratio for testing
4226 composite hypotheses”, *Annals Math. Statist.*, vol. 9, no. 1, pp. 60–62, 1938.
4227 DOI: 10.1214/aoms/1177732360.
- 4228 [129] A. Wald, “Tests of statistical hypotheses concerning several parameters when
4229 the number of observations is large”, *Trans. Am. Math. Soc.*, vol. 54, no. 3,
4230 pp. 462–482, 1942. DOI: 10.1090/S0002-9947-1943-0012401-3.
- 4231 [130] T. Junk, “Confidence level computation for combining searches with small
4232 statistics”, *Nucl. Instrum. Meth. A*, vol. 434, p. 435, 1999. DOI: 10.1016/
4233 S0168-9002(99)00498-2. arXiv: hep-ex/9902006.
- 4234 [131] A. L. Read, “Presentation of search results: The CL_s technique”, *J. Phys. G*,
4235 vol. 28, p. 2693, 2002. DOI: 10.1088/0954-3899/28/10/313.
- 4236 [132] CMS Collaboration, “The CMS Statistical Analysis and Combination Tool:
4237 Combine”, *Comput. Softw. Big Sci.*, vol. 8, no. 1, p. 19, 2024. DOI: 10.1007/
4238 s41781-024-00121-4. arXiv: 2404.06614 [physics.data-an].
- 4239 [133] L. Heinrich, M. Feickert, G. Stark, and K. Cranmer, “Pyhf: Pure-Python
4240 implementation of HistFactory statistical models”, *Journal of Open Source
4241 Software*, vol. 6, no. 58, p. 2823, 2021. DOI: 10.21105/joss.02823. [Online].
4242 Available: <https://doi.org/10.21105/joss.02823>.

- 4243 [134] CMS Collaboration, “First measurement of the top quark pair production
4244 cross section in proton-proton collisions at $\sqrt{s} = 13.6\text{TeV}$ ”, CMS Physics
4245 Analysis Summary CMS-PAS-TOP-22-012, 2022. [Online]. Available: <https://cds.cern.ch/record/2834110>.
- 4247 [135] ATLAS Collaboration, “Measurement of the $t\bar{t}$ cross section and its ratio to
4248 the Z production cross section using pp collisions at $\sqrt{s} = 13.6$ TeV with the
4249 ATLAS detector”, *Phys. Lett. B*, vol. 848, p. 138376, 2024. DOI: 10.1016/
4250 j.physletb.2023.138376. arXiv: 2308.09529 [hep-ex].
- 4251 [136] M. Czakon and A. Mitov, “TOP++: A program for the calculation of the top-
4252 pair cross-section at hadron colliders”, *Comput. Phys. Commun.*, vol. 185,
4253 p. 2930, 2014. DOI: 10.1016/j.cpc.2014.06.021. arXiv: 1112.5675
4254 [hep-ph].
- 4255 [137] J. Campbell, T. Neumann, and Z. Sullivan, “Single-top-quark production
4256 in the t -channel at NNLO”, *JHEP*, vol. 02, p. 040, 2021. DOI: 10.1007/
4257 JHEP02(2021)040. arXiv: 2012.01574 [hep-ph].
- 4258 [138] S. Camarda et al., “DYTURBO: Fast predictions for Drell–Yan processes”,
4259 *Eur. Phys. J. C*, vol. 80, p. 251, 2020. DOI: 10.1140/epjc/s10052-020-
4260 7757-5. arXiv: 1910.07049 [hep-ph].
- 4261 [139] M. Grazzini, S. Kallweit, and M. Wiesemann, “Fully differential NNLO com-
4262 putations with MATRIX”, *Eur. Phys. J. C*, vol. 78, p. 537, 2018. DOI: 10.
4263 1140/epjc/s10052-018-5771-7. arXiv: 1711.06631 [hep-ph].
- 4264 [140] N. Kidonakis and N. Yamanaka, “Higher-order corrections for tW production
4265 at high-energy hadron colliders”, *JHEP*, vol. 05, p. 278, 2021. DOI: 10.1007/
4266 JHEP05(2021)278. arXiv: 2102.11300 [hep-ph].
- 4267 [141] CMS Collaboration, “Performance of the CMS muon detector and muon
4268 reconstruction with proton-proton collisions at $\sqrt{s} = 13$ TeV”, *JINST*, vol. 13,
4269 no. 06, P06015, 2018. DOI: 10.1088/1748-0221/13/06/P06015. arXiv:
4270 1804.04528 [physics.ins-det].
- 4271 [142] CMS Collaboration, “Identification of heavy-flavour jets with the CMS de-
4272 tector in pp collisions at 13 TeV”, *JINST*, vol. 13, no. 05, P05011, 2018. DOI:
4273 10.1088/1748-0221/13/05/P05011. arXiv: 1712.07158 [physics.ins-
4274 det].
- 4275 [143] CMS Collaboration, “Jet energy scale and resolution in the CMS experiment
4276 in pp collisions at 8 TeV”, *JINST*, vol. 12, P02014, 2017. DOI: 10.1088/1748-
4277 0221/12/02/P02014. arXiv: 1607.03663 [hep-ex].
- 4278 [144] CMS Collaboration, “Determination of Jet Energy Calibration and Trans-
4279 verse Momentum Resolution in CMS”, *JINST*, vol. 6, P11002, 2011. DOI:
4280 10.1088/1748-0221/6/11/P11002. arXiv: 1107.4277 [physics.ins-det].

- 4281 [145] CDF Collaboration, “Measurement of $\sigma \cdot B(W \rightarrow e\nu)$ and $\sigma \cdot B(Z^0 \rightarrow e^+e^-)$
4282 in $p\bar{p}$ Collisions at $\sqrt{s} = 1.8$ TeV”, *Phys. Rev. Lett.*, vol. 76, pp. 3070–3075,
4283 1996. DOI: 10.1103/PhysRevLett.76.3070. arXiv: hep-ex/9509010.
- 4284 [146] CDF Collaboration, “Measurement of the W boson mass with the Collider
4285 Detector at Fermilab”, *Phys. Rev. D*, vol. 64, p. 052001, 2001. DOI: 10.1103/
4286 PhysRevD.64.052001. arXiv: hep-ex/0007044.
- 4287 [147] CMS Collaboration, “Search for dark matter particles produced in association
4288 with a top quark pair at $\sqrt{s} = 13$ TeV”, *Phys. Rev. Lett.*, vol. 122, no. 1,
4289 p. 011803, 2019. DOI: 10.1103/PhysRevLett.122.011803. arXiv: 1807.
4290 06522 [hep-ex].
- 4291 [148] CMS Collaboration, “Luminosity monitoring with z counting in early 2022
4292 data”, CMS Detector Performance Note CMS-DP-2023-003, 2023. [Online].
4293 Available: <https://cds.cern.ch/record/2851655>.
- 4294 [149] CMS Collaboration, “Luminosity measurement in proton-proton collisions at
4295 13.6 TeV in 2022 at CMS”, CERN, Geneva, CMS Physics Analysis Summary,
4296 2024. [Online]. Available: <http://cds.cern.ch/record/2890833>.
- 4297 [150] M. Cacciari, S. Frixione, M. L. Mangano, P. Nason, and G. Ridolfi, “The $t\bar{t}$
4298 cross-section at 1.8 and 1.96 TeV: A study of the systematics due to parton
4299 densities and scale dependence”, *JHEP*, vol. 04, p. 068, 2004. DOI: 10.1088/
4300 1126-6708/2004/04/068. arXiv: hep-ph/0303085.
- 4301 [151] J. Butterworth et al., “PDF4LHC recommendations for LHC Run II”, *J.
4302 Phys. G*, vol. 43, p. 023001, 2016. DOI: 10.1088/0954-3899/43/2/023001.
4303 arXiv: 1510.03865 [hep-ph].
- 4304 [152] CMS Collaboration, “Investigations of the impact of the parton shower tuning
4305 in PYTHIA 8 in the modelling of $t\bar{t}$ at $\sqrt{s} = 8$ and 13 TeV”, CMS Physics
4306 Analysis Summary CMS-PAS-TOP-16-021, 2016. [Online]. Available: <https://cds.cern.ch/record/2235192>.
- 4308 [153] CMS Collaboration, “Measurements of $t\bar{t}$ differential cross sections in proton-
4309 proton collisions at $\sqrt{s} = 13$ TeV using events containing two leptons”, *JHEP*,
4310 vol. 02, p. 149, 2019. DOI: 10.1007/JHEP02(2019)149. arXiv: 1811.06625
4311 [hep-ex].
- 4312 [154] CMS Collaboration, “Measurement of normalized differential $t\bar{t}$ cross sections
4313 in the dilepton channel from pp collisions at $\sqrt{s} = 13$ TeV”, *JHEP*, vol. 04,
4314 p. 060, 2018. DOI: 10.1007/JHEP04(2018)060. arXiv: 1708.07638 [hep-ex].
- 4315 [155] CMS Collaboration, “Measurement of differential cross sections for top quark
4316 pair production using the lepton+jets final state in proton-proton collisions
4317 at 13 TeV”, *Phys. Rev. D*, vol. 95, no. 9, p. 092001, 2017. DOI: 10.1103/
4318 PhysRevD.95.092001. arXiv: 1610.04191 [hep-ex].

- [156] M. Czakon, D. Heymes, A. Mitov, D. Pagani, I. Tsinikos, and M. Zaro, “Top-pair production at the LHC through NNLO QCD and NLO EW”, *JHEP*, vol. 10, p. 186, 2017. DOI: 10.1007/JHEP10(2017)186. arXiv: 1705.04105 [hep-ph].
- [157] R. Barlow and C. Beeston, “Fitting using finite Monte Carlo samples”, *Comput. Phys. Commun.*, vol. 77, p. 219, 1993. DOI: 10.1016/0010-4655(93)90005-W.
- [158] CMS Collaboration, “Measurement of the $t\bar{t}$ production cross section, the top quark mass, and the strong coupling constant using dilepton events in pp collisions at $\sqrt{s} = 13$ TeV”, *Eur. Phys. J. C*, vol. 79, p. 368, 2019. DOI: 10.1140/epjc/s10052-019-6863-8. arXiv: 1812.10505 [hep-ex].
- [159] ATLAS Collaboration, “Measurement of the $t\bar{t}$ production cross-section in the lepton+jets channel at $\sqrt{s} = 13$ TeV with the ATLAS experiment”, *Phys. Lett. B*, vol. 810, p. 135 797, 2020. DOI: 10.1016/j.physletb.2020.135797. arXiv: 2006.13076 [hep-ex].
- [160] CMS Collaboration, “Measurement of the $t\bar{t}$ production cross section in the all-jet final state in pp collisions at $\sqrt{s} = 7$ TeV”, *JHEP*, vol. 05, p. 065, 2013. DOI: 10.1007/JHEP05(2013)065. arXiv: 1302.0508 [hep-ex].
- [161] CMS Collaboration, “Measurement of the $t\bar{t}$ production cross section in the all-jets final state in pp collisions at $\sqrt{s} = 8$ TeV”, *Eur. Phys. J. C*, vol. 76, p. 128, 2016. DOI: 10.1140/epjc/s10052-016-3956-5. arXiv: 1509.06076 [hep-ex].
- [162] CMS Collaboration, “Measurements of the $t\bar{t}$ production cross section in lepton+jets final states in pp collisions at 8 TeV and ratio of 8 to 7 TeV cross sections”, *Eur. Phys. J. C*, vol. 77, p. 15, 2017. DOI: 10.1140/epjc/s10052-016-4504-z. arXiv: 1602.09024 [hep-ex].
- [163] CMS Collaboration, “Measurement of the $t\bar{t}$ production cross section in the $e\mu$ channel in proton-proton collisions at $\sqrt{s} = 7$ and 8 TeV”, *JHEP*, vol. 08, p. 029, 2016. DOI: 10.1007/JHEP08(2016)029. arXiv: 1603.02303 [hep-ex].
- [164] CMS Collaboration, “Measurement of the top quark pair production cross section in dilepton final states containing one τ lepton in pp collisions at $\sqrt{s} = 13$ TeV”, *JHEP*, vol. 02, p. 191, 2020. DOI: 10.1007/JHEP02(2020)191. arXiv: 1911.13204 [hep-ex].
- [165] CMS Collaboration, “Measurement of differential $t\bar{t}$ production cross sections in the full kinematic range using lepton+jets events from proton-proton collisions at $\sqrt{s} = 13$ TeV”, *Phys. Rev. D*, vol. 104, p. 092 013, 2021. DOI: 10.1103/PhysRevD.104.092013. arXiv: 2108.02803 [hep-ex].

- 4356 [166] CMS Collaboration, “Measurement of the inclusive $t\bar{t}$ production cross sec-
4357 tion in proton-proton collisions at $\sqrt{s} = 5.02$ TeV”, *JHEP*, vol. 04, p. 144,
4358 2022. DOI: 10.1007/JHEP04(2022)144. arXiv: 2112.09114 [hep-ex].
- 4359 [167] M. Czakon, P. Fiedler, and A. Mitov, “Total top-quark pair-production cross
4360 section at hadron colliders through $\mathcal{O}(\alpha_S^4)$ ”, *Phys. Rev. Lett.*, vol. 110,
4361 p. 252004, 2013. DOI: 10.1103/PhysRevLett.110.252004. arXiv: 1303.
4362 6254 [hep-ph].
- 4363 [168] R. Tarrach, “The Pole Mass in Perturbative QCD”, *Nucl. Phys. B*, vol. 183,
4364 pp. 384–396, 1981. DOI: 10.1016/0550-3213(81)90140-1.
- 4365 [169] M. C. Smith and S. S. Willenbrock, “Top quark pole mass”, *Phys. Rev. Lett.*,
4366 vol. 79, pp. 3825–3828, 1997. DOI: 10.1103/PhysRevLett.79.3825. arXiv:
4367 hep-ph/9612329.
- 4368 [170] A. H. Hoang, “What is the Top Quark Mass?”, *Ann. Rev. Nucl. Part. Sci.*,
4369 vol. 70, pp. 225–255, 2020. DOI: 10.1146/annurev-nucl-101918-023530.
4370 arXiv: 2004.12915 [hep-ph].
- 4371 [171] ATLAS Collaboration, “Probing the quantum interference between singly
4372 and doubly resonant top-quark production in pp collisions at $\sqrt{s} = 13$ TeV
4373 with the ATLAS detector”, *Phys. Rev. Lett.*, vol. 121, p. 152002, 2018. DOI:
4374 10.1103/PhysRevLett.121.152002. arXiv: 1806.04667 [hep-ex].
- 4375 [172] T. Ježo, J. M. Lindert, and S. Pozzorini, “Resonance-aware NLOPS matching
4376 for off-shell $t\bar{t} + tW$ production with semileptonic decays”, *JHEP*, vol. 10,
4377 p. 008, 2023. DOI: 10.1007/JHEP10(2023)008. arXiv: 2307.15653 [hep-ph].
- 4378 [173] T. Ježo and P. Nason, “On the treatment of resonances in next-to-leading
4379 order calculations matched to a parton shower”, *JHEP*, vol. 12, p. 065, 2015.
4380 DOI: 10.1007/JHEP12(2015)065. arXiv: 1509.09071 [hep-ph].
- 4381 [174] <https://powhegbox.mib.infn.it>.
- 4382 [175] S. Frixione, E. Laenen, P. Motylinski, and B. R. Webber, “Angular corre-
4383 lations of lepton pairs from vector boson and top quark decays in Monte Carlo
4384 simulations”, *JHEP*, vol. 04, p. 081, 2007. DOI: 10.1088/1126-6708/2007/
4385 04/081. arXiv: hep-ph/0702198.
- 4386 [176] E. Re, “Single-top Wt -channel production matched with parton showers us-
4387 ing the powheg method”, *Eur. Phys. J. C*, vol. 71, p. 1547, 2011. DOI: 10.
4388 1140/epjc/s10052-011-1547-z. arXiv: 1009.2450 [hep-ph].
- 4389 [177] S. Frixione, E. Laenen, P. Motylinski, B. R. Webber, and C. D. White,
4390 “Single-top hadroproduction in association with a W boson”, *JHEP*, vol. 07,
4391 p. 029, 2008. DOI: 10.1088/1126-6708/2008/07/029. arXiv: 0805.3067
4392 [hep-ph].

- 4393 [178] T. M. P. Tait, “The tW^- mode of single top production”, *Phys. Rev. D*,
 4394 vol. 61, p. 034 001, 1999. DOI: 10.1103/PhysRevD.61.034001. arXiv: hep-
 4395 ph/9909352.
- 4396 [179] J. M. Campbell, R. K. Ellis, P. Nason, and E. Re, “Top-pair production and
 4397 decay at NLO matched with parton showers”, *JHEP*, vol. 04, p. 114, 2015.
 4398 DOI: 10.1007/JHEP04(2015)114. arXiv: 1412.1828 [hep-ph].
- 4399 [180] S. Ferrario Ravasio, T. Ježo, P. Nason, and C. Oleari, “A theoretical study of
 4400 top-mass measurements at the LHC using NLO+PS generators of increasing
 4401 accuracy”, *Eur. Phys. J. C*, vol. 78, p. 458, 2018. DOI: 10.1140/epjc/s10052-018-5909-7. arXiv: 1906.09166 [hep-ph].
- 4403 [181] C. Bierlich et al., “Robust independent validation of experiment and theory: Rivet version 3”, *SciPost Phys.*, vol. 8, p. 026, 2020. DOI: 10.21468/SciPostPhys.8.2.026. arXiv: 1912.05451 [hep-ph].
- 4406 [182] M. Cacciari and G. P. Salam, “Pileup subtraction using jet areas”, *Phys. Lett. B*, vol. 659, pp. 119–126, 2008. DOI: 10.1016/j.physletb.2007.09.077. arXiv: 0707.1378 [hep-ph].
- 4409 [183] M. Cacciari, G. P. Salam, and G. Soyez, “The Catchment Area of Jets”, *JHEP*, vol. 04, p. 005, 2008. DOI: 10.1088/1126-6708/2008/04/005. arXiv: 0802.1188 [hep-ph].
- 4412 [184] ATLAS Collaboration, “Studies of $t\bar{t}/tW$ interference effects in $b\bar{b}\ell^+\ell^-\nu\bar{\nu}'$ final states with POWHEG and MG5_AMC@NLO setups”, ATLAS PUB Note ATL-PHYS-PUB-2021-042, 2021. [Online]. Available: <https://cds.cern.ch/record/2792254>.
- 4416 [185] D. Boer et al., “Gluons and the quark sea at high energies: Distributions, polarization, tomography”, Aug. 2011. arXiv: 1108.1713 [nucl-th].
- 4418 [186] H. Brooks and P. Skands, “Coherent showers in decays of colored resonances”, *Phys. Rev. D*, vol. 100, no. 7, p. 076 006, 2019. DOI: 10.1103/PhysRevD.100.076006. arXiv: 1907.08980 [hep-ph].
- 4421 [187] ATLAS Collaboration, “Measurement of the top-quark mass using a leptonic invariant mass in pp collisions at $\sqrt{s} = 13$ TeV with the ATLAS detector”, *JHEP*, vol. 06, p. 019, 2023. DOI: 10.1007/JHEP06(2023)019. arXiv: 2209.00583 [hep-ex].
- 4425 [188] ATLAS Collaboration, “Search for Heavy Higgs Bosons A/H Decaying to a Top Quark Pair in pp Collisions at $\sqrt{s} = 8$ TeV with the ATLAS Detector”, *Phys. Rev. Lett.*, vol. 119, no. 19, p. 191 803, 2017. DOI: 10.1103/PhysRevLett.119.191803. arXiv: 1707.06025 [hep-ex].

- ⁴⁴²⁹ [189] ATLAS Collaboration, “Search for heavy neutral Higgs bosons decaying into
⁴⁴³⁰ a top quark pair in 140 fb^{-1} of proton-proton collision data at $\sqrt{s} = 13$
⁴⁴³¹ TeV with the ATLAS detector”, *JHEP*, vol. 08, p. 013, 2024. DOI: 10.1007/
⁴⁴³² JHEP08(2024)013. arXiv: 2404.18986 [hep-ex].
- ⁴⁴³³ [190] ATLAS Collaboration, “Observation of a cross-section enhancement near the
⁴⁴³⁴ $t\bar{t}$ production threshold in $\sqrt{s} = 13$ TeV pp collisions with the ATLAS de-
⁴⁴³⁵ tector”, ATLAS Conference Note ATLAS-CONF-2025-008, 2025. [Online].
⁴⁴³⁶ Available: <https://cds.cern.ch/record/2937636>.
- ⁴⁴³⁷ [191] CMS Collaboration, “Search for heavy pseudoscalar and scalar bosons de-
⁴⁴³⁸ caying to top quark pairs in proton-proton collisions at $\sqrt{s} = 13$ TeV”, CMS
⁴⁴³⁹ Physics Analysis Summary CMS-PAS-HIG-22-013, 2024. [Online]. Available:
⁴⁴⁴⁰ <https://cds.cern.ch/record/2911775>.
- ⁴⁴⁴¹ [192] J. Rübenach, “Search for Heavy Higgs Bosons in Conjunction with Neural-
⁴⁴⁴² Network-Driven Reconstruction and Upgrade of the Fast Beam Condition
⁴⁴⁴³ Monitor at the CMS Experiment”, PhD thesis, DESY, Hamburg, May 2023.
- ⁴⁴⁴⁴ [193] CMS Collaboration, “Simulation of the silicon strip tracker pre-amplifier in
⁴⁴⁴⁵ early 2016 data”, CMS Detector Performance Note CMS-DP-2020-045, 2020.
⁴⁴⁴⁶ [Online]. Available: <https://cds.cern.ch/record/2740688>.
- ⁴⁴⁴⁷ [194] P. F. Monni, P. Nason, E. Re, M. Wiesemann, and G. Zanderighi, “MiNNLO_{PS}:
⁴⁴⁴⁸ a new method to match NNLO QCD to parton showers”, *JHEP*, vol. 05,
⁴⁴⁴⁹ p. 143, 2020, [Erratum: JHEP 02, 031 (2022)]. DOI: 10.1007/JHEP05(2020)
⁴⁴⁵⁰ 143. arXiv: 1908.06987 [hep-ph].
- ⁴⁴⁵¹ [195] P. F. Monni, E. Re, and M. Wiesemann, “MiNNLO_{PS}: optimizing $2 \rightarrow 1$
⁴⁴⁵² hadronic processes”, *Eur. Phys. J. C*, vol. 80, no. 11, p. 1075, 2020. DOI:
⁴⁴⁵³ 10.1140/epjc/s10052-020-08658-5. arXiv: 2006.04133 [hep-ph].
- ⁴⁴⁵⁴ [196] M. Aliev, H. Lacker, U. Langenfeld, S. Moch, P. Uwer, and M. Wiedermann,
⁴⁴⁵⁵ “HATHOR: Hadronic top and heavy quarks cross section calculator”, *Comput.*
⁴⁴⁵⁶ *Phys. Commun.*, vol. 182, p. 1034, 2011. DOI: 10.1016/j.cpc.2010.12.040.
⁴⁴⁵⁷ arXiv: 1007.1327 [hep-ph].
- ⁴⁴⁵⁸ [197] P. Kant et al., “HatHor for single top-quark production: Updated predictions
⁴⁴⁵⁹ and uncertainty estimates for single top-quark production in hadronic col-
⁴⁴⁶⁰ lisions”, *Comput. Phys. Commun.*, vol. 191, pp. 74–89, 2015. DOI: 10.1016/
⁴⁴⁶¹ j.cpc.2015.02.001. arXiv: 1406.4403 [hep-ph].
- ⁴⁴⁶² [198] K. Melnikov and F. Petriello, “Electroweak gauge boson production at hadron
⁴⁴⁶³ colliders through $\mathcal{O}(\alpha_S^2)$ ”, *Phys. Rev. D*, vol. 74, p. 114017, 2006. DOI: 10.
⁴⁴⁶⁴ 1103/PhysRevD.74.114017. arXiv: hep-ph/0609070.
- ⁴⁴⁶⁵ [199] Y. Li and F. Petriello, “Combining QCD and electroweak corrections to dilep-
⁴⁴⁶⁶ ton production in FEWZ”, *Phys. Rev. D*, vol. 86, p. 094034, 2012. DOI:
⁴⁴⁶⁷ 10.1103/PhysRevD.86.094034. arXiv: 1208.5967 [hep-ph].

- 4468 [200] T. Gehrmann et al., “ W^+W^- Production at Hadron Colliders in Next to Next
4469 to Leading Order QCD”, *Phys. Rev. Lett.*, vol. 113, no. 21, p. 212001, 2014.
4470 DOI: 10.1103/PhysRevLett.113.212001. arXiv: 1408.5243 [hep-ph].
- 4471 [201] J. M. Campbell and R. K. Ellis, “MCFM for the Tevatron and the LHC”,
4472 *Nucl. Phys. B Proc. Suppl.*, vol. 205-206, J. Blümlein, S.-O. Moch, and T.
4473 Riemann, Eds., pp. 10–15, 2010. DOI: 10.1016/j.nuclphysbps.2010.08.
4474 011. arXiv: 1007.3492 [hep-ph].
- 4475 [202] CMS Collaboration, “Measurement of the differential cross section for top
4476 quark pair production in pp collisions at $\sqrt{s} = 8\text{TeV}$ ”, *Eur. Phys. J. C*,
4477 vol. 75, no. 11, p. 542, 2015. DOI: 10.1140/epjc/s10052-015-3709-x.
4478 arXiv: 1505.04480 [hep-ex].
- 4479 [203] L. Sonnenschein, “Analytical solution of ttbar dilepton equations”, *Phys. Rev.*
4480 *D*, vol. 73, p. 054015, 2006, [Erratum: Phys.Rev.D 78, 079902 (2008)]. DOI:
4481 10.1103/PhysRevD.78.079902. arXiv: hep-ph/0603011.
- 4482 [204] I. Korol, “Measurement of double differential $t\bar{t}$ production cross sections with
4483 the CMS detector”, CERN-THESIS-2016-060, DESY-THESIS-2016-011, Ph.D.
4484 dissertation, Universität Hamburg, 2016. DOI: 10.3204/DESY-THESIS-2016-
4485 011.
- 4486 [205] J. H. Kühn, A. Scharf, and P. Uwer, “Electroweak corrections to top-quark
4487 pair production in quark-antiquark annihilation”, *Eur. Phys. J. C*, vol. 45,
4488 p. 139, 2006. DOI: 10.1140/epjc/s2005-02423-6. arXiv: hep-ph/0508092.
- 4489 [206] J. H. Kühn, A. Scharf, and P. Uwer, “Electroweak effects in top-quark pair
4490 production at hadron colliders”, *Eur. Phys. J. C*, vol. 51, p. 37, 2007. DOI:
4491 10.1140/epjc/s10052-007-0275-x. arXiv: hep-ph/0610335.
- 4492 [207] J. H. Kühn, A. Scharf, and P. Uwer, “Weak interactions in top-quark pair
4493 production at hadron colliders: An update”, *Phys. Rev. D*, vol. 91, p. 014020,
4494 2015. DOI: 10.1103/PhysRevD.91.014020. arXiv: 1305.5773 [hep-ph].
- 4495 [208] CMS Collaboration, “Combined measurements of Higgs boson couplings in
4496 proton–proton collisions at $\sqrt{s} = 13\text{TeV}$ ”, *Eur. Phys. J. C*, vol. 79, no. 5,
4497 p. 421, 2019. DOI: 10.1140/epjc/s10052-019-6909-y. arXiv: 1809.10733
4498 [hep-ex].
- 4499 [209] CMS Collaboration, “Measurement of the top quark mass using a profile
4500 likelihood approach with the lepton + jets final states in proton–proton col-
4501 lisions at $\sqrt{s} = 13\text{TeV}$ ”, *Eur. Phys. J. C*, vol. 83, no. 10, p. 963, 2023. DOI:
4502 10.1140/epjc/s10052-023-12050-4. arXiv: 2302.01967 [hep-ex].
- 4503 [210] CMS Collaboration, “CMS pythia 8 colour reconnection tunes based on
4504 underlying-event data”, *Eur. Phys. J. C*, vol. 83, no. 7, p. 587, 2023. DOI:
4505 10.1140/epjc/s10052-023-11630-8. arXiv: 2205.02905 [hep-ex].

- 4506 [211] ATLAS Collaboration, “Measurement of the inclusive cross-sections of single
4507 top-quark and top-antiquark t -channel production in pp collisions at $\sqrt{s} = 13$
4508 TeV with the ATLAS detector”, *JHEP*, vol. 04, p. 086, 2017. DOI: 10.1007/
4509 JHEP04(2017)086. arXiv: 1609.03920 [hep-ex].
- 4510 [212] CMS Collaboration, “Measurement of the single top quark and antiquark
4511 production cross sections in the t channel and their ratio in proton-proton
4512 collisions at $\sqrt{s} = 13$ TeV”, *Phys. Lett. B*, vol. 800, p. 135042, 2020. DOI:
4513 10.1016/j.physletb.2019.135042. arXiv: 1812.10514 [hep-ex].
- 4514 [213] CMS Collaboration, “Measurement of the production cross section for single
4515 top quarks in association with W bosons in proton-proton collisions at $\sqrt{s} =$
4516 13 TeV”, *JHEP*, vol. 10, p. 117, 2018. DOI: 10.1007/JHEP10(2018)117.
4517 arXiv: 1805.07399 [hep-ex].
- 4518 [214] CMS Collaboration, “Measurement of the cross section for top quark pair
4519 production in association with a W or Z boson in proton-proton collisions at
4520 $\sqrt{s} = 13$ TeV”, *JHEP*, vol. 08, p. 011, 2018. DOI: 10.1007/JHEP08(2018)011.
4521 arXiv: 1711.02547 [hep-ex].
- 4522 [215] ATLAS Collaboration, “Measurement of the $t\bar{t}Z$ and $t\bar{t}W$ cross sections in
4523 proton-proton collisions at $\sqrt{s} = 13$ TeV with the ATLAS detector”, *Phys.*
4524 *Rev. D*, vol. 99, p. 072009, 2019. DOI: 10.1103/PhysRevD.99.072009. arXiv:
4525 1901.03584 [hep-ex].
- 4526 [216] ATLAS Collaboration, “Measurements of top-quark pair to Z-boson cross-
4527 section ratios at $\sqrt{s} = 13, 8, 7$ TeV with the ATLAS detector”, *JHEP*, vol. 02,
4528 p. 117, 2017. DOI: 10.1007/JHEP02(2017)117. arXiv: 1612.03636 [hep-ex].
- 4529 [217] CMS Collaboration, “CMS luminosity measurement for the 2017 data-taking
4530 period at $\sqrt{s} = 13$ TeV”, CMS Physics Analysis Summary CMS-PAS-LUM-
4531 17-004, 2018. [Online]. Available: <https://cds.cern.ch/record/2621960>.
- 4532 [218] CMS Collaboration, “CMS luminosity measurement for the 2018 data-taking
4533 period at $\sqrt{s} = 13$ TeV”, CMS Physics Analysis Summary CMS-PAS-LUM-
4534 18-002, 2019. [Online]. Available: <https://cds.cern.ch/record/2676164>.
- 4535 [219] CMS Collaboration, “Measurement of the inelastic proton-proton cross sec-
4536 tion at $\sqrt{s} = 13$ TeV”, *JHEP*, vol. 07, p. 161, 2018. DOI: 10.1007/JHEP07(2018)
4537 161. arXiv: 1802.02613 [hep-ex].
- 4538 [220] W. S. Cleveland, “Robust locally weighted regression and smoothing scat-
4539 terplots”, *Journal of the American Statistical Association*, vol. 74, no. 368,
4540 pp. 829–836, 1979. DOI: 10.1080/01621459.1979.10481038.
- 4541 [221] W. S. Cleveland and S. J. Devlin, “Locally weighted regression: An approach
4542 to regression analysis by local fitting”, *Journal of the American Statistical
4543 Association*, vol. 83, no. 403, pp. 596–610, 1988. DOI: 10.1080/01621459.
4544 1988.10478639.

- 4545 [222] CMS Collaboration, “Measurement of differential cross sections for the pro-
 4546 duction of top quark pairs and of additional jets in lepton+jets events from
 4547 pp collisions at $\sqrt{s} = 13$ TeV”, *Phys. Rev. D*, vol. 97, no. 11, p. 112003, 2018.
 4548 DOI: [10.1103/PhysRevD.97.112003](https://doi.org/10.1103/PhysRevD.97.112003). arXiv: [1803.08856](https://arxiv.org/abs/1803.08856) [hep-ex].
- 4549 [223] CMS Collaboration, “Development and validation of HERWIG 7 tunes from
 4550 CMS underlying-event measurements”, *Eur. Phys. J. C*, vol. 81, no. 4, p. 312,
 4551 2021. DOI: [10.1140/epjc/s10052-021-08949-5](https://doi.org/10.1140/epjc/s10052-021-08949-5). arXiv: [2011.03422](https://arxiv.org/abs/2011.03422) [hep-
 4552 ex].
- 4553 [224] B. R. Webber, “A QCD Model for Jet Fragmentation Including Soft Gluon
 4554 Interference”, *Nucl. Phys. B*, vol. 238, pp. 492–528, 1984. DOI: [10.1016/0550-3213\(84\)90333-X](https://doi.org/10.1016/0550-3213(84)90333-X).
- 4556 [225] F. J. Llanes-Estrada, “Ensuring that toponium is glued, not nailed”, Nov.
 4557 2024. arXiv: [2411.19180](https://arxiv.org/abs/2411.19180) [hep-ph].
- 4558 [226] D. d’Enterria and K. Kang, “Exclusive photon-fusion production of even-
 4559 spin resonances and exotic QED atoms in high-energy hadron collisions”,
 4560 Mar. 2025. arXiv: [2503.10952](https://arxiv.org/abs/2503.10952) [hep-ph].
- 4561 [227] A. Djouadi, J. Ellis, A. Popov, and J. Quevillon, “Interference effects in $t\bar{t}$
 4562 production at the LHC as a window on new physics”, *JHEP*, vol. 03, p. 119,
 4563 2019. DOI: [10.1007/JHEP03\(2019\)119](https://doi.org/10.1007/JHEP03(2019)119). arXiv: [1901.03417](https://arxiv.org/abs/1901.03417) [hep-ph].
- 4564 [228] A. Djouadi, J. Ellis, and J. Quevillon, “Discriminating between Pseudoscalar
 4565 Higgs and Toponium States at the LHC and Beyond”, Dec. 2024. arXiv:
 4566 [2412.15138](https://arxiv.org/abs/2412.15138) [hep-ph].
- 4567 [229] B. A. Betchart, R. Demina, and A. Harel, “Analytic solutions for neutrino
 4568 momenta in decay of top quarks”, *Nucl. Instrum. Meth. A*, vol. 736, p. 169,
 4569 2014. DOI: [10.1016/j.nima.2013.10.039](https://doi.org/10.1016/j.nima.2013.10.039). arXiv: [1305.1878](https://arxiv.org/abs/1305.1878) [hep-ph].
- 4570 [230] R. Demina, A. Harel, and D. Orbaker, “Reconstructing $t\bar{t}$ events with one
 4571 lost jet”, *Nucl. Instrum. Meth. A*, vol. 788, p. 128, 2015. DOI: [10.1016/j.nima.2015.03.069](https://doi.org/10.1016/j.nima.2015.03.069). arXiv: [1310.3263](https://arxiv.org/abs/1310.3263) [hep-ex].
- 4573 [231] G. J. Feldman and R. D. Cousins, “Unified approach to the classical statistical
 4574 analysis of small signals”, *Phys. Rev. D*, vol. 57, p. 3873, 1998. DOI: [10.1103/PhysRevD.57.3873](https://doi.org/10.1103/PhysRevD.57.3873). arXiv: [physics/9711021](https://arxiv.org/abs/physics/9711021).
- 4576 [232] R. D. Cousins and V. L. Highland, “Incorporating systematic uncertainties
 4577 into an upper limit”, *Nucl. Instrum. Meth. A*, vol. 320, pp. 331–335, 1992.
 4578 DOI: [10.1016/0168-9002\(92\)90794-5](https://doi.org/10.1016/0168-9002(92)90794-5).
- 4579 [233] HEPData record for analysis “Search for heavy pseudoscalar and scalar bosons
 4580 decaying to a top quark pair in proton-proton collisions at $\sqrt{s} = 13$ TeV”
 4581 (CMS-HIG-22-013), 2025. DOI: [10.17182/hepdata.159298](https://doi.org/10.17182/hepdata.159298).

- 4582 [234] ATLAS Collaboration, “Measurement of the $t\bar{t}$ production cross-section and
4583 lepton differential distributions in $e\mu$ dilepton events from pp collisions at
4584 $\sqrt{s} = 13$ TeV with the ATLAS detector”, *Eur. Phys. J. C*, vol. 80, no. 6,
4585 p. 528, 2020. DOI: [10.1140/epjc/s10052-020-7907-9](https://doi.org/10.1140/epjc/s10052-020-7907-9). arXiv: [1910.08819](https://arxiv.org/abs/1910.08819)
4586 [[hep-ex](#)].
- 4587 [235] CMS Collaboration, “Differential cross section measurements for the produc-
4588 tion of top quark pairs and of additional jets using dilepton events from pp
4589 collisions at $\sqrt{s} = 13$ TeV”, *JHEP*, vol. 02, p. 064, 2025. DOI: [10.1007/JHEP02\(2025\)064](https://doi.org/10.1007/JHEP02(2025)064). arXiv: [2402.08486](https://arxiv.org/abs/2402.08486) [[hep-ex](#)].
- 4591 [236] ATLAS Collaboration, “Inclusive and differential cross-sections for dilepton $t\bar{t}$
4592 production measured in $\sqrt{s} = 13$ TeV pp collisions with the ATLAS detector”,
4593 *JHEP*, vol. 07, p. 141, 2023. DOI: [10.1007/JHEP07\(2023\)141](https://doi.org/10.1007/JHEP07(2023)141). arXiv: [2303.15340](https://arxiv.org/abs/2303.15340) [[hep-ex](#)].
- 4595 [237] J. Gallicchio and M. D. Schwartz, “Seeing in Color: Jet Superstructure”,
4596 *Phys. Rev. Lett.*, vol. 105, p. 022001, 2010. DOI: [10.1103/PhysRevLett.105.022001](https://doi.org/10.1103/PhysRevLett.105.022001). arXiv: [1001.5027](https://arxiv.org/abs/1001.5027) [[hep-ph](#)].
- 4598 [238] ATLAS Collaboration, “Measurement of colour flow using jet-pull observables
4599 in $t\bar{t}$ events with the ATLAS experiment at $\sqrt{s} = 13$ TeV”, *Eur. Phys. J. C*,
4600 vol. 78, no. 10, p. 847, 2018. DOI: [10.1140/epjc/s10052-018-6290-2](https://doi.org/10.1140/epjc/s10052-018-6290-2).
4601 arXiv: [1805.02935](https://arxiv.org/abs/1805.02935) [[hep-ex](#)].
- 4602 [239] J. A. Raine, M. Leigh, K. Zoch, and T. Golling, “Fast and improved neu-
4603 trino reconstruction in multineutrino final states with conditional normalizing
4604 flows”, *Phys. Rev. D*, vol. 109, no. 1, p. 012005, 2024. DOI: [10.1103/PhysRevD.109.012005](https://doi.org/10.1103/PhysRevD.109.012005). arXiv: [2307.02405](https://arxiv.org/abs/2307.02405) [[hep-ph](#)].
- 4606 [240] CMS Collaboration, “High-precision measurement of the W boson mass with
4607 the CMS experiment at the LHC”, Dec. 2024. arXiv: [2412.13872](https://arxiv.org/abs/2412.13872) [[hep-ex](#)].
- 4608 [241] S.-J. Jiang, B.-Q. Li, G.-Z. Xu, and K.-Y. Liu, “Study on Toponium: Spec-
4609 trum and Associated Processes”, Dec. 2024. arXiv: [2412.18527](https://arxiv.org/abs/2412.18527) [[hep-ph](#)].
- 4610 [242] I. Brivio et al., “ALPs Effective Field Theory and Collider Signatures”, *Eur.
4611 Phys. J. C*, vol. 77, no. 8, p. 572, 2017. DOI: [10.1140/epjc/s10052-017-5111-3](https://doi.org/10.1140/epjc/s10052-017-5111-3). arXiv: [1701.05379](https://arxiv.org/abs/1701.05379) [[hep-ph](#)].
- 4613 [243] J. Bonilla, I. Brivio, M. B. Gavela, and V. Sanz, “One-loop corrections to ALP
4614 couplings”, *JHEP*, vol. 11, p. 168, 2021. DOI: [10.1007/JHEP11\(2021\)168](https://doi.org/10.1007/JHEP11(2021)168).
4615 arXiv: [2107.11392](https://arxiv.org/abs/2107.11392) [[hep-ph](#)].
- 4616 [244] H. Bahl et al., “HiggsTools: BSM scalar phenomenology with new versions of
4617 HiggsBounds and HiggsSignals”, *Comput. Phys. Commun.*, vol. 291, p. 108803,
4618 2023. DOI: [10.1016/j.cpc.2023.108803](https://doi.org/10.1016/j.cpc.2023.108803). arXiv: [2210.09332](https://arxiv.org/abs/2210.09332) [[hep-ph](#)].

- 4619 [245] ATLAS Collaboration, “Search for resonances decaying into photon pairs in
4620 139 fb^{-1} of pp collisions at $\sqrt{s}=13 \text{ TeV}$ with the ATLAS detector”, *Phys.*
4621 *Lett. B*, vol. 822, p. 136 651, 2021. DOI: [10.1016/j.physletb.2021.136651](https://doi.org/10.1016/j.physletb.2021.136651).
4622 arXiv: [2102.13405](https://arxiv.org/abs/2102.13405) [hep-ex].
- 4623 [246] ATLAS Collaboration, “Search for heavy resonances decaying into a Z or W
4624 boson and a Higgs boson in final states with leptons and b -jets in 139 fb^{-1}
4625 of pp collisions at $\sqrt{s} = 13 \text{ TeV}$ with the ATLAS detector”, *JHEP*, vol. 06,
4626 p. 016, 2023. DOI: [10.1007/JHEP06\(2023\)016](https://doi.org/10.1007/JHEP06(2023)016). arXiv: [2207.00230](https://arxiv.org/abs/2207.00230) [hep-ex].
- 4627 [247] CMS Collaboration, “Observation of four top quark production in proton-
4628 proton collisions at $\sqrt{s} = 13 \text{ TeV}$ ”, *Phys. Lett. B*, vol. 847, p. 138 290, 2023.
4629 DOI: [10.1016/j.physletb.2023.138290](https://doi.org/10.1016/j.physletb.2023.138290). arXiv: [2305.13439](https://arxiv.org/abs/2305.13439) [hep-ex].
- 4630 [248] A. Biekötter, J. Fuentes-Martín, A. M. Galda, and M. Neubert, “A global
4631 analysis of axion-like particle interactions using SMEFT fits”, *JHEP*, vol. 09,
4632 p. 120, 2023. DOI: [10.1007/JHEP09\(2023\)120](https://doi.org/10.1007/JHEP09(2023)120). arXiv: [2307.10372](https://arxiv.org/abs/2307.10372) [hep-ph].

*This was a triumph.
I'm making a note here: HUGE SUCCESS.
It's hard to overstate my satisfaction.*

— GLaDOS

4633 B Acknowledgements

4634 I wish to thank, first and foremost, my excellent PhD supervisors: Christian Schwan-
4635 nenberger and Alexander Grohsjean. You gave me feedback when I needed it, left
4636 me space when I did not, and always had my back in our common (mis-)adventures
4637 in the wide and wonderful and sometimes wondrous world that is Experimental
4638 Particle Physics. You also gave me great (and honest) advice and support for my
4639 further career, for which I am extremely thankful. Working with you has been a
4640 pleasure.

4641 I am also deeply grateful to the many colleagues, postdocs and other PhD stu-
4642 dents, who taught me the intricacies of CMS and provided technical and moral
4643 support: Afiq Anuar, for unleashing $A/H \rightarrow t\bar{t}$ in the first place, and for always
4644 distracting me with interesting physics; Evan Ranken, who for some reason agreed
4645 to help perform a measurement in only two months; Jonas Rübenach and Dominic
4646 Stafford, for collectively sparing me from ROOT with their framework; again Jonas,
4647 for setting up the A/H analysis and giving me an excess to interpret; and again
4648 Dominic, for tolerating me as an officemate. Thanks to all of you.

4649 Furthermore, I would like to thank my additional collaborators and supervisors
4650 on the different projects I worked on: Maria Aldaya and Andreas Meyer for the $t\bar{t}$
4651 cross section in Run 3; Simone Amoroso for $bb4l$; as well as Georg Weiglein, Sven
4652 Heinemeyer, and the Biekötter Cousins for ALPs $\rightarrow t\bar{t}$.

4653 Finally, I wish to give a huge thanks to the DESY CMS group for being a great
4654 place to work.

4655 C Appendices

4656 C.1 Sample normalizations in the matrix element 4657 reweighting

4658 In this section, a derivation of the optimal way to combine multiple independent
4659 origin samples for the purpose of matrix element reweighting, as described in Sec. 7.4
4660 is given. In particular, Eq. (7.16) is proven for the case that the cross section
4661 corresponding to the target hypothesis is known from an external calculation.

4662 The notation used is the same as in Sec. 7.4. Let $\hat{w}_{i,j}$ be the weight of event i in
4663 origin sample j after reweighting, i.e. the product of ME weight and generator weight
4664 of the origin sample, and v_j the per-sample normalization that is to be determined.
4665 The per-event weight after normalization is $v_j \hat{w}_{i,j}$.

4666 First, consider the case that the total cross section σ is known for the target
4667 hypothesis, meaning that the ME reweighting needs to only predict the shapes
4668 of the distributions. In Sec. 7.4, this is achieved by explicitly calculating σ with
4669 MG5_AMC@NLO for each target A/H hypothesis. The goal is now to minimize
4670 the total variance of the sample, given by

$$V = \sum_{i,j} v_j^2 \hat{w}_{i,j}^2, \quad (\text{C.1})$$

4671 under the constraint that the total yield is

$$N = \sum_{i,j} v_j \hat{w}_{i,j} \equiv \sigma L, \quad (\text{C.2})$$

4672 where L is the integrated luminosity. This is done with the method of Lagrange
4673 multipliers, giving the Lagrange function

$$\mathcal{L}(v_j, \lambda) = \sum_{i,j} v_j^2 \hat{w}_{i,j}^2 + \lambda \left(\sum_{i,j} v_j \hat{w}_{i,j} - \sigma L \right) \quad (\text{C.3})$$

4674 which needs to be minimized simultaneously over v_j and λ . Differentiating by v_j
4675 gives

$$\frac{\partial \mathcal{L}}{\partial v_j} = 2v_j \sum_i \hat{w}_{i,j}^2 + \lambda \sum_i \hat{w}_{i,j} \equiv 0 \quad \Rightarrow \quad v_j = -\frac{\lambda}{2} \frac{\sum_i \hat{w}_{i,j}}{\sum_i \hat{w}_{i,j}^2}. \quad (\text{C.4})$$

⁴⁶⁷⁶ By substituting this into Eq. (C.2) to find λ , one obtains

$$v_j = \sigma L \left(\sum_k \frac{\sum_i \hat{w}_{i,k}}{\sum_i \hat{w}_{i,k}^2} \right)^{-1} \frac{\sum_i \hat{w}_{i,j}}{\sum_i \hat{w}_{i,j}^2} \quad (\text{C.5})$$

⁴⁶⁷⁷ which has the form of Eq. (7.16).

⁴⁶⁷⁸ Alternatively, one might consider the case that the cross section σ is not known
⁴⁶⁷⁹ and should be predicted by the reweighting. In this case, one should require that
⁴⁶⁸⁰ the normalizations v_j do not change the total yield in the limit of large statistics,
⁴⁶⁸¹ implying $\sum_j v_j = 1$. This leads to the Lagrange function

$$\mathcal{L}(v_j, \lambda) = \sum_{i,j} v_j^2 \hat{w}_{i,j}^2 + \lambda \left(\sum_j v_j - 1 \right) \quad (\text{C.6})$$

⁴⁶⁸² from which one finds through an analogous calculation

$$v_j = \left(\sum_k \frac{1}{\sum_i \hat{w}_{i,k}^2} \right)^{-1} \frac{1}{\sum_i \hat{w}_{i,j}^2}. \quad (\text{C.7})$$